



HAL
open science

Photo-isomerization and photo-induced NO release in ruthenium nitrosyl compounds

Liya Khadeeva

► **To cite this version:**

Liya Khadeeva. Photo-isomerization and photo-induced NO release in ruthenium nitrosyl compounds. Material chemistry. Université de Rennes, 2016. English. NNT : 2016REN1S067 . tel-01450396

HAL Id: tel-01450396

<https://theses.hal.science/tel-01450396>

Submitted on 31 Jan 2017

HAL is a multi-disciplinary open access archive for the deposit and dissemination of scientific research documents, whether they are published or not. The documents may come from teaching and research institutions in France or abroad, or from public or private research centers.

L'archive ouverte pluridisciplinaire **HAL**, est destinée au dépôt et à la diffusion de documents scientifiques de niveau recherche, publiés ou non, émanant des établissements d'enseignement et de recherche français ou étrangers, des laboratoires publics ou privés.

THÈSE / UNIVERSITÉ DE RENNES 1
sous le sceau de l'Université Bretagne Loire

pour le grade de

DOCTEUR DE L'UNIVERSITÉ DE RENNES 1

Mention : Physique

Ecole doctorale Science de la Matière

présentée par

Liya KHADEEVA

préparée à l'unité de recherche

Institut de Physique de Rennes UMR CNRS 6251

Université de Rennes 1

**Photoisomerization and
photoinduced NO release
in Ruthenium nitrosyl
compounds**

**Thèse soutenue à
Université de Rennes 1
le 13 Octobre 2016**

devant le jury composé de :

Guy BUNTINX

Directeur de recherche CNRS, LASIR,
France / examinateur

Ryszard NASKRĘCKI

Professeur, Université Adam Mickiewicz
de Poznań, Pologne / rapporteur

Philippe GUIONNEAU

Professeur, Université de Bordeaux,
France / rapporteur

Isabelle DIXON

Chargée de recherche CNRS, LCPQ,
France / examinatrice

Isabelle MALFANT

Professeur, LCC Toulouse,
France / membre

Marylise BURON

Professeur, Université de Rennes 1,
France / directrice de thèse

*Abstract***PHOTOISOMERIZATION and PHOTOINDUCED NO^\bullet RELEASE in RUTHENIUM NITROSYL COMPOUNDS**

by Liya KHADEEVA

This Ph. D. thesis is focused on the experimental study of two photoinduced processes observed in various $[ML_5NO]$ complexes, where $M = Fe, Ru, \dots$, $L = CN, Cl, \dots$: (i) photoisomerization, where the system goes from N-bound state ($M - NO$, stable GS state) to O-bound state ($M - ON$, metastable MSI state) and a second metastable state, ‘side-on’ MSII ($M <_O^N$) is observed during the inverse phototransformation, $MSI \rightarrow$ ‘side-on’ MSII \rightarrow GS; (ii) photoinduced release of NO^\bullet radical.

The photoisomerization is investigated in single crystals of $[Ru(py)_4Cl(NO)](PF_6)_2 \cdot 1/2H_2O$ compound by means of X-Ray diffraction, steady state visible and time-resolved UV-visible absorption spectroscopies. During these experiments we observed the evidence of a two-step photon absorption process ($\lambda = 473 \text{ nm}$), we followed the dynamics of direct and inverse photoswitching by the evolution of lattice parameters and absorption in the visible range and we characterized the structure of ‘side-on’ MSII state. The nature of MSII in the direct photoswitching, $GS \rightarrow MSI$, seems to be different from the ‘side-on’ configuration, however, we do not have a direct access to this state due to its low population.

The role of water molecule in the unit cell of $[Ru(py)_4Cl(NO)](PF_6)_2 \cdot 1/2H_2O$ complex was tested by X-Ray diffraction studies on hydrated, dehydrated and rehydrated samples. The effect of sample dehydration on the unit cell parameters evolution and MSII species generation during the $MSI \rightarrow MSII \rightarrow GS$ inverse photoswitching is presented.

The photoinduced NO^\bullet release in *trans*– $(Cl, Cl)[Ru^{II}(FT)Cl_2(NO)]PF_6$ system in acetonitrile solution is studied by the UV-visible and mid-IR absorption spectroscopies, both steady state and time-resolved. By observing the ultra-fast dynamics of phototransformation we evidenced a secondary photochemistry. The nature of photoproduct is discussed within the recent theoretical calculations and the photoisomerization process.

UNIVERSITÉ DE RENNES 1

Résumé

PHOTOISOMÉRIISATION et LIBÉRATION PHOTOINDUITE de NO^\bullet RADICAL dans les COMPLEXES de RUTHÉNIUM à LIGAND NITROSYLE

par Liya KHADEEVA

Ce travail de thèse est centré sur l'étude expérimentale de deux types de transformations photoinduites observées dans différents complexes métalliques (Fe, Ru, \dots) à ligand nitrosyle: (i) la photoisomérisation au cours de laquelle le ligand NO passe d'un état lié par l'azote ($M - NO$, état stable GS) à un état lié par l'oxygène ($M - ON$, état métastable MSI). C'est un processus réversible et un second état métastable, 'side-on' MSII ($M < \overset{N}{O}$) est observable au cours du processus inverse, $MSI \rightarrow$ 'side-on' MSII \rightarrow GS; (ii) la libération photoinduite du radical NO^\bullet .

La photoisomérisation a été étudiée dans le système $[Ru(py)_4Cl(NO)](PF_6)_2 \cdot 1/2H_2O$ (sur monocristal) par la diffraction des RX, l'absorption visible statique et l'absorption UV-Vis résolue en temps. Nous avons pu mettre en évidence un processus d'absorption de photons ($\lambda = 473 \text{ nm}$) en deux étapes, suivre la dynamique des transformations directes et inverses par l'évolution des paramètres de maille et des l'absorption optique visible, caractériser structuralement l'état 'side-on' MSII. La nature de l'état intermédiaire, MSII, lors du processus direct semble être différente de l'état 'side-on' mais la très faible population de cet intermédiaire n'a pas permis de trancher définitivement.

Le rôle de la molécule d'eau dans la maille du complexe $[Ru(py)_4Cl(NO)](PF_6)_2 \cdot 1/2H_2O$ a été testé par diffraction des RX sur les échantillons hydratées, déshydratées et réhydratées. L'effet de déshydratation sur l'évolution des paramètres de maille et sur la génération d'espèces MSII au cours de la photocommutation inverse, $MSI \rightarrow$ MSII \rightarrow GS, est présenté.

La libération photoinduite du radical NO^\bullet a été étudiée dans une solution d'acétonitrile du complexe *trans* - $(Cl, Cl)[Ru^II(FT)Cl_2(NO)]PF_6$ par spectroscopies d'absorption UV-Vis et Mi-IR, statiques et résolues en temps. En observant la dynamique ultra-rapide de la phototransformation, nous avons mis en évidence une photochimie secondaire. La nature de photoproduit est discuté par rapport à de récents calculs théoriques et au processus de photoisomérisation.

Acknowledgements

I would like to thank first my thesis advisor Prof. Marylise BURON at Institut de Physique de Rennes, Université de Rennes 1 (IPR UR1), who gave me a lot of autonomy and independence during these three years, and at the same time who was always there to provide me with valuable insights and suggestions on possible development of the research project. I learnt a lot from her and I am grateful for such a wise supervision.

I would also like to thank the experts at IPR UR1, Rennes, who were involved in this research project: Maciej LORENC and Marina SERVOL with whom I worked a lot on the time-resolved optical experiments; Wawrzyniec KASZUB with whom we did the steady state visible spectroscopy; Loïc TOUPET and Elżbieta TRZOP with whom we worked closely on X-Ray diffraction data collection and refinement; Marco CAMMARATA and Sergio DI MATTEO who helped a lot with the X-Ray absorption experiment setup and data analysis; Hervé CAILLEAU for valuable comments on the paper. Without their deep understanding of the subject and experimental techniques this thesis work would not be successfully finished.

I would like to thank our collaborators: Prof. Isabelle MALFANT, Laboratoire de Chimie de Coordination du CNRS, Toulouse, for providing us with high-quality samples and fruitful discussions on research work during these years; Prof. Jacek KUBICKI, Adam Mickiewicz University, Poznań, for welcoming us in his laboratory in Poznań, Poland, for working with us on the experimental setup and the interpretation of the results.

I would like to thank the reporters of this thesis, Prof. Ryszard NASKREŃCKI, Adam Mickiewicz University, Poznań, and Prof. Philippe GUIONNEAU, Université de Bordeaux, for their valuable comments and proposed corrections on thesis manuscript, as well as the rest of thesis jury: Guy BUNTINX, directeur de recherche CNRS, Laboratoire de Spectrochimie Infrarouge et Raman in Lille and Isabelle DIXON, Chargée de recherche CNRS, Laboratoire de Chimie et Physique Quantiques in Toulouse, for exciting debate and new ideas proposed during the thesis defense.

I would also like to say thanks to my colleagues at IPR UR1, Rennes: Serhane ZERDANE, Andrea MARINO, Xu DONG, Laurent GUÉRIN, Eric COLLET, Bertrand TOUDIC for being great part of the team and making my work interesting.

Finally, I must express my very profound gratitude to my parents and to my friends for providing me with support and encouragement throughout these years of research work. This thesis would not have been possible without them.

Thank you, guys !

Liya Khadeeva

Contents

Abstract	i
Résumé	ii
Acknowledgements	iii
Contents	iv
GENERAL INTRODUCTION	1
1 Photoisomerization in a single crystal of ruthenium nitrosyl compound: two-step photon absorption process	5
1.1 Structural studies by X-Ray diffraction	6
1.1.1 Unit-cell parameters as a tool to probe linkage isomers	8
1.1.2 Temperature dependence of photoisomerization kinetics	10
1.1.3 Structure of MSI state under 473 nm irradiation at 8 K and 100 K	12
1.1.4 Structural determination of MSII state under IR irradiation at 8 K and at 100 K	13
1.2 Visible absorption spectroscopy studies	18
1.2.1 Evidence of a two-step photon absorption driving the <i>Ru – NO</i> to <i>Ru – ON</i> photoswitching under the blue light irradiation	18
1.2.2 The <i>Ru – ON</i> to <i>Ru – NO</i> reverse photoswitching probed by visible spec- troscopy	21
1.2.3 Optical density spectrum and properties of intermediate MSII species	24
1.2.4 Nature of intermediate MSII species under the blue light irradiation	26
1.2.5 Independence of MSI population dynamics from the polarization of irradi- ation	27
2 Role of water molecule during the photoisomerization process in single crystal	31
2.1 Unit cell parameters evolution followed by single crystal X-Ray diffraction	32
2.1.1 Dehydration process during the heating of a single crystal	32
2.1.2 Comparison of hydrated and dehydrated GS structures at 100 K.	34
2.1.3 Photoisomerization of the dehydrated crystal in comparison with its hy- drated form	36
2.2 Structure of a dehydrated MSI and MSII ^{IR} states determined by means of X-Ray diffraction	42
2.2.1 Comparison of MSI state in dehydrated and rehydrated crystal	42
2.2.2 MSII ^{IR} structural determination in dehydrated and rehydrated forms	44

2.2.3	Influence of water in the crystal on the MSII ^{IR} species population	48
3	Photoisomerization in $[Ru(py)_4Cl(NO)](PF_6)_2 \cdot 1/2H_2O$ single crystal: chasing MSII state by ultrafast optical experiments in the visible range	51
3.1	Introduction	52
3.2	Time-resolved studies: chasing MSII optical signature	55
3.2.1	Monochromatic pump-probe measurements	55
3.2.2	Monochromatic pump white light probe experiment	57
3.2.3	Single shot experiment	58
3.3	Discussion	60
4	<i>NO</i> release in <i>trans</i> – (Cl, Cl)$[Ru^{II}(FT)Cl_2(NO)]PF_6$ isomer: studies in acetonitrile solution	65
4.1	Photosteady measurements: electronic and vibrational spectra	67
4.1.1	UV-visible measurements	67
4.1.2	FTIR measurements	69
4.2	Time-resolved studies of the photoinduced <i>NO</i> release	72
4.2.1	Time-resolved UV-visible measurements with magnetic stirrer and static cell	72
4.2.2	Time-resolved mid-IR studies with circulation system and flow cell	76
4.2.3	Monochromatic pump-probe studies in UV-visible range with circulation system and flow cell	79
	CONCLUSIONS	85
	APPENDIX A: X-Ray diffraction studies	93
	APPENDIX B: Experimental details of X-Ray data collections presented in Chapter 1	95
	APPENDIX C: Experimental details of X-Ray data collections in dehydration studies presented in Chapter 2	101
	APPENDIX D: Selected bond lengths and angles in dehydrated and rehydrated crystals during the photo-isomerization	121
	APPENDIX E: Experimental details of absorption spectroscopy	125
	APPENDIX F: X-Ray absorption spectroscopy studies	137
	Publications, Conferences	143

GENERAL INTRODUCTION

Thanks to constant development and improvement of scientific methods we got to the point where we can control the properties of materials by light, temperature, pressure on molecular level. This progress in materials is focused on many challenges of modern life and among those are high-capacity information storage devices and medical applications (heart diseases, cancer, sexual health etc.). The photosensitive metallic nitrosyl, nitro or sulfoxide systems have drawn a particular attention as they can address both of these challenges due to their unique properties directly controlled by the light [1]. These metallic complexes undergo the photoswitching from one state (ground state or metastable) to another under the light irradiation of a certain wavelength.

Perhaps one of the most studied complexes of metallic nitrosyl family is sodium nitroprusside dehydrate compound (SNP), $Na_2[Fe(CN)_5(NO)] \cdot 2H_2O$, this system became a prototype complex for the whole family of analogous $[ML_5NO]$ compounds. The first long-lived metastable state, MSI, was observed in SNP in the series of studies performed by Hauser et al. in 1977 [2, 3, 4] and the second long-lived state, ‘side-on’ MSII, was evidenced twelve years later in works [5, 6, 7]. The structures of light-induced isomers of SNP compound were first probed by Rüdlinger and co-workers in neutron diffraction experiments [8, 9] and were solved later on by group of Coppens in low temperature X-Ray diffraction experiment [10, 11]. It was found that the photoexcitation initiates the metal-to-ligand charge transfer (MLCT), from Fe atom to its NO -ligand, and rearrangement of molecular structure: the nitrosyl ligand rotates from initial ground state, $M-NO$ either by 180° to form isonitrosyl $M-ON$ species called MSI metastable state [6, 10, 12, 13] or by 90° to generate the ‘side-on’ configuration, $M <^N_O$, so-called MSII state as shown in Figure 1 [14, 15, 16].

The spectral range of photon energy for the isomerization process has been reported in several works [6, 10, 12, 17] and it was shown that by exposure of SNP to light in the blue-green spectral range [350 – 580 nm] we observe the photoisomerization either to MSI or MSII states. Moreover, the complete reverse photoswitching is possible under the red and NIR spectral range [8] as presented in Figure 1. Remarkably, the theoretical calculation using density functional theory (DFT) have confirmed the experimental results obtained in SNP [17, 18].

If early studies were mostly focused on first row transition metals, the last 30 years brought more interest in metals of 2nd and 3rd rows [19], particularly, the research on ruthenium complexes

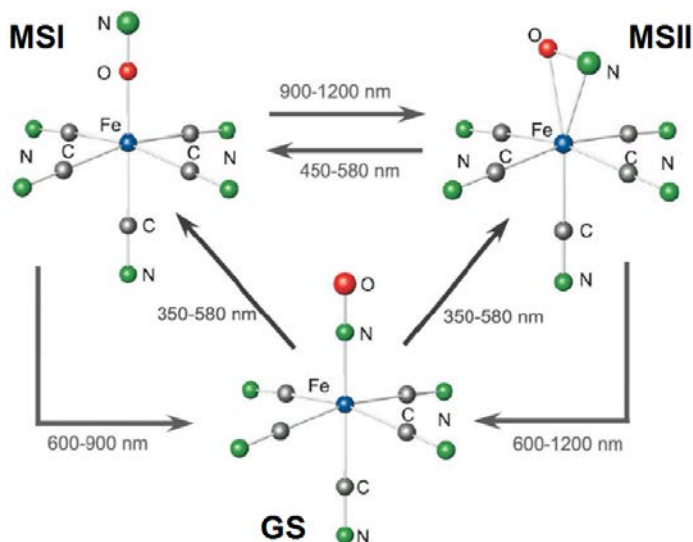


FIGURE 1: The spectral ranges used for photoswitching between GS ($M - NO$), metastable MSI ($M - NO$) and ‘side-on’ MSII ($M <^N_O$) states in $[Fe(CN)_5NO]^{2-}$ at low temperatures [15].

was largely launched when the application of ruthenium polypyridyl in dye-sensitised solar cells was reported [20, 21]. Since then, multiple studies were performed on various ruthenium compounds and their photophysical properties [22, 23, 24, 25, 26], moreover these advances have also triggered a wider research on systems with Mn metallic center [27, 28, 29]. The research of metal complexes resulted in such potential applications as oxygen sensors [30, 31], OLEDs [32, 33], holographic recording [34]. Through various experiments it was shown that such properties as lifetime of metastable states can be tuned by ligand substitution [1, 5, 35], while preserving its photosensitivity [15].

Other valuable photophysical properties are shown in ruthenium sulfoxide systems. In 2002 the group of Coppens demonstrated the linkage photoisomerization from η^1 to $\eta^2 - SO_2$ in ruthenium sulfoxide, $[Ru(SO_2)(NH_3)_4Cl]Cl$, under the 355 nm at 100 K [36]. Another ruthenium sulfoxide, $[Ru(bpy)_2(OSO)]^+$, was also reported to be highly photosensitive with $S \rightarrow O$ isomerization quantum yield of up to 0.8 [37, 38]. Ruthenium sulfoxide compounds were demonstrated to be promising complexes for high-density storage devices [39, 40], the research was performed in solution as well as in solid state in range of works [38, 41, 42, 43].

A complicated ‘double’ photoisomerization in $[Ru(bpy)_2(NO)(NO_2)](PF_6)_2$, where the nitrosyl (NO) and nitro (NO_2) groups transform into isonitrosyl and nitrito ligands, respectively was reported in work [44]. The same type of ‘double’ linkage isomerization was detected by IR measurements and density functional theory (DFT) in (*tetraphenylporphyrinatodianion*) $Fe(NO)(NO_2)$ in work of Novozhilova et al. [45]. Photoisomerization in complexes containing $\eta^2 - N_2$, $NO-$ and SO_2- -based ligands is thoughtfully described in the review of 2002 by Coppens group [1], where the mechanisms of photoisomerization are similar to the SNP case. The complexes with double NO -based ligand were reported in work [46], where authors show multiple light-induced metastable NO linkage isomers in dinitrosyl compound $[RuCl(NO)_2(PPh_3)_2]BF_4$ by means of X-Ray diffraction and IR spectroscopy, specifically a peculiar geometry with 130° angle of

$Ru - N - O$ observed in GS and its bending to 109° in one of the metastable states, see Figure 2.

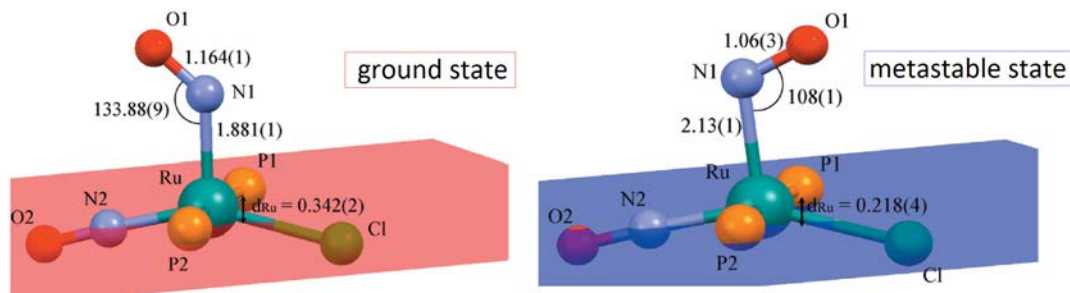


FIGURE 2: Structural model of ground state of $[RuCl(NO)_2(PPh_3)_2]BF_4$ and one of metastable states. The basal planes are depicted in red and blue [46].

In spite of all this progress on the photosensitive materials there are still a lot of drawbacks and challenges to overcome, and probably one of the most difficult one is the efficiency of the photoisomerization. Most of the discussed compounds show a limited photoconversion rate, which is strong limitation for the practical applications in devices [34, 47, 48]. Therefore, a lot of efforts are focused on the search for the high photoreactivity which is essential for the storage devices. Such systems are proposed, for example, in work of Warren et al. on nickel(II) nitro compounds with a 100% reversible transformation from nitro to nitrito complex under the 400 nm at 100 K, $Ni - NO_2 \rightarrow Ni - ONO$ [49, 50]. But those are not the only complexes found to have complete photoconversion, another example is the $[Ru(py)_4Cl(NO)](PF_6)_2 \cdot 1/2H_2O$ with a 100% of $Ru - NO \rightarrow Ru - ON$ which is nowadays a unique complex in the family of ML_5NO systems, where the typical conversion rate does not exceed 50% (SNP case) [15]. From experimental point of view this system gives a great opportunity of photocrystallographic analysis as well as direct comparison of X-ray structural determinations and ab-initio calculations.

What is more important, a lot of research is concentrated on the metallic nitrosyl complexes due to crucial biological functions of nitric oxide [51, 52], such as immune and blood pressure regulation [53], neurotransmission [54], anti-tumor activity [55]. It has led to the development of NO -releasing drugs, based on the NO liberation process in the nitrosyl compounds under the light irradiation. The iron nitrosyl complexes release large amounts of NO when irradiated with low energy light, however, due its lack of stability and toxicity in physiological conditions a search for suitable $M - NO^6$ alternatives using Ru or Mn, for example, is required. The ruthenium complexes were found to be very stable over a long time in physiological conditions, which makes them great candidates for anticancer drugs [56, 57]. However, there is still an on-going fight for a higher quantum yield in these complexes. Meyer and co-workers observed that the NO release process can be strongly dependent on the solvent used [58]. Nevertheless, the NO -releasing drugs are successfully developing and not only as cancer treatment, but also in cardiovascular therapy [59], as multifunctional agents for photodynamic therapy [60] and at present a possible role of NO molecule in AIDS is discussed [61].

Surely, to make potential applications work efficiently we have to understand the underlying mechanisms of photoisomerization and of NO^\bullet release processes. In this Thesis the ruthenium

nitrosyl complexes are studied as they are offering high photoconversion rates, which makes it possible to have a direct access to the metastable states through the experiments. The goal of this Thesis is to observe and study the mechanisms of photoreactions as well as to probe and analyse the metastable states experimentally. The two investigated photoprocesses were:

- the photoisomerization in the solid state at the molecular level as well as the complete photoconversion in $[Ru(py)_4Cl(NO)](PF_6)_2 \cdot 1/2H_2O$ in single crystals (Chapters 1, 2, 3);
- the NO^\bullet release in $trans(Cl, Cl) - [Ru^{II}(FT)Cl_2(NO)]PF_6$ in acetonitrile solution under the light irradiation (Chapter 4).

In this Thesis several different methods are employed to understand the light-induced changes in ruthenium nitrosyl compounds: the X-Ray diffraction for structural studies, the static UV-visible and IR spectroscopy to access the absorption spectra, the time-resolved optical experiments to detect the intermediate states during the photoswitching and the X-Ray absorption spectroscopy to access the nature of the photoproduct.

In Chapter 1 the two-step photon absorption process during the photoswitching in $[Ru(py)_4Cl(NO)](PF_6)_2 \cdot 1/2H_2O$ complex is proposed as a result of the visible absorption measurements under the continuous light irradiation. The structural studies are also presented in this Chapter following the change of lattice parameters during the photoisomerization.

The dehydrated form of $[Ru(py)_4Cl(NO)](PF_6)_2 \cdot 1/2H_2O$ single crystals are investigated in comparison with their hydrated and rehydrated forms, the significant changes in structural rearrangement and the role of crystal water during the photoswitching are discussed in Chapter 2.

Direct structural and optical characterization of the transient MSII state is needed during the $Ru - NO$ to $Ru - ON$ process. Several attempts to catch this transient state by time-resolved optical studies, the associated experimental challenges and main results are discussed in Chapter 3.

In Chapter 4 the mechanisms of NO^\bullet release are studied in $trans(Cl, Cl) - [Ru^{II}(FT)Cl_2(NO)]PF_6$ isomer in acetonitrile solution by time-resolved and steady state measurements in IR and UV-visible regions performed in Poznań and Rennes.

The Appendices include all the experimental details of performed experiments.

Chapter 1

Photoisomerization in a single crystal of ruthenium nitrosyl compound: two-step photon absorption process

Photoisomerization is the conversion of one isomer into another under the light irradiation. Various systems containing $[ML_5NO]$ molecule, where $M=Fe, Ru...$ and $L=F, Cl, Br, CN...$ exhibit photoswitching under continuous light (CW) irradiation between the ground state N-bound nitrosyl (GS, $M-NO$), isonitrosyl (MSI, $M-ON$) and side-on (MSII, $M < \overset{N}{O}$) configurations [1, 62]. Identification of MSI and MSII as linkage isomers occurred in the 1990s on the prototype SNP compound (see General Introduction) thanks to accurate diffraction studies: in MSI, the NO ligand is rotated by 180° to an O-bound configuration of the NO ligand, while the MSII state adopts a side-on configuration of the NO ligand [10, 14]. Metastable populations vary from one compound to another and are often limited to a few percent. The $[Ru(py)_4Cl(NO)](PF_6)_2 \cdot 1/2H_2O$ system is at present unique compound in that the GS to MSI transformation is nearly complete in a single crystal, as observed in previous structural studies combined with solid-state calculations based on density functional theory (DFT) [62].

The $[Ru(py)_4Cl(NO)](PF_6)_2 \cdot 1/2H_2O$ compound is presently the model system for the study of photoswitching between $Ru-NO$ and $Ru-ON$ which is associated with a clear colour change (see Figure 1.1).

During my PhD I have continued this work by:

- quantifying the colour change in the visible range by optical density (OD) measurements
- focussing on the photoswitching dynamics, measuring changes during the light irradiation
 - Bragg peak and lattice parameters changes
 - OD changes

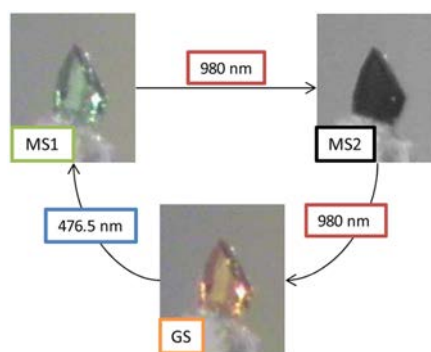


FIGURE 1.1: colour change of $[Ru(py)_4Cl(NO)](PF_6)_2 \cdot 1/2H_2O$ single crystal at low temperatures under the blue and IR light irradiation (taken from [62, 63], Figure 1).

- testing various pumping wavelengths, in particular red and green (see Figure 1.2)

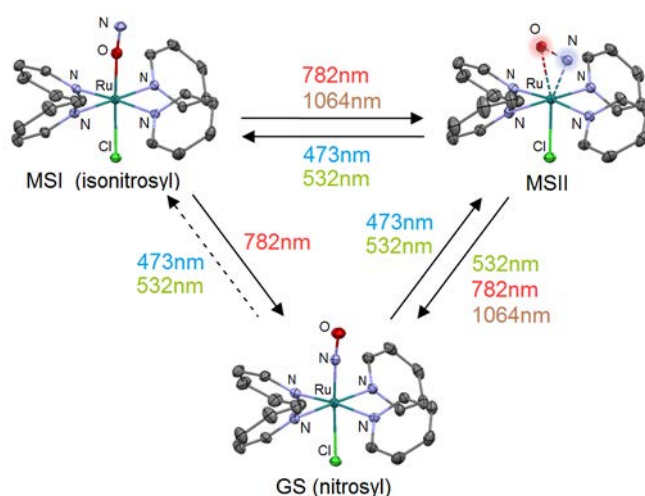


FIGURE 1.2: Probed wavelengths for the photoswitching between GS, MSI and MSII states (schematic molecular views, see ref. [62] and [15]); here the MSII state view is the side-on configuration of the $[Ru(py)_4Cl(NO)](PF_6)_2 \cdot 1/2H_2O$ single crystal at low temperatures.

1.1 Structural studies by X-Ray diffraction

A hydrated form of $[Ru(py)_4Cl(NO)](PF_6)_2 \cdot 1/2H_2O$ single crystal was studied. The monoclinic unit cell of a single crystal consists of two independent sites, shown in blue and orange colours in Figure 1.3, the counter anions $(PF_6)^-$ are presented in grey and water molecule in red colours. The space group is $P2_1/c$, $Z = 8$. At 100 K values of the lattice parameters in the ground state (GS) are $\mathbf{a} = 15.748(2)$, $\mathbf{b} = 13.43(2)$, $\mathbf{c} = 26.794(4)$, $\beta = 92.504(12)$ (see Table 1.1). The independent sites form layers along \mathbf{a} -axis, however, there are no $\pi \cdots \pi$ interactions between pyridine cycles as distances are quite large: 7.249 Å and 7.770 Å, while the typical distance of $\pi \cdots \pi$ interaction is around 3 Å. It is interesting to note as well that the water molecule is located not far from the NO ligand of molecule $Ru1$, the distance is around 3.07 Å, and this close location of water gives a disorder on one of the pyridine cycles of the molecule (see the structure of GS state in Chapter 2).

	Crystal data		
	GS	MSI	MSII ^{IR}
Chemical formula	$2(C_{20}H_{20}ClN_5ORu) \cdot 4PF_6 \cdot H_2O$		
M_r	1563.8		
Cell setting, space group	Monoclinic, $P2_1/c$		
Z	8		
Temperature, K	100		
Radiation type	Mo K_α		
Crystal colour	orange	green	black
a , Å	15.748(2)	15.781(2)	15.777(2)
b , Å	13.43(2)	13.419(2)	13.444(2)
c , Å	26.794(4)	26.810(4)	26.817(4)
β , °	92.504(12)	92.640(12)	92.081(12)
V , Å ³	5661(2)	5671(2)	5684(2)

TABLE 1.1: Experimental details of studied system [64].

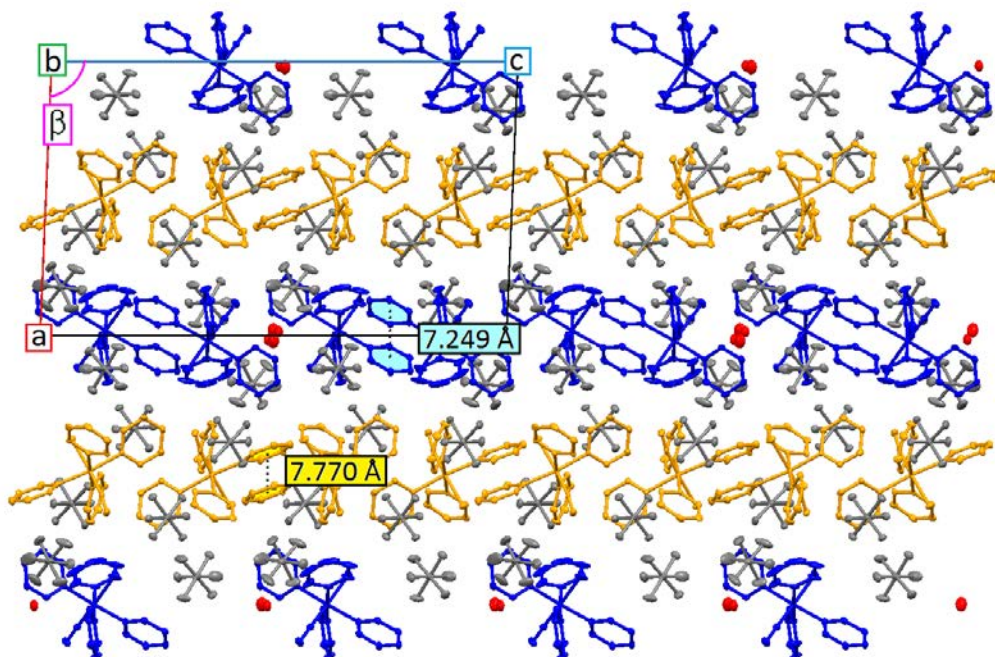


FIGURE 1.3: The packing of single crystal in ac plane in its hydrated form: two independent sites of $[Ru(py)_4Cl(NO)]^{2+}$ cation (blue and orange), anions $(PF_6)^-$ (grey) and water molecule (red). The hydrogen atoms are omitted for clarity. The plot is based on the refinement with GS model at 100 K. The distances between pyridine cycles are indicated, 7.249 Å and 7.770 Å.

Single crystals of $[Ru(py)_4Cl(NO)](PF_6)_2 \cdot 1/2H_2O$ compound undergo the photoisomerization process with formation of two metastable states, MSI under the blue light irradiation and MSII under the IR light irradiation (see Figures 1.1 and 1.2 [62]). The monoclinic space group ($P2_1/c$) of studied system does not change during the photoconversion. The isostructural nature of photochemical reaction is presented in Figure 1.4 through the plane reconstruction for GS, MSI and MSII^{IR} (the mixture of GS and MSII species): in all three cases we evidence the screw axis 2_1 (parallel to b) and a glide plane c (perpendicular to b), which gives us reflections like $(0K0)$,

$K=2n$, $n=0,1,2,\dots$, (H0L) with only $L=2n$, $n=0,1,2,\dots$ presented. The experimental details are summarized in Appendix A and B.

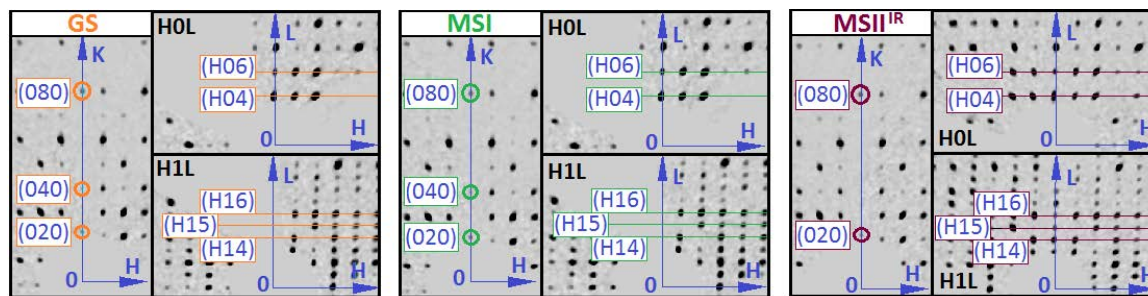


FIGURE 1.4: Plane reconstruction from data collections during the photoisomerization of the $[Ru(py)_4Cl(NO)](PF_6)_2 \cdot 1/2H_2O$ single crystal by irradiation with 473 nm , $280\text{ mW} \cdot \text{cm}^{-2}$ and then 1064 nm , $130\text{ mW} \cdot \text{cm}^{-2}$ at 100 K . The same space group is observed in all three cases, i.e. $P2_1/c$ with typical reflections $(0K0)$, $K=2n$, $n=0,1,2,\dots$, (H0L) $L=2n$, $n=0,1,2,\dots$. The plane (H1L) is given for comparison.

1.1.1 Unit-cell parameters as a tool to probe linkage isomers

The $Ru - NO$ to $Ru - ON$ photoswitching and the reverse process in hydrated form of single crystals of $[Ru(py)_4Cl(NO)](PF_6)_2 \cdot 1/2H_2O$ compound were followed through the change of structural signatures, such as unit cell parameters and Bragg peaks intensities [64]. At 100 K with 473 nm a saturation of the signal happens after around one hundred minutes of laser exposure with around 280 mW/cm^2 , i.e. around $2000\text{ J} \cdot \text{cm}^{-2}$. Note that for the X-Ray studies polarization of the laser beam is not important as the crystal is rotated along different axes during the data collection.

The complete or quasi-complete $Ru - NO$ to $Ru - ON$ photoisomerization under blue light irradiation has been investigated by single-crystal X-Ray diffraction (see MSI structural refinement later in this Chapter and the following Chapter, as well as refinement details in Appendix B and C): it shows no clear difference between a model with total conversion (100% of MSI) and a mixed GS-MSI model refining the MSI conversion rate. The latter shows a mixing of 93(2)% of MSI and 7(2)% of GS states, but average atomic positions and thermal parameters obtained from two models are identical within error bars. In other words, the GS to MSI photochemical reaction is either complete or quasi-complete since the presence of a few % of GS species cannot be excluded.

Following the evolution of lattice parameters under the blue light irradiation, the structural changes between GS and MSI show the highest change on evolution of \mathbf{a} crystallographic axis ($\Delta\mathbf{a} = +0.032(2)\text{\AA}$, Figure 1.5 (a)). They are greater than those measured in the SNP compound [10], most likely due to the higher photoconversion rates in $[Ru(py)_4Cl(NO)](PF_6)_2 \cdot 1/2H_2O$. Observed structural evolution during the $Ru - NO$ to $Ru - ON$ photoswitching with 473 nm is continuous, i.e. does not show any signature of an intermediate state. Differently, evidence of MSII state as an intermediate was obtained under IR irradiation of MSI [10, 14, 62]. The long lifetime of MSII species allows the recording of specific structural signatures on both unit

cell parameters and Bragg peak intensities. The side-on configuration of MSII species is seen through additional electronic densities on both sides of the $Ru - N - O$ axis (see [62] and MSII structure refinement presented later in this Chapter). Population of MSII species (few tens %) is the highest when the monoclinic unit cell volume is maximum and β angle is minimum during MSI to GS transition (Figure 1.5 (b,c)).

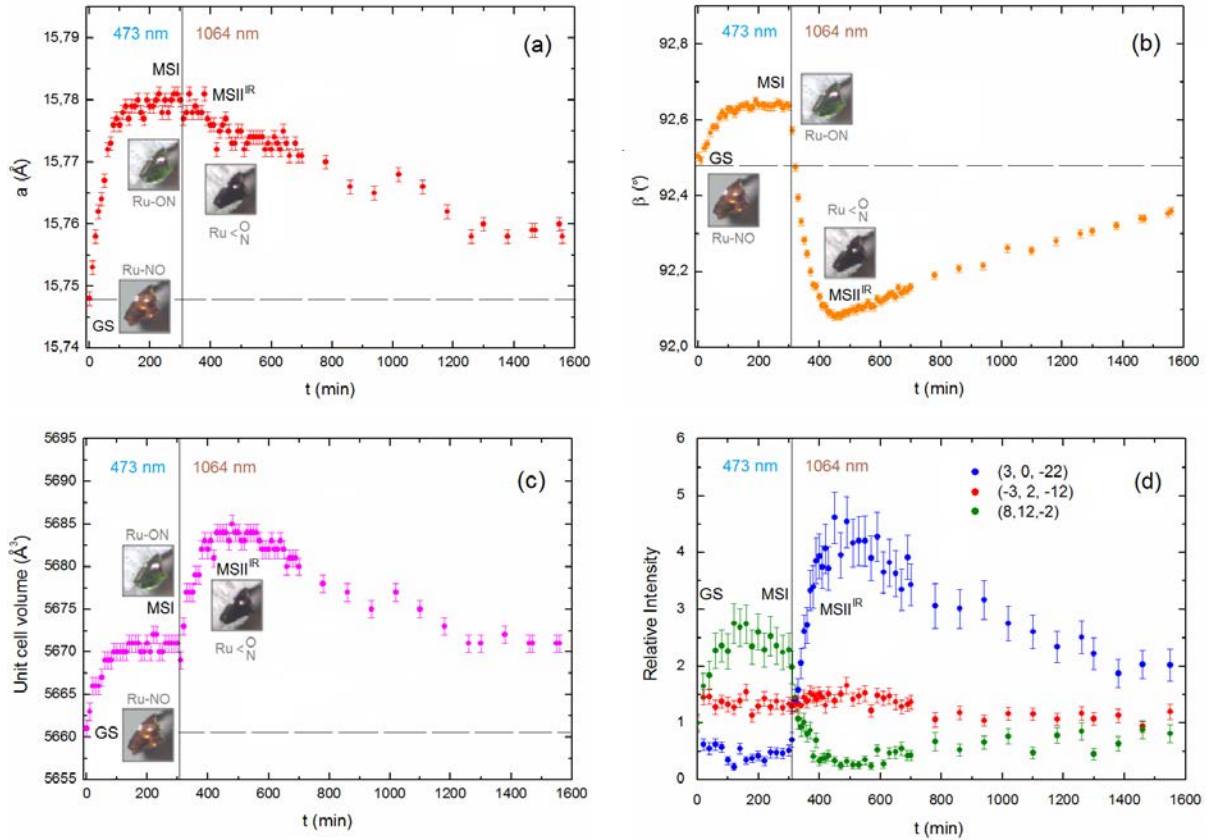


FIGURE 1.5: Time evolution of (a) lattice parameter a (Å), (b) the β angle (°), (c) unit cell volume (Å³) and (d) Bragg peak intensities during the light irradiation of the $[Ru(py)_4Cl(NO)](PF_6)_2 \cdot 1/2H_2O$ single crystal with 473 nm, 280 $mW \cdot cm^{-2}$ and then 1064 nm, 130 $mW \cdot cm^{-2}$ at 100 K.

The evolution of unit cell parameters thus offers a precise way to follow the MSI to GS photochemical reaction under IR light. At 100 K, the maximum of MSII population is observed here after 120 minutes of irradiation with a fluence of about 130 mW/cm^2 , i.e. $Q \approx 900 J/cm^2$, while the crystal turns dark. As pure MSII state cannot be reached, this mixed GS-MSII state is hereafter referred to as MSII^{IR} state. The evolution of lattice parameters during $Ru - ON$ to $Ru - NO$ photoswitching (Figure 1.5) differs from that during $Ru - NO$ to $Ru - ON$ phototransformation under the blue light. Moreover, evolution of some Bragg peaks intensities (Figure 1.5 (d)) also show significant dissimilarities between blue and IR light excitation, implying that the average atomic positions in the crystal evolve differently during these two photoprocesses. Very different molecular geometries between GS, MSI and MSII can explain the important structural rearrangements (lattice and Bragg peak intensities) resolved during the solid state photochemical reactions (see [62], structural refinements of MSI and MSII presented later in this Chapter, experimental and the structure refinement details in Appendix B).

Following the few tens of minutes of relative stability of the MSII^{IR} state (minimum of β angle and maximum of unit cell volume, see Figure 1.5), a slow evolution towards the GS state is observed. Nonetheless, at 100 *K* the GS state is not reached even after 15 hours of CW irradiation, which might be caused either by a very slow thermal relaxation or by a low population (a few %) of MSI state, as seen in the SNP compound [18].

1.1.2 Temperature dependence of photoisomerization kinetics

The structural studies of Ruthenium nitrosyl system were performed at three different temperatures: 140 *K*, 100 *K* and 10 *K*. First of all, we found out that the complete transformation back to GS under IR irradiation is possible at higher temperatures, 140 *K* in our case (see Figure 1.6 (a, b)). Second of all, one can notice that the lower the temperature is the stronger change in structural signatures is observed (higher growth of unit cell volume, stronger decrease in β angle value, Figure 1.6 and Table 1.2). This implies that the lifetime and population of MSII^{IR} species grow with the decrease of temperature. The most sudden and unexpected change is observed in unit cell parameter **c**, while at 100 *K* and 140 *K* it shows no specific behaviour, at 10 *K* one can notice a significant growth of **c** under IR light. The maximum of **c** is associated with minimum of β angle and therefore with the maximum of MSII^{IR} population.

GS \rightarrow MSI					
Temperature	$\Delta\mathbf{a}, \text{\AA}$	$\Delta\mathbf{b}, \text{\AA}$	$\Delta\mathbf{c}, \text{\AA}$	$\Delta\beta, ^\circ$	$\Delta V, \text{\AA}^3$
140 <i>K</i>	+0.035(2)	-0.016(2)	+0.012(4)	+0.117(12)	+8(2)
100 <i>K</i>	+0.033(2)	-0.011(2)	+0.016(4)	+0.136(12)	+10(2)
10 <i>K</i>	+0.020(2)	-0.016(2)	+0.026(4)	+0.141(12)	+5(1)
MSI \rightarrow MSII^{IR}					
Temperature	$\Delta\mathbf{a}, \text{\AA}$	$\Delta\mathbf{b}, \text{\AA}$	$\Delta\mathbf{c}, \text{\AA}$	$\Delta\beta, ^\circ$	$\Delta V, \text{\AA}^3$
140 <i>K</i>	-0.008(2)	+0.011(2)	-0.007(4)	-0.288(12)	+1(2)
100 <i>K</i>	-0.004(2)	+0.026(2)	+0.007(4)	-0.559(12)	+13(2)
10 <i>K</i>	-0.016(2)	+0.047(2)	+0.064(4)	-0.648(12)	+30(1)

TABLE 1.2: Comparative table of the changes in the unit cell parameters during the photoisomerization at 140 *K*, 100 *K* and 10 *K*.

The pronounced temperature dependence of the reaction kinetics during IR irradiation demonstrates that thermal decay of the MSII population drives the relaxation back to GS just as previously shown in the prototype SNP compound. The total conversion of the metastable MSI species back to GS state occurs rapidly by heating the sample above 260 *K*. Moreover, the single crystal preserves its switching yield after several photoswitching cycles. On the contrary, the repetition of photoswitching in the powder results into the sample ‘fatigue’ (decrease of

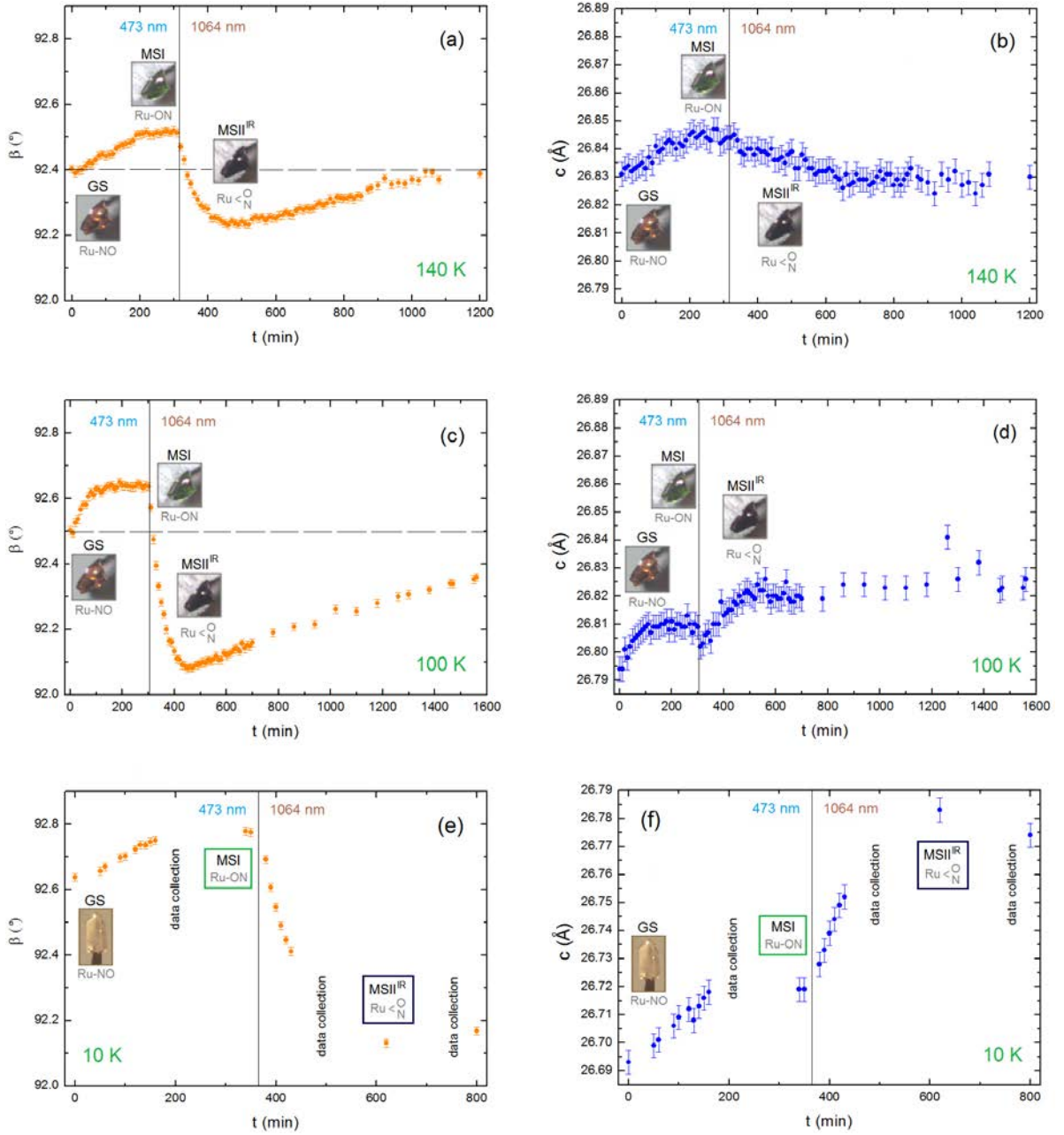


FIGURE 1.6: Time evolution of β angle (°) and unit cell parameter c (Å) of the $[Ru(py)_4Cl(NO)](PF_6)_2 \cdot 1/2H_2O$ single crystal during the irradiation of 473 nm, $280 mW \cdot cm^{-2}$ and then of 1064 nm, $130 mW \cdot cm^{-2}$ (a)-(b) at 140 K, (c)-(d) at 100 K, (e)-(f) at 10 K.

the metastable species populations) [15], which might be explained by defects, such as grain boundaries or impurities.

1.1.3 Structure of MSI state under 473 nm irradiation at 8 K and 100 K

The full data collection was taken at 8 K during the photoisomerization process from GS to MSI under the CW irradiation of 473 nm (Figure 1.7). For more experimental and the structure refinement details see Appendix B.

Previously, the structure of MSI state was reported at 100 K in work [62]. The data collection at 8 K was refined with MSI model with no restraints on geometry for non-hydrogen atoms and compared to the structure at 100 K in Table 1.3.

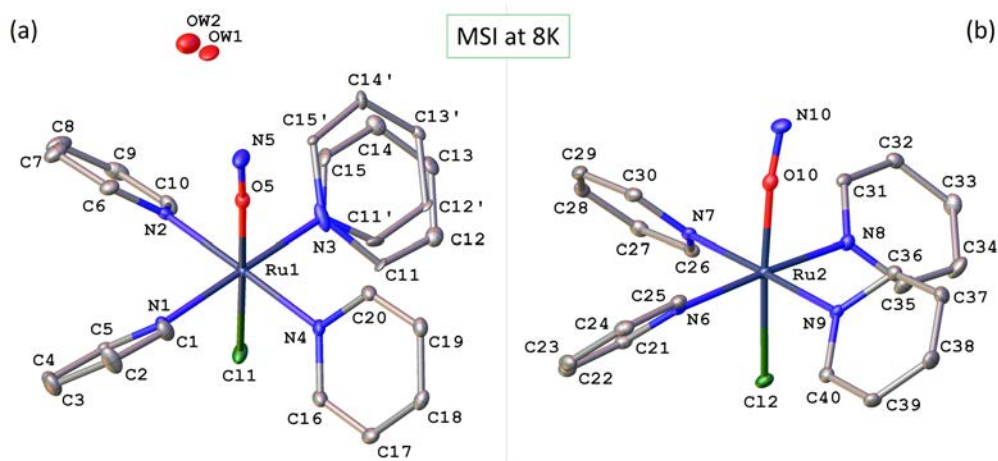


FIGURE 1.7: Structure of two independent sites of $[Ru(py)_4Cl(NO)]^{2+}$ cation and water molecule under the 473 nm irradiation at 8 K. The hydrogen atoms and anions $(PF_6)^-$ are omitted for clarity. The plot is based on the refinement with MSI model.

As expected, the $R1$ – factor is improving with temperature decrease, as we deal with less of thermal disorder. There is also a predictable reduction in unit-cell volume $V_{100K} = 5629.5(3) \text{ \AA}^3$ and $V_{8K} = 5605.94(14) \text{ \AA}^3$. Moreover, a very small elongation of $Ru1 - O5$ and $Ru2 - O10$ bonds is detected, while the distances of $N5 - O5$ and $N10 - O10$ stay close to 1.14 Å during the temperature decline. The angles presented in Table 1.3 do not change much either, and overall structure keeps its geometry at 8 K.

Distance/angle, $\text{\AA}/^\circ$	X-Ray	
	8 K	100 K [‡]
Ru1 – O5	1.8720(15)	1.8630(13)
N5 – O5	1.138(2)	1.140(2)
Ru1 – O5 – N5	178.26(15)	178.12(12)
Ru1 – N1	2.0995(17)	2.0949(13)
Ru1 – N2	2.0955(17)	2.0958(14)
Ru1 – N3	2.0984(18)	2.0932(14)
Ru1 – N4	2.1055(18)	2.1023(14)
Cl1 – Ru1 – O5	178.83(5)	178.93(4)
Ru1 – Cl1	2.2795(5)	2.2782(5)
Ru2 – O10	1.8664(15)	1.8619(12)
N10 – O10	1.141(2)	1.142(2)
Ru2 – O10 – N10	171.58(15)	171.43(13)
Ru2 – N6	2.0978(18)	2.1061(13)
Ru2 – N7	2.0946(17)	2.0954(15)
Ru2 – N8	2.0955(17)	2.0900(13)
Ru2 – N9	2.1114(17)	2.0930(15)
Cl2 – Ru2 – O10	175.70(5)	175.73(4)
Ru2 – Cl2	2.2825(5)	2.2798(5)
<i>Cell setting, space group</i>	Monoclinic, P 1 2 ₁ /c 1	
<i>a</i> , \AA	15.6738(2)	15.7224(4)
<i>b</i> , \AA	13.3899(2)	13.3917(4)
<i>c</i> , \AA	26.7423(4)	26.7648(7)
β , $^\circ$	92.7474(13)	92.603(2)
<i>V</i> , \AA^3	5605.94(14)	5629.5(3)
<i>R1-factor</i>	3.35%	4.2%
<i>GooF</i>	1.021	1.10
<i>No. of reflections</i>	12217	18723
<i>No. of parameters</i>	828	775
$\Delta\rho_{max}, \Delta\rho_{min}$, $\text{e}\text{\AA}^{-3}$	0.886, -0.889	0.66, -0.76

TABLE 1.3: MSI structure at 8 K and 100 K: selected bond distances (\AA) and angles ($^\circ$). For more experimental and the structure refinement details see Appendix B. [‡] Selected bond distances and angles from X-Ray refinement published in work [62].

1.1.4 Structural determination of MSII state under IR irradiation at 8 K and at 100 K

The full data collections were taken at 8 K and 100 K during the photoisomerization process from MSI to GS through MSII^{IR} under the CW irradiation of 1064 nm. The refinement in case of MSII^{IR} state (90° isomerization) is challenging as it is impossible to have 100% of pure transient state within the present experimental setup. All non-hydrogen atoms were refined anisotropically, while all hydrogen atoms were constrained by geometry. For more experimental and the structure refinement details see Appendix B.

We have followed the evolution of unit-cell parameters at 8 K and 100 K, in particular the β angle, to verify when we reach its minimum, which is associated with the maximum of MSII^{IR} population [64]. At 100 K the three consequent data collections (~ 4 hours each) did not give any strong variation in MSII population, around 40%, therefore all three data collections were merged and refined together to have one averaged structure, see Figure 1.9.

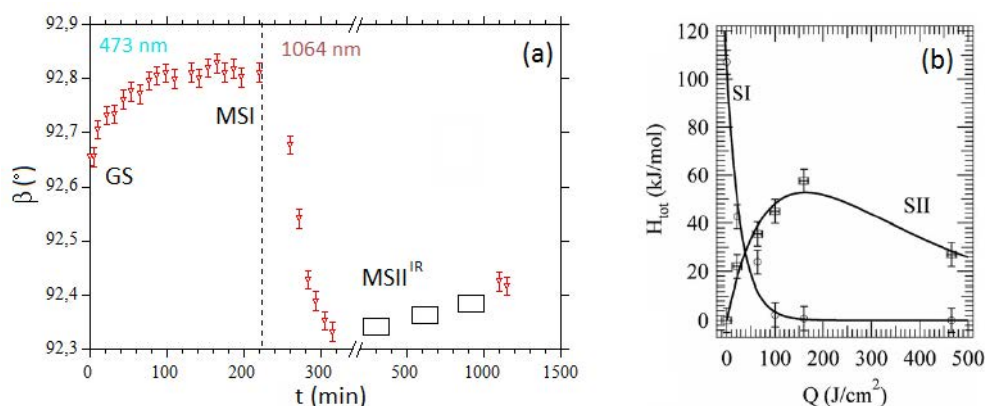


FIGURE 1.8: (a) Time evolution of β angle ($^{\circ}$) of the $[Ru(py)_4Cl(NO)](PF_6)_2 \cdot 1/2H_2O$ single crystal during the irradiation of 473 nm, $280 mW \cdot cm^{-2}$ and then of 1064 nm, $130 mW \cdot cm^{-2}$ at 100 K; (b) population conversion from MSI to MSII by 1064 nm irradiation at 120 K. The population of MSI decreases quite fast with exposure Q , while MSII population passes through a maximum first and then decreases slowly [15].

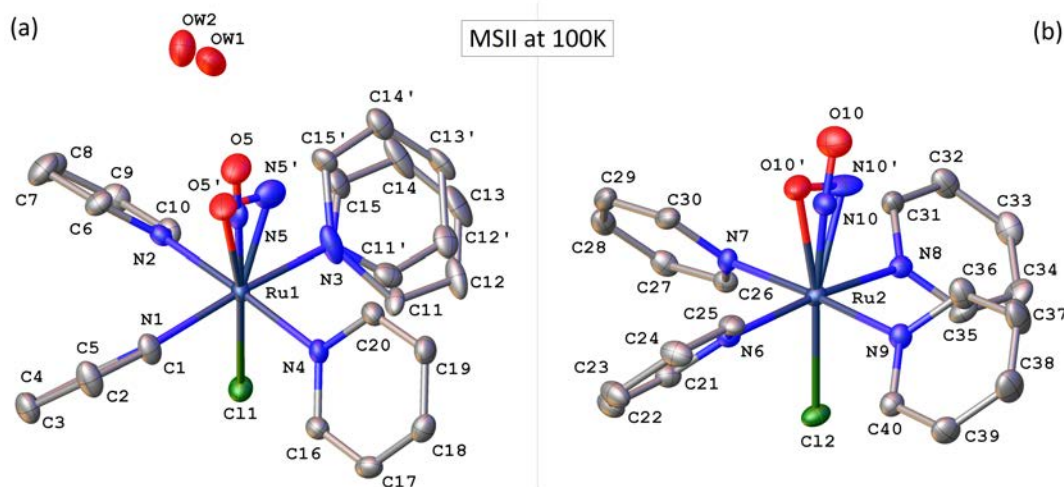


FIGURE 1.9: Structure of two independent sites of $[Ru(py)_4Cl(NO)]^{2+}$ cation and water molecule under the IR irradiation at 100 K. The hydrogen atoms and anions $(PF_6)^-$ are omitted for clarity. The plot is based on the refinement with GS/MSII^{IR} model.

From Figure 1.8 (b) from IR experiment on powder sample published in work [15] we expect to see a very fast depopulation of MSI, while the MSII population passes through maximum and then decreases slowly. Therefore, at the maximum population of MSII we would have a negligible population of MSI, and due to this argument we chose the mixture of GS/MSII^{IR} to refine our data collection. The unique restraint of the $N - O$ distance to be equal to value of 1.14 Å was applied during the refinement and the $Ru1 - N5$ and $Ru2 - N10$ refined distances were found to be of 1.775(8) Å and 1.768(5) Å, respectively (Figure 1.9), which is close to the $Ru - N$

bond length, 1.755(2) Å, of pure GS state [62] (see Table 1.4 last column). Thus our refinement confirms that GS/MSII^{IR} model is the suitable one at 100 K.

For the 8 K data collection the mix model GS/MSII^{IR} does not fit well. As both *N* and *O* are light atoms with a very close number of electrons, to choose the suitable model we check the distance between *Ru* and its closest neighbour. From previous experimental work on GS and MSI states (this PhD thesis, and work [62]) we know that in case of *N* atom as a closest neighbour we have *Ru* – *N* bond length close to 1.76 Å and in case of *O* we deal with *Ru* – *O* distance close to 1.86 Å (see Table 1.4 data collections at 8 K). For the first data collection taken at 8 K we observe the distances from *Ru* atoms to their first neighbours being close to *Ru* – *O* bond length, therefore, we consider the mix model MSI/MSII^{IR} to be an appropriate one in this case (see Figure 1.10 (a)-(b)), with ~ 40% of MSII^{IR} species.

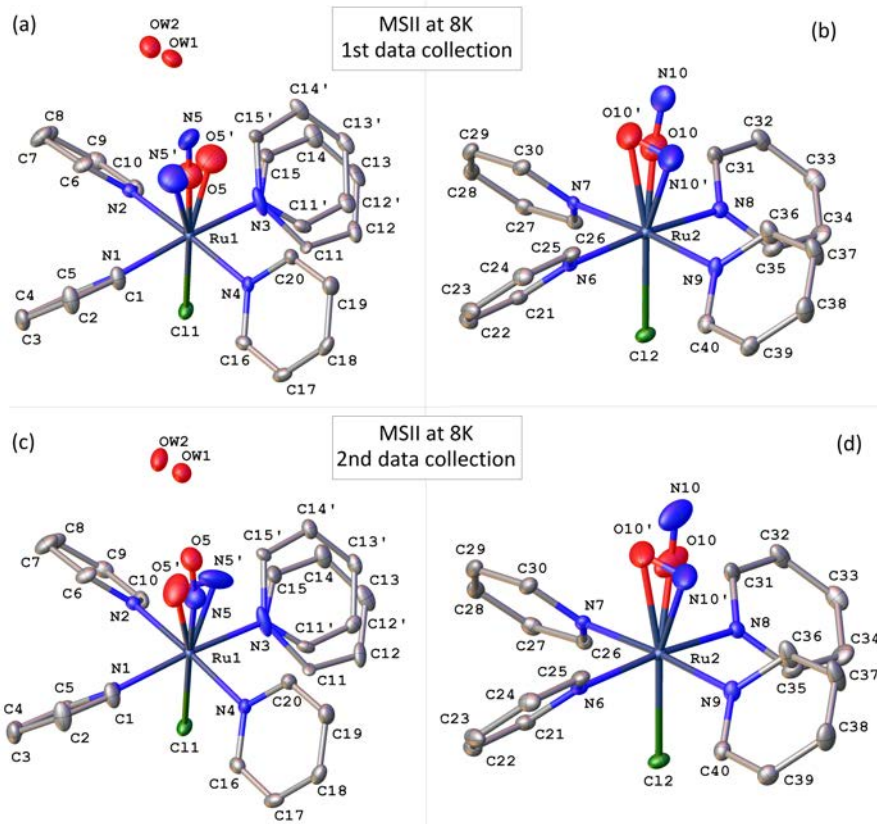


FIGURE 1.10: Structure of two independent sites of $[Ru(py)_4Cl(NO)]^{2+}$ cation and water molecule under the IR irradiation at 8 K: (a)-(b) the first data collection after around 150 min of IR irradiation, (c)-(d) the second data collection after around 400 min of IR irradiation (see Figure 1.6 (e)-(f)). The hydrogen atoms and anions $(PF_6)^-$ are omitted for clarity. The plot is based on the refinement with MSI/MSII^{IR} and GS/MSII^{IR} model.

For the second data collection at 8 K we have a different picture, one of the independent sites shows the distance close to *Ru* – *N* bond length, while the other one is clearly a mixture of MSI/MSII^{IR} (see Figure 1.10 (c)-(d)). Therefore, we use in here MSI/MSII^{IR} model for one independent site and GS/MSII^{IR} for another one. In agreement with the decreased value of β angle during the second data collection, the population of MSII^{IR} increases to reach ~ 50% as indicated in Table 1.4.

With these structural refinements we can see that the temperature decrease to 8 K slows down the dynamics of phototransformation and it is possible to detect the MSI state, while at 100 K the MSI state conversion to MSII is very fast (see Figure 1.8 (b) [15]). We detect with the first data collection at 8 K that both independent sites in unit-cell started to convert to MSII^{IR}, while some molecules are still in MSI state. Then with the second data collection at 8 K we observe the coexistence of three states, GS, MSI and ‘side-on’ MSII, while at 100 K we see the conventional model with GS/MSII^{IR} reported in [15].

The short contacts were also checked and they are presented in Table 1.5. The distance between atoms is considered a short contact if it is smaller than the sum of the Van der Waals radii of these two atoms. As the determination of Van der Waals radius for different elements is an on-going research, there are several values proposed by various physical methods, see Table 1 in [65]. We will work with the default values adopted in structure visualization tool, Mercury [66], i.e. the values proposed by Bondi [67]. In Table 1.5 the short contacts are listed for MSI state at 8 K , two consequent data collections of MSII^{IR} at 8 K and data collection of MSII^{IR} at 100 K . From Table 1.5 it is obvious that short contacts depend neither on the photoisomerization nor on the temperature. Such stability in short contacts values explains the significant change in lattice parameters during the photoswitching or temperature variation.

Distance/angle, Å/°	100 K		8 K		100 K
	GS [‡]	MSI [‡]	dat col 1 MSI/MSII ^{IR}	dat col 2 GS/MSII ^{IR}	GS/MSII ^{IR}
N5' – O5'	–	–	1.076(5)	1.052(5)	1.090(16)
Ru1 – N5'	–	–	2.001(5)	2.012(4)	1.948(9)
Ru1 – O5'	–	–	2.093(9)	2.042(7)	2.119(13)
N5' – Ru1 – O5'	–	–	30.38(16)	30.06(15)	30.7(5)
Cl1 – Ru1 – N5'	–	–	165.9(3)	160.8(2)	157.6(4)
Cl1 – Ru1 – O5'	–	–	163.6(3)	168.45(17)	171.1(4)
Ru1 – N5	1.7550(17)	–	–	1.786(6)	1.775(8)
Ru1 – N5 – O5	178.30(16)	–	–	169.0(8)	179.1(9)
Cl1 – Ru1 – N5	178.96(6)	–	–	176.7(3)	178.7(3)
Ru1 – O5	–	1.8630(13)	1.853(5)	–	–
Ru1 – O5 – N5	–	178.12(12)	178.5(7)	–	–
Cl1 – Ru1 – O5	–	178.93(4)	178.01(17)	–	–
N5 – O5	1.146(2)	1.140(2)	1.091(4)	1.115(5)	1.124(10)
Ru1 – Cl1	2.3206(6)	2.2782(5)	2.2940(7)	2.3007(6)	2.3007(7)
<i>Population of MSII^{IR}</i>	–	–	39%	53.9%	37.6%
	GS [‡]	MSI [‡]	MSI/MSII ^{IR}	MSI/MSII ^{IR}	GS/MSII ^{IR}
N10' – O10'	–	–	1.052(5)	1.024(5)	1.072(5)
Ru2 – N10'	–	–	1.992(4)	1.990(4)	1.988(8)
Ru2 – O10'	–	–	2.139(8)	2.125(5)	2.160(7)
N10' – Ru2 – O10'	–	–	29.24(16)	28.57(14)	29.58(15)
Cl2 – Ru2 – N10'	–	–	159.8(2)	159.41(17)	159.00(18)
Cl2 – Ru2 – O10'	–	–	170.11(19)	170.73(14)	170.86(16)
Ru2 – N10	1.7537(16)	–	–	–	1.768(5)
Ru2 – N10 – O10	172.42(16)	–	–	–	168.4(6)
Cl2 – Ru2 – N10	175.47(6)	–	–	–	174.8(2)
Ru2 – O10	–	1.8619(12)	1.841(5)	1.861(5)	–
Ru2 – O10 – N10	–	171.43(13)	173.1(6)	163.0(7)	–
Cl2 – Ru2 – O10	–	175.73(4)	172.8(2)	168.3(2)	–
N10 – O10	1.147(2)	1.142(2)	1.098(4)	1.079(4)	1.123(6)
Ru2 – Cl2	2.3231(5)	2.2798(5)	2.2937(7)	2.2987(6)	2.2985(7)
<i>Population of MSII^{IR}</i>	–	–	43.9%	47.1%	41.9%
<i>Cell setting, space group</i>	Monoclinic, P 1 2 ₁ /c 1				
a , Å	15.7016(4)	15.7224(4)	15.6498(2)	15.65792(18)	15.7462(2)
b , Å	13.4512(4)	13.3917(4)	13.4329(2)	13.43400(18)	13.4453(2)
c , Å	26.8147(7)	26.7648(7)	26.7836(5)	26.8100(4)	26.8024(6)
β , °	92.436(2)	92.603(2)	92.1845(15)	92.1158(11)	92.1921(17)
V , Å ³	5658.3(3)	5629.5(3)	5626.40(16)	5635.59(13)	5670.25(18)
<i>R1-factor</i>	3.3%	4.2%	4.54%	4%	5.2%
<i>GooF</i>	1.22	1.10	1.029	1.029	1.017
<i>No. of reflections</i>	18099	18723	12262	12283	12371
<i>No. of parameters</i>	768	775	854	965	866
$\Delta\rho_{max}, \Delta\rho_{min}, e\text{Å}^{-3}$	1.25, -0.93	0.66, -0.76	2.274, -1.287	1.567, -0.920	0.849, -0.491

TABLE 1.4: Selected bond distances (Å) and angles (°) in pure GS, pure MSI at 100 K [62] and mix models GS/MSII^{IR}, MSI/MSII^{IR} at 100 K and 8 K. For more experimental and structure refinement details see Appendix B. We present here data collections where maximum population of MSII^{IR} was observed. [‡] From the X-Ray refinement at 100 K of paper [62].

Short contact, Å	MSI at 8 K	MSI ^{IR} at 8 K		MSI ^{IR} at 100 K
		1st dat col	2nd dat col	
		P1 _{anion} ··· N5	2.88 (b)	
P1 _{anion} ··· O5	–	–	2.94 (b)	2.95 (b)
P1 _{anion} ··· N4 _{py}	3.14 (b)	3.24 (b)	3.24 (b)	3.13 (b)
P2 _{anion} ··· N2 _{py}	3.28 (b)	3.29 (b)	3.29 (b)	3.30 (b)
P2 _{anion} ··· N1 _{py}	3.27 (a)	–	–	–
H ₂ O ··· N5	3.07 (c)	3.13 (c)	–	–
H ₂ O ··· O5	–	–	3.15 (c)	3.12 (c)
H ₂ O ··· N2 _{py}	3.52 (b)	3.46 (b)	3.46 (b)	3.49 (b)
P3 _{anion} ··· N10	2.903 (b)	–	–	–
P4 _{anion} ··· N10	2.89 (c)	–	–	–
P2 _{anion} ··· N8 _{py}	3.10 (a)	3.16 (a)	3.17 (a)	3.17 (a)
P2 _{anion} ··· N9 _{py}	3.24 (a)	3.19 (a)	3.18 (a)	3.25 (a)
P3 _{anion} ··· N8 _{py}	3.20 (b)	3.33 (b)	3.22 (b)	3.21 (b)
P4 _{anion} ··· N6 _{py}	3.19 (a)	–	–	–

TABLE 1.5: The list of short contacts on two independent sites for the MSI at 8 K, two consequent data collections of MSI^{IR} at 8 K and data collection of MSI^{IR} at 100 K. P1, P2, P3 and P4 are the central atoms of (PF₆)[−] anion involved in the short contacts with pyridine group labelled through its nitrogen atom (N_{py}), as well as with N and O atoms of nitrosyl group (N5, O5, N10, O10). In the brackets we also present the direction of the main component of the short contact in relation with axes **a**, **b**, **c**.

1.2 Visible absorption spectroscopy studies

1.2.1 Evidence of a two-step photon absorption driving the

Ru – NO to *Ru – ON* photoswitching under the blue light irradiation

The significant colour change observed in [Ru(py)₄Cl(NO)](PF₆)₂ · 1/2H₂O single crystals during the photochemical reaction has been quantitatively followed by visible (VIS) absorption spectroscopy. Measurements were performed with home-made spectrograph which is able to cover visible range with accuracy down to dλ = 5 nm (see Experimental details in Appendix D). Whether X-Ray diffraction can capture transient species depends essentially on the concentration of those species and their structure factors (atomic constitution). Visible absorption spectroscopy can be more sensitive in capturing transients, in that low concentration of species can be compensated by their significant extinction coefficients. Electronic transition moments may be very different despite identical atomic constitution of molecules under consideration.

Fig. 1.11 (a) shows the time evolution of the optical density (OD) under blue light irradiation after different time delays of irradiation at 100 K. A stable OD spectrum is obtained after less than two hours of irradiation (total exposure Q around 8000 J · cm^{−2}) and for spectral

discrimination of any intermediates hereafter, we consider that 100% of MSI population is reached after such prolonged irradiation with a blue laser.

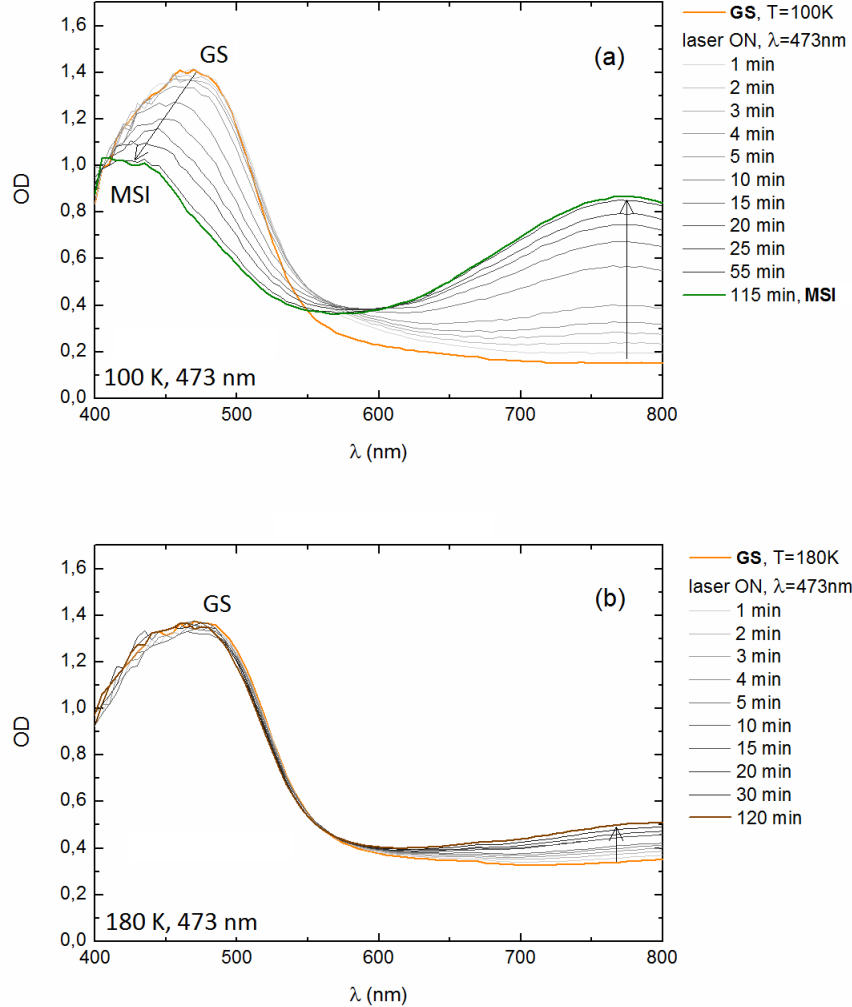


FIGURE 1.11: $Ru-NO$ to $Ru-ON$ photoswitching probed by time evolution of optical density (OD) of $[Ru(py)_4Cl(NO)](PF_6)_2 \cdot 1/2H_2O$ single crystal with 473 nm , around 1100 mW/cm^2 (a) at 100 K and (b) at 180 K .

At 100 K , the time evolution of the OD under the blue light irradiation (Figure 1.11 (a)) cannot be explained by a sum of only two contributions, i.e. GS and MSI: the lack of isobestic point during spectral evolution unambiguously indicates the existence of intermediate(s) state(s). The possibility of MSII being an intermediate state can be tested at 180 K , when MSII species relax too quickly to transfer enough population to MSI with CW [15] (Figure 1.11 (b)). The difference with the case of 100 K is significant: in spite of a small evolution on the red side of the OD, the quasi-complete MSI state cannot be reached.

At 180 K , the saturation of the signal is observed after 30 minutes and all spectra can be interpreted as a weighted contribution of GS and MSI with MSI population not exceeding 10%. Therefore, a two-step photon absorption process through MSII has to be considered as the most likely pathway for the $Ru-NO$ to $Ru-ON$ photoswitching in the model of

$[Ru(py)_4Cl(NO)](PF_6)_2 \cdot 1/2H_2O$ system (Fig. 1.12). Such predominant two-step photon absorption in the blue spectral range differs from that observed on SNP where both direct and two-step channels are equally involved [12]. A two-step photon absorption process had been also previously observed on another ruthenium nitrosyl compound $[Ru(NH_3)_5NO]Cl_3 \cdot H_2O$ [68], however, in this case it is associated with a quasi-complete GS to MSI photochemical efficiency (only 11% in $[Ru(NH_3)_5NO]Cl_3 \cdot H_2O$).

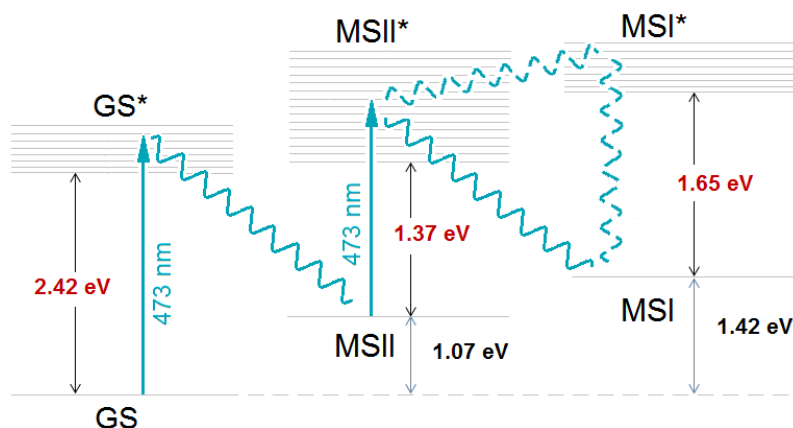


FIGURE 1.12: Relative positions of MSI and MSII states of $[Ru(py)_4Cl(NO)]$ molecule, their excited states and excited level of the GS state (from Ref. [15]). Vertical arrows represent irradiation of 473 nm. The dark red numbers stand for the calculated values of energy, while the black ones for the measured values.

The major result of visible absorption spectroscopy studies is thus the experimental evidence of a two-step photon absorption process during the $Ru - NO$ to $Ru - ON$ photoswitching under blue light irradiation at 100 K through the absence of isosbestic point on the time evolution of the OD spectra (Figure 1.11 (a)), which is also supported by recent DFT calculations [69].

In the prototype SNP, a two-step process is favoured by shifting the wavelength to the green range, however, its efficiency is low (only a few %) [12]. For $[Ru(py)_4Cl(NO)](PF_6)_2 \cdot 1/2H_2O$ system, the change of wavelength to green, i.e. 532 nm, strongly affects the photochemical reaction too and at 100 K the MSI population reaches 10% at most (Figure 1.13). Under 532 nm, the low transformation rate results in the absence of lattice parameters' evolution during the X-Ray diffraction experiment. The higher sensitivity of the optical measurements, as it was mentioned above, is better suited to follow low percentage of metastable species. The dependency of transformation rate on the irradiation wavelength is rationalised in the following paragraphs.

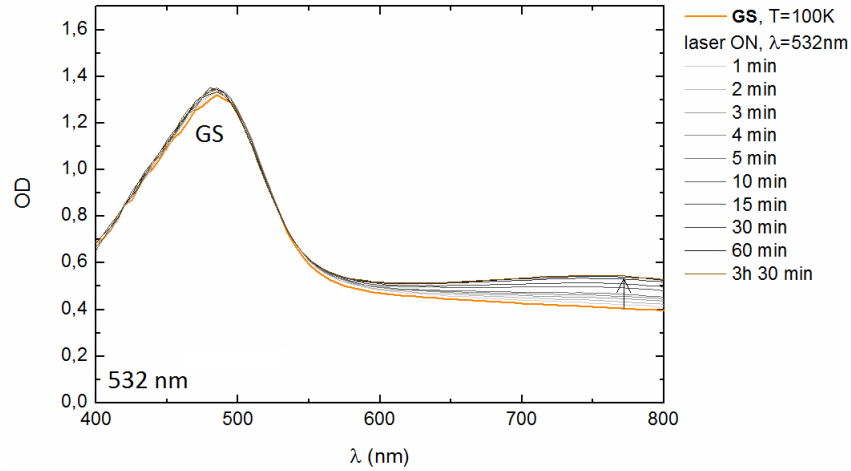


FIGURE 1.13: Evolution of the OD during the light irradiation of the $[Ru(py)_4Cl(NO)](PF_6)_2 \cdot 1/2H_2O$ single crystal at 100 K with 532 nm, $1500 mW \cdot cm^{-2}$.

1.2.2 The $Ru - ON$ to $Ru - NO$ reverse photoswitching probed by visible spectroscopy

The reverse photochemical process, i.e. the $Ru - ON$ to $Ru - NO$ photoswitching in red and IR spectral regions has been also followed with visible absorption spectroscopy. The irradiation of IR light, 1064 nm, causes the blackening of the crystal [62] as illustrated by the increase of the OD within the whole visible range. We obtained a high population of MSII species, labelled as $MSII^{IR}$, after around 25 minutes during the irradiation with power of about $600 mW/cm^2$, i.e. $Q \approx 900 J/cm^2$, as shown in Figure 1.14. Opposite to the $Ru - NO$ to $Ru - ON$ photoswitching, which predominantly proceeds through two-step photon absorption, the reverse process under IR irradiation proceeds through thermal decay of MSII species, which substantially slows down the kinetics of photochemical reaction with the temperature decrease.

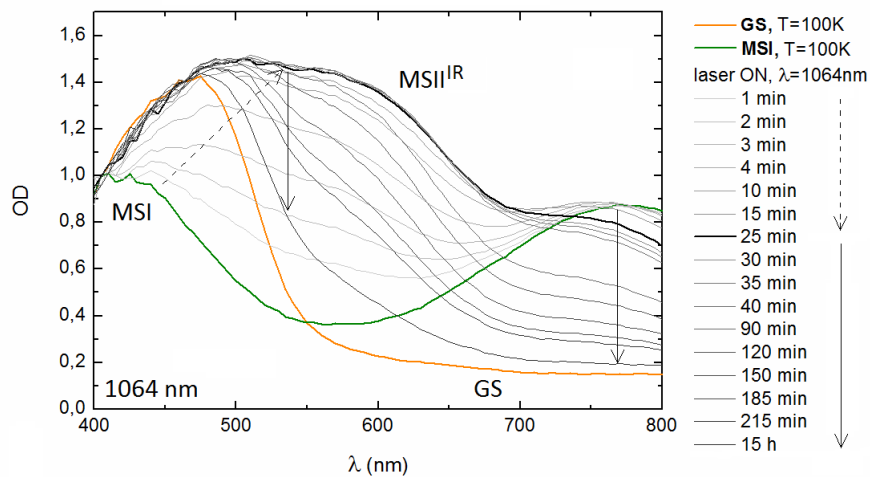


FIGURE 1.14: $Ru - ON$ to $Ru - NO$ photoswitching probed by the time evolution of the OD of one $[Ru(py)_4Cl(NO)](PF_6)_2 \cdot 1/2H_2O$ single crystal at 100 K with 1064 nm, around $600 mW \cdot cm^{-2}$. $MSII^{IR}$ indicates the highest population of MSII species reached during the experiment.

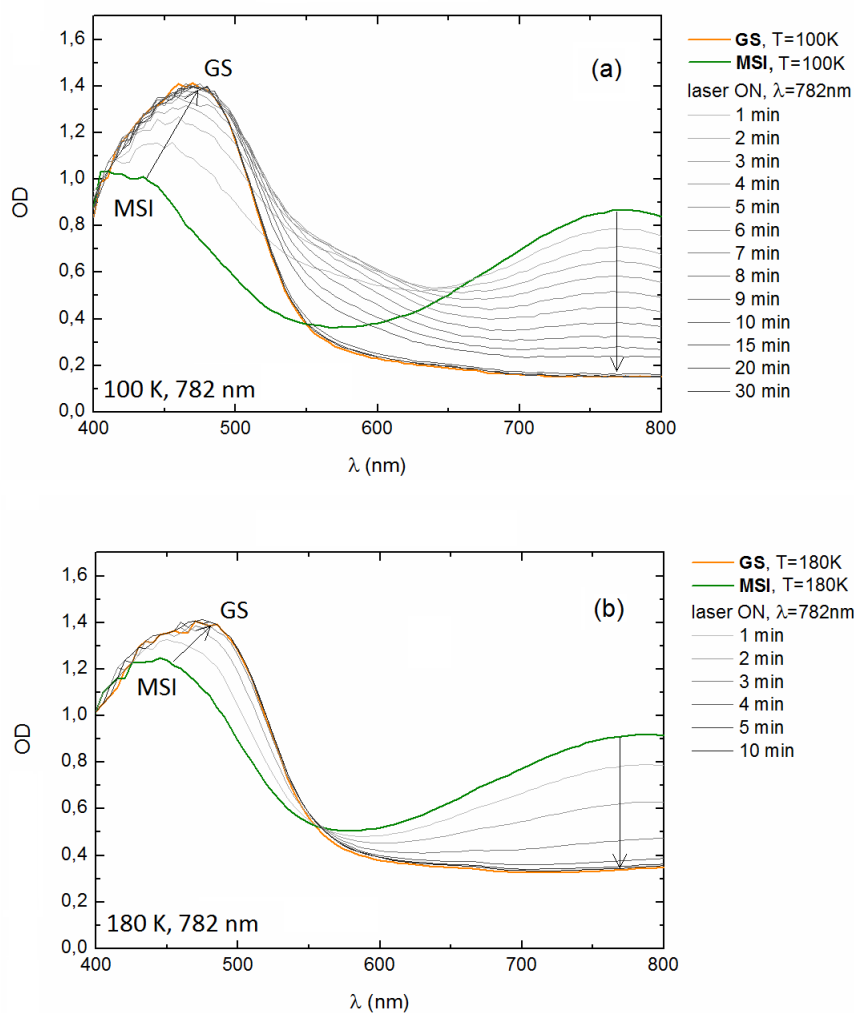


FIGURE 1.15: Evolution of the OD during the light irradiation of the $[Ru(py)_4Cl(NO)](PF_6)_2 \cdot 1/2H_2O$ single crystal with 782 nm, 180 mW · cm⁻² (a) at 100 K and (b) at 180 K.

The irradiation of MSI state of $[Ru(py)_4Cl(NO)](PF_6)_2 \cdot 1/2H_2O$ complex at 100 K in the red region, 782 nm, leads to the complete and quite fast relaxation back to GS state (Figure 1.15 (a)) as in the prototype SNP compound [12]. Missing isosbestic point in time evolution at 100 K and its observation at 180 K (compare (a) and (b) in Figure 1.15) support the idea of an intermediate MSII state. Unlike the $Ru - NO$ to $Ru - ON$ photoswitching with the blue light, at 180 K (see and compare Figure 1.11 (b) and Figure 1.15 (b)), the complete transformation to GS with the red irradiation suggests that both two-step process through MSII and direct de-excitation to GS coexist. Unfortunately, we cannot distinguish between these two channels with measurements under CW irradiation.

Scheme 1.16 summarizes the various possibilities for the $Ru - ON$ to $Ru - NO$ photoswitching. Two main differences between red and IR light irradiations can be underlined. Under the red light irradiation a very efficient back switching occurs either through a direct de-excitation or through a two-step process via MSII and MSII* species. In case of IR irradiation the MSI state does not absorb IR light, one can notice that the gap between MSI and MSII*, i.e. 1.65 eV [15], is much higher than IR light energy, 1064 nm=1.16 eV. From the recent DFT calculations on singlet

and triplet GS, MSI and MSII states [69] there are two hypothesis explaining the depopulation of MSI. In the first one, the two-photon absorption process promotes singlet ^1MSI to the higher singlet state, which by the intersystem crossing populates the triplet ^3MSI , which absorbs IR light. In the second hypothesis, the system can partially exist as ^3MSI due to the spin-orbit coupling and a low activation energy. In both hypothesis when the system reaches ^3MSI state, it absorbs the IR light and then relaxes to the MSII state. The photoswitching back to GS from the MSII state is then dominated by thermal decay of MSII species as they do not absorb IR light. Even though with the CW light irradiation we are not able to detect the triplet states, as their lifetime is too short, thanks to DFT calculations it is possible to explain the absorption of IR light by MSI state and further relaxation of the system to the MSII. Irradiation with IR light is the unique way to observe both clear optical and structural signatures of intermediate MSII species (Figure 1.5 and 1.14) thanks to their non-absorption of IR light (Scheme 1.16).

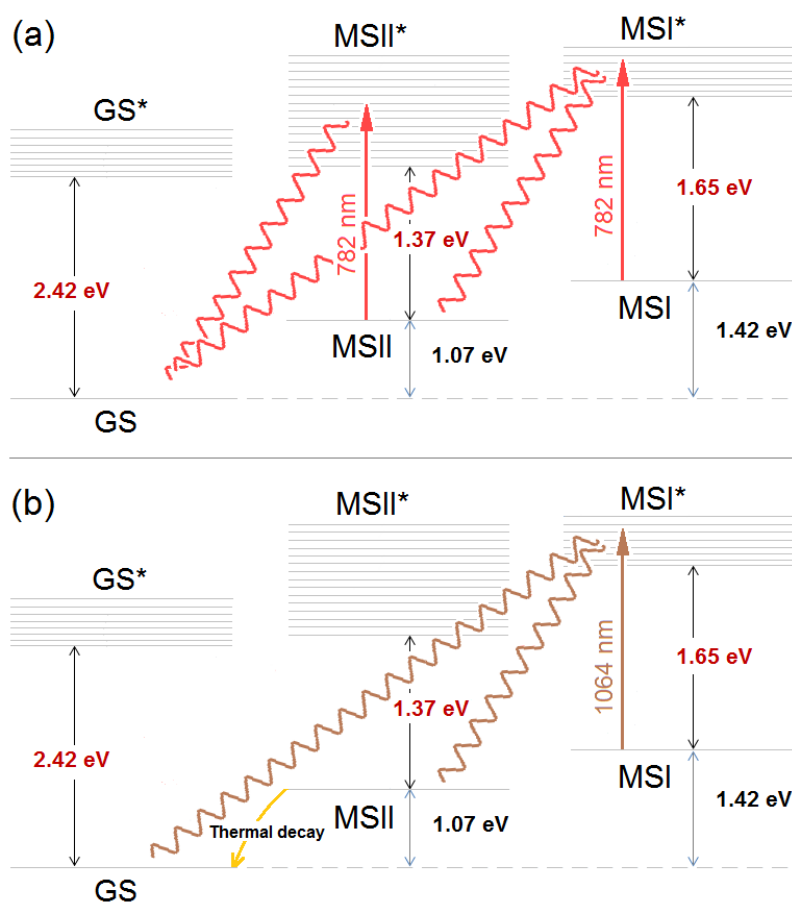


FIGURE 1.16: Relative positions of MSI and MSII states of $[\text{Ru}(\text{py})_4\text{Cl}(\text{NO})]$ molecule, their excited states and excited level of the GS state (from Ref. [15]). Vertical arrows represent irradiation of (a) 782 nm and (b) 1064 nm. The dark red numbers stand for the calculated values of energy, while the black ones for the measured values.

1.2.3 Optical density spectrum and properties of intermediate MSII species

The CW light allows to probe only species with long lifetime, i.e. GS, MSI and MSII presented on schemes 1.12, 1.16 and 1.17, and not corresponding excited states, labelled GS*, MSI* and MSII*. All intermediate spectra observed during the photoswitching (Figures 1.11 (a) and 1.14) result then from a combination of GS, MSI and MSII. The MSII state (side-on configuration) is clearly the transient state observed during the $Ru - ON$ to $Ru - NO$ switching under IR light [62] (see also Chapter 2).

The OD spectrum of the MSII^{IR}, the mixture of MSII (side-on configuration) and GS (see Figure 1.14), corroborates the idea of MSII species (side-on configuration) as a possible intermediate during the two-step process from $Ru - NO$ to $Ru - ON$: the dark colour evidences an absorption in the visible range, though it does not explain the difference between the results at 100 K upon irradiation with the blue, 473 nm, and green light, 532 nm (compare Figures 1.11 (a) and 1.13). To understand it we studied the effect of these two wavelengths on the MSII^{IR} (dark colour) (Figure 1.18). With the blue light irradiation of the MSII^{IR} the crystal returns to the MSI state, while the green light irradiation brings the system to the mixed GS-MSI state with a population of MSI species not higher than 10%. Therefore, the predominant relaxation of the excited MSII species (MSII*) back to GS instead of MSI state under the green light irradiation is responsible for the obtained differences (compare Figure 1.12 and 1.17). The final mixed GS-MSI state under the green light irradiation results from the stationary equilibrium between all involved molecular states (Figure 1.17) and the very high efficiency of the photoprocess in the blue spectral range means that the relaxation between MSII* and GS is negligible (therefore not represented on Figure 1.12).

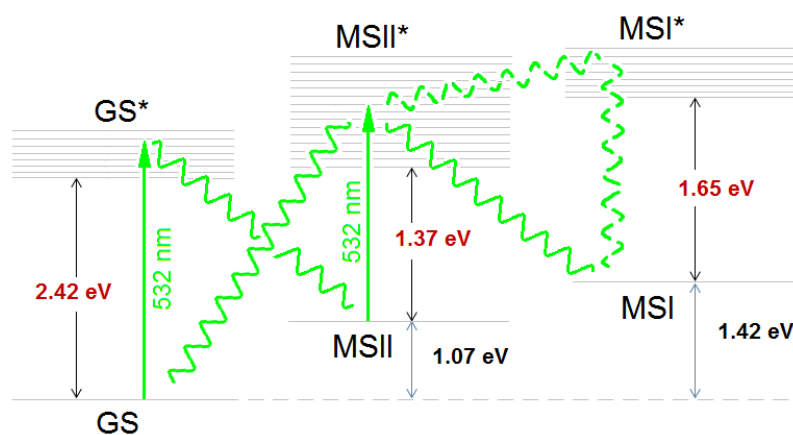


FIGURE 1.17: Relative positions of MSI and MSII states of $[Ru(py)_4Cl(NO)]$ molecule, their excited states and excited level of the GS state (from Ref. [15]). Vertical arrows represent irradiation of 532 nm. The dark red numbers stand for the calculated values of energy, while the black ones for the measured values.

Oppositely, the negligible relaxation between MSII* and MSI in the red spectral range explains the high efficiency of $Ru - ON$ back to $Ru - NO$ process under the red light. We have observed it experimentally by studying the effect of 782 nm starting from the MSII^{IR} OD spectrum, where the final OD spectrum goes back to the GS one (Figure 1.18 (c)).

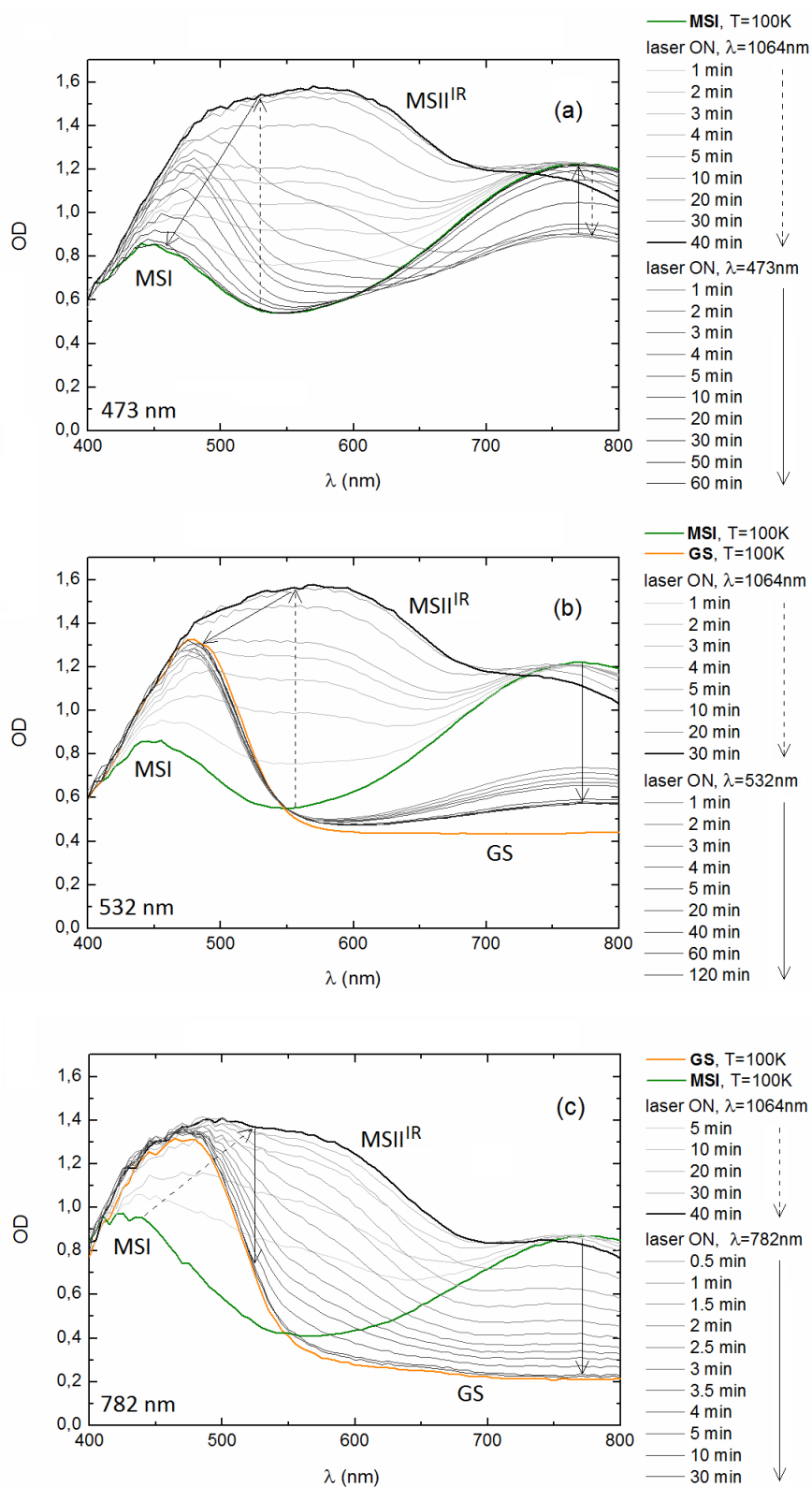


FIGURE 1.18: Evolution of the OD during the light irradiation of the $[Ru(py)_4Cl(NO)](PF_6)_2 \cdot 1/2H_2O$ single crystal at 100 K with 1064 nm , $600\text{ mW} \cdot \text{cm}^{-2}$ up to $MSII^{IR}$ (black thick line) and consequent irradiation (a) with 473 nm , $1100\text{ mW} \cdot \text{cm}^{-2}$, (b) with 532 nm , $1500\text{ mW} \cdot \text{cm}^{-2}$, (c) with 782 nm , $180\text{ mW} \cdot \text{cm}^{-2}$ at 100 K. The measurements in case (c) were done on a different crystal, which explains the slight difference in the OD spectra of MSI, MSII and GS from cases (a), (b). $MSII^{IR}$ indicates the highest population of MSII species reached during the experiment.

1.2.4 Nature of intermediate MSII species under the blue light irradiation

All intermediate OD spectra observed during the $Ru - NO$ to $Ru - ON$ and the reverse photo-switching process result from a combination of GS, MSI and MSII. It seems then that transient MSII species reveal different OD spectra during the $Ru - NO$ to $Ru - ON$ switching under blue light and during the reverse process under the red light irradiation (compare Figure 1.11 (a) and Figure 1.15 (a)). On one hand, under 782 nm , quite high OD in the interval $[550\text{ nm} - 650\text{ nm}]$ is consistent with the MSII OD signature observed under IR light in Figure 1.14. On the other hand, intermediate OD in the interval $[550\text{ nm} - 650\text{ nm}]$ observed during the $Ru - NO$ to $Ru - ON$ process under 473 nm irradiation (Figure 1.11 (a)) does not exhibit similar high values.

Under CW light irradiation, the unique possibility to obtain an absorption spectrum of the intermediate state is to retrieve it with a kinetic model [70]. The simplest one considers three states (GS, MSI and MSII) and two kinetic constants ($K_{GS \rightarrow MSII}$, $K_{MSII \rightarrow MSI}$), i.e. it neglects the direct transformation from GS to MSI because of the predominant two-step photon absorption process. The model optimizes the contribution of the residual spectrum to reproduce the time evolution of OD spectra during the photoconversion (Figure 1.11 (a)) with GS and MSI OD spectra unambiguously determined. Thus the calculated OD spectrum of the intermediate MSII state is obtained (see Figure 1.19), the agreement between the experiment and model is shown in Figure 1.20. The retrieved MSII OD spectrum reveals a maximum of absorption in the blue region. The attempt to use the deduced OD signature of MSII under the blue light to reproduce the experimental spectrum of $MSII^{IR}$ (mixed GS and MSII state on Figure 1.14 (a)) was not successful due to the broad maximum of the $MSII^{IR}$ OD spectrum in the green-yellow region (Figure 1.14 (a)).

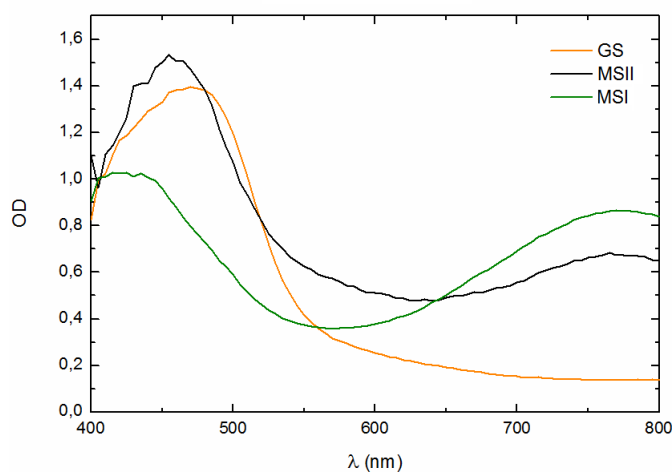


FIGURE 1.19: OD spectra of the GS and MSI states (experimental data) and OD spectra of the intermediate MSII state deduced from the kinetic model reproducing the OD evolution under 473 nm .

As molecular geometry can strongly influence the optical properties (see Figures 1.5 and 1.11), we suggest that the geometry of transient MSII species under the blue light might be different from the 90° side-on configuration seen under the IR irradiation [62].

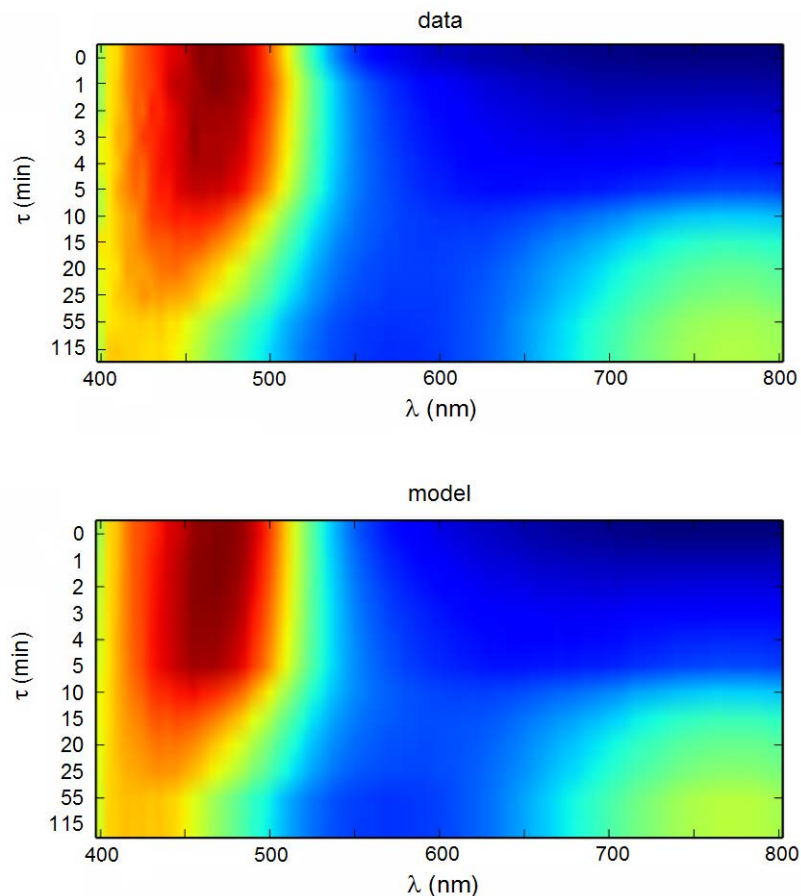


FIGURE 1.20: Agreement between the experimental data and the three state (GS, MSI and MSII) kinetic model reproducing the experimental intermediate OD spectra during the GS to MSI phototransformation. View in 3D.

Nevertheless, optical signature of pure transient MSII species and/or structural signature of transient species during $Ru-NO$ to $Ru-ON$ process will be necessary for a clear-cut evidence. Ultra-short laser pump and time-resolved experiments promise an access to the dynamics of the photochemical reaction at a much shorter time scale and will allow to characterize both long-lived MSII state and transient short-lived GS^* , MSI^* and $MSII^*$ species. We address this issue in Chapter 3.

1.2.5 Independence of MSI population dynamics from the polarization of irradiation

In 1993 in the work [12] by means of differential scanning calorimetry it was shown that the SNP compound demonstrates a strong dependence of its population saturation on the polarization direction of the irradiated light. The maximum population of MSI (around 50%) was observed when the polarization of the light was perpendicular to the axis Fe-N-O (Figure 1.21). In case of SNP the four molecules per unit cell are arranged antiparallel in couples and the c -axis of a crystal is perpendicular to the Fe-N-O line.

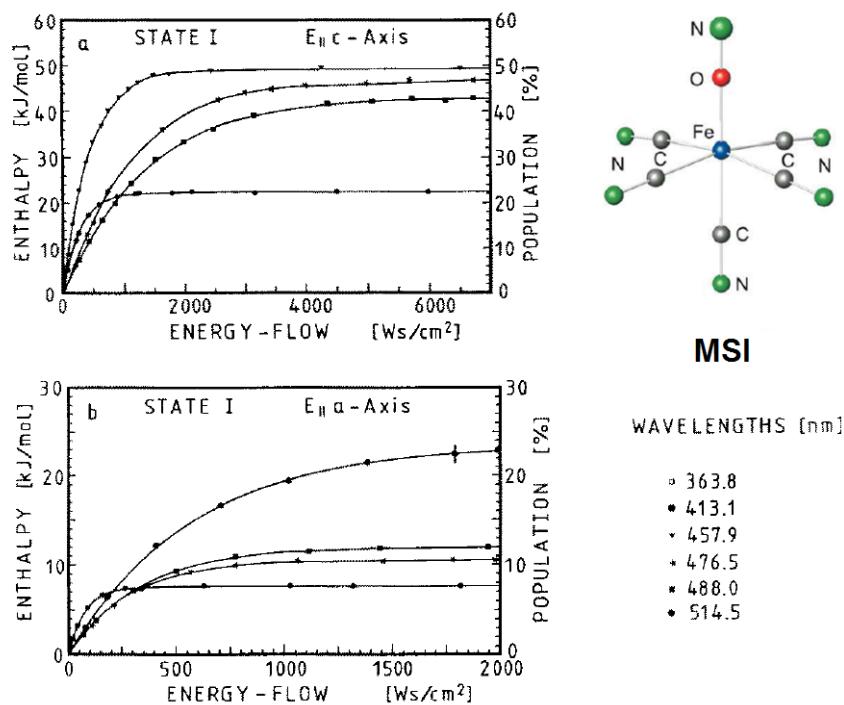


FIGURE 1.21: Dependence of the population of MSI from the polarization direction of the light and irradiation wavelength. The figure is taken from the work [12], Figure 2a-b. The schematic view of linkage isomer MSI is added, from Figure 1 of work [15].

To see if there is a strong influence of light polarization on the MSI population in ruthenium nitrosyl complex the visible absorption spectroscopy was performed with the use of the Berek Polarization Compensator on (ab) platelets and it was found that the polarization of the laser light, either parallel to **a** or parallel to **b** crystallographic axis does not play an important role in the $Ru - NO$ to $Ru - ON$ photoswitching. The population of MSI does not change, i.e. the identical final OD spectra are observed in both cases (see Figure 1.22).

It can be explained by the fact that eight molecules per unit cell in ruthenium nitrosyl compound have only a slight preference to lie along the direction of **a**-axis comparing to **b**, **c**-axes (see Figure 1.23). Therefore, unlike the SNP case the light polarization has no significant effect on the MSI population in the $[Ru(py)_4Cl(NO)](PF_6)_2 \cdot 1/2H_2O$ single crystal.

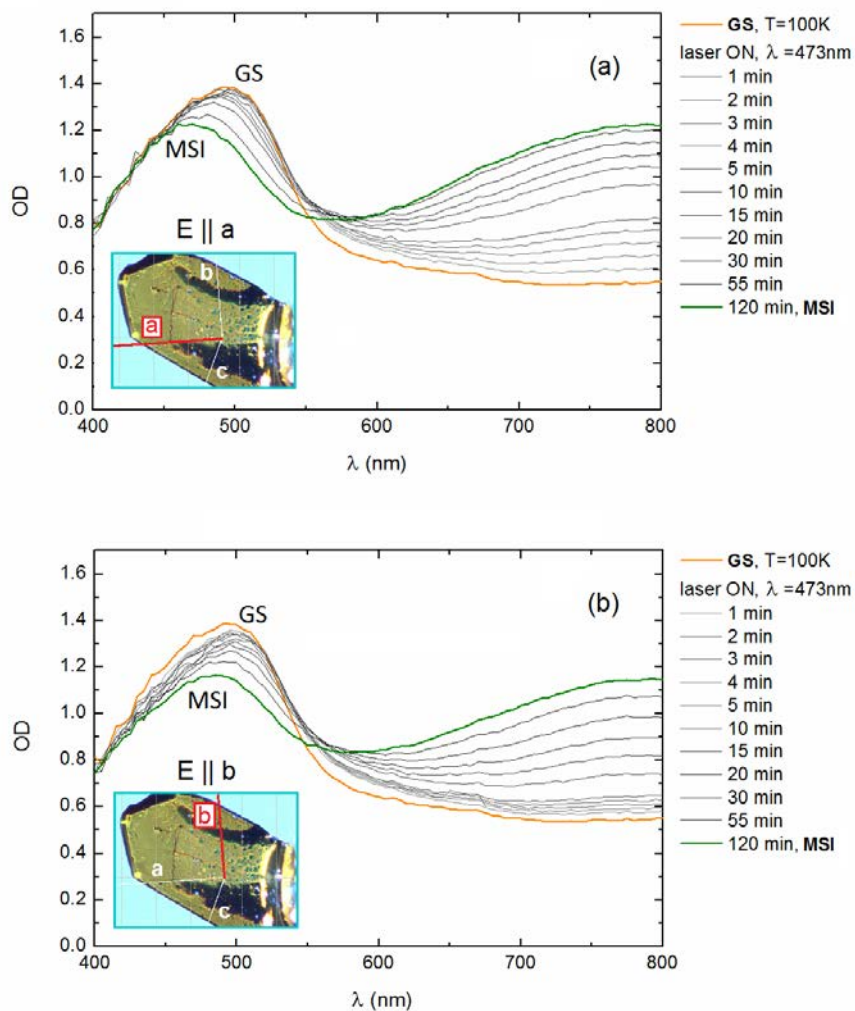


FIGURE 1.22: Evolution of the OD during the light irradiation of the $[Ru(py)_4Cl(NO)](PF_6)_2 \cdot 1/2H_2O$ single crystal at 100 K with 473 nm along (a) a-axis, (b) b-axis of the crystal.

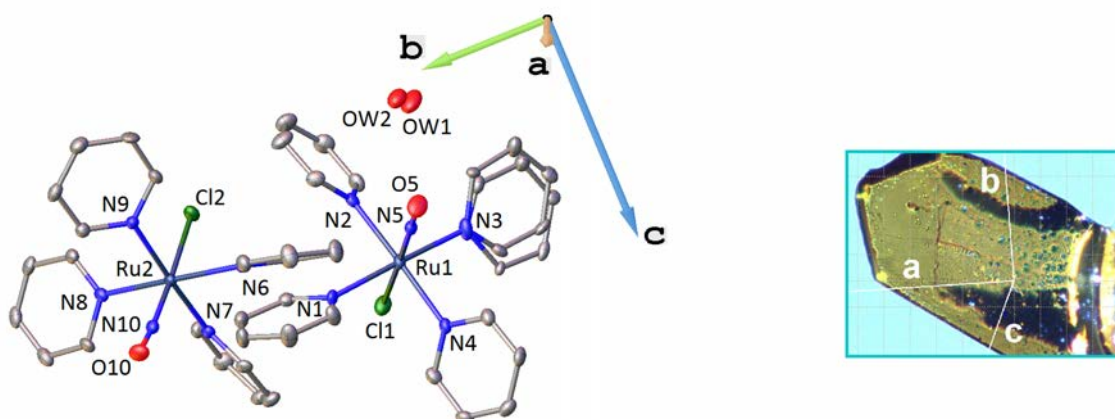


FIGURE 1.23: On the left: the molecular structure of $[Ru(py)_4Cl(NO)](PF_6)_2 \cdot 1/2H_2O$ at 100 K in GS state with crystallographic axes. The hydrogen atoms and anions $(PF_6)^-$ are omitted for clarity. The plot is based on the GS refinement. On the right: the typical crystal used for optical measurements with its crystallographic axes.

The main results of this Chapter can be summarized as follows:

- The low concentration of transient MSII state hinders the detection of any structural signature during the X-Ray diffraction studies. Nevertheless, a predominant two-step absorption process through long-lived MSII species is observed during the $Ru - NO$ to $Ru - ON$ photoswitching under the blue CW irradiation by means of visible absorption spectroscopy.
- The visible absorbance spectrum and the side-on configuration of MSII^{IR} state (mixture of GS and MSII side-on configuration) has been experimentally determined. The effect of blue and green CW light on MSII^{IR} was also shown: the blue light transfer system to MSI state, while the green light brings system back to GS state. Unlike the SNP case, the green range of irradiation in $[Ru(py)_4Cl(NO)](PF_6)_2 \cdot 1/2H_2O$ single crystal is not efficient to reach the MSI state.
- The simple kinetic model employed to deduce the transient MSII spectra observed in $Ru - NO$ to $Ru - ON$ photoconversion under the blue light. When retrieved OD spectrum was compared to the OD evolution of reverse $Ru - ON$ to $Ru - NO$ photoswitching under the IR irradiation, it was found that the optical signature of transient MSII species depends on the direction of the photochemical reaction. The nature of MSII species during the photoswitching under the blue light irradiation is not clear as we do not have direct access to the MSII signature. To clarify this point further investigations using the time-resolved techniques are discussed in Chapter 3.
- The polarization of the irradiated blue CW light does not play any significant role on the population of the MSI species $[Ru(py)_4Cl(NO)](PF_6)_2 \cdot 1/2H_2O$ single crystal, which is different from the case of SNP prototype compound.

Chapter 2

Role of water molecule during the photoisomerization process in single crystal

The role of water molecule in the $[Ru(py)_4Cl(NO)](PF_6)_2 \cdot 1/2H_2O$ single crystal was investigated by X-Ray diffraction during the photoisomerization under continuous light (CW) in hydrated and dehydrated samples using 473 nm for $Ru - NO$ to $Ru - ON$ isomerization and 1064 nm for the reverse process (see Figure 2.1). Several samples were dehydrated by heating up to 348 K , and the structures have been determined using the single crystal X-Ray diffraction. The rehydrated single crystals and the recover of structural signatures have been also tested during this study.

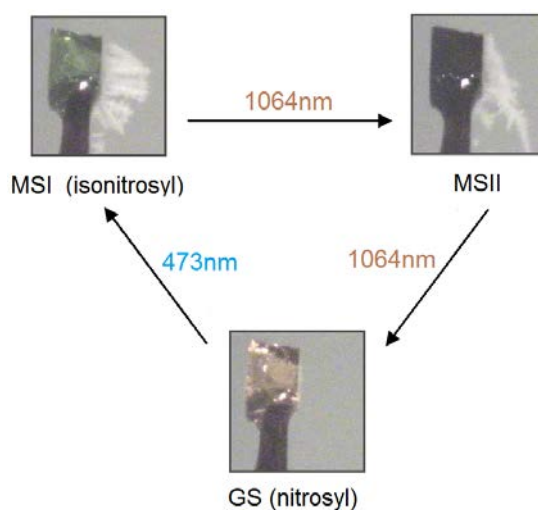


FIGURE 2.1: The colour change of the $[Ru(py)_4Cl(NO)](PF_6)_2 \cdot 1/2H_2O$ single crystal at low temperatures during the photoswitching between GS, MSI and MSII states under 473 nm and 1064 nm .

2.1 Unit cell parameters evolution followed by single crystal X-Ray diffraction

2.1.1 Dehydration process during the heating of a single crystal

The process of dehydration of the $[Ru(py)_4Cl(NO)](PF_6)_2 \cdot 1/2H_2O$ single crystal was studied by X-Ray diffraction through the change of unit cell parameters of monoclinic system. Data was collected on the four-circle Oxford Diffraction Xcalibur 3 diffractometer (Mo K_α radiation) with a two-dimensional sapphire 3 CCD detector, on samples with typical sizes around $300 \times 200 \times 100 \mu m^3$ (see Table 2.1). The single crystals were mounted in an Oxford Cryosystems nitrogen-flow cryostat (CryoJet 700) allowing a precise control of temperature of the sample during the heating up to $348 K$ and the cooling down to $100 K$. The unit cell parameters and intensities of Bragg reflections were obtained with CrysAlis software (CrysAlis RED, Oxford Diffraction Ltd, Version 1.171.38.41). The structure determination was done on samples №1, №3, №4 and №5, while the lattice parameter evolution was followed for samples №2 and №6 (see Table 2.1) to confirm the obtained results on different samples. In this chapter we present our results for sample №6 with lattice parameters evolution and for samples №4, №5 with its structural determination.

Sample, date	max, μm	mid, μm	min, μm	Crystal faces, T=100K
№1, 10/2013	225	162	72	
№2, 06/2015	365	195	70	
№3, 11/2015	268	158	106	
№4, 11/2015	275	217	96	
№5, 11/2015	246	207	60	
№6, 03/2016	183	230	296	

TABLE 2.1: The typical dimensions of studied single crystals.

In Figure 2.2 the unit cell parameters evolution is presented during the sample heating and cooling. During the dehydration process the sample was heated up to $348 K$ with the rate

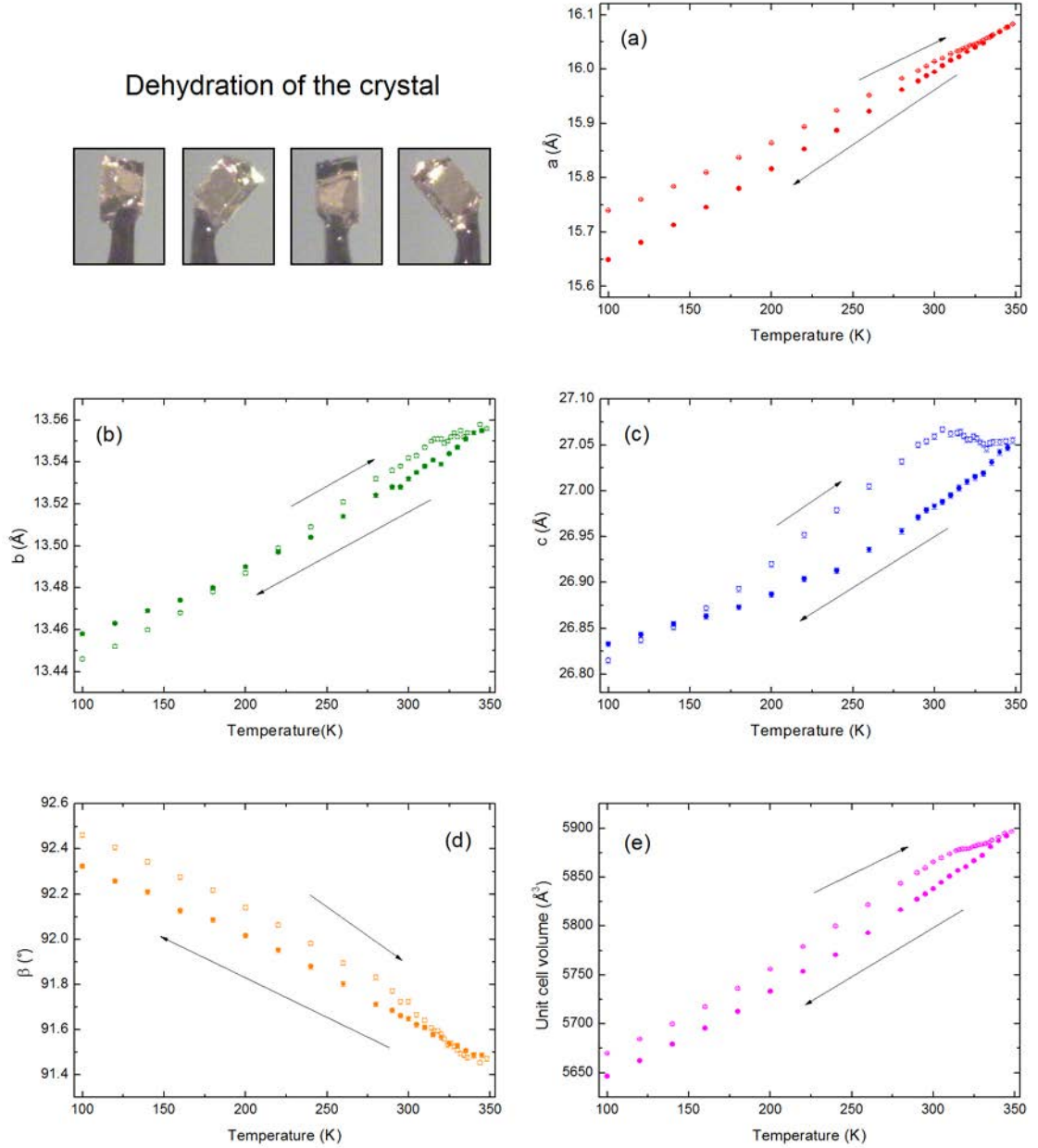


FIGURE 2.2: Evolution of the lattice parameters (a) \mathbf{a} (Å), (b) \mathbf{b} (Å), (c) \mathbf{c} (Å), (d) β angle (°), (e) unit cell volume (Å³) of the $[Ru(py)_4Cl(NO)](PF_6)_2 \cdot 1/2H_2O$ single crystal during the dehydration by the heating up to 348 K.

120 K/h, the data was collected every 20 K at low temperatures and every 2 K or 5 K in the region of interest, [314 K – 336 K] with thermal stabilization time of two/one minutes. Then the sample was left at 348 K for half an hour, and after it was cooled down to 100 K with the steps of 2 K, 5 K or 10 K. During the lattice parameters measurement the temperature was kept constant at each step.

During the crystal heating the sudden drop in \mathbf{c} crystallographic axis value, $\Delta\mathbf{c} = -0.021(3)\text{Å}$ between 305 K and 332 K is observed, while other parameters gradually grow, except for β angle which gradually decreases. After keeping the sample for around half an hour at 348 K to make sure that the water leaves completely the crystal, it was cooled down back to 100 K. Comparing to the unit cell parameters of hydrated sample at 100 K the \mathbf{a} crystallographic axis and the β

angle showed the highest variation in values, while **b** and **c** values are almost recovered after the heating/cooling cycle ($\Delta\mathbf{a} = -0.091(1) \text{ \AA}$, $\Delta\mathbf{b} = +0.012(1) \text{ \AA}$, $\Delta\mathbf{c} = +0.018(3) \text{ \AA}$, $\Delta\beta = -0.14(1)^\circ$ from Figure 2.2). As expected, the unit cell volume has decreased $\Delta V = -23(1) \text{ \AA}^3$.

2.1.2 Comparison of hydrated and dehydrated GS structures at 100 K.

With a significant change of lattice parameters during the dehydration process as shown in previous section, it is curious to see the effect of water molecule departure on the GS structure. Therefore, the GS structure was solved and refined for dehydrated and rehydrated forms of sample №4 (see Table 2.1). All non-hydrogen atoms were refined anisotropically, while all hydrogen atoms were constrained by geometry. For more experimental and structure refinement details see Appendix C.

The GS structure of two symmetry-independent cations with nearby anions and water molecule is presented for the rehydrated system only in Figure 2.3. In dehydrated form we observe the same structural arrangement of the atoms with only a loss of a water molecule and insignificant change in the certain bond lengths and angles, therefore we do not present its geometry in here, but the *.cif files will be available in Crystallographic Structural database. The monoclinic space group ($P2_1/c$) of the crystal also does not change during the dehydration as it is seen from Figure 2.4 through the plane reconstruction for GS in hydrated and dehydrated cases. We observe in both case the screw axis 2_1 (parallel to **b**) and a glide plane *c* (perpendicular to **b**), which gives us reflections like (0K0), $K=2n$, $n=0,1,2,\dots$, (H0L) with only $L=2n$, $n=0,1,2,\dots$ presented.

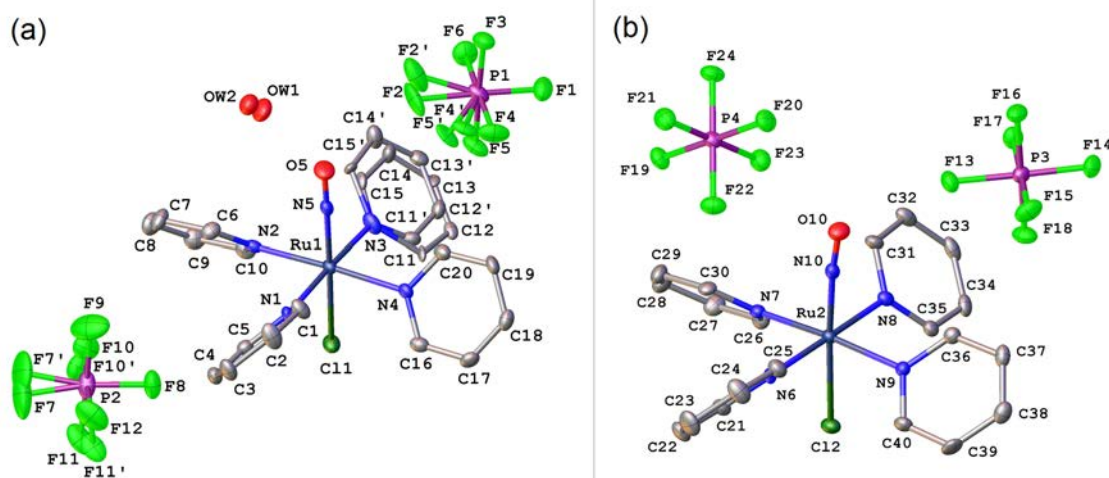


FIGURE 2.3: The structure of the two cations $[Ru(py)_4Cl(NO)]^{2+}$, four anions $(PF_6)^-$ and water molecule in GS state. The hydrogen atoms are omitted for clarity. For more experimental and structure refinement details see Appendix C.

The most interesting distances and angles of dehydrated and rehydrated systems are compared with DFT calculations [62] in Table 2.2. Only a small changes in molecular geometries were observed, the obtained values are comparable with the DFT calculations [62]. First, it is important to note that the presence of water in the crystal plays a role in the disorder of nearby molecules, specifically it affects one of pyridine rings of *Ru1* molecule, $N3 - C11 - C12 - C13 - C14 - C15$

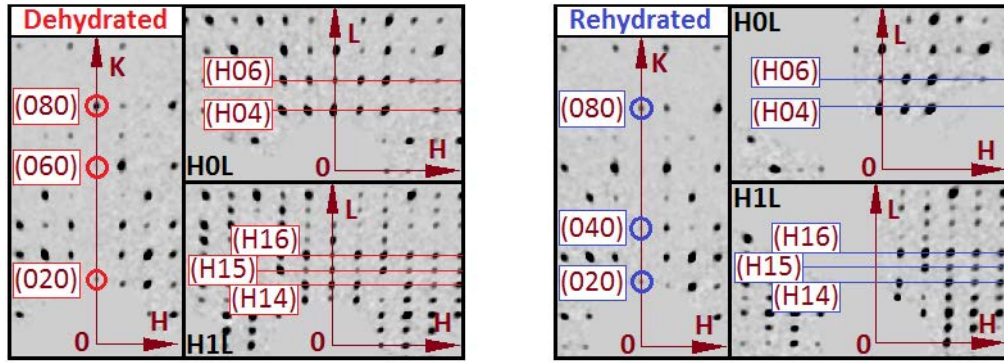


FIGURE 2.4: Plane reconstruction from data collections of GS in hydrated and dehydrated samples of the $[Ru(py)_4Cl(NO)](PF_6)_2 \cdot 1/2H_2O$ single crystal at 100 K. The same space group is observed in both cases, i.e. $P2_1/c$ with typical reflections $(0K0)$, $K=2n$, $n=0,1,2,\dots$, $(H0L)$ $L=2n$, $n=0,1,2,\dots$. The plane (H1L) is given for comparison.

(see Figure 2.3). Second, even though we do not see significant difference in the molecule geometry there is a decrease in the unit cell volume in the dehydrated crystal by $\Delta V \simeq 17 \text{ \AA}^3$, which is in agreement of volume change found through lattice parameters evolution on sample №6 in previous section.

Distance/angle, Å/°	GS, X-Ray			X-Ray [‡]	DFT [‡]
	Hydrated sample №5	Dehydrated sample №4	Rehydrated sample №4	Hydrated	
Ru1 – N5	1.750(4)	1.755(3)	1.759(3)	1.7550(17)	1.7848
N5 – O5	1.147(5)	1.146(4)	1.144(3)	1.146(2)	1.152
Ru1 – N5 – O5	177.7(4)	179.1(3)	178.6(3)	178.30(16)	178.48
Ru1 – N1	2.103(4)	2.101(3)	2.106(3)	2.1044(17)	2.1388
Ru1 – N2	2.100(3)	2.103(3)	2.105(3)	2.1041(17)	2.1299
Ru1 – N3	2.097(4)	2.099(3)	2.097(3)	2.1069(18)	2.1311
Ru1 – N4	2.113(3)	2.115(3)	2.117(3)	2.1142(17)	2.1493
Cl1 – Ru1 – N5	178.87(12)	179.01(10)	178.84(9)	178.96(6)	179.17
Ru1 – Cl1	2.3186(13)	2.3161(10)	2.3194(9)	2.3206(6)	2.3409
Ru2 – N10	1.744(4)	1.755(3)	1.757(3)	1.7537(16)	1.7818
N10 – O10	1.147(4)	1.143(4)	1.141(3)	1.147(2)	1.152
Ru2 – N10 – O10	172.2(3)	172.9(3)	172.5(3)	172.42(16)	172.36
Ru2 – N6	2.103(4)	2.121(3)	2.115(3)	2.1213(16)	2.1507
Ru2 – N7	2.095(4)	2.111(3)	2.106(3)	2.1051(17)	2.1367
Ru2 – N8	2.103(4)	2.102(3)	2.101(3)	2.1036(16)	2.1365
Ru2 – N9	2.114(4)	2.105(3)	2.101(3)	2.1050(17)	2.1334
Cl2 – Ru2 – N10	175.70(12)	174.93(10)	175.63(9)	175.47(6)	175.09
Ru2 – Cl2	2.3196(12)	2.3196(9)	2.3211(9)	2.3231(5)	2.3366
<i>Cell setting, space group</i>		Monoclinic, P 1 2 ₁ /c 1			
a , Å	15.7277(8)	15.6486(3)	15.7473(3)	15.7016(4)	–
b , Å	13.4551(7)	13.4525(2)	13.4389(2)	13.4512(4)	–
c , Å	26.7672(13)	26.8254(5)	26.8141(5)	26.8147(7)	–
β , °	92.429(4)	92.265(2)	92.4287(16)	92.436(2)	–
V , Å ³	5659.3(5)	5642.68(17)	5669.48(17)	5658.3(3)	–
<i>R1-factor</i>	5.29%	4.49%	4.30%	3.3%	–
<i>Goof</i>	0.956	1.003	0.994	–	–
<i>No. of reflections</i>	12339	12298	12355	18099	–
<i>No. of parameters</i>	828	767	872	768	–
$\Delta\rho_{max}, \Delta\rho_{min}$, eÅ ⁻³	0.673, -0.698	0.723, -0.607	0.461, -0.586	1.25, -0.93	–

TABLE 2.2: Dehydrated and Rehydrated systems: selected bond distances (Å) and angles (°) in GS state. More structure refinement details can be found in Appendix C. [‡] Selected bond distances and angles in GS in hydrated system and solid state DFT calculations published in work [62].

2.1.3 Photoisomerization of the dehydrated crystal in comparison with its hydrated form

To go deeper in understanding the role of water molecule in the crystal the photoisomerization in dehydrated form of the $[Ru(py)_4Cl(NO)](PF_6)_2 \cdot 1/2H_2O$ compound was studied under CW irradiation of 473 nm and 1064 nm (see Figure 2.5). Moreover, the rehydration process was also tested. The sample was left for two days in the room with a high humidity to have water

molecules trapped back in the sample (hereafter, rehydrated form), which was then verified with the structural determination of data collection.

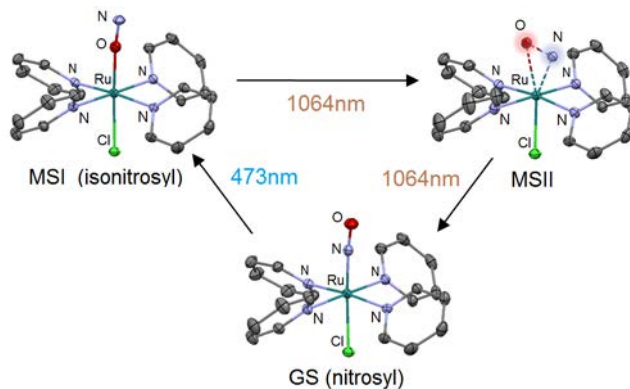


FIGURE 2.5: Photoswitching between GS, MSI and MSII states under 473 nm and 1064 nm (schematic molecular views, see ref. [62] and [15]); here the MSII state view is the side-on configuration of the $[Ru(py)_4Cl(NO)](PF_6)_2 \cdot 1/2H_2O$ single crystal at low temperatures.

The $Ru-NO$ to $Ru-ON$ photoswitching ($GS \rightarrow MSI$) and the reverse process ($MSI \rightarrow MSII^{IR} \rightarrow GS$) in hydrated, dehydrated and rehydrated forms of sample №6 were followed through the change of unit cell parameters and the results are presented in Figures 2.6, 2.7 and 2.8. We should remind that MSII species which are referred as $MSII^{IR}$ correspond to the side-on configuration, and normally found at its maximum population when the minimum of β angle is reached during the $MSI \rightarrow GS$ under the IR irradiation (see Chapter 1).

In Figure 2.6 we see that the colour change from one state to another does not depend on the water and the colour shifts from orange to green and then to black in the same way in all three cases during the irradiation. As for the lattice parameter \mathbf{a} there is a small change in behaviour after the water departure, i.e. a sudden growth around 700 minutes (see Figure 2.6 (b)). Overall in both hydrated and dehydrated forms of crystal we see the growth of \mathbf{a} under blue light and its decrease under IR irradiation.

A rather different behaviour is observed in \mathbf{b} and \mathbf{c} parameters after dehydration process. In Figure 2.7 (a,c,e) one can notice that during the $GS \rightarrow MSI$ transformation the dehydrated form of crystal shows similar decrease in \mathbf{b} , however the change, $\Delta\mathbf{b}$ is four times smaller than the decrease of \mathbf{b} in the hydrated crystal and three times smaller than in the rehydrated form (see Table 2.3). Under the IR irradiation, in a contrast to the hydrated case where \mathbf{b} is growing, $\Delta\mathbf{b} = +0.0254(16)$ Å in hydrated sample and $\Delta\mathbf{b} = +0.0194(16)$ Å in rehydrated form, we see unexpected decrease $\Delta\mathbf{b} = -0.0190(16)$ Å in dehydrated case, Table 2.3.

Even more unusual change is happening in the behaviour of parameter \mathbf{c} after the water is gone, which usually has no strong features to follow in hydrated crystals (see Figure 2.7 (b,f)). While under blue light we see no particular difference in evolution of \mathbf{c} with the hydrated form $\Delta\mathbf{c} = +0.017(3)$ Å for hydrated crystal, $\Delta\mathbf{c} = +0.022(3)$ Å for dehydrated and $\Delta\mathbf{c} = +0.013(3)$ Å for rehydrated forms, under IR irradiation an unexpectedly strong increase $\Delta\mathbf{c} = +0.064(3)$ Å takes place in dehydrated form which is five times higher than in hydrated crystal, $\Delta\mathbf{c} = +0.012(3)$ Å.

GS → MSI					
Sample	$\Delta\mathbf{a}, \text{\AA}$	$\Delta\mathbf{b}, \text{\AA}$	$\Delta\mathbf{c}, \text{\AA}$	$\Delta\beta, ^\circ$	$\Delta V, \text{\AA}^3$
Hydrated	+0.031(2)	-0.0121(16)	+0.017(3)	+0.118(10)	+9(1)
Dehydrated	+0.017(2)	-0.0035(16)	+0.022(3)	+0.041(10)	+9(1)
Rehydrated	+0.021(2)	-0.0091(16)	+0.013(3)	+0.098(10)	+6(1)

MSI → MSII^{IR}					
Sample	$\Delta\mathbf{a}, \text{\AA}$	$\Delta\mathbf{b}, \text{\AA}$	$\Delta\mathbf{c}, \text{\AA}$	$\Delta\beta, ^\circ$	$\Delta V, \text{\AA}^3$
Hydrated	-0.001(2)	+0.0254(16)	+0.012(3)	-0.521(10)	+15(1)
Dehydrated	+0.003(2)	-0.0190(16)	+0.064(3)	-0.441(10)	+8(1)
Rehydrated	+0.002(2)	+0.0194(16)	+0.004(3)	-0.396(10)	+12(1)

TABLE 2.3: Comparative table of the changes in the unit cell parameters during the photoisomerization in hydrated, dehydrated and rehydrated crystals.

The crucial point here is that the maximum of \mathbf{c} coincides with the minimum of β angle, and thus corresponds to the maximum population of MSII^{IR} species, Figure 2.8 (c)). Therefore, a strong structural signature of \mathbf{c} in dehydrated case can serve as another indicator of MSII^{IR} species evolution.

During the GS to MSI transformation both hydrated and dehydrated samples undergo growth in β angle and unit cell volume. However, the change of β in hydrated sample is three times higher than in dehydrated form (see Table 2.3), while volume change remains the same. Nevertheless, under the IR light the change in the unit cell volume is twice weaker in dehydrated form, $\Delta V = +8(1) \text{\AA}^3$, comparing to the $\Delta V = +15(1) \text{\AA}^3$ in hydrated sample and $\Delta V = +12(1) \text{\AA}^3$ in rehydrated form (see panels (b,d,f) in Figure 2.8).

In hydrated sample at 100 K with 473 nm complete or quasi-complete GS to MSI conversion happens after around 400 minutes of laser exposure with around 280 mW/cm^2 , i.e. around $2000 \text{ J}\cdot\text{cm}^{-2}$, while the maximum of MSII population is observed here after around 170 minutes of irradiation with a fluence of about 130 mW/cm^2 , i.e. $Q \approx 900 \text{ J/cm}^2$, which is also true for dehydrated form of the sample. However, even though in rehydrated case the initial behaviour of unit cell parameters during photoisomerization is recovered, the changes of unit cell parameters are weaker than in the hydrated crystal and the GS → MSI seems to be slower (see Table 2.3). In here we can think of either a certain fatigue of a sample or just partial return of water molecules inside the crystal during the rehydration (perhaps water did not get into the central part of the crystal volume). Nevertheless, the unusual and significant changes in the lattice parameters behaviour show an important role played by water molecule in studied sample.

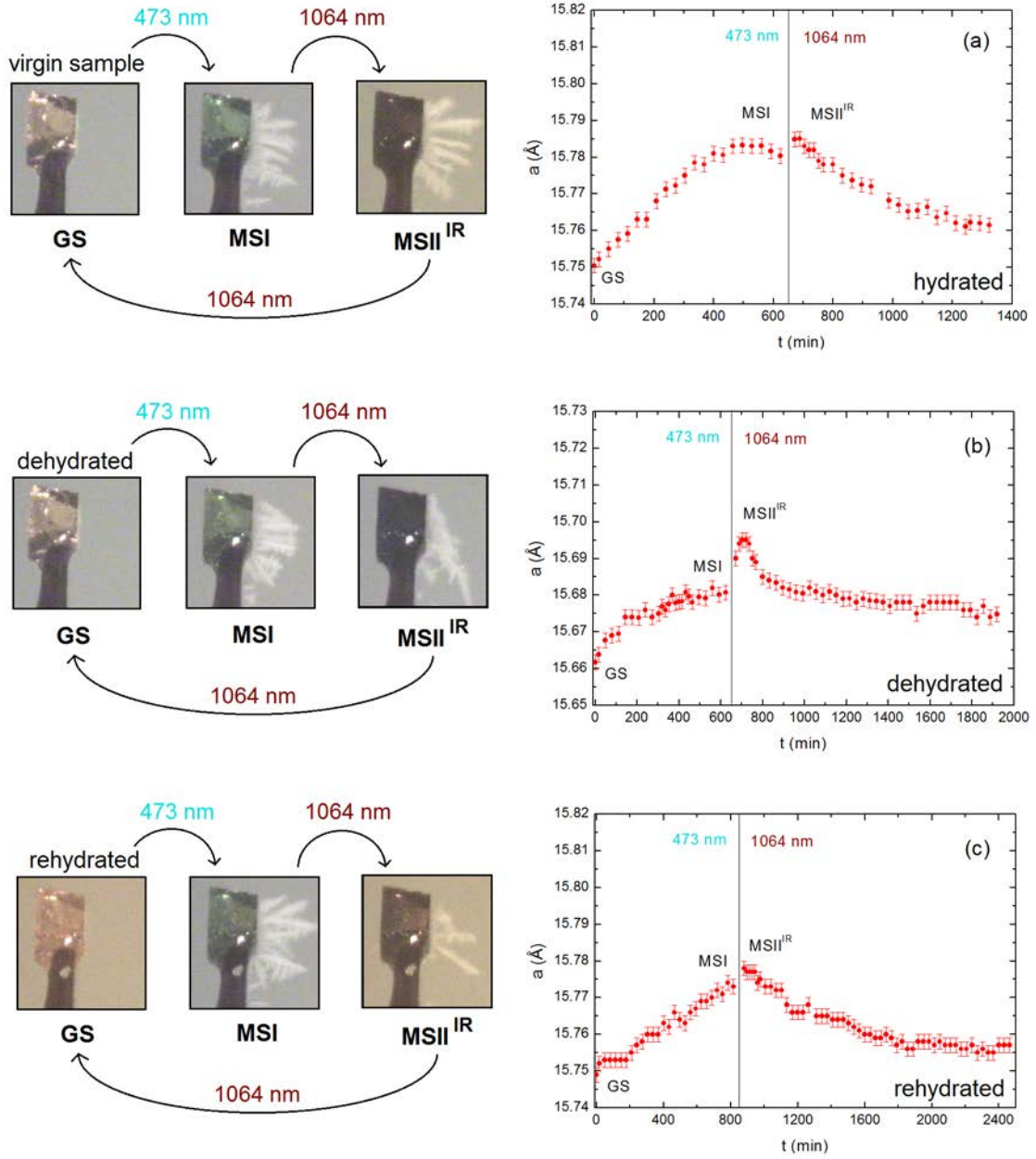


FIGURE 2.6: Evolution of the colour and lattice parameter \mathbf{a} of the $[Ru(py)_4Cl(NO)](PF_6)_2 \cdot 1/2H_2O$ single crystal at 100 K for (a) hydrated sample, (b) its dehydrated (c) and its rehydrated forms during the light irradiation with 473 nm, $280 \text{ mW} \cdot \text{cm}^{-2}$ and then 1064 nm, $130 \text{ mW} \cdot \text{cm}^{-2}$.

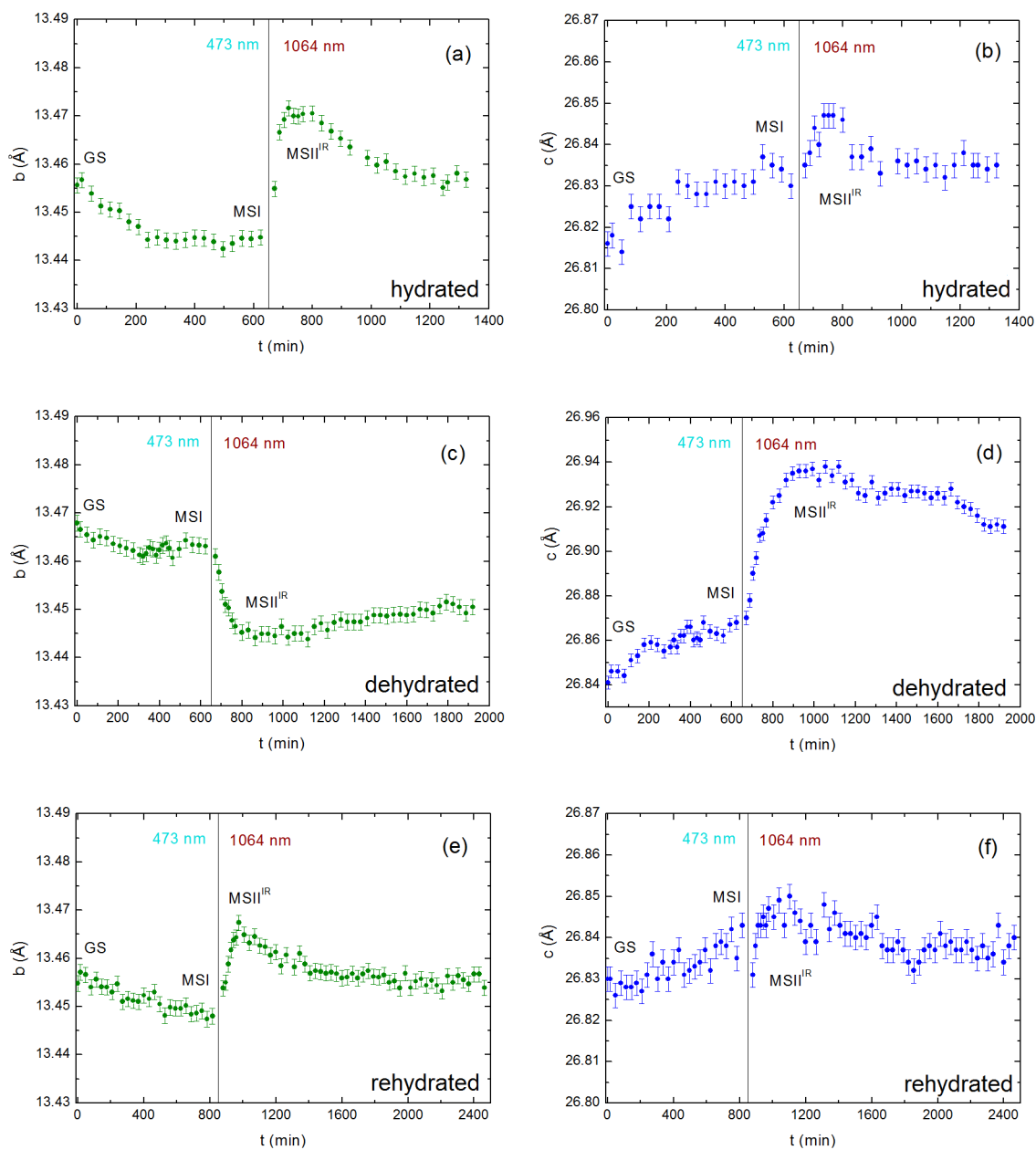


FIGURE 2.7: Evolution of the b and c lattice parameters of the $[Ru(py)_4Cl(NO)](PF_6)_2 \cdot 1/2H_2O$ single crystal at 100 K for (a), (b) hydrated sample, (c), (d) its dehydrated (e), (f) and its rehydrated forms during the light irradiation with 473 nm, 280 $mW \cdot cm^{-2}$ and then 1064 nm, 130 $mW \cdot cm^{-2}$.

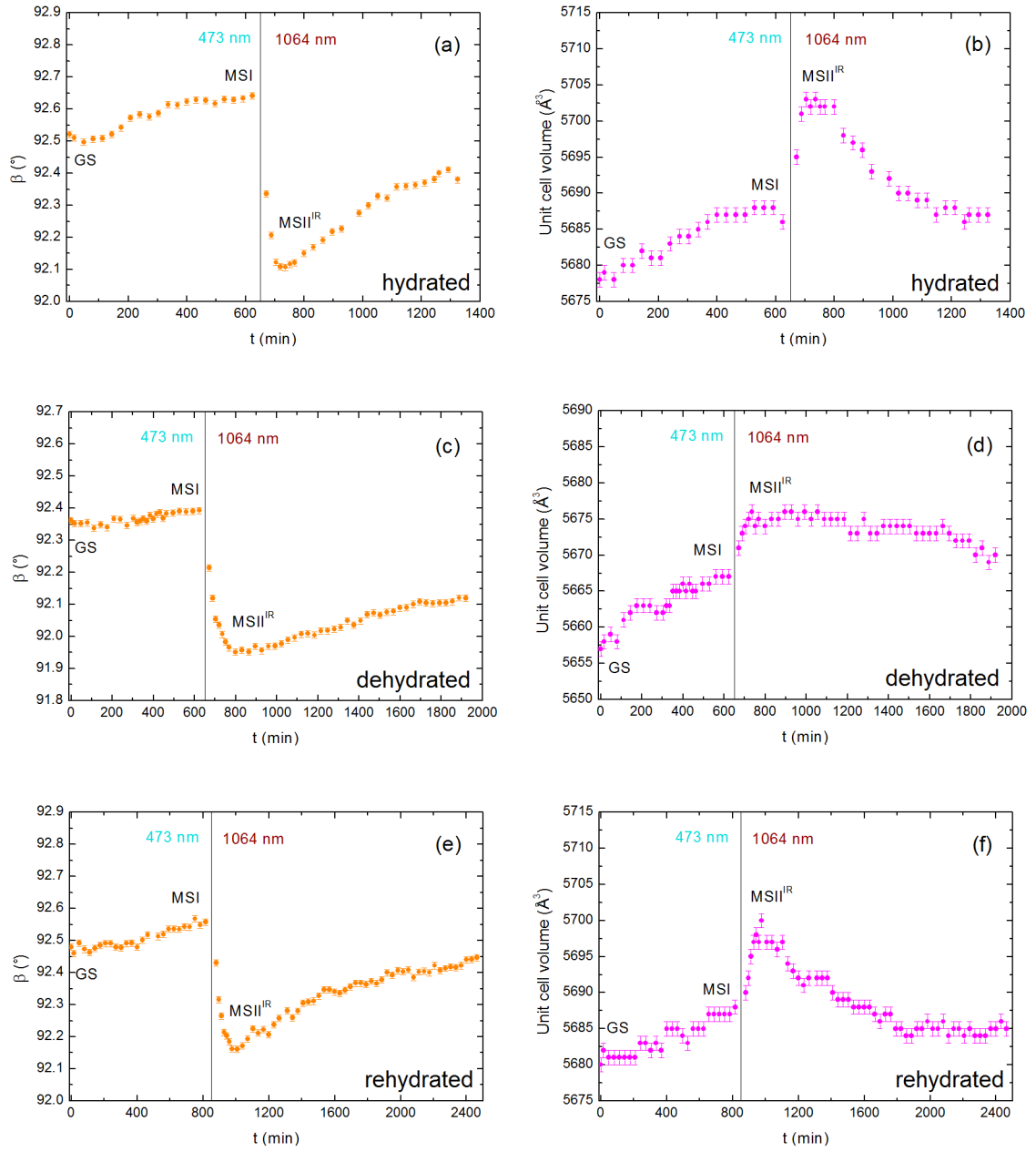


FIGURE 2.8: Evolution of the β angle and unit cell volume of the $[Ru(py)_4Cl(NO)](PF_6)_2 \cdot 1/2H_2O$ single crystal at 100 K for (a), (b) hydrated sample, (c), (d) its dehydrated (e), (f) and its rehydrated forms during the light irradiation with 473 nm, 280 $mW \cdot cm^{-2}$ and then 1064 nm, 130 $mW \cdot cm^{-2}$.

2.2 Structure of a dehydrated MSI and MSII^{IR} states determined by means of X-Ray diffraction

At 100 K the full data collections on GS, MSI and MSII^{IR} states were taken at 100 K for dehydrated and rehydrated forms of the sample N^o4 (see Table 2.1). All non-hydrogen atoms were refined anisotropically, while all hydrogen atoms were constrained by geometry. The experimental and structure refinement details can be found in Appendix C.

2.2.1 Comparison of MSI state in dehydrated and rehydrated crystal

The full data collection was taken on the sample N^o4 at 100 K under the CW irradiation of 473 nm. In Figure 2.9 the structure of two symmetry-independent cations with nearby anions and water molecules in MSI state are presented for the rehydrated system only as in dehydrated case the structure is the same with only an absence of water molecule. The most interesting distances and angles of dehydrated and rehydrated systems are compared with DFT calculations [62] in Table 2.4. We note that the difference in unit-cell volume between dehydrated and rehydrated forms is the expected value, $\Delta V = -24.67(17) \text{ \AA}^3$. However, the structural refinement of MSI shows partial transformation detected by short $Ru - O$ distances on rehydrated sample.

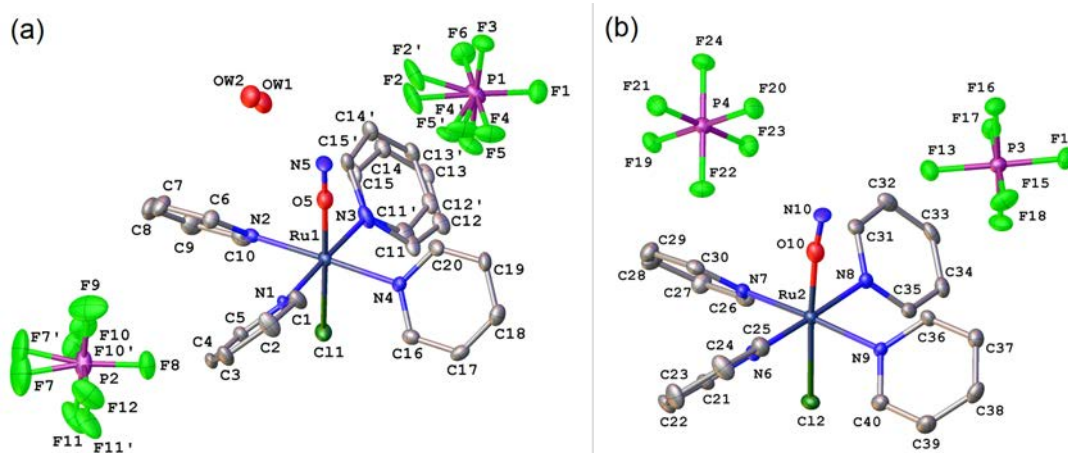


FIGURE 2.9: The structure of the two cations $[Ru(py)_4Cl(NO)]^{2+}$, four anions $(PF_6)^-$ and water molecule in MSI state. The hydrogen atoms are omitted for clarity. The plot is based on the MSI refinement. For more experimental and structure refinement details see Appendix C.

Another interesting aspect to look at is the short intermolecular contacts and how do they change with the water departure. The distance between atoms is considered a short contact if it is smaller than the sum of the Van der Waals radii of these two atoms. As the determination of Van der Waals radius for different elements is an on-going research, there are several values proposed by various physical methods, see Table 1 in [65]. We will work with the default values adopted in structure visualization tool, Mercury [66], i.e. the values proposed by Bondi [67]. In Table 2.5 the short contacts are listed for MSI state at 100 K, rehydrated and dehydrated forms are presented for comparison. It is clear that there is no significant difference in short contacts after

Distance/angle, Å/°	MSI, X-Ray		MSI, DFT [‡]
	Dehydrated sample №4	Rehydrated sample №4	
Ru1 – O5	1.864(3)	1.846(3)	1.9036
N5 – O5	1.147(4)	1.140(4)	1.1514
Ru1 – O5 – N5	178.7(3)	178.1(3)	179.04
Ru1 – N1	2.098(3)	2.099(3)	2.1241
Ru1 – N2	2.104(3)	2.094(3)	2.1192
Ru1 – N3	2.098(3)	2.086(3)	2.1344
Ru1 – N4	2.106(3)	2.112(3)	2.1209
Cl1 – Ru1 – O5	179.26(8)	178.90(8)	178.98
Ru1 – Cl1	2.2807(9)	2.2941(10)	2.3015
Ru2 – O10	1.866(3)	1.838(2)	1.8962
N10 – O10	1.142(4)	1.141(3)	1.1497
Ru2 – O10 – N10	171.2(2)	172.3(2)	173.22
Ru2 – N6	2.105(3)	2.106(3)	2.1363
Ru2 – N7	2.101(3)	2.102(3)	2.1252
Ru2 – N8	2.095(3)	2.097(3)	2.1227
Ru2 – N9	2.096(3)	2.098(3)	2.1246
Cl2 – Ru2 – O10	175.28(8)	175.44(8)	175.63
Ru2 – Cl2	2.2832(9)	2.2966(10)	2.2950
<i>Cell setting, space group</i>	Monoclinic, P 1 2 ₁ /c 1		
a , Å	15.6690(3)	15.7696(3)	–
b , Å	13.4439(2)	13.4309(2)	–
c , Å	26.8473(5)	26.8230(5)	–
β , °	92.292(2)	92.5143(16)	–
V , Å ³	5650.93(17)	5675.60(17)	–
<i>R1-factor</i>	4.41%	4.67%	–
<i>GooF</i>	0.988	0.999	–
<i>No. of reflections</i>	12307	12373-	–
<i>No. of parameters</i>	767	866	–
$\Delta\rho_{max}, \Delta\rho_{min}$, eÅ ⁻³	0.537, -0.600	0.589, -1.300	–

TABLE 2.4: Dehydrated and Rehydrated systems: selected bond distances (Å) and angles (°) in MSI state. The experimental and structure refinement details can be found in Appendix C.
[‡] Selected bond distances and angles from solid-state DFT calculations published in work [62].

the crystal dehydration, which explains the change in the lattice parameters after the water is gone.

Short contact, Å	MSI at 100 K	
	Dehydrated	Rehydrated
P1 _{anion} ··· N5	2.91 (b)	2.86 (b)
P1 _{anion} ··· N4 _{py}	3.10 (b)	3.14 (b)
P2 _{anion} ··· N2 _{py}	3.27 (b)	3.31 (b)
P2 _{anion} ··· N1 _{py}	3.29 (a)	3.32 (a)
H ₂ O ··· N5	–	3.07 (c)
H ₂ O ··· N2 _{py}	–	3.58 (b)
P3 _{anion} ··· N10	2.903 (b)	2.911 (b)
P4 _{anion} ··· N10	2.86 (c)	2.85 (c)
P2 _{anion} ··· N6 _{py}	3.23 (a)	3.23 (a)
P2 _{anion} ··· N9 _{py}	3.17 (a)	3.20 (a)
P3 _{anion} ··· N9 _{py}	3.23 (b)	3.25 (b)
P4 _{anion} ··· N7 _{py}	3.22 (a)	3.21 (a)

TABLE 2.5: The list of short contacts on two independent sites for the MSI at 100 K. P1, P2, P3 and P4 are the central atoms of $(PF_6)^-$ anion involved in the short contacts with pyridine group labelled through its nitrogen atom (N_{py}), as well as with N and O atoms of nitrosyl group (N5, O5, N10, O10). In the brackets we also present the main component of the short contact along the axes **a**, **b**, **c**. The Van der Waals radii used in calculations are default values adopted in structure visualization tool, Mercury [66], i.e. the values proposed by Bondi [67].

2.2.2 MSII^{IR} structural determination in dehydrated and rehydrated forms

The series of full data collections on rehydrated and dehydrated sample №4 (see Table 2.1) were taken one after another during the photoisomerization process from MSI to GS through MSII^{IR} at 100 K under the CW irradiation of 1064 nm (hereafter IR data collection series). These series of data collections permit to follow the evolution of the structure during the phototransition. The most difficult task was to identify the final disorder model: GS/MSII^{IR} or MSI/MSII^{IR}. The refinement in case of MSII^{IR} state (90° isomerization) is challenging as it is impossible to have 100% of pure transient state within the present experimental setup. Therefore, we will always deal with either mixture of GS/MSII^{IR} or MSI/MSII^{IR} on both symmetry-independent cations. To find out which model is more physical we went through the initial refinement with both models for all IR series with reference models of pure GS and pure MSI described in previous sections and unique restraint of the *N* – *O* distance to be equal to value of 1.14 Å. The mix model GS/MSII^{IR} was found to be the suitable one with the *Ru* – *N* refined distance of 1.75 Å. The GS/MSII^{IR} model was also shown previously to be the appropriate one by IR spectroscopy on powder sample in [15], and in our refinements we confirm that this model is the suitable one.

Restraints of geometry and ADPs. The restraint on *N*5 – *O*5 and *N*10 – *O*10 is 1.14 Å and applied by DFIX instruction with a certain parameter of deviation, which means that our distances are not completely fixed at 1.14 Å, and may vary around this value, as we didn't want to constrain our model too much. This value was chosen based on GS and MSI structural

determinations done on various samples during my PhD and it is also in agreement with works [10, 62].

With chosen model of GS/MSII^{IR} we keep restraints on $N5 - O5$ and $N10 - O10$ distances (GS) and apply a restraint on $N5' - O5'$ and $N10' - O10'$ (side-on MSII^{IR}) to maintain physically reasonable geometry of molecules during the refinement (Figure 2.10). For side-on MSII^{IR} part we restrained $N5' - O5'$ and $N10' - O10'$ distances to 1.09 Å, only when the population of MSII^{IR} is low. This value was taken from the experimental data collection with the maximum population of MSII^{IR} on dehydrated sample when refined with GS/MSII^{IR} model without any restraints. This value is also supported by DFT calculation and experimental results presented in [62]. Disordered sites were also restrained with ISOR and SIMU.

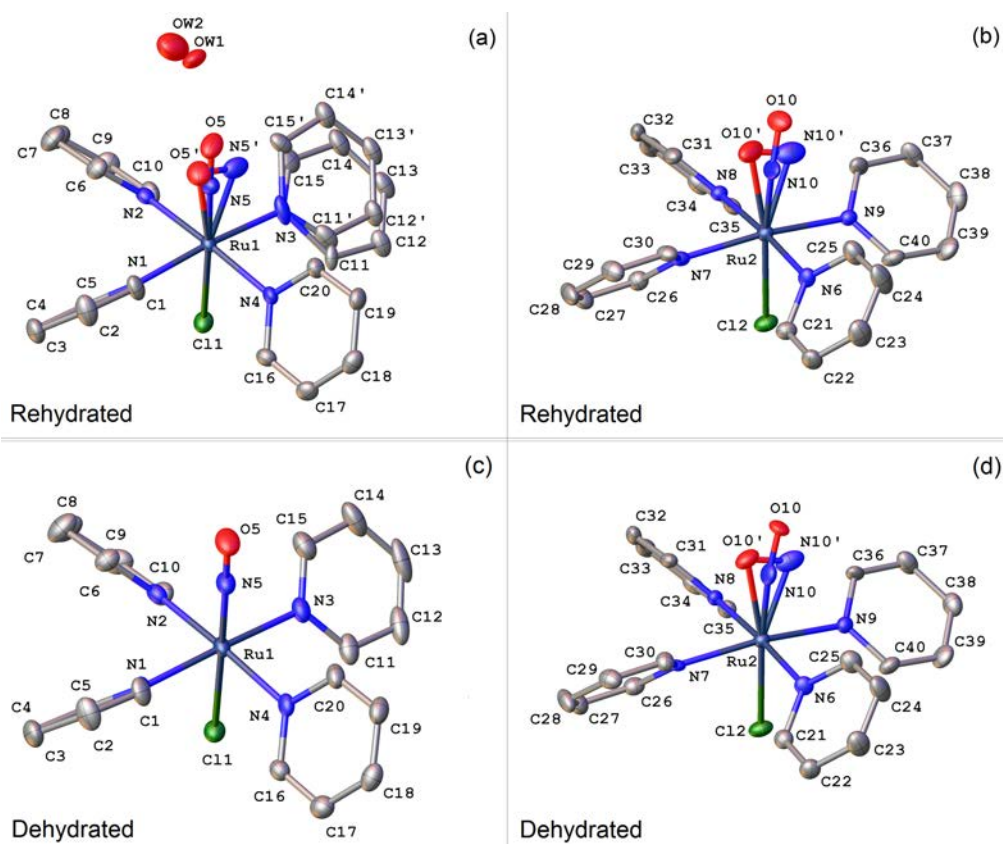


FIGURE 2.10: Rehydrated (a-b) and dehydrated (c-d) systems: structure of two independent sites of $[Ru(py)_4Cl(NO)]^{2+}$ cation and water molecule for the rehydrated form. The hydrogen atoms and anions $(PF_6)^-$ are omitted for clarity. The plot is based on the refinement with GS/MSII^{IR} model.

Rehydrated crystal. With mix model GS/MSII^{IR} and applied restraints on bond lengths $N5 - O5$ and $N10 - O10$ (GS) and on $N5' - O5'$ and $N10' - O10'$ (side-on MSII^{IR}) the refined structures are presented in Figure 2.10 (a-b). The selected bond lengths and angles are presented in Table 2.7. The structure of the two symmetry-independent cations and the water molecule of the rehydrated system in MSII^{IR} state is shown in Figure 2.11 [010] crystallographic direction.

Dehydrated crystal. In dehydrated form of the crystal the GS/MSII^{IR} mix model is used to refine the structures and in this case we observe only Ru2 molecule transformed into MSII^{IR} under IR light irradiation (Figure 2.10 (c-d)). Ru1 molecule directly relaxes back to GS as

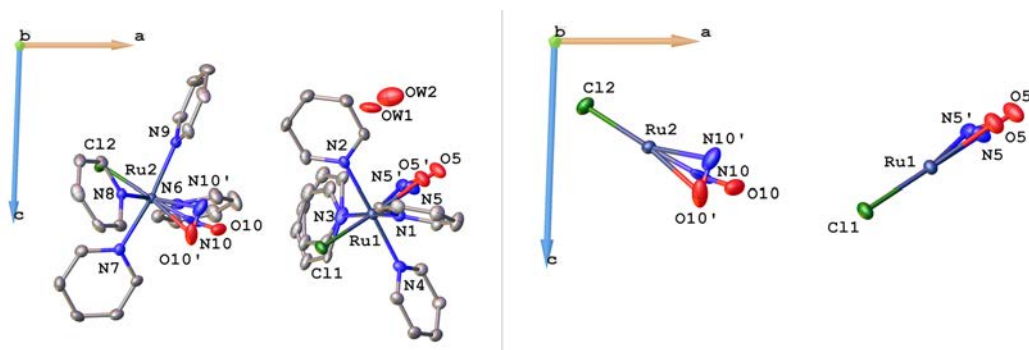


FIGURE 2.11: Rehydrated system: structure of the two cations $[Ru(py)_4Cl(NO)]^{2+}$ and water molecule projected in the crystallographic plane $[010]$. On the left the hydrogen atoms and anions $(PF_6)^-$ are omitted for clarity, while on the right only nitrosyl and Cl ligands are left. The plot is based on the refinement with GS/MSII^{IR} model. For more structure refinement details see Appendix C.

observed from the $Ru1 - Cl1$ distance with around $2.315 - 2.320 \text{ \AA}$ for pure GS state (Table 2.7). The discussion of this phenomenon will be done in the next section.

Short contacts. We would also like to compare the short contacts in the MSII^{IR} in rehydrated and dehydrated forms, see Table 2.6. Once more we do not observe any significant change in short contacts of MSII^{IR} after the dehydration process. The distance with water is quite large ($>3 \text{ \AA}$) which might also explain that there is not much influence of dehydration on the short contacts. We only observe the change in the lattice parameters after the water is gone.

Short contact, \AA	MSII ^{IR} at 100 K	
	Dehydrated	Rehydrated
$P1_{anion} \cdots O5$	2.91 (b)	3.02 (b)
$P1_{anion} \cdots N4_{py}$	3.09 (b)	3.12 (b)
$P2_{anion} \cdots N2_{py}$	3.27 (b)	3.31 (b)
$P2_{anion} \cdots N1_{py}$	3.27 (a)	3.38 (a)
$H_2O \cdots O5$	–	3.15 (c)
$H_2O \cdots N2_{py}$	–	3.49 (b)
$P3_{anion} \cdots O10$	2.90 (b)	2.93 (b)
$P4_{anion} \cdots O10$	2.91 (c)	2.89 (c)
$P2_{anion} \cdots N6_{py}$	3.19 (a)	3.21 (a)
$P2_{anion} \cdots N9_{py}$	3.18 (a)	3.19 (a)
$P3_{anion} \cdots N9_{py}$	3.34 (b)	3.35 (b)
$P4_{anion} \cdots N7_{py}$	3.27 (a)	3.23 (a)

TABLE 2.6: The list of short contacts on two independent sites for the MSII^{IR} at 100 K. P1, P2, P3 and P4 are the central atoms of $(PF_6)^-$ anion involved in the short contacts with pyridine group labelled through its nitrogen atom (N_{py}), as well as with N and O atoms of nitrosyl group ($N5$, $O5$, $N10$, $O10$). In the brackets we also present the main component of the short contact along the axes **a**, **b**, **c**. The Van der Waals radii used in calculations are default values adopted in structure visualization tool, Mercury [66], i.e. the values proposed by Bondi [67].

Distance/angle, Å/°	Dehydrated		Rehydrated	
	GS	GS/MSII ^{IR}	GS	GS/MSII ^{IR}
N5' – O5'	–	–	–	1.093(5)
Ru1 – N5'	–	–	–	1.944(11)
Ru1 – O5'	–	–	–	2.164(14)
N5' – Ru1 – O5'	–	–	–	30.3(2)
Cl1 – Ru1 – N5'	–	–	–	158.0(3)
Cl1 – Ru1 – O5'	–	–	–	170.9(3)
Ru1 – N5	1.755(3)	1.756(3)	1.759(3)	1.753(9)
N5 – O5	1.146(4)	1.137(4)	1.144(3)	1.144(8)
Ru1 – N5 – O5	179.1(3)	178.9(3)	178.6(3)	179.0(10)
Ru1 – N1	2.101(3)	2.100(3)	2.106(3)	2.104(3)
Ru1 – N2	2.103(3)	2.100(3)	2.105(3)	2.103(3)
Ru1 – N3	2.099(3)	2.105(3)	2.097(3)	2.104(3)
Ru1 – N4	2.115(3)	2.118(3)	2.117(3)	2.112(3)
Cl1 – Ru1 – N5	179.01(10)	179.04(11)	178.84(9)	178.2(3)
Ru1 – Cl1	2.3161(10)	2.3167(10)	2.3194(9)	2.3077(10)
<i>Population of MSII^{IR}</i>	–	0%	–	40.1%
N10' – O10'	–	1.104(14)	–	1.039(8)
Ru2 – N10'	–	1.964(11)	–	1.985(10)
Ru2 – O10'	–	2.159(9)	–	2.133(10)
N10' – Ru2 – O10'	–	30.6(4)	–	28.9(2)
Cl2 – Ru2 – N10'	–	158.4(3)	–	159.4(2)
Cl2 – Ru2 – O10'	–	170.7(2)	–	171.07(19)
Ru2 – N10	1.755(3)	1.752(7)	1.757(3)	1.751(4)
N10 – O10	1.143(4)	1.144(8)	1.141(3)	1.128(5)
Ru2 – N10 – O10	172.9(3)	169.5(10)	172.5(3)	163.4(10)
Ru2 – N6	2.121(3)	2.118(3)	2.115(3)	2.120(3)
Ru2 – N7	2.111(3)	2.112(3)	2.106(3)	2.110(3)
Ru2 – N8	2.102(3)	2.096(3)	2.101(3)	2.103(3)
Ru2 – N9	2.105(3)	2.114(3)	2.101(3)	2.109(3)
Cl2 – Ru2 – N10	174.93(10)	175.1(4)	175.63(9)	172.8(4)
Ru2 – Cl2	2.3196(9)	2.3047(10)	2.3211(9)	2.3048(10)
<i>Population of MSII^{IR}</i>	–	49.4%	–	49.9%
<i>Cell setting, space group</i>		Monoclinic, P 1 2 ₁ /c 1		
a , Å	15.6486(3)	15.6635(3)	15.7473(3)	15.7721(3)
b , Å	13.4525(2)	13.4341(2)	13.4389(2)	13.4506(2)
c , Å	26.8254(5)	26.9085(6)	26.8141(5)	26.8351(5)
β , °	92.265(2)	92.0001(18)	92.4287(16)	92.0993(17)
V , Å ³	5642.68(17)	5658.73(19)	5669.48(17)	5689.08(18)
<i>R1-factor</i>	4.49%	4.62%	4.30%	4.62%
<i>GooF</i>	1.003	1.01	0.994	1.007
<i>No. of reflections</i>	12298	12335	12355	12409
<i>No. of parameters</i>	767	813	872	922
$\Delta\rho_{max}, \Delta\rho_{min}$, eÅ ⁻³	0.723, -0.607	0.779, -0.695	0.461, -0.586	0.628, -0.545

TABLE 2.7: Dehydrated and Rehydrated systems (sample №4): selected bond distances (Å) and angles (°) in pure GS and mix model GS/MSII^{IR}. The experimental and structure refinement details can be found in Appendix C. We present here only IR series where maximum population of MSII^{IR} was observed.

2.2.3 Influence of water in the crystal on the MSII^{IR} species population

After water departure we do not observe MSII^{IR} species formation under the CW IR irradiation on one of the molecules, i.e. *Ru1* which is located close to the water in rehydrated case as shown Figure 2.10 (a). Instead in dehydrated case the molecule with *Ru1* metallic center relaxes very fast to GS state without passing through MSII^{IR} under the CW IR irradiation, while the molecule with *Ru2* adopts the expected MSII^{IR} structure (compare (a-b) and (c-d) of Figure 2.10). No strong *Q*-peaks are presented on the side of *Ru1* – *N5* – *O5* axis, and the value of the *Ru1* – *Cl1* bond is exactly the same as in GS state. When *Ru1* molecule is refined with MSI state we have to apply a very strong restraints on geometry in order to adopt MSI geometry. Therefore, there is no doubt of *Ru1* molecule relaxing to GS state. This reveals a strong influence of water molecule on the MSII^{IR} species formation on the *Ru1* molecule.

In case of *Ru2* molecule as shown in Figure 2.12 a different evolution of the MSII^{IR} population under the continuous IR irradiation in dehydrated and rehydrated samples is observed. While in the rehydrated compound we see the maximum population of MSII^{IR} on both molecules after first hour of IR irradiation with its linear decrease afterwards, in the dehydrated case we observe the gradual growth of MSII^{IR} population with its maximum reached after almost 8 hours of IR irradiation. One can also notice that the population of MSII^{IR} in dehydrated system stays around 40% twice longer than in the hydrated sample. This shows crucial role of water molecule in the crystal on the MSII^{IR} generation process and its population dynamics. The evolution of the most interesting distances and angles of dehydrated and rehydrated systems during the continuous IR irradiation are summarized in Appendix D.

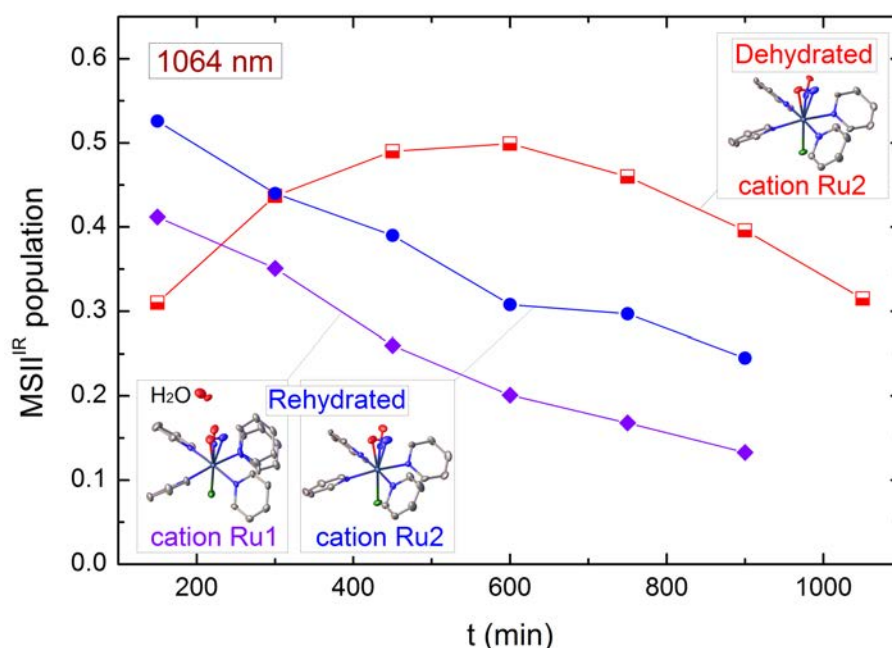


FIGURE 2.12: The evolution of the MSII^{IR} population during the continuous IR irradiation with 1064 nm, 130mW · cm⁻² in dehydrated and rehydrated systems of $[Ru(py)_4Cl(NO)](PF_6)_2 \cdot 1/2H_2O$ single crystal.

We can list several consequences of the crystal dehydration, which shows clearly the important role of water molecule in the phototransformation process:

- First of all, we observe a significant difference in lattice parameters evolution in dehydrated sample comparing to the hydrated one, particularly on parameters **b** and **c** under the IR irradiation. Parameter **b** unexpectedly decreases under the IR irradiation with water departure, while in hydrated sample it always grows during the first hour of irradiation. Parameter **c** undergoes a strong change in dehydrated sample, which is five times higher than the evolution observed in hydrated case during the $MSI \rightarrow MSII^{IR}$ transformation, where the change of **c** is negligible.
- The β angle in dehydrated crystal, which we follow to detect the maximum population of $MSII^{IR}$ species, does not deviate much from the evolution in the hydrated sample, nevertheless, it shows a much slower kinetics of relaxation towards the GS state. This is also in agreement with the fact that the maximum of $MSII^{IR}$ population is reached within first two hours of IR irradiation in hydrated case, while in dehydrated system it takes almost 8 hours. Therefore, the kinetics of the system strongly depends on the water presence in the crystal structure for the MSI back to GS photoreaction under the 1064 nm. The kinetics for GS to MSI under the blue light seems to be the same (with the same pump power and time irradiation) in dehydrated crystal, the complete phototransformation is observed as in hydrated case.
- Another surprising effect of water departure is the direct transformation of one of the independent sites in the unit cell to GS without passing through $MSII^{IR}$ under the IR irradiation. In hydrated sample we clearly see the ‘side-on’ $MSII^{IR}$ species on both independent sites ($Ru1 \langle N_5^{O5}, Ru2 \langle N_{10}^{O10}$) after IR light, however, in dehydrated sample the $Ru1 - O5 - N5$ molecule in MSI state does not transform to the ‘side-on’ MSII configuration under CW IR irradiation, it relaxes very fast to GS instead. It seems that there is a strong influence of water presence on the $Ru1 \langle N_5^{O5}$ species formation, taking into account that water is located next to this molecule.
- As for the rehydration of the sample, we can only notice that it does not appear to be complete. We do see the water presence in the structure of the molecule, so we are sure that it came back, and the lattice parameters evolution is typical for the hydrated sample, but they are less pronounced than in the initial crystal. When we observe the MSI state $Ru - O$ bond lengths (around 1.84 Å) in rehydrated crystal, we notice that they are a little bit shorter than a typical 1.86 Å value. These arguments suggest that we might have slower kinetics in the rehydrated crystals. Even if we irradiate the rehydrated sample longer time we do not succeed in observing the complete phototransformation of $GS \rightarrow MSI$.
- As a last point we would like to discuss the short contact list in both MSI and $MSII^{IR}$ for dehydrated and rehydrated samples. From the calculations of these contacts we can notice that there is no significant changes during the dehydration process, so it seems that

after the departure of water the molecules in the unit cell rearrange themselves in a way to keep the existing short contacts. Such rearrangements and small deviation of short contact values after the dehydration explains drastic changes observed in the lattice parameters evolution.

Chapter 3

Photoisomerization in

$[Ru(py)_4Cl(NO)](PF_6)_2 \cdot 1/2H_2O$ single crystal: chasing MSII state by ultrafast optical experiments in the visible range

The stop-motion photography and time-resolved experiments share the same basic principles: short light flashes to illuminate the object and high-speed shutter cameras to catch the motion of this object [71]. The concept of high-speed photography was first tried in 1872 by Eadweard Muybridge during his investigation of horses' feet during the gallop (Figure 3.1 (a)) and later in photographs of falling cat in 1894 by Etienne-Jules Marey [72], the inventor of 'chronophotography', a special technique to capture several sequential frames of motion, which can be then merged into a single image (see Figure 3.1 (b)).

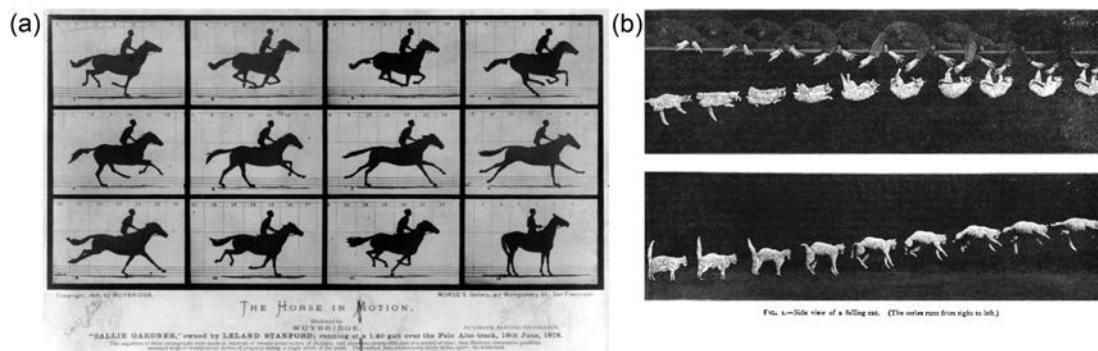


FIGURE 3.1: (a) The horse running over the Palo Alto track, 19 June 1878. Photographs by Eadweard Muybridge. (b) Photographs of a tumbling cat by Etienne-Jules Marey, 1894 [72].

In stop-motion photography we follow an animal or a human with a duration of camera shutter opening of some milliseconds to get a spatial resolution of some centimeters. In time-resolved experiments to observe the motion of atoms with typical speed of the order of a few 100 m/s and with a spatial resolution smaller than 1 Å we need a shutter opening (or light flashes) of

the order of 10 – 100 femtoseconds. With the fast development of femtosecond laser experiments over the past decades we are able now to ‘freeze’ atoms in motion and study the transition states involved at each step of the chemical reaction.

3.1 Introduction

During this PhD work single crystals of $[Ru(py)_4Cl(NO)](PF_6)_2 \cdot 1/2H_2O$ compound have been investigated with a steady state absorption spectroscopy (see Chapter 1, [64]) and we remind in this section the main results of this study. As shown in Figure 3.2 (a-b) absorption spectra in the visible range has been measured for the GS state ($Ru - NO$) as well as for two photoinduced isomers: MSI ($Ru - ON$) and MSII^{IR} (a combination of GS and MSII states observed under IR continuous light irradiation). A predominant two-step photon absorption process during the $Ru - NO$ to $Ru - ON$ phototransformation (GS to MSI) under the 473 nm light irradiation was observed experimentally (Figure 3.2 (a), (d)) but the nature of the transient, so-called MSII state (scheme Figure 3.2 (d)), could not have been unambiguously determined: we can’t claim that the intermediate MSII state is the same for both $Ru - NO$ to $Ru - ON$ and the reverse phototransformation. Indeed, direct structural determination of the transient MSII species was

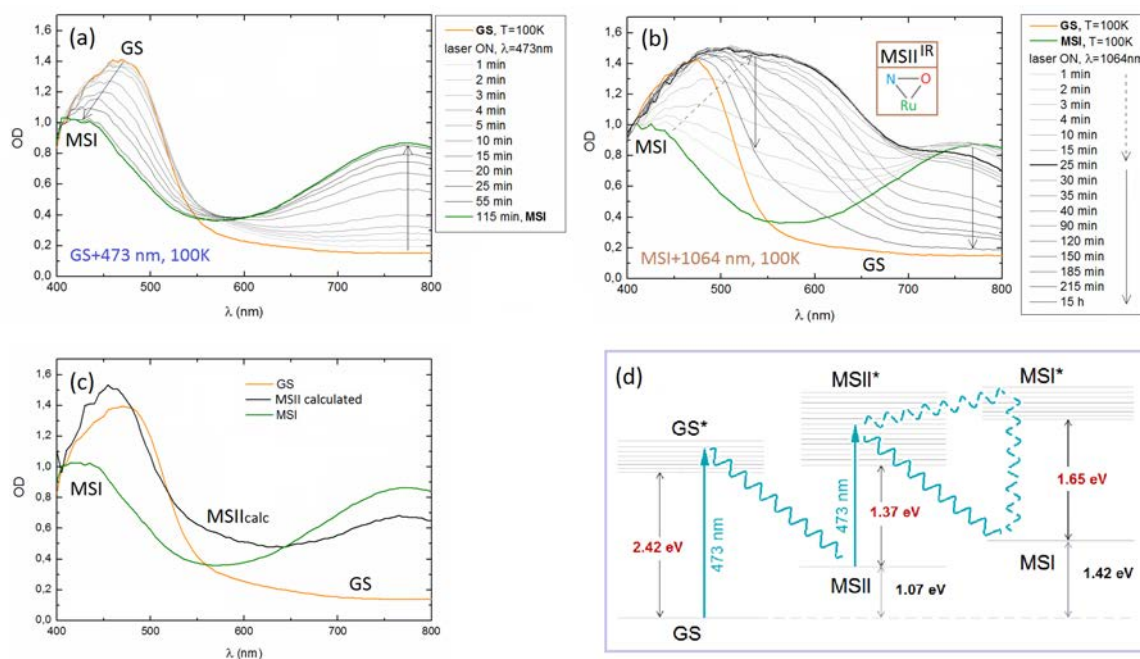


FIGURE 3.2: (a) $Ru - NO$ to $Ru - ON$ photoswitching probed by the time evolution of the OD of one $[Ru(py)_4Cl(NO)](PF_6)_2 \cdot 1/2H_2O$ single crystal with 473 nm, around $1100 mW \cdot cm^{-2}$ at 100 K; (b) $Ru - ON$ to $Ru - NO$ photoswitching probed by the time evolution of the OD of one $[Ru(py)_4Cl(NO)](PF_6)_2 \cdot 1/2H_2O$ single crystal at 100 K with 1064 nm, around $600 mW \cdot cm^{-2}$; (c) OD spectra of the GS and MSI states (experimental data) and OD spectra of the intermediate MSII state deduced from the kinetic model reproducing the OD evolution under 473 nm; (d) Proposed scheme of two-step photon absorption under the blue light: relative positions of MSI and MSII states of $[Ru(py)_4Cl(NO)]$ molecule, their excited states and excited level of the GS state (from Ref. [15]). Vertical arrows represent irradiation of 473 nm. The dark red numbers stand for the calculated values of energy, while the black ones for the measured values.

possible only under IR light during the $Ru - ON$ back to $Ru - NO$ transformation where the side-on geometry was observed (see [62, 64] and Chapter 1 for details). The necessity of an intermediate MSII state for the $Ru - NO$ towards $Ru - ON$ photoisomerization under the blue light was evidenced through the absence of an isosbestic point on the optical spectra evolution at 100 K (Figure 3.2 (a)). Curiously, at 180 K the phototransformation from GS to MSI under continuous blue light is limited to around 10% (see Figure 1.11 (b) in Chapter 1). To explain this temperature dependence we refer to thermal decay curves presented in Figure 3.3 from work [15]. By means of differential scanning calorimetry (DSC) the authors measured the variation of enthalpy, dH/dt , for MSI and side-on MSII states during the heating cycle of DCS, where the maximum of heat release occurs at 246(1) K for MSI and at 161(1) K for MSII state. The activation energy, E_A , and prefactor, Z , were deduced from data fitting (see Table 3.1). With obtained parameters and Arrhenius law it is possible to calculate lifetimes of metastable MSI and MSII states at different temperatures as shown in Table 3.1. At 180 K the lifetime of MSII state is quite short, $\tau_{MSII} = 6.24$ s and so in photoisomerization process $GS \rightarrow MSII \rightarrow MSI$ there is less probability of MSII state to reabsorb second photon, as this transient state does not live long enough.

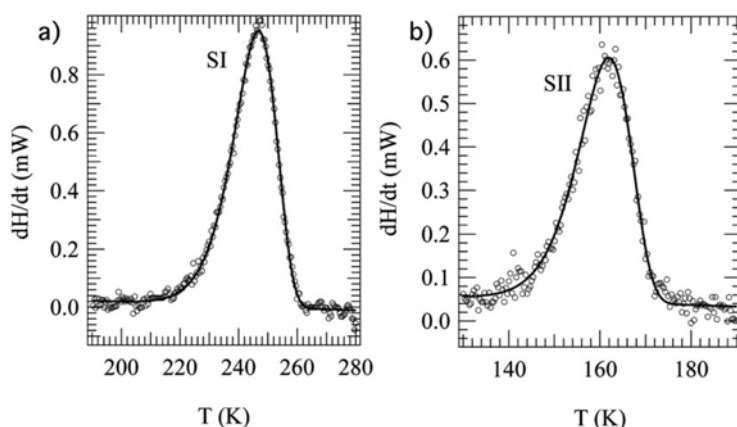


FIGURE 3.3: Thermal decay curves of (a) MSI reached by 476.5 nm irradiation and (b) MSII populated from MSI by 1064 nm at 120 K in $[Ru(py)_4Cl(NO)](PF_6)_2 \cdot 1/2H_2O$, solid lines correspond to fitting curves. The activation energy and frequency factor found from fitting are used in the metastable states lifetime calculations (Figure is taken from [15]).

Other configuration than the side-on of metastable MSII state is also possible as an intermediate state for $Ru - NO$ to $Ru - ON$ transition as long as it has short lifetime at 180 K. Nor direct structural determination of the transient MSII state during the GS to MSI photoswitching, neither the experimental observation of its optical spectrum can be obtained using continuous light irradiation (low concentration of the transient species due to their fast absorption of blue light). Nevertheless, as it was shown in Chapter 1 we could extract the shape of the optical density (OD) of the transient state from a simple kinetic model (Figure 3.2 (c) [64]), where 3 states (GS, MSI and MSII) and two kinetic constants ($K_{GS \rightarrow MSII}$, $K_{MSII \rightarrow MSI}$) are considered (see Chapter 1 for more details).

The OD spectrum of transient state extracted with this kinetic model looks different from the spectrum of the side-on $MSII^{IR}$ measured during the MSI back to GS photochemical process

	MSI	MSII
Activation energy E_A , eV	0.70(3)	0.38(3)
Frequency factor Z , s^{-1}	2×10^{12}	7×10^9
Lifetime, s Arrhenius law, $\tau = Z^{-1} \exp(E_A/k_B T)$		
Temperature, K	MSI	MSII
100	9.52×10^{22}	2.03×10^9
140	7.92×10^{12}	6.84×10^3
180	1.99×10^7	6.24
220	5.44×10^3	7.25×10^{-2}
300	0.29	3.46×10^{-4}

TABLE 3.1: The calculated lifetimes of metastable states MSI and MSII at various temperatures. The activation energy and frequency factors were found from fitting the thermal decay curves measured by differential scanning calorimetry in work [15], see Figure 3.3.

under IR irradiation. Indeed, the latter one has strong absorption in a wide range of visible yellow-red region (compare black curves in Figure 3.2 panels (b), (c)).

As the molecular geometry can strongly influence the optical properties, the difference between transient spectrum found from kinetic model in $Ru - NO$ towards $Ru - ON$ photoswitching under the blue light and $MSII^{IR}$ spectra observed in reverse photochemical process under the IR irradiation could indicate that the geometry of transient $MSII$ species under blue light irradiation differs from the 90° side-on configuration of $MSII^{IR}$. Even though up to now only two long-lived photoisomers, MSI and side-on configuration $MSII$, have been experimentally evidenced in the studied compound of $[Ru(py)_4Cl(NO)](PF_6)_2 \cdot 1/2H_2O$, as well as in SNP prototype compound (see Introduction), other configurations have been proposed by Carducci et al. [10] as well as by recent calculations of Garcia et al. [69] (see Figure 3.4). An experimental observation, however, is needed to confirm the existence of different $MSII$ geometries, and unfortunately, the CW light in case of $MSII$ state under the blue light irradiation does not give a direct access to its signature. Nevertheless, the direct signature might be detected in time-resolved experiments.

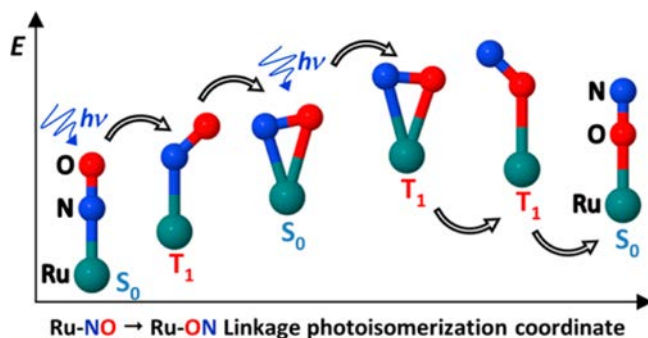


FIGURE 3.4: A scheme of structural transformations and two-step photon absorption process proposed by density functional theory calculations of Garcia et al. [69].

The aim of our work presented in this Chapter is to catch experimentally the optical signature of MSII during the GS \rightarrow MSI photochemical reaction under blue light (473 nm). Indeed, the use of ultrafast pulses (a few 10 fs) prevents the same molecule to absorb a second photon (473 nm) after its transformation into MSII state, which takes the order of ps. Thus, we should mainly observe the first part of two-step photon absorption process, i.e. GS \rightarrow MSII (see Scheme 3.2 (d)). Besides, the lifetime of MSII species at room temperature (346 μ s from Table 3.1) allows to perform stroboscopic measurements at 1 kHz (Table 3.1). By giving access to the ultrashort dynamics of the photoinduced chemical reaction, in addition to the long-lived photoisomers the time-resolved optical measurements might also give information on excited short-lived transient states, as those labelled with a star (*) on Scheme 3.2 (d).

3.2 Time-resolved studies: chasing MSII optical signature

Time-resolved experiment allows to follow the evolution of visible spectra on a short time scale with resolution of 80 fs by exciting single crystal of $[Ru(py)_4Cl(NO)](PF_6)_2 \cdot 1/2H_2O$ with femtosecond pulses of monochromatic pump and measuring changes of absorption with femtosecond pulses of mono- or polychromatic probe at room temperature. However, the pump-probe measurements on single crystal are quite challenging as the signal strongly depends on the surface of the crystal as well as the purity and homogeneity of its volume. These crystals are very sensitive to the light and they are damaged easily with power of pump pulses. Therefore, we had to find a compromise between the usable pump power and the absolute signal value: the pump power was kept low enough to preserve a sample and the absolute value of signal was registered before and after the scans to be sure that the sample does not degrade. The thickness of crystals was chosen such that we probe the volume with molecules which are mostly transformed after the excitation which is the case when the crystal is thin enough. For both monochromatic pump-probe and white light probe experiments typical size of the signal spot was around $80 \times 80 \mu m^2$ and typical size of the crystal was $200 \times 150 \mu m^2$. For more details see experimental part in Appendix E.

3.2.1 Monochromatic pump-probe measurements

The data collections were made at room temperature at three different probe wavelengths: 580 nm, 610 nm and 700 nm with a monochromatic pump in the region of 470 – 490 nm. In Figure 3.5 we present scans for (a) 610 nm and (b) 700 nm probes up to 20 ps. The obtained curves consist of sharp peak due to the electronic excitation from GS and quite long decay toward a ‘plateau’ starting around delay of 15 – 20 ps. This ‘plateau’ is shown here in Figure 3.5 (c) for 580 nm probe. We have reproduced several times the same experiments on different samples. On every data the obtained experimental curves required a fitting with at least two exponentials to reproduce the decay towards the ‘plateau’. More precisely, the data was fitted with convolution of double exponential decay and gaussian, $G(t)$, i.e. with function $[(A_1 \exp^{-t/\tau_1} + A_2 \exp^{-t/\tau_2}) \times u(t)] \otimes G(t)$, where gaussian represents the shape of laser pulse in

time and $u(t)$ is the step function. Two time constants were obtained, 1.9 ps , 7.2 ps for 610 nm and 2.3 ps , 7.8 ps for 700 nm . The data fitting shows that at least two processes are involved in the formation of the ‘plateau’.

The longer scan at 580 nm (Figure 3.5 (c)) shows that the ‘plateau’ is still present at 2 ns and remarkably the sign of the ‘plateau’ stays negative which means that the absorption of the intermediate state observed in here has the OD higher than the GS state, which is similar feature of MSII optical signature seen in static measurements (see Figure 3.2 (b), (c)). This is a good argument to suggest that the observed signal corresponds to MSII state. However, with the current setup (scan up to 2 ns) it was not possible to verify the expected lifetime of MSII, $\tau_{MSII} = 346 \mu\text{s}$ at 300 K (see Table 3.1). Therefore, even though it is a good argument in favour of observed signal being the MSII state, we cannot consider it as a clear evidence, as the lifetime of caught state is not determined. With the longer time delay setup, which can measure the signal up to 1 ms , we couldn’t detect optical signature of transient state, as the signal was very weak and comparable to the noise.

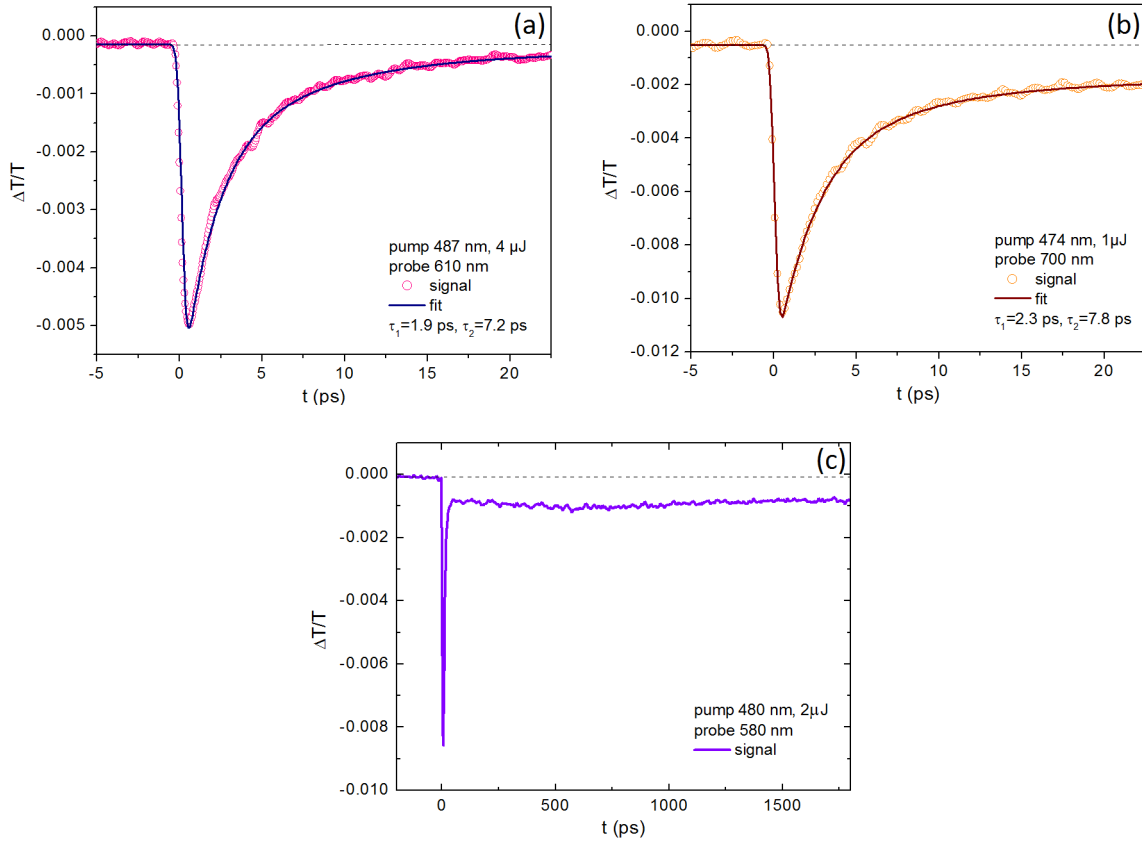


FIGURE 3.5: Pump-probe experimental results: (a) pump 487 nm , $4 \mu\text{J}$, probe 610 nm ; (b) pump 474 nm , $1 \mu\text{J}$, probe 700 nm ; (c) pump 480 nm , $2 \mu\text{J}$, probe 580 nm . Data is fitted with double exponential decay, gaussian and step function.

These experimental observations clearly differ from those made on the prototype SNP compound, as shown in Figure 3.6 [47]. In SNP system the time-resolved studies showed the build-up of MSII state after less than 1 ps , which decays back to GS within 270 ns at 300 K [47]. The monoexponential fit with time constant of 300 fs is in agreement with the idea of fast relaxation from GS^* to MSII without any other intermediate state involved. Note that in SNP

case the experimental lifetime of the ‘plateau’ (MSII) is in accordance with the calculated lifetime, $\tau = 300 \text{ ns}$, deduced from Arrhenius equation with $E_A = 0.43 \text{ eV}$ and $Z = 7 \times 10^{13} \text{ s}^{-1}$ for SNP compound [14].

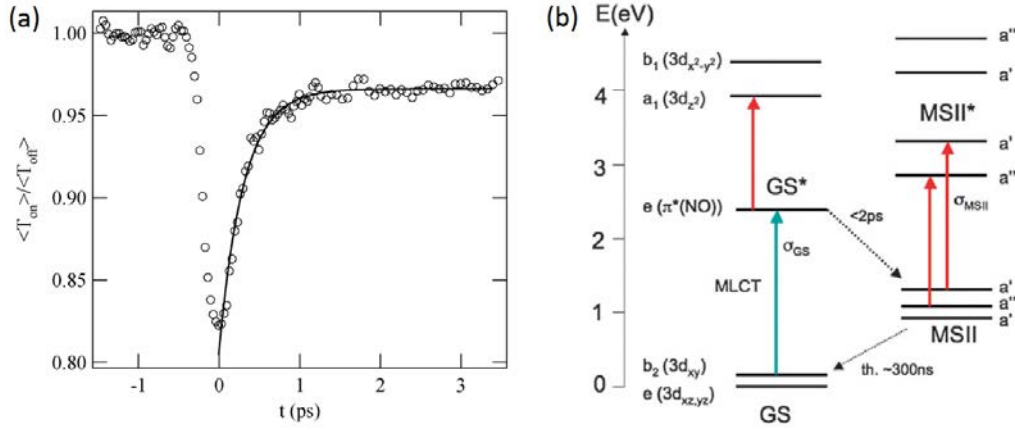


FIGURE 3.6: SNP compound: (a) normalized transmission after pulsed excitation with exponential fit (time const=300 fs) and (b) orbital scheme for GS and MSII states. The Figures are taken from [47].

Main features of our experimental results on $[Ru(py)_4Cl(NO)](PF_6)_2 \cdot 1/2H_2O$ are (i) very weak intensity of the ‘plateau’, (ii) increased OD at probed wavelengths, 580 nm, 610 nm and 700 nm, (iii) two characteristic times of relaxation, 2 ps and 7 ps, (iv) longer decay towards ‘plateau’ comparing to SNP prototype. These results will be discussed in the end of this Chapter.

3.2.2 Monochromatic pump white light probe experiment

Another way to study the transient species is by the time-resolved white light experiment. It allows us to access the spectrum of transient states during the GS \rightarrow MSI photoisomerization. The experimental setup and detection system of these measurements are described in details in Appendix E. In here we will just give some short description of the performed experiment.

The 20 000 spectra were collected by CCD detection system during each scan, then averaged and analysed with double reference technique, i.e. the relative intensities of spectra from the sample with and without pump were divided as follows:

$$\Delta OD = \log_{10} \frac{\frac{I_{sig}}{I_{ref}}}{\frac{I_{sig}^{pump}}{I_{ref}^{pump}}} = \log_{10} \left(\frac{I_{sig}}{I_{sig}^{pump}} \cdot \frac{I_{ref}^{pump}}{I_{ref}} \right) \quad (3.1)$$

where the I_{sig}^{pump} is the spectrum obtained with pump, I_{sig} - without pump, and I_{ref}^{pump} , I_{ref} are the reference spectra collected together with the signals. This method of tracing ΔOD helps to reduce the noise from the white light generation instability, but it does not allow us to have a direct comparison with the absolute value of absorption spectra obtained in steady state measurements from Chapter 1, [64] (the double reference technique is very sensitive to the OD change but does not provide us with information on absolute OD values). Nevertheless,

the differential optical density measurements provide with direct information on photoinduced changes in absorption spectra of single crystal.

Several single crystals were studied under the 470 nm, 250 Hz pumping with a 500 Hz white light probe. All crystals preserve the same features at roughly similar time delays showing the consistency of the results. The typical evolution of ΔOD for $[Ru(py)_4Cl(NO)](PF_6)_2 \cdot 1/2H_2O$ single crystal at 290 K is presented in Figure 3.7. The shape of curves are changing from crystal to crystal due to the instability of the laser system, the white light generation process and different crystal thickness. Nevertheless, the observed typical signatures are the higher OD change in green region comparing to yellow-red region around 2 ps – 5 ps and similar OD change from green to red regions at around 8 ps. This evolution might be explained by the mixture of several transient states between GS and MSII states with their own decay times, which makes the ΔOD evolve differently throughout the observed wavelength region.

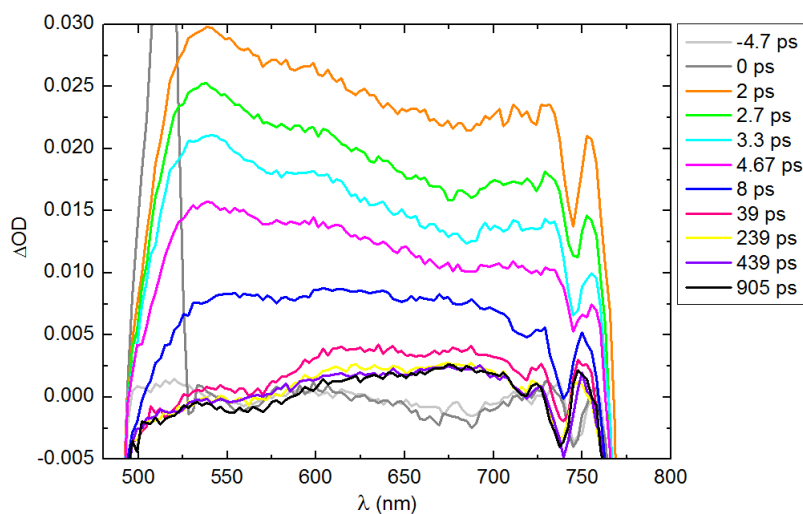


FIGURE 3.7: ΔOD evolution of $[Ru(py)_4Cl(NO)](PF_6)_2 \cdot 1/2H_2O$ single crystal at room temperature during the time-resolved white light experiment.

At longer time delay, around 40 ps, the signal either returns to the initial value or the final signal is simply very weak and comparable with the noise of experiment. One possible explanation of this weak signal is that the power of the pump we use is not enough to excite significant population of molecules and observe a strong signature of MSII state. Nevertheless, from the white light experiment we suggest the existence of at least two processes, which is coherent with our results of monochromatic experiment. This will be discussed in the end of this Chapter.

3.2.3 Single shot experiment

In order to catch the transient MSII state one can use a much higher power of the pump. However, as the crystal breaks fast there is only one shot to measure transmission. Single shot measurements were performed by Ciro D'Amico, postdoc at IPR, with a setup of time-resolved white light experiment, but with power of the pump ten times higher than we used in our pump-probe experiments presented in the beginning of this Chapter. I did not participate in this

experiment, but I would like to compare Ciro's results on observed intermediate state with the spectrum of MSII state during $GS \rightarrow MSI$ photoconversion deduced from our kinetic model $GS \rightarrow MSII \rightarrow MSI$ in Chapter 1, see Figure 3.2 (c) (for convenience, MSII and GS OD signatures will be presented in form of transmission in this section).

In Figure 3.8 the single shot experimental setup is presented. As a first step the light intensity transmitted by single crystal, I_{sig} , is measured without the pump, then sequential measurement of transmitted light intensity, I_{sig}^{pump} , is taken every 2 ms in presence of pump (480 nm, 46 μJ). Then both spectra are divided by the reference signal, which is proportional to the incident light, I_{ref} , to obtain the transmission of the single crystal with and without the pump. The pump always arrives before the probe, and after the first shot with 46 μJ pump the crystal is already destroyed.

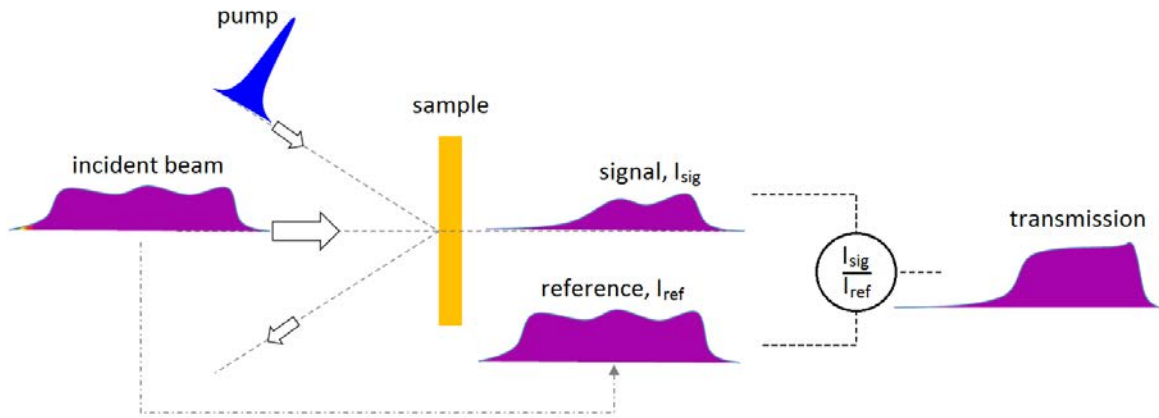


FIGURE 3.8: Single shot experimental concept. The same setup as for time-resolved white light was used with pump pulse of 50 fs at 480 nm and probe pulse of 2 ps (chopped) and 450 nm – 750 nm continuum (experiment is performed by Ciro D’Amico, unpublished results).

To gather some statistics and confirm obtained spectra Ciro D’Amico measured several single crystals, and in Figure 3.9 the typical transmission spectra of $[Ru(py)_4Cl(NO)](PF_6)_2 \cdot 1/2H_2O$ single crystal at room temperature is presented. The crystal was measured several times without the pump and then once with the pump before it was damaged (Figure 3.9(c)). At short time delay ($\Delta t = 20$ ps, Figure 3.9(a,b)) we might see a crossing point and if we compare single shot spectra evolution with the MSII spectrum estimated in this work (Figure 3.9 (d)) we can see the following similarities: (i) crossing point of MSII and GS spectra around 515 nm at $\Delta t = 20$ ps; (ii) growth of the transmission just below 515 nm and decrease of the transmission just above 515 nm at $\Delta t = 20$ ps (compare Figure 3.9 (b) and (d), purple arrows); (iii) we also observe strong decrease of transmission in the region of 600 nm – 700 nm at long time delay $\Delta t = 660$ ps with the flat form of the curve being preserved (compare Figure 3.9 (d) and (e), light blue arrow). Therefore, we can conclude that transient state observed in single shot experiment is similar to the optical signature of MSII transient state under the blue light and different from side-on MSII^{IR} observed under the IR irradiation, which is another experimental evidence in favour of the different MSII geometries during the $GS \rightarrow MSI$ and reverse $MSI \rightarrow GS$ photoswitching.

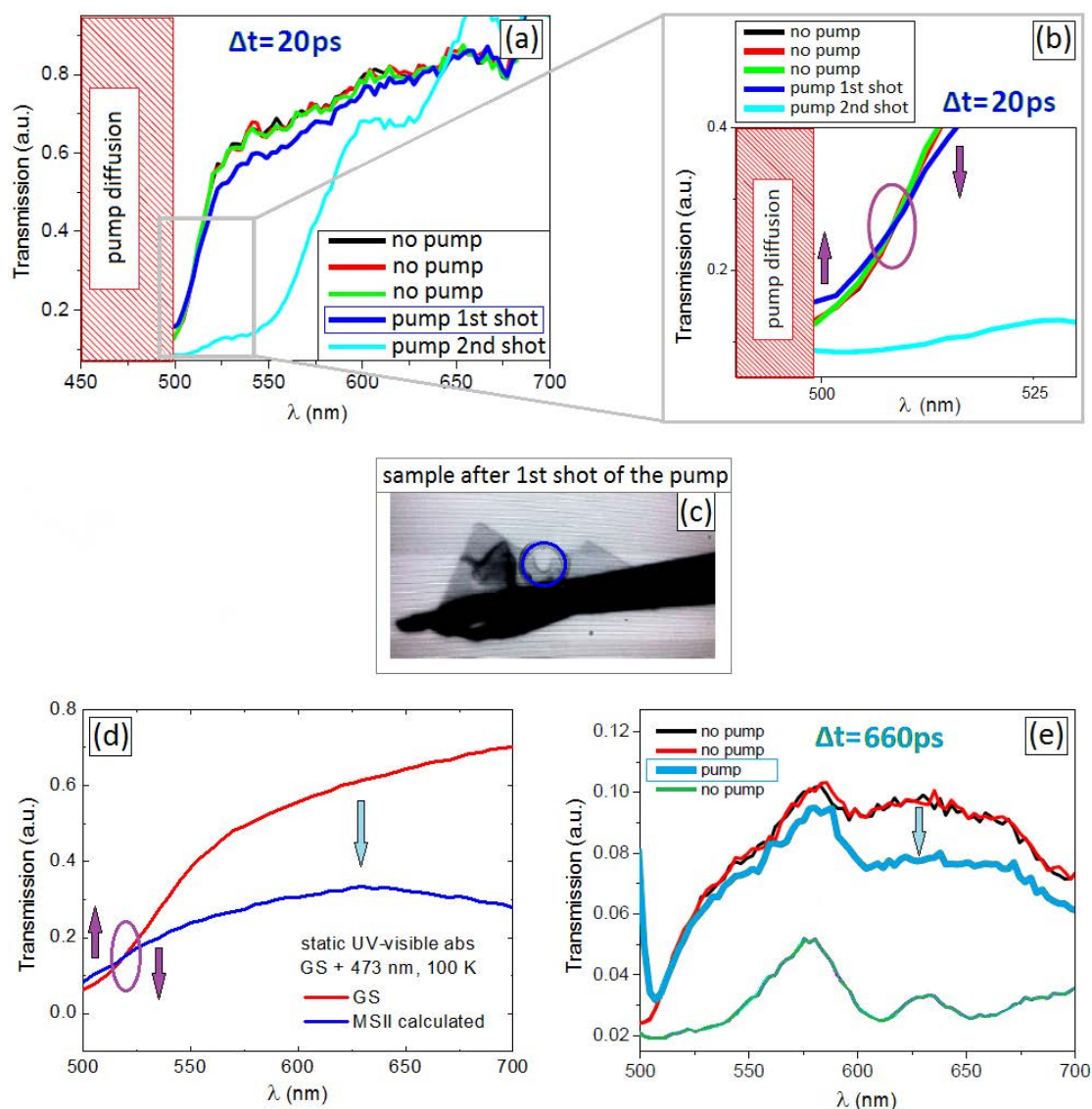


FIGURE 3.9: (a) Single shot experimental results at short time delay $\Delta t = 20$ ps, pump is $46 \mu\text{J}$, 480 nm, probe is 450 nm – 750 nm. (performed by Ciro D’Amico); (b) zoom in of (a); (c) damaged sample; (d) MSII state deduced from the kinetic model used to fit the static state absorption measurements done during this PhD, in here presented as Transmission for convenience (described in Chapter 1); (e) single shot experimental results at a long time delay $\Delta t = 660$ ps, pump is $46 \mu\text{J}$, 480 nm, probe is 450 nm – 750 nm (performed by Ciro D’Amico).

3.3 Discussion

Three different ultrafast experimental setups were used to access the intermediate MSII state, which lifetime is expected to be $\tau = 346 \mu\text{s}$ at $T = 300$ K. We can summarize our results as following:

- In time-resolved pump-probe experiment in Figure 3.5 we observe the formation of ‘plateau’ of weak intensity starting from around $15 - 20$ ps delay up to at least 2 ns and two times of relaxation from the fit (~ 2 ps, ~ 8 ps), i.e. the existence of at least two processes before the formation of the ‘plateau’.

- Time-resolved white light probe experiment provides us with information on the visible spectrum evolution at short time delay (< 10 ps) and again the existence of two different processes is observed.
- For time delay > 2 ns in monochromatic experiment and for delay > 40 ps for white light setup, the signal becomes of the order of the background, so that lifetime of the state corresponding to the ‘plateau’ (expected to be the MSII state) could not be determined.
- Single shot measurements show optical signature of the transient state which is in a good agreement with the MSII spectrum deduced from kinetic model $GS \rightarrow MSII \rightarrow MSI$ under blue light irradiation, i.e. MSII configuration different from the side-on.

To estimate the efficiency of photochemical reaction of time-resolved experiments comparing to CW laser irradiation we present the calculations of number of absorbed photons and percentage of excited molecules in Table 3.2. It is not possible to compare directly experiments under CW light with pump-probe measurements as under CW light we are not able to access the first step of photochemical reaction, $GS \rightarrow MSII$, as the second photon is reabsorbed immediately by a molecule after the transition to MSII state. Nevertheless, we can still discuss the overall efficiency of the photoreaction and in case of CW light irradiation the number of photons sent and absorbed per hour per molecule is around 670, which is enormous, if we take into account the fact that we need only two photons to transform GS to MSI according to the two-step photon absorption process (3.2 (d)). The fact that we need to send so many photons means that in the photoswitching $GS \rightarrow MSII \rightarrow MSI$ at least one of steps is not efficient. First of all, it is important to note that photons in blue range are equally absorbed by GS and MSII state (similar OD values), so there is no difference in efficiency in this respect. Now, if we suppose that the $MSII \rightarrow MSI$ transition is less efficient than the $GS \rightarrow MSII$, then in such case we would rather see the population of MSII species under the blue CW light which is not the case, see Figure 3.2 (a). So we can suggest that it is the transition $GS \rightarrow MSII$, that has a lower efficiency. Therefore, a large amount of photons is needed to promote GS to MSII, which further easily reabsorbs a second photon and transforms into MSI.

Contrary to the CW light irradiation with the pump-probe and white light experiments (femto-second pulses) we actually able to observe directly the first step of reaction, $GS \rightarrow MSII$. In these experiments, however, we excite only 2.53% of molecules (Table 3.2), which explains the weak signal of the ‘plateau’ observed in Figure 3.5. In single shot experiment with the higher pump power it is possible to excite 29.5% of molecules, which gives ten times higher signal. Obtained from single shot experiments results give us some evidence of transient state under the blue light irradiation with geometry different from the side-on MSII configuration observed under the IR irradiation. We remind, that with ultrafast white light probe experiment it was not possible to observe clearly an optical spectrum of MSII species under the blue irradiation, as the signal was very weak and comparable to the noise. Overall, in case of ultrafast experiments we cannot make any solid conclusions on the efficiency of photochemical reaction as the fragility of samples prevents us sending more photons. Nevertheless, even with such a low population of transient

Complete reaction, GS \rightarrow MSI	CW laser irradiation	
λ , nm	473	
Intensity, mW \cdot cm $^{-2}$	1100	
Energy/hour, mJ \cdot h $^{-1}$ \cdot cm $^{-2}$	3.96×10^6	
Nb of photons \cdot h $^{-1}$ \cdot cm $^{-2}$	9.43×10^{21}	
Nb of molecules per cm for 100 μ m depth	1.41×10^{19}	
Nb of photons per molecule	670	
First step of reaction, GS \rightarrow MSII	Time-resolved experiment	Single shot experiment
λ , nm	487	480
Energy, μ J	4	46
Fluence, mJ \cdot cm $^{-2}$	149.94	1724.35
Nb of photons absorbed per pulse per cm 2	3.57×10^{17}	4.17×10^{18}
Nb of molecules per cm for 100 μ m depth	1.41×10^{19}	
% of excited molecules	2.53	29.5

TABLE 3.2: Number of molecules excited during CW laser irradiation, time-resolved measurements and single shot experiment.

species (2.53% for pump-probe experiment) we are sensitive enough to detect a weak signal of transient state.

Another interesting point to discuss in respect with transient species is the evolution of OD in MSII^{IR} \rightarrow MSI under the 473 nm CW light irradiation presented in Figure 3.10. We proposed earlier that transient state in two-step photon absorption process GS \rightarrow MSI under blue light irradiation is not the same as the MSII^{IR} obtained from MSI after 1064 nm irradiation (compare black thick curves in Figure 3.2 (b) and (c)). We would like to provide another argument which supports this statement by analysing OD evolution MSI $\xrightarrow{1064 \text{ nm}}$ MSII^{IR} $\xrightarrow{473 \text{ nm}}$ MSI in Figure 3.10 (b). When MSI state is irradiated with 1064 nm we observe the transformation to MSII^{IR} within 30-40 minutes. When then the MSII^{IR} (black thick curve) is irradiated with 473 nm, the OD in [700 nm – 800 nm] region, instead of increasing directly to MSI optical signature, goes first down and only then goes back to MSI (see blue arrow in Figure 3.10 (b)). The pink curve, obtained after one minute of irradiation with blue light of MSII^{IR}, is obviously not a combination of MSII^{IR} and MSI states, neither GS state is considered in here as we know that blue light do not promote the relaxation back to GS. Therefore, we can state that there is an intermediate step in MSII^{IR} \rightarrow MSI transformation. We can also notice that this pink curve is quite similar to the intermediate state we found from the kinetic model (see black curve in Figure 3.9 (d)). Future X-Ray diffraction experiment is planned to structurally characterize this MSII^{IR} \rightarrow MSI transformation under 473 nm irradiation.

Let us compare now our experimental results with DFT calculations performed on the system of *trans* – [RuCl(NO)(py)₄]²⁺ in work of Garcia et al. [69]. In Figure 3.11 taken from work [69] the scheme of photoreaction explains possible pathways during the two-step photon absorption under the blue light irradiation with calculated singlet and triplet states. With absorption of first

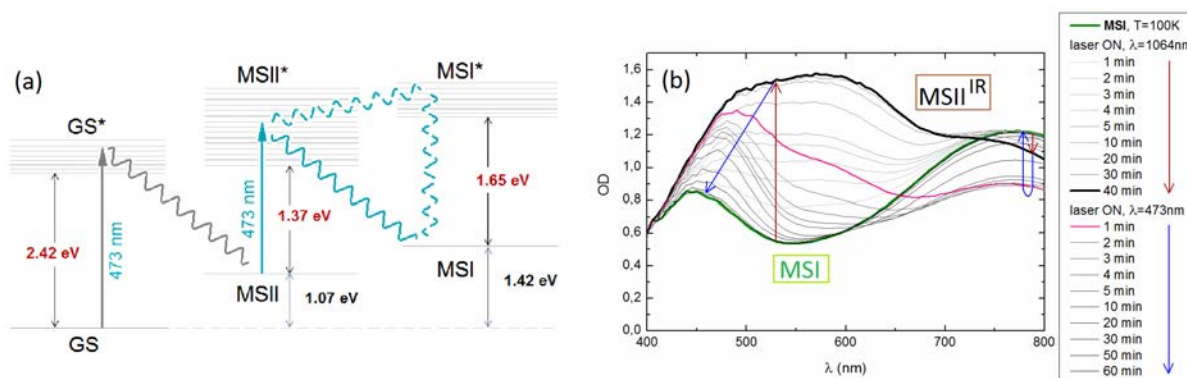


FIGURE 3.10: (a) Proposed schema of two-step photon absorption under the blue light: relative positions of MSI and MSII states of $[Ru(py)_4Cl(NO)]$ molecule, their excited states and excited level of the GS state (from Ref. [15]). Vertical arrows represent irradiation of 473 nm . The dark red numbers stand for the calculated values of energy, while the black ones for the measured values; (b) Evolution of the OD during the light irradiation of the $[Ru(py)_4Cl(NO)](PF_6)_2 \cdot 1/2H_2O$ single crystal at 100 K with 1064 nm , $600\text{ mW} \cdot \text{cm}^{-2}$ up to $MSII^{IR}$ (dark red thick arrows) and then with 473 nm , $1100\text{ mW} \cdot \text{cm}^{-2}$. $MSII^{IR}$ (blue thick arrows) indicates the highest population of MSII species reached during the experiment.

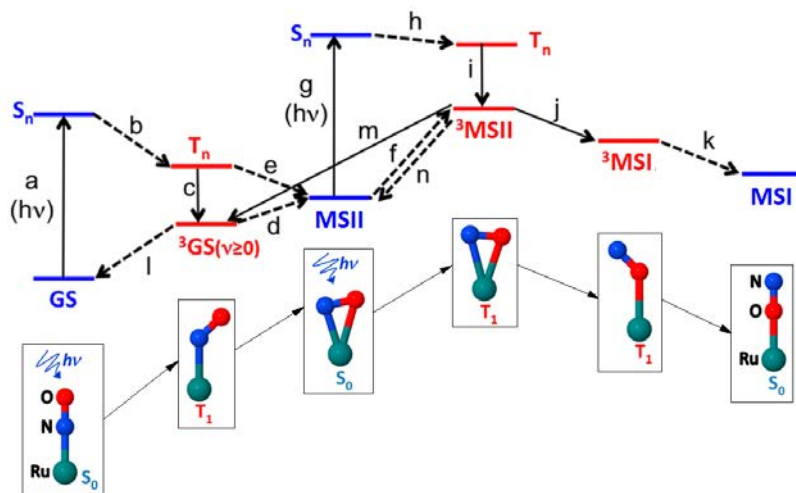


FIGURE 3.11: The main events involved in the $GS \rightarrow MSI$ photoisomerization, the steps are labelled sequentially (a-k), the singlet states are presented in blue and triplet states are shown in red. Figure is taken and modified from work of Garcia et al. [69].

photon the system goes from GS to S_n , step **a** in Figure 3.11 (referred as GS^* in this Thesis), then it relaxes to T_n (step **b**) from which it either goes to MSII through **e** or relaxes to 3GS triplet (step **c**). Once the system in MSII state, it immediately reabsorbs the second photon and relaxes to MSI state.

Existence of intermediate triplet state(s) between GS and MSII was also observed experimentally in several *Ru* complexes [69, 73, 74, 75, 76]. Those intermediate triplet state(s), absent in the prototype SNP system, explain that much longer time delay (of the order of $15 - 20\text{ ps}$) is needed to reach the ‘plateau’ in comparison to the time delay of less than 1 ps in case of SNP [47]. DFT calculations with an energy level of 3GS lower than the one of MSII, also offer an explanation for the weak signal of the ‘plateau’: once the 3GS state is reached, the relaxation back to GS state is favoured.

The energy diagram presented in Figure 3.11 is also consistent with our observations of two time constants for the signal decay towards the ‘plateau’, even though the precise assignment of these time constants to specific transient states is difficult. Within 80 *fs* time resolution of our experiments we probably do not catch the first $S_n \rightarrow T_n$ decay, as it takes only several tens of fs [73]. We assign two time constants found from fitting to $T_n \rightarrow$ MSII conversion and following vibrational cooling. We propose that system takes 2 *ps* for transition from T_n to MSII (step **e**), and 7 *ps* for following vibrational cooling of hot MSII state, however, we cannot confirm it with present DFT calculations or our experimental results. Simultaneously there are transitions of T_n to 3GS (step **c**) and then back to GS (step **1**), however we believe them to be really fast and not possible to detect with our experimental setup.

From our experimental results and recent DFT calculations [69] we can make following conclusions:

- The performed experiments proved to be very challenging. The signal of transient state is quite weak, which can be explained by the low efficiency of the first step of photoreaction, $GS \rightarrow MSII$. The calculations of sent and absorbed photons as well as DFT calculations confirm the inefficiency of MSII species formation. Once system absorbed a photon and went to the excited triplet T_n , it relaxes fast to either MSII or 3GS . Relaxation to 3GS is more favourable as it is an internal conversion, from which it decays back to the GS. Therefore, we need to send a lot of photons to increase the probability of conversion towards MSII.
- We evidenced the necessity of double exponential fit, i.e. the observation of at least two processes with different decay times. It could be assigned to either decay of two transient states or relaxation of a transient state and a vibrational cooling process. We consider the latter one to be most probable with the decay from T_n towards MSII and then its vibrational cooling, though neither recent DFT calculations nor experimental results give a clear-cut evidence of such statement.

Chapter 4

NO release in

trans – (Cl, Cl)[Ru^{II}(FT)Cl₂(NO)]PF₆

isomer: studies in acetonitrile solution

During the past three decades the vital role of nitric oxide, *NO*, has been shown in many biological processes [51, 52], such as immune and blood pressure regulation [53], neurotransmission [54], anti-tumor activity [55]. Since then research efforts were focused on the compounds that liberate *NO* under light irradiation. Indeed, light irradiation allows the delivery of *NO* to specific targets, thus avoiding global toxicity. Among them, ruthenium nitrosyl compounds are of particular interest because of their inherent stability in aqueous media in comparison with most of alternative metallic complexes (*Fe*, *Mn*, *Cr*) [57]. In addition, clinical trials of cancer therapy with Ruthenium nitrosyl complexes showed that small quantities of *Ru* compounds are well tolerated by the patient [55]. However, the typical *NO* release in ruthenium nitrosyl complexes is occurring under the UV light exposure, which is not suitable for photodynamic therapy. To overcome this issue different ligand modifications were probed and variety of ruthenium nitrosyls efficiently releasing *NO* at wavelengths up to 600 nm were obtained [77, 78]. The ‘smart design’ of ligands leads researchers to successful synthesis of ruthenium-*NO* donors sensitive to visible light. As another way to shift the wavelength range from UV light to lower energies was demonstrated in work [79], where instead of one-photon excitation with UV light, a two-photon excitation in the NIR region was successfully used for *NO* release in *terpyridine* – *Ru(NO)* compound.

The [Ru^{II}(*py*)₄Cl(*NO*)]²⁺ cations presented in previous chapters show a high photosensitivity in solid state and therefore the *NO* release process could be interesting to investigate in this system. Unfortunately, in work [80] it was shown that quantum yield for product formation obtained spectroscopically was quite small for any practical application, reaching the value of $1.6 \cdot 10^{-3}$. Fortunately, *terpyridine* – *Ru(NO)* compounds demonstrate quantum yield of two

orders of magnitude higher [81, 82], and therefore, could be promising candidates for anti-cancer drugs within the photodynamic therapy [83, 84].

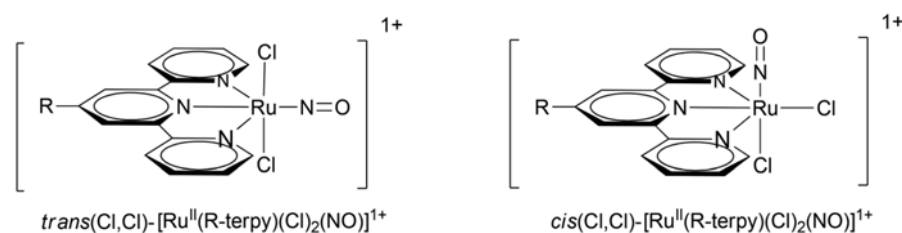
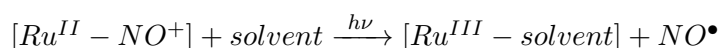


FIGURE 4.1: The cations of *trans* and *cis* – $(\text{Cl}, \text{Cl})[\text{Ru}^{\text{II}}(\text{FT})\text{Cl}_2(\text{NO})]\text{PF}_6$ systems [82].

In this chapter we will focus on one of *terpyridine* – *Ru* – (*NO*) complexes, the *trans* – $(\text{Cl}, \text{Cl})[\text{Ru}^{\text{II}}(\text{FT})\text{Cl}_2(\text{NO})]\text{PF}_6$ isomer (Figure 4.1) [82], which shows a quite high quantum yield of 0.106 for *NO* release and the *cis*-isomer of this complex shows even higher yield of 0.307.

According to the review of ruthenium *NO* donors by Michael Rose and Pradip Mascharak [57] the *NO* release under continuous light irradiation is accompanied by change of oxidation state of *Ru* from *II* to *III* and the formation of *Ru(III)* – *solvent* photoproduct:



Both metal nitrosyl isomerization and *NO* release are based on the same general concept of photoreactivity. The role of metastable states MSI (isonitrosyl configuration, *Ru* – *ON*) and MSII (side-on configuration, *Ru* < $\overset{\text{N}}{\text{O}}$) in the *NO* release process has been investigated by different groups and several ideas are proposed:

(i) the photoproduct *Ru* – *solvent* is formed from either first excited state (3), metastable MSII or MSI states or *NO* liberated state (4) presented in Figure 4.2, i.e. the photoproduct formation can occur at any step of photoisomerization [85, 86];

(ii) the competing photoinduced processes lead either to NO^\bullet liberation or linkage isomers formation, e.g. coexistence of photoproduct and photoisomers is observed in prototype SNP compound in methanol (see Figure 4.3) [87].

Nevertheless, in *trans* – $(\text{Cl}, \text{Cl})[\text{Ru}^{\text{II}}(\text{FT})\text{Cl}_2(\text{NO})]\text{PF}_6$ complex the photoisomerization was shown to be weakly efficient in solid state [63], while the *NO* release and its high quantum yield (0.1) in acetonitrile solution was detected by several different experimental techniques [82]. These experimental results gives us a solid argument to consider the *NO* release process in *trans* – $(\text{Cl}, \text{Cl})[\text{Ru}^{\text{II}}(\text{FT})\text{Cl}_2(\text{NO})]\text{PF}_6$ in acetonitrile solution to be the leading process under the light irradiation comparing to the photoisomerization. However, the photoisomers might be still detectable as a possible transient species before the *NO* release.

DFT calculations on *trans* – $(\text{Cl}, \text{Cl})[\text{Ru}^{\text{II}}(\text{FT})\text{Cl}_2(\text{NO})]\text{PF}_6$ suggest two effects at the origin of the *NO* release: elongation of the *Ru* – *NO* bond of about 0.1 Å, and then bending of a linear

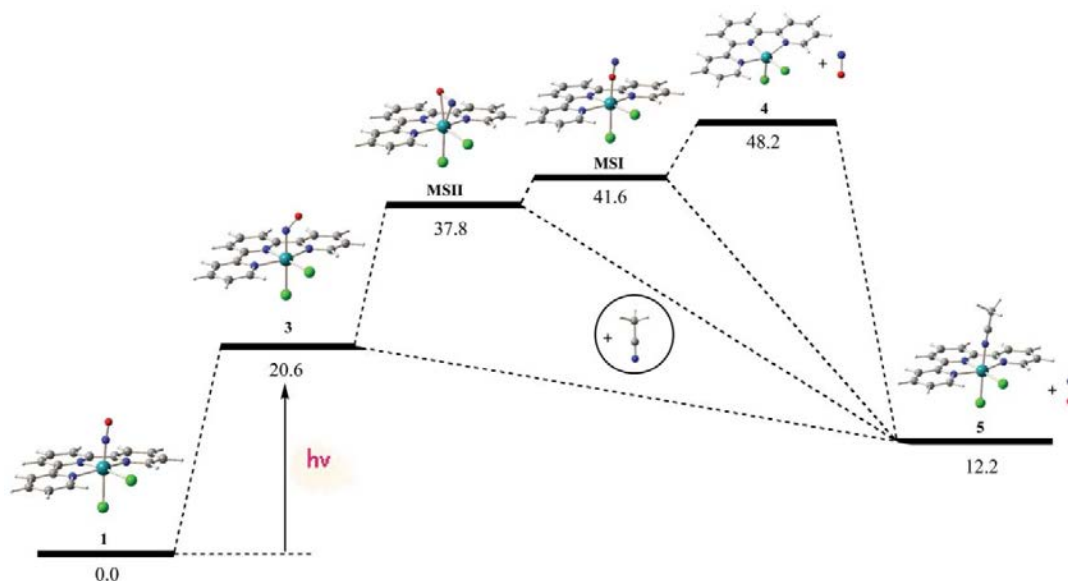


FIGURE 4.2: The proposed mechanism of photoinduced NO release of $cis - (Cl, Cl)[RuCl_2(NO)(terpy)]^+$ in acetonitrile, taken from [85].

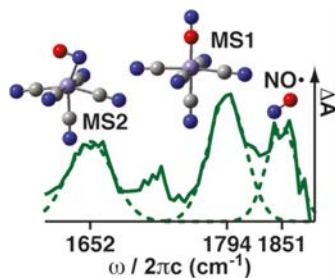


FIGURE 4.3: Coexistence of photoproduct and metastable states in SNP solution in methanol observed by time-resolved IR measurements [87].

$Ru - NO$ to an angular value around 145° [82]. This bending is related to a significant metal to ligand charge transfer which precedes the NO release. In this PhD thesis the photoinduced processes in $trans - (Cl, Cl)[Ru^{II}(FT)Cl_2(NO)]PF_6$ system in acetonitrile solution are studied by the UV-visible absorption spectroscopy and IR measurements (both steady state and time-resolved techniques are used).

4.1 Photosteady measurements: electronic and vibrational spectra

4.1.1 UV-visible measurements

In work of Akl et al. [82] the complete photoinduced NO release is observed by UV-visible absorption spectroscopy in $trans - (Cl, Cl)[Ru^{II}(FT)Cl_2(NO)]PF_6$ isomer in acetonitrile solution ($MeCN$) after around 40 minutes of 405 nm continuous light (CW) irradiation (Figure 4.4). The strong band around 410 nm is assigned to MLCT transition, from $Ru(II)$ metal to NO ligand. When solution is exposed to UV light, the rise of broad band with maximum around

620 nm is observed, which is usually associated with ligand to *Ru(III)* charge transfer (LMCT) after the *NO* release [78, 82, 88, 89]. The presence of isosbestic points at 284, 376 and 468 nm shows a clean conversion of trans-isomer into photoproduct, no back-reaction (recombination of NO^\bullet with the ruthenium complex) is detected when the laser is turned off, which confirms that it is an irreversible *NO* release process. It is important to remember that solvent plays a crucial role in the photoreactivity, in particular it seems that acetonitrile solvent strongly decreases or removes any back-reaction [90].

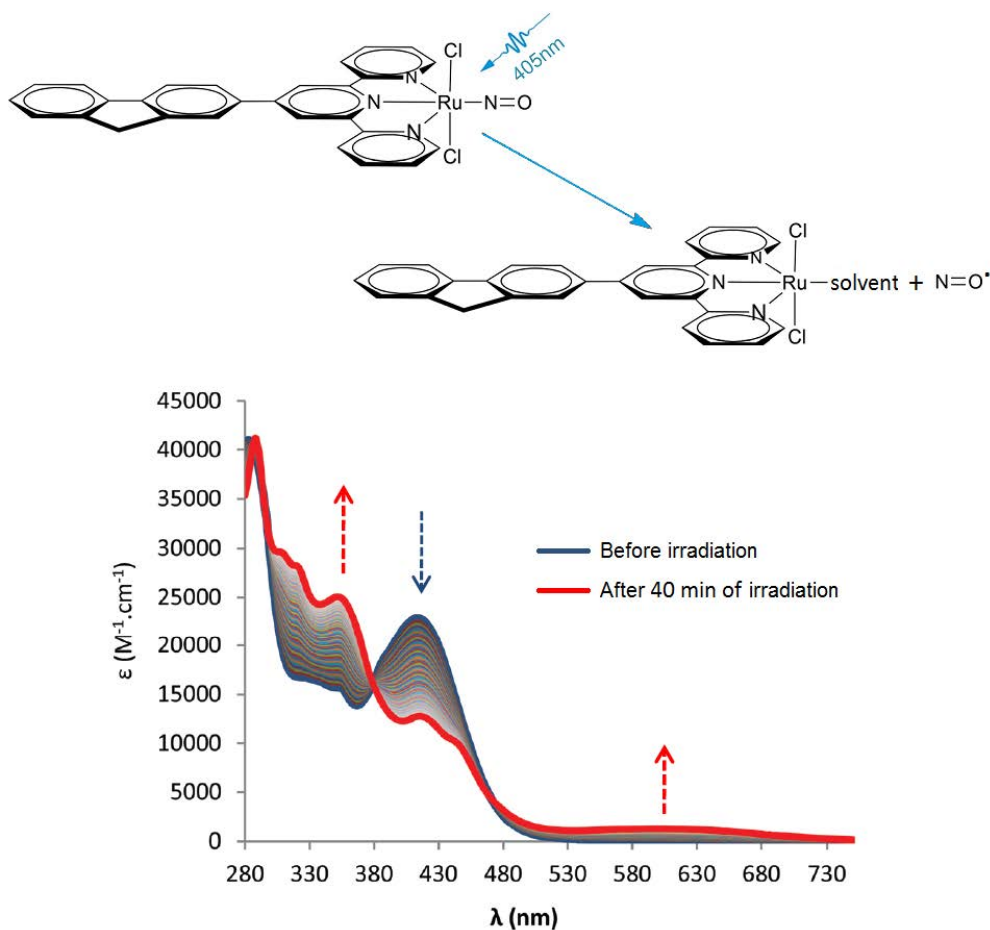


FIGURE 4.4: The schematised *NO* release process and UV-visible absorption spectra evolution of *trans* - $(Cl, Cl)[Ru^{II}(FT)Cl_2(NO)]PF_6$ compound in acetonitrile during the 405 nm light irradiation (the spectra is taken from [82]).

Additional experiments were also performed to confirm the photoreaction: the Griess test, which indeed showed the *NO* release under 405 nm irradiation, and electrochemical measurements (cyclic voltammograms) also demonstrated the complete *NO* release after irradiation as well as the formation of *Ru^{III}* species. Recent crystallographic studies have also shown the *Ru^{III}* oxidation state after the *NO* photodissociation in solution, crystals used in studies were obtained through the evaporation of acetonitrile solvent [79].

Sample preparation and characterization. We reproduced the UV-visible steady measurements reported in [82] to follow the spectra evolution under continuous laser irradiation of 404 nm at room temperature (Figure 4.5 (a,b)). First, the acetonitrile (HPLC grade, Sigma-Aldrich) was degassed (Figure 4.5 (c)) and then the solution was prepared in dark room by mixing 3.5 mg of

powder of *trans* - (Cl, Cl)[Ru^{II}(FT)Cl₂(NO)]PF₆ isomer (synthesized by I. Malfant group in LCC, Toulouse) with 5 ml of degassed acetonitrile (Figure 4.5 (d)). Prepared solution was placed in a UV-visible cell with depth of $l = 0.1 \text{ cm}$ (Figure 4.5 (a)). The concentration and optical density of prepared sample were calculated as follows:

$$C = \frac{m}{V \cdot M} = 9.4 \cdot 10^{-4} \text{ mol/l},$$

$$OD_{405} = \epsilon_{405} \cdot c \cdot l = 2.06 \text{ in } 1 \text{ mm cell},$$

where $M = 744.45 \text{ g/mol}$, $\epsilon_{405} = 21952 \text{ l/(mol} \cdot \text{cm)}$ [82]



FIGURE 4.5: (a) The sample holder and the empty cell with laser spot on it, (b) experimental setup: sample holder, the lense of 50 mm to focus the beam and 404 nm continuous laser, (c) degassing of the acetonitrile, (d) mixing the powder and the solvent.

The evolution of UV-visible absorption spectra was measured by Cary 5000 spectrometer (Agilent) [91] following a short time exposure of the sample (0 sec, 15 sec, 30 sec, 45 sec, etc.) with continuous laser of 404 nm and $P = 140 \text{ mW/cm}^2$ (radius of light spot is 0.05 cm) (Figure 4.6). As the sample is highly photosensitive, its exposure even to weak ambient light can trigger photochemical reactions. To ensure that studied photoprocesses are caused by 404 nm irradiation only, all measurements were performed in the dark room.

The *OD* calculations at 405 nm based on sample preparation are in agreement with the experimental *OD* found from obtained spectra. The same evolution of UV-visible spectra is observed in this experiment as reported in paper of Akl et al. [82], even though the concentration of our solution is higher, 9.4×10^{-4} , comparing to 3×10^{-5} used in work [82].

4.1.2 FTIR measurements

While the UV-visible spectra give us information about the charge transfer during the *NO* release, the IR spectroscopy can provide us with details on the *NO* bond bending and stretching during the photoreaction. Therefore, we investigate *NO* release in this compound by FTIR measurements in parallel with UV-visible spectroscopy. Our goal is to find strong signatures of photoproduct in IR region during the *NO* release and to follow those signatures during the photoreaction with further IR time-resolved measurements.

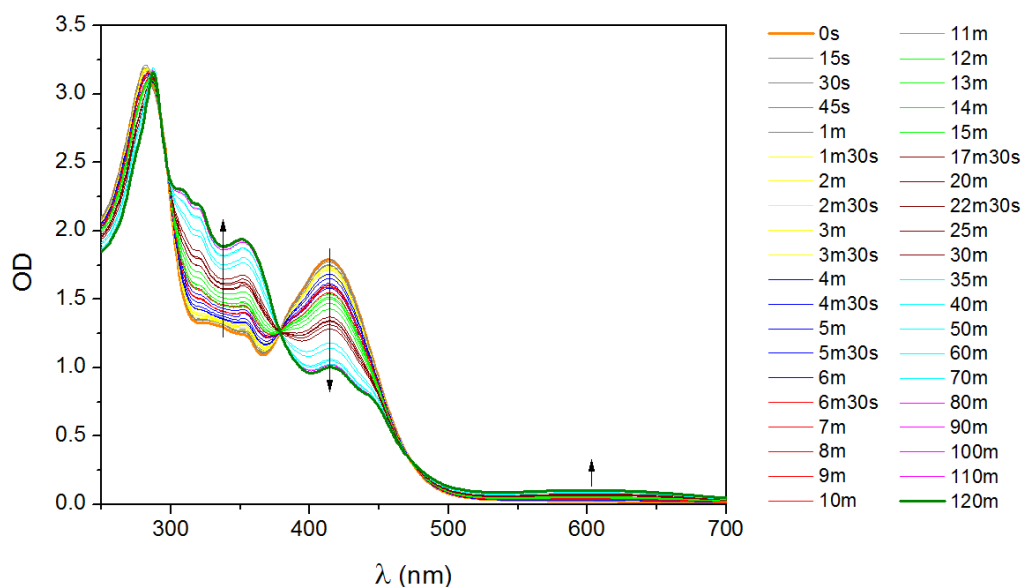


FIGURE 4.6: UV-visible absorption spectra evolution of *trans* – $(Cl, Cl)[Ru^{II}(FT)Cl_2(NO)]PF_6$ compound in acetonitrile during the 404 nm continuous laser irradiation.

$Na_2[Fe^{II}(CN)_5NO] \cdot 2H_2O$ (SNP) compound and $[Ru(py)_4Cl(NO)](PF_6)_2 \cdot 1/2H_2O$ system (studied in Chapters 1, 2, 3) were investigated previously in works [13, 15, 87] with IR measurements to follow the formation of linkage isomers under light irradiation. For example, with FTIR measurements on powder sample in *KBr* pellet at 100 K it was shown that in SNP compound (sodium nitroprusside) the $\nu(NO)$ stretching vibrations of MSII is at 1664 cm^{-1} and for MSI at 1835 cm^{-1} (see Figure 4.7 (a) [13]). SNP was recently studied in aqueous media (methanol) at room temperature using picosecond transient IR spectroscopy and the following stretching frequencies were observed: 1794 cm^{-1} for MSI, 1652 cm^{-1} for MSII and 1851 cm^{-1} for NO^\bullet (see Figure 4.7 (b) [87]). One can see that there is only a small shift in the values of stretching vibrations for MSI and MSII, coming from the change of the molecular environment (compare powder sample in Figure 4.7 (a) and methanol solvent in Figure 4.7 (b)).

The IR measurements were also carried out on $[Ru(py)_4Cl(NO)](PF_6)_2 \cdot 1/2H_2O$ compound with *KBr* pellet at 100 K as presented in Figure 4.8 (taken from [15]): the $\nu(NO)$ vibrational band was found around 1605 cm^{-1} for the MSII species. Even though this MSII band overlaps with water deformation mode, the difference spectra in panel (d) of Figure 4.8 shows clear signature of MSII species. The MSI species are detected by vibrational band in the range $[1758 - 1775\text{ cm}^{-1}]$. The major signature of GS species is found around $[1900 - 1920\text{ cm}^{-1}]$ for the $\nu(NO)$ vibrational band. By exploring the range of $[1750 - 1800\text{ cm}^{-1}]$ in metal-ligand nitrosyl compound, we should be able to detect the presence of MSI species, while MSII ones should appear in the range of $[1600 - 1680\text{ cm}^{-1}]$.

In present work we focus on *trans* – $(Cl, Cl)[Ru^{II}(FT)Cl_2(NO)]PF_6$ isomer in acetonitrile solution and two photoprocesses: the photoisomerization and *NO* photorelease. We test the hypothesis about photoisomerization occurring before the *NO* liberation as well as study the *NO* release process itself. As a first step we verified if our complex has similar features of IR

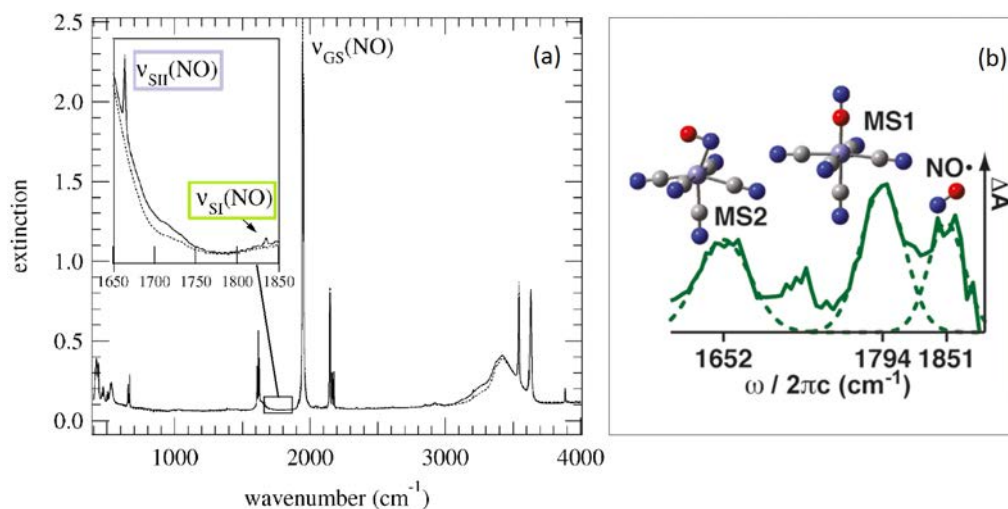


FIGURE 4.7: (a) IR spectra of SNP in GS and after irradiation with 325 nm : $\nu(NO)$, stretching vibrations, are observed for MSII at 1664 cm^{-1} and for MSI at 1835 cm^{-1} (taken from [13]); (b) picosecond transient IR spectra of SNP in methanol in the NO stretching region at 294 ps time delay. Dotted lines are Gaussian fits of MSI (1794 cm^{-1}), MSII (1652 cm^{-1}) and NO^\bullet (1851 cm^{-1}) IR data (taken from [87]).

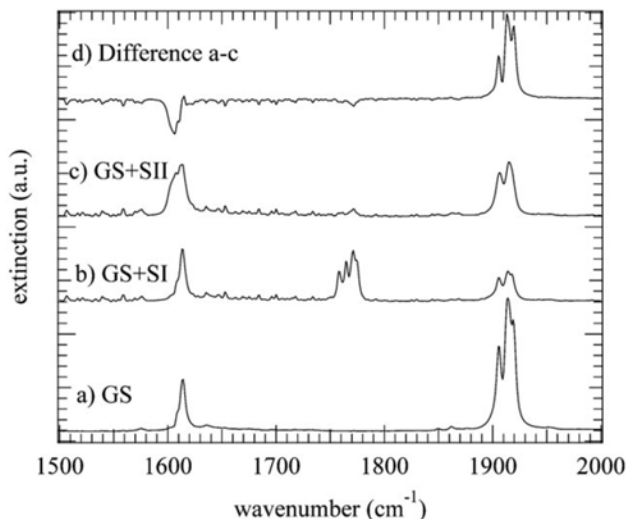


FIGURE 4.8: IR spectra of $[Ru(py)_4Cl(NO)](PF_6)_2 \cdot 1/2H_2O$ in KBr at 100 K : (a) GS state, (b) GS + MSI after irradiation with $\lambda = 476.5\text{ nm}$, (c) GS + MSII states generated with $\lambda = 1064\text{ nm}$ irradiation of GS + MSI states, (d) difference spectrum which shows the $\nu(NO)$ vibrational band arises at 1605 cm^{-1} during the MSII species formation.

spectra change as reported in work [15] for $[Ru(py)_4Cl(NO)](PF_6)_2 \cdot 1/2H_2O$ by performing the FTIR measurements in $[1600 - 2000\text{ cm}^{-1}]$ range. The depopulation of GS state should affect the vibrational mode of NO ligand around 1900 cm^{-1} frequency reported in works [15, 87], the intensity of this mode is expected to decrease after the UV irradiation. It is important to mention that in the presence of oxygen atmosphere the released NO^\bullet radicals are unstable and immediately form NO_2^- species.

Sample preparation and characterization. The sample solution was prepared with 3 mg of powder of $trans - (Cl, Cl)[Ru^{II}(FT)Cl_2(NO)]PF_6$ isomer and 4 ml of acetonitrile (HPLC, Sigma-Aldrich). For the FTIR measurements done on BRUKER spectrometer we used KBr cell of 0.02 cm depth (volume of 0.4 ml) and for the UV-visible studies performed on Cary

5000 spectrometer the depth of cell was 0.1 cm (volume 0.4 ml). The concentration and optical density of prepared sample were calculated as previously: $C = 10^{-3}\text{ mol/l}$ and $OD_{405} = 2.2$ for UV-visible cell and $OD_{405} = 0.44$ for IR cell, where $M = 744.45\text{ g/mol}$, $\epsilon_{405} = 21952\text{ l/(mol}\cdot\text{cm)}$ [82]. During one scan of FTIR measurements 48 spectra were taken with resolution of 2 cm^{-1} and then averaged.

In Figure 4.9 we present (a) FTIR spectra and (b) UV-visible spectra of the same solution before and after 10 minutes of 404 nm irradiation with $P = 1020\text{ mW/cm}^2$ (radius of laser spot is 0.05 cm). The expected evolution of UV-visible spectra is observed which indicates that the *NO* photorelease process is in progress. From UV-visible spectra we also see that *OD* calculations at 405 nm are in agreement with the experimental *OD*. Now, if we look at corresponding FTIR spectra we notice significant decrease of peak at 1900 cm^{-1} associated with *NO* vibrational mode, which confirms the *NO* bond breaking. The peak did not disappear completely indicating that the photoconversion is not finished which is in good agreement with the incomplete evolution of UV-visible spectrum (peak around 350 nm is still slightly lower than the 410 nm band, compare Figure 4.9(b) after 10 minutes of irradiation and Figure 4.6 after 40 minutes of irradiation). Another interesting feature is found at 1630 cm^{-1} , which might be associated with residual water and/or intermediate states of photoisomerization. To avoid such strong signal of water in FTIR spectra special measures should be taken in future, like degasing of the solvent as well as the dehumidification of the FTIR spectrometer's sample environment.

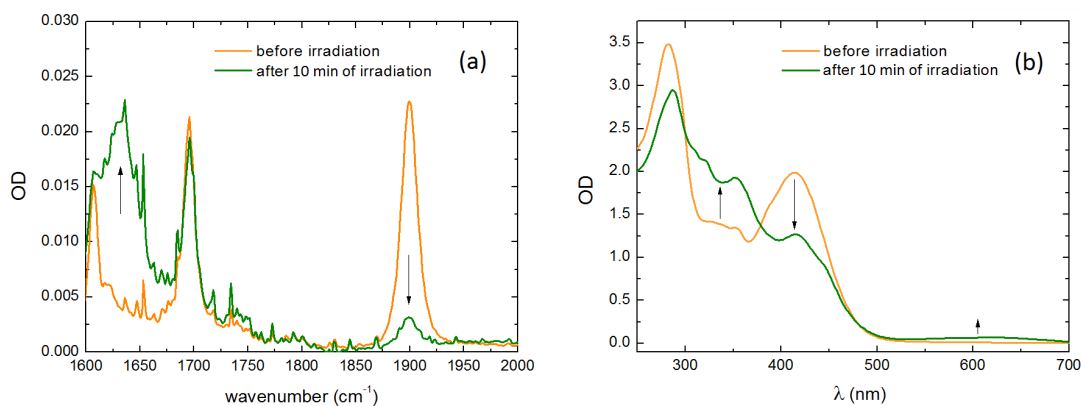


FIGURE 4.9: (a) FTIR and (b) UV-visible absorption spectra evolution of *trans* – $(Cl, Cl)[Ru^{II}(FT)Cl_2(NO)]PF_6$ compound in acetonitrile before and after 10 minutes of continuous laser irradiation with 404 nm and $P = 800\text{ mW/cm}^{-2}$.

4.2 Time-resolved studies of the photoinduced *NO* release

4.2.1 Time-resolved UV-visible measurements with magnetic stirrer and static cell

UV-visible and IR time-resolved experiments along with UV-visible steady state measurements were performed in collaboration with Jacek Kubicki in University Adam Mickiewicz of Poznań, Poland. The evolution of UV-visible absorption spectra of *trans*– $(Cl, Cl)[Ru^{II}(FT)Cl_2(NO)]PF_6$

isomer in acetonitrile solution was measured by means of time-resolved pump-probe experiment with pump of 406 nm and [350 nm – 750 nm] probe. The pump beam was generated by OPA and then chopped to 500 Hz, while the UV-visible probe of 1000 Hz was obtained through Sapphire crystal by generating white light (general mechanisms of pump-probe experiments as well as white light generation are described in Appendix E).

Experimental details. The solution was prepared with *trans*-(Cl, Cl)[Ru^{II}(FT)Cl₂(NO)]PF₆ isomer in acetonitrile (HPLC, Sigma-Aldrich) with concentration $c = 1.8 \cdot 10^{-4}$ mol/l with $OD_{406} = 0.8$ for 0.2 cm cell. The prepared sample solution was placed in a cell with volume of 0.7 ml and 0.2 cm depth. The circulation of solution inside the cell during the measurements was done by a small magnetic stirrer.

Results and discussion. In Figure 4.10 we present (a) transient UV-visible spectra at selected time delays and (b) kinetics for a selected wavelengths after the first run of measurements (one run is a cycle of data collection at chosen time delays up to 180 ps), (c) transient time-resolved UV-visible spectra after long irradiation (tens of runs) and (d) UV-visible steady state absorption spectra evolution taken after time-resolved UV-visible measurements to follow the photoreaction and compare it to already published static UV-visible evolution under light irradiation [82]. The range of [390 nm – 420 nm] is cut, as there is a strong scattering signal from the 406 nm pump.

In panel (a) in Figure 4.10 we observe the evolution of UV-visible spectra upon electronic excitation during the first run of measurements. The simultaneous UV-visible steady state measurements provided us with the information on the concentration of the prepared sample (information given by the OD measured before the irradiation) as well as allow us to follow photochemical reaction evolution (Figure 4.10 (d)). The steady state measurements of UV-visible absorption spectra were done in this case before the time-resolved experiment, after four runs and after long time irradiation (tens of runs).

If we compare time-resolved spectra with the steady state (panels (a) and (d)) then we can see the full agreement between two experiments: the growth of OD at 0.293 ps delay below isosbestic point of 380 nm and above isosbestic point of 460 nm, and OD decrease in the region of [376 – 460 nm]. It is also easy to see these similarities from the kinetics at chosen wavelengths: 367 nm, 380 nm and 429 nm (Figure 4.10 (b)), while the signal increases and forms a plateau at 367 nm, it decreases at 429 nm (negative ΔOD), and in case of 380 nm which is an isosbestic point in steady measurements we see the return of the signal to zero as there is no change in the OD . We can also notice that between the first run and the last one in Figure 4.10 (a), (c) the ΔOD signal decreases in agreement with the loss of primary photo-reactant molecules, except the signal around 640 nm. This latter signal, which is associated with the photoproduct of Ru^{III} – solvent, continues to grow with a longer time of irradiation (Figure 4.10 (c)), and it means that we deal with the main effect of secondary photochemistry.

If we look at one specific kinetics at 640 nm presented in Figure 4.11 (a), we can see that at time delay around 5 – 10 ps the process is finished already and the signal becomes flat, but does not go completely to zero. This indicates the formation of an intermediate state. The fit of

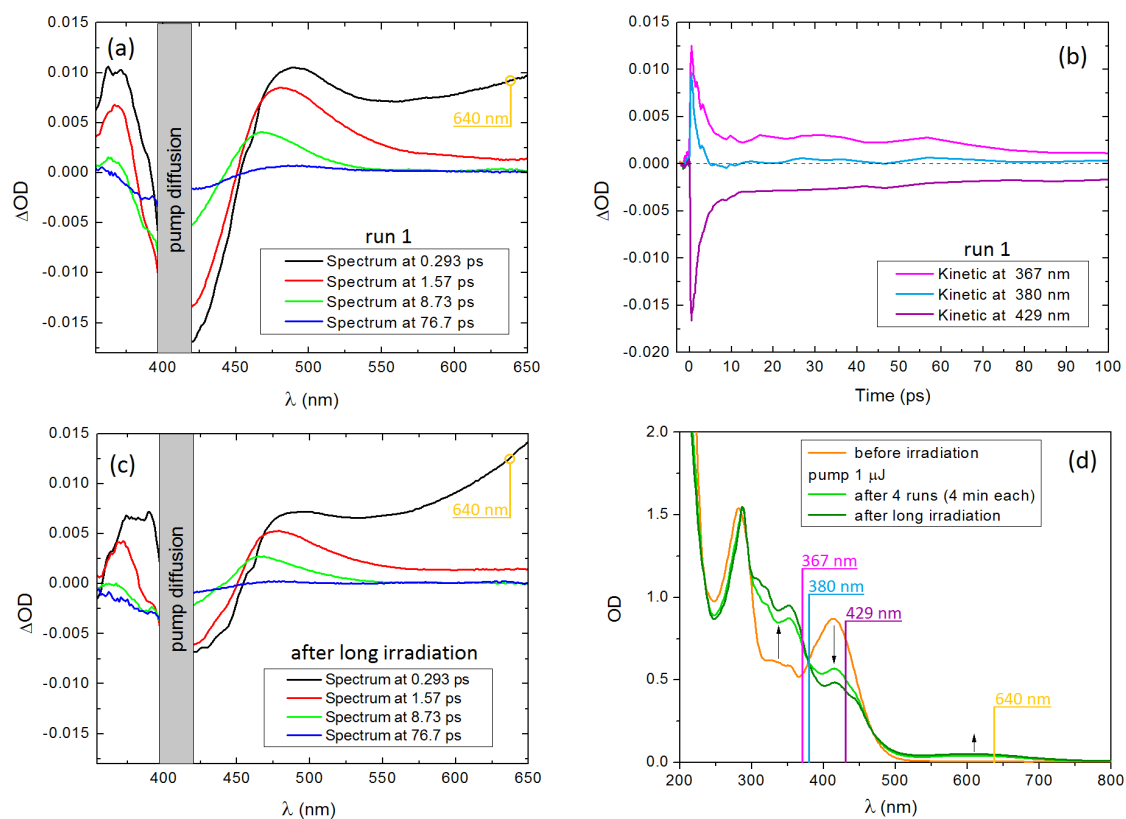


FIGURE 4.10: (a) Spectra and (b) kinetics observed by time-resolved pump-probe experiment of *trans*-(Cl,Cl)[Ru^{II}(FT)Cl₂(NO)]PF₆ compound in acetonitrile during the first run of measurements under the pump of 406 nm, 1 μJ (one run is a cycle of data collection at chosen time delays up to 180 ps); (c) time-resolved UV-visible spectra taken after long time irradiation (tens of runs) with 406 nm, 1 μJ; (d) UV-visible steady state absorption spectra evolution taken simultaneously with time-resolved UV-visible measurements: before irradiation (pristine solution), after 4 runs and after long time irradiation $OD_{406} = 0.8$ for 2 mm solvent layer.

signal (convolution of gaussian and exponential decay) gives us two time constants, 0.7 ps and 12 ps, which means that we have at least two processes involved in the photoreaction before the formation of the ‘plateau’. In this case the simultaneous UV-visible steady state measurements show the incomplete phototransformation of the solution (Figure 4.11 (b)).

These results give us following features: (i) the very fast kinetics of the photoreaction (the ‘plateau’ is formed after 5–10 ps), (ii) two time constants found from the fit of the experimental data and (iii) secondary photochemistry. Our experimental evidence of secondary photochemistry is in a good agreement with the DFT calculations, where two photons are necessary for the *NO* liberation [92]. As to the nature of the intermediate state we observe through the signal at 640 nm, then several interpretations are possible. On one hand, the TD-DFT calculations show that 640 nm signature is associated not only with the Ru^{III} photoproduct but also with the formation of MSI species (see the MSI spectra in Figure 4.12 [92]). Therefore, we might evidence both MSI photoisomer and Ru^{III} photoproduct in experimental signal. On the other hand, the formation of MSI species is more probable at observed time scales (in Figure 4.10 (a) the signal at 640 nm appears already after 0.293 ps) if we take into account the recombination of the molecule with the solvent. According to work [87] the solvent association time scale in prototype SNP compound is around 130 ps, which is significantly longer than the time of photoproduct

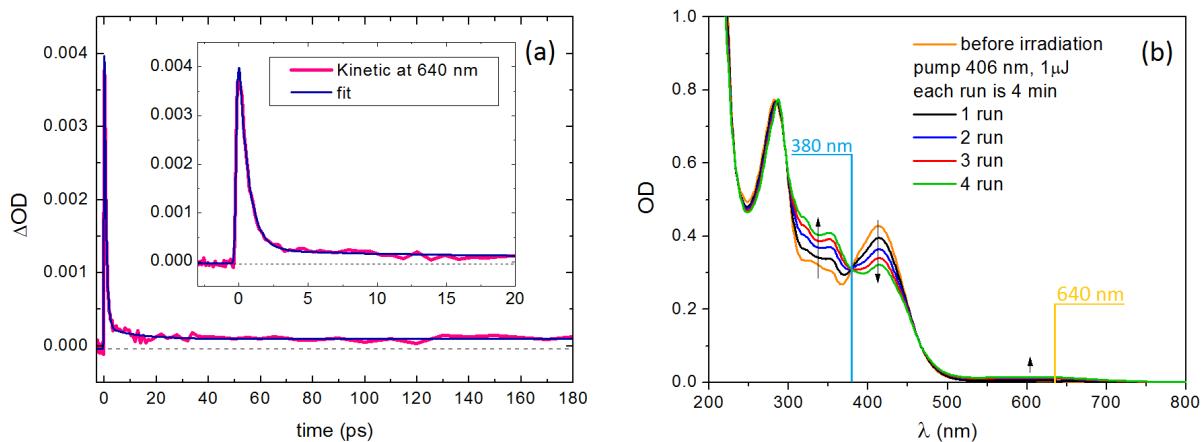


FIGURE 4.11: (a) Kinetics at selected 640 nm probe measured by time-resolved pump-probe experiment of $trans - (Cl, Cl)[Ru^{II}(FT)Cl_2(NO)]PF_6$ compound in acetonitrile under the pump of 406 nm , $1\ \mu\text{J}$; (b) UV-visible steady state absorption spectra evolution taken simultaneously with time-resolved UV-visible measurements: before irradiation and after each cycle of measurements under 406 nm pump, $OD_{406} = 0.47$ for 2 mm solvent layer.

formation observed in our experiment. It could be interesting to follow 640 nm signal at longer time delays. Within present experimental results and due to the similar optical signatures of MSI state and Ru^{III} photoproduct in UV-visible region it is difficult to give a clear interpretation of the observed signal.

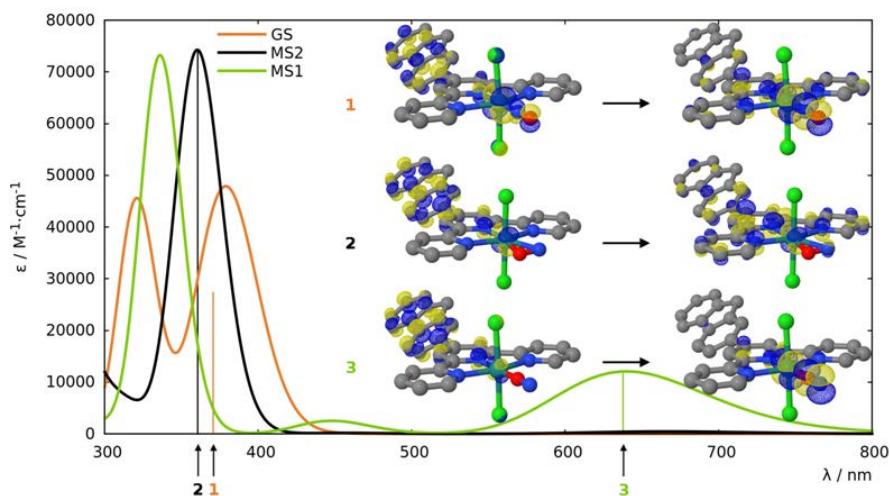


FIGURE 4.12: TD-DFT spectra of the three linkage isomers (GS in orange, MSII in black and MSI in green) of $trans - (Cl, Cl)[RuCl_2(NO)(Fl - terpy)]^+$ computed in acetonitrile [92].

4.2.2 Time-resolved mid-IR studies with circulation system and flow cell

With time-resolved IR spectroscopy we investigate the region of $[1560 - 1950 \text{ cm}^{-1}]$. While around 1900 cm^{-1} (5300 nm) we expect to observe the strong signal from *NO* stretching vibration decreasing with the *NO* release, in the window of $[1600 \text{ cm}^{-1} - 1780 \text{ cm}^{-1}]$ we hope to see the signatures of transient states (MSI or MSII as in [15]) if the photoisomerization process occurs, for example, before the *NO* photorelease (see two scenarios of *NO* release process mentioned in introduction part of current Chapter).

Experimental details. Solution of 1.9 mg of *trans* - $(Cl, Cl)[Ru^{II}(FT)Cl_2(NO)]PF_6$ compound and 12 ml acetonitrile (HPLC, Sigma-Aldrich) was prepared and the concentration was calculated to be $c = 2 \cdot 10^{-4} \text{ mol/l}$. Measurements were performed with a circulation system to avoid exposure of already excited molecules. The $500 \mu\text{m}$ cell with BaF_2 front window and CaF_2 for back window was used. The flow velocity was set such as to not create any air bubbles during the circulation. During the experimental run the absorption variation, $\Delta A = A_{\text{pump}} - A_{\text{no pump}}$, is measured. Any new species in this case appear as a positive signal while the depopulation of initial state as a negative one.

Results and discussion. In Figure 4.13 (a) the evolution of time-resolved IR spectra around 1900 cm^{-1} shows the appearance of positive band (population of hot ground state) and negative band (depopulation of ground state) at 0.8 ps after a laser pulse. The peak at 1900 cm^{-1} assigned for the *NO* vibrational mode is compared here with a steady state IR absorption (see FTIR spectrum on Figure 4.9 (a)). The shape of the transient spectrum recorded at 50 ps and longer time delays are very similar to the steady state spectrum (almost no change of the shape and amplitude).

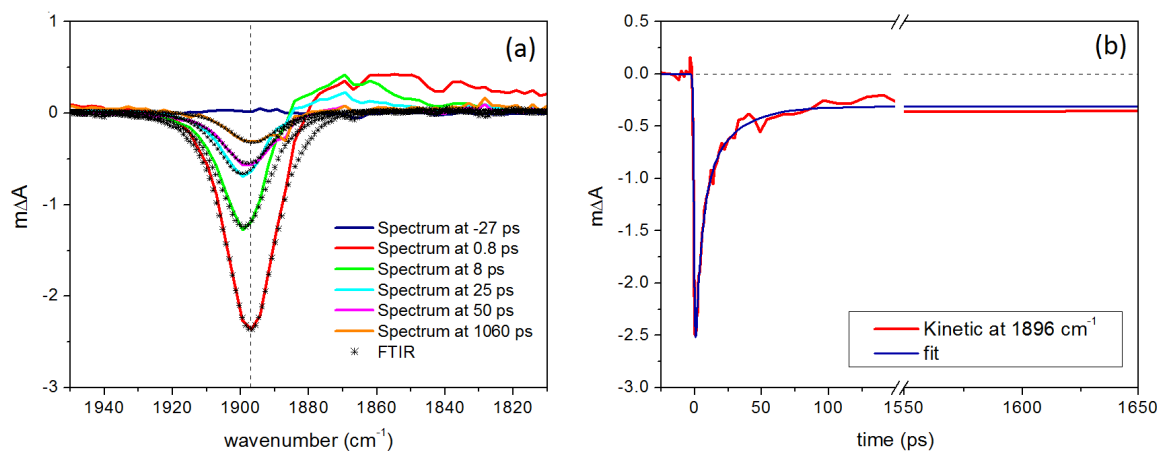


FIGURE 4.13: (a) Time-resolved IR absorption spectra evolution (around 5300 nm , 1900 cm^{-1}) and (b) kinetics of *trans* - $(Cl, Cl)[Ru^{II}(FT)Cl_2(NO)]PF_6$ compound in acetonitrile during the irradiation of 406 nm , $2 \mu\text{J}$. IR experiment was performed with cell of $500 \mu\text{m}$ ($OD_{406} = 0.24$ measured by UV-visible steady state) and circulation system.

If we look at the kinetics at 1900 cm^{-1} (Figure 4.13 (b)) from fitting curve with two exponentials we get two time constants, 4.9 ps and 23 ps , and we think that both kinetics maybe related to the process of vibrational cooling (VC) of hot ground state. One can see that the transient signal

does not go to zero up to 1.7 ns in accordance with the irreversible nature of this photochemical reaction: some excited molecules were decomposed and we observe now the decrease of absorption (liberation of NO^\bullet species). The decrease of NO stretching mode signal is in agreement with FTIR measurements (compare with the decrease of peak at 1900 cm^{-1} in Figure 4.9 (a)). As we mentioned earlier, in the presence of oxygen atmosphere the released NO^\bullet radicals immediately recombine to form the NO_2^- species, however, the NO_2^- vibrational mode was not in our experimental window.

In Figure 4.14 (a) the spectra evolution around 1600 cm^{-1} shows similar results as IR spectra around 1900 cm^{-1} : the formation of negative and positive bands right after laser pulse at 1 ps delay. We interpret the positive signal as a vibrational cooling, while the negative one as a depopulation of fundamental vibrational level (GS), and, therefore, we do not evidence the formation of new species at least within the time resolution of experimental setup. Note that peak at 1615 cm^{-1} might be due to the water presence in the acetonitrile solution, what is more, the fit with FTIR GS below 1600 cm^{-1} seems problematic, perhaps, due to the water presence in FTIR signal.

From the kinetics at 1600 cm^{-1} (see Figure 4.14 (b)) we observe that after 140 ps signal decays almost to zero. The signal is fitted with one exponential decay with time constant of 26 ps, which probably corresponds to the vibrational cooling. Nevertheless, from Figure 4.14 (b) we clearly see a fast component of the order of several ps as well, but it seems that the number of experimental points in this scan was not enough to make a good fit. The decrease of the signal to zero means that the excited vibrational mode around 1600 cm^{-1} is not affected by the irreversible photochemical process. It might concern the FT ligand.

As a result, for both $[1560 - 1670\text{ cm}^{-1}]$ and $[1810 - 1950\text{ cm}^{-1}]$ regions it is only observed the vibrational cooling and no clear signature of new species formation. We also examined the region of $[1670 - 1810\text{ cm}^{-1}]$, which is associated with the IR signature of MSI species, however, we did not observe any signal. It might be due to the sensitivity of the experimental setup, low population of MSI species or simply their absence.

Simultaneously with time-resolved IR experiment we followed the steady state UV-visible spectral changes of the sample. In Figure 4.15 (a) UV-visible spectra reveals quite unexpected evolution. After first six runs of circulation with 1 μJ pump we can observe the decrease of the signal over all visible range (dark cyan curve). It can be explained by the decrease in concentration of photoreactant molecules (pristine solution, orange curve), however, it seems that the final photoproduct has not formed yet. After the following six runs with increased pump power to 2 μJ we observe further decrease of a signal in UV region while there are both an increase of band around 320 nm and around 600 nm, the latter is normally associated with $Ru^{III} - \text{solvent}$ photoproduct (purple curve).

In Figure 4.15 (b) we rescale the experimental data to bring peak at 290 nm to the same value for comparison. From normalized curves we see that there is almost no difference between fresh sample (orange curve) and the sample after first six runs (dark cyan curve), which indicates a

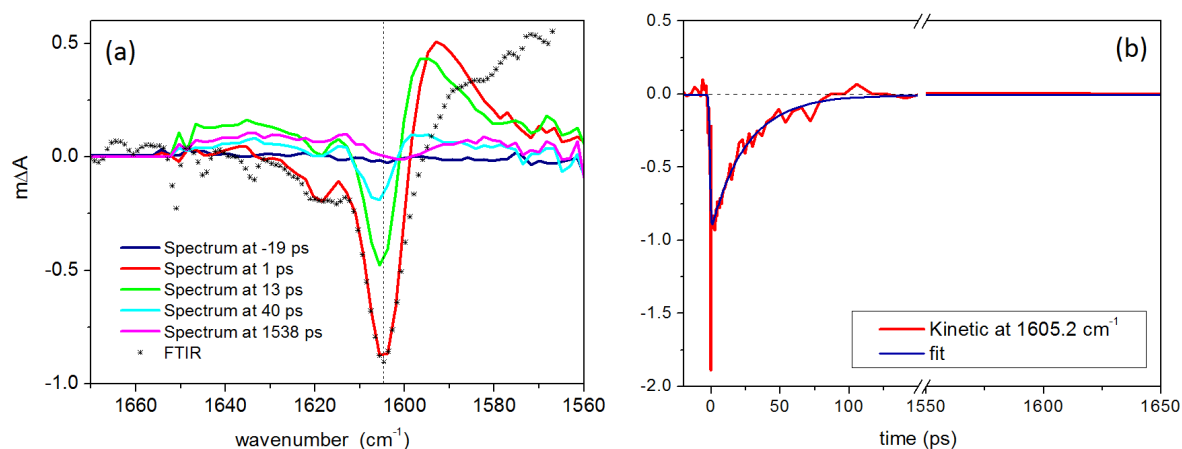


FIGURE 4.14: (a) Time-resolved IR absorption spectra evolution (around 6200 nm, 1600 cm⁻¹) and (b) kinetics of *trans*-(Cl, Cl)[Ru^{II}(FT)Cl₂(NO)]PF₆ compound in acetonitrile during the irradiation of 406 nm, 2 μJ. IR experiment was performed with cell of 500 μm ($OD_{406} = 0.24$ measured by UV-visible steady state) and circulation system.

decrease of fresh solution concentration. After the following six runs (purple curve) we observe the evolution with some signatures similar to previous steady state measurements: isobestic point at 380 nm, decrease of OD above 380 nm and OD growth below 380 nm, even though the OD growth is not exactly as in experiment with small volume solution (Figures 4.6, 4.10 (d), 4.11 (b)).

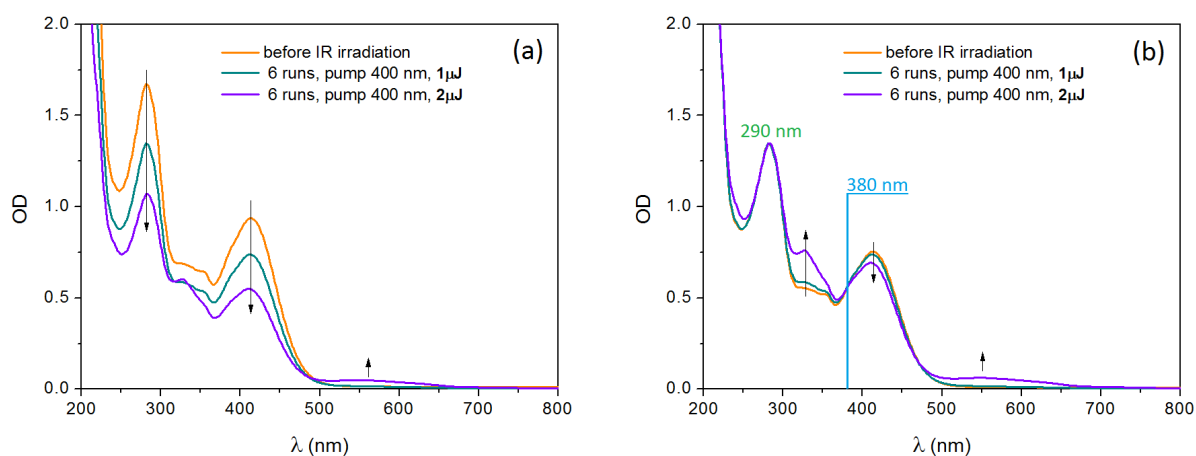


FIGURE 4.15: (a) UV-visible steady state absorption spectra evolution of *trans*-(Cl, Cl)[Ru^{II}(FT)Cl₂(NO)]PF₆ compound in acetonitrile with 500 μm of solvent layer of $OD_{406} = 0.24$ taken simultaneously with time-resolved IR measurements; (b) the same spectra but normalized, OD at 280 nm is brought to the same value with dividing by constant.

As a result we have two different sets of UV-visible OD evolution obtained with two different sample volumes. On one hand, when we use the small cell with volume of 0.7 ml as in time-resolved UV-visible measurements and mix the solution with a magnetic stirrer we observe the same OD evolution in UV-visible steady state spectroscopy as reported in work of Akl et al., compare Figure 4.10 (d) and Figure 4.4 [82]. On the other hand, when we prepare large volume of the sample, 12 ml, and circulate it with flow cell then we obtain a very different OD evolution in UV-visible region. We suspect that the volume of solution plays an important role in the different OD evolutions we see in the UV-visible range.

4.2.3 Monochromatic pump-probe studies in UV-visible range with circulation system and flow cell

To understand the unexpected evolution of steady state UV-visible absorption spectra observed simultaneously with time-resolved IR measurements in flow cell we decided to reproduce in Rennes the same experimental setup we did in Poznań using circulation system with large volume of solution. This time, however, we will perform monochromatic pump-probe experiment in the visible range. We chose to follow kinetics at 650 nm, as it is associated with the Ru^{III} – solvent photoproduct formation [82] or possible MSI species generation [92].

Sample preparation. For this experiment sample was prepared with 4.51 mg of *trans* – (Cl, Cl)[$Ru^{II}(FT)Cl_2(NO)$] PF_6 and 24 ml of acetonitrile (HPLC, Fisher). Concentration and OD_{405} were calculated as follows:

$$c = \frac{m}{V \cdot M} = 2.5 \cdot 10^{-4} \text{ mol/l},$$

$$OD_{405} = \epsilon_{405} \cdot c \cdot l = 1.1 \text{ in } 2 \text{ mm cell},$$

where $M = 744.45 \text{ g/mol}$, $\epsilon_{405} = 21952 \text{ l/(mol} \cdot \text{cm)}$ [82].

The prepared sample was then separated into two solutions of 12 ml, first one was circulated for several hours while measurements were carried out and the second one was circulated only during 15 minutes. We used the circulation system with estimated circulation rate of 1.6 ml/sec.

Results and discussion. Solution 1. With pump of 400 nm and probe of 650 nm we follow the signal from the circulating sample as shown in Figure 4.16 (a). The fit of this kinetics gives us two time constants: 0.3 ps and 1.5 ps, which means that we have at least two processes during the photochemical reaction, either intermediate states or vibrational cooling. When the flow of solution in the cell is stopped we observe an increase of the peak intensity (Figure 4.16 (b)), which indicates the secondary photochemical reaction (excitation of the first photoproduct), as with a stopped flow of solution we irradiate now the same small volume of the sample several times. When the flow is on again and our solution is circulating we can estimate the sample degradation by measuring the absolute value of transmission (Figure 4.16 (c)) and it is clear that there is almost no change of a transmission, thus showing that the flow rate is fast enough and there is a low probability of irradiating the excited molecules twice during the first circulations of the sample.

Solution 2. A second solution was studied by the same 650 nm probe but during only 15 minutes of pump-probe measurements (3 scans, 15 minutes of 404 nm light exposure). In Figure 4.16 (d) third scan of these measurements is fitted with two exponentials and with the same time constants as **solution 1**, 0.3 ps and 1.5 ps. The signal is becoming flat quite fast, after around 10 ps and it doesn't go back to zero which signifies the irreversible photochemical reaction with either formation of MSI species or the formation of final photoproduct, Ru^{III} – MeCN, which is less likely as we explained in previous section (similar to the results we got from time-resolved UV-visible experiment in Figure 4.11).

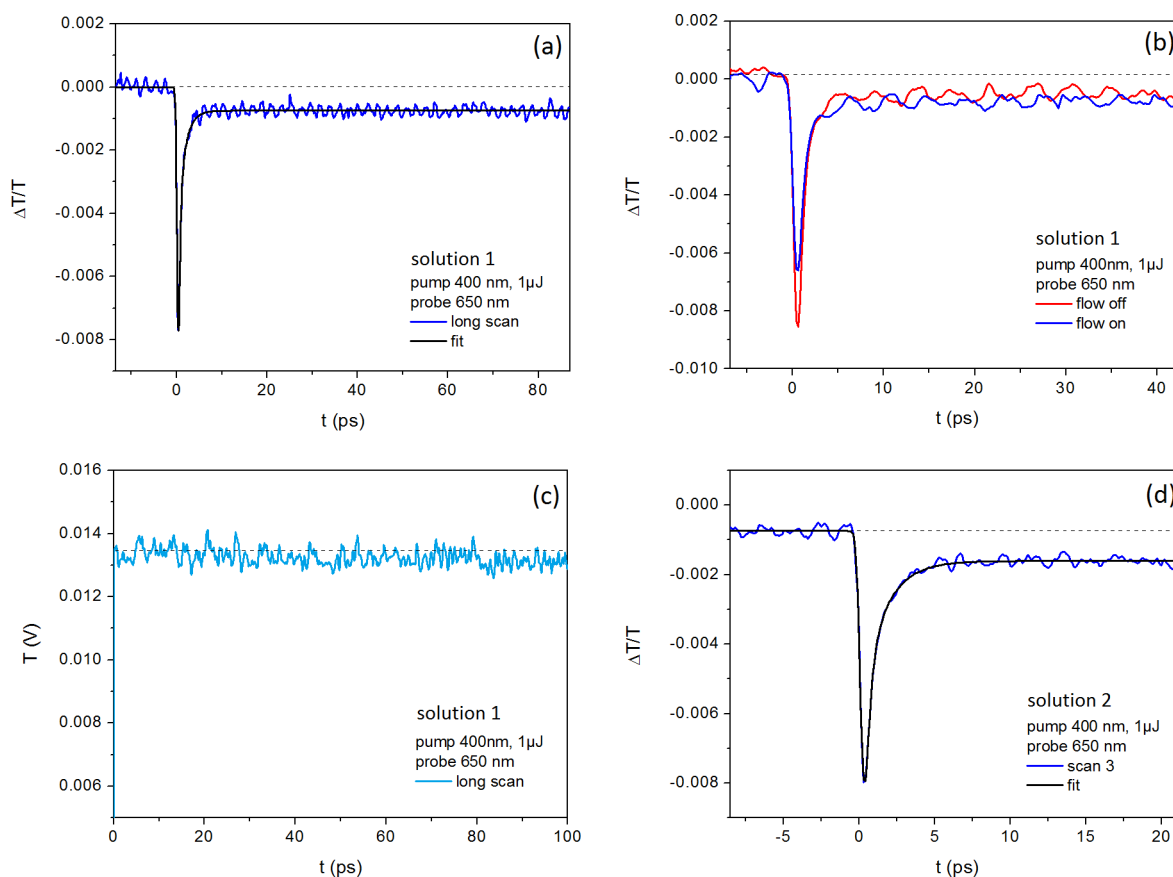


FIGURE 4.16: **Solution 1:** (a) kinetics at 640 *nm* up to 100 ps; (b) comparison between kinetics when pump is on (stable flow) and when it is off (similar to static cell); (c) absolute value of transmission during the scan to verify how fast the sample is degrading. **Solution 2:** (d) kinetics at 640 *nm* in *trans*–(*Cl*, *Cl*)[*Ru*^{II}(*FT*)*Cl*₂(*NO*)]*PF*₆ compound in acetonitrile with circulation system during scan 3.

As for the UV-visible absorption spectra after several hours of pump-probe experiment on first solution with a flow cell ($V = 12$ ml), we were able to reproduce exactly the same unusual *OD* evolution as seen in time-resolved IR experiment with a flow cell in Poznań, compare Figure 4.17 (a-b) after 12 runs and Figure 4.15. For second solution right after third scan of pump-probe experiment (15 minutes of 404 *nm* exposure) the steady state UV-visible spectra is also similar to the UV-visible after IR experiment (compare Figure 4.17 (c-d) and Figure 4.15 after 6 runs). We see the same decrease in concentration of the photoreactant molecules (pristine sample) as in Poznań with no formation of *Ru*^{III} – *MeCN* photoproduct which normally gives the rise to the broad band around 640 *nm*. And even when the sample is left overnight in the dark room there is no significant change in the *OD*, the solution is thermally stable. Interestingly, when sample is exposed to ambient light the *OD* starts to evolve in the similar way as in small sample volume experiments (without flow cell and circulation), see Figure 4.17 (e-f).

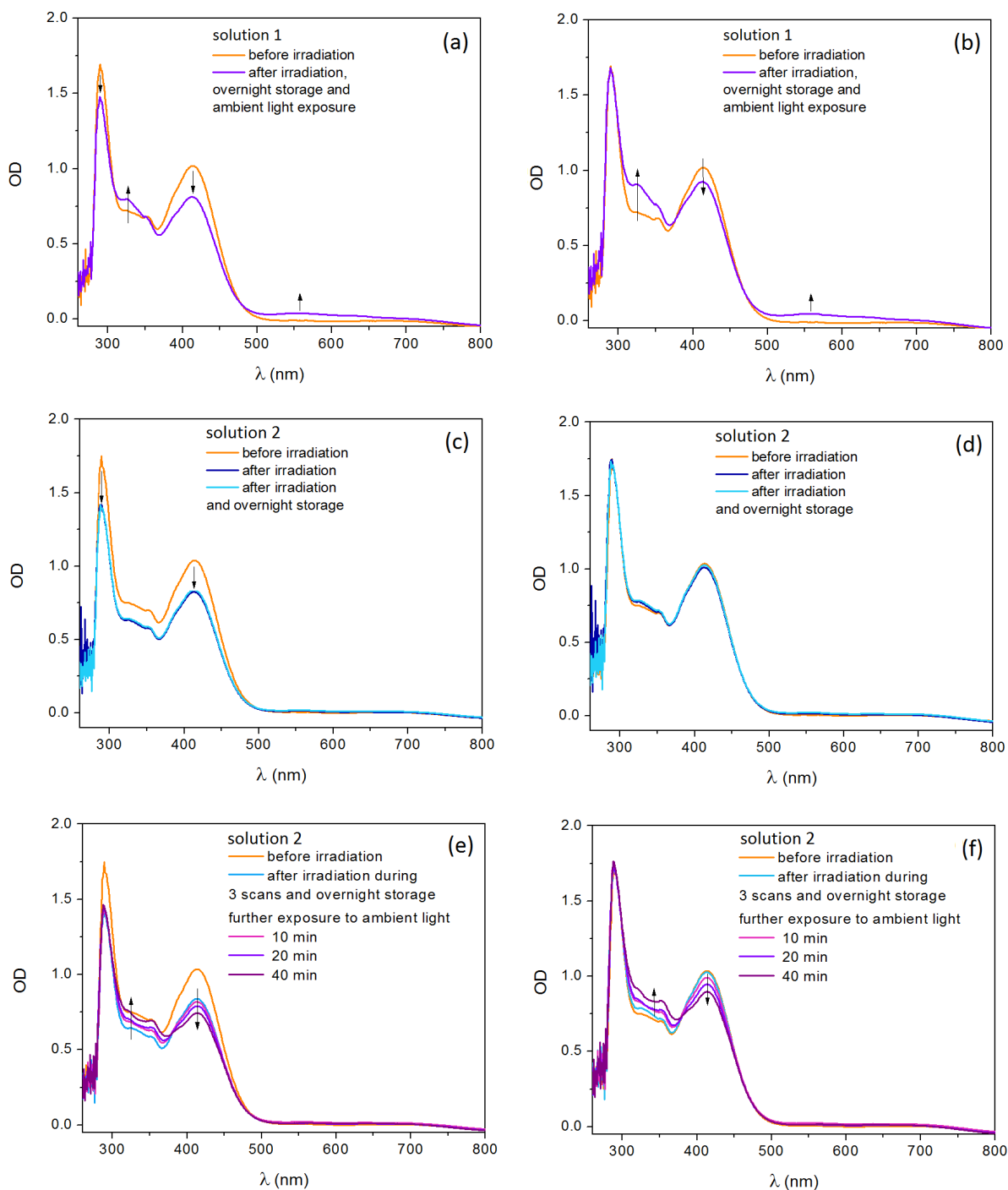


FIGURE 4.17: The steady state UV-visible absorption of *trans* – $(Cl, Cl)[Ru^{II}(FT)Cl_2(NO)]PF_6$ compound in acetonitrile. **Solution 1:** (a) *OD* evolution before and after pump-probe measurements, as well as ambient light exposure; (b) the same as (a) but normalized. **Solution 2:** (c) *OD* evolution before and after 3 scans of pump-probe measurements plus the spectrum after overnight storage; (d) the same as (c) but normalized; (e) the same as (c) plus ambient light exposure during 10, 20 and 40 minutes; (f) the same as (e) but normalized. To rescale curves the *OD* at 290 nm peak is brought to the same value by dividing it by a constant. Cells used in these experiments were not perfectly adapted for the UV range measurements. Therefore, a strong signal is appearing below 300 nm from the cell itself. All the data were obtained by the subtraction of pure acetonitrile spectra measured in the same cell.

Based on our experimental observations the following scheme for the *NO* release is proposed:



Indeed, in recent DFT calculations on *trans* - (Cl, Cl)[Ru^{II}(FT)Cl₂(NO)]PF₆ compound [92], authors propose the metastable MSII state (side-on configuration of *NO* ligand, $Ru <^N_O$) as an intermediate step preceding the *NO* release process, i.e. the two-step photon absorption process is needed to liberate the *NO*[•] (Figure 4.18). The triplet ³MSII shows the lowest dissociation energy and thus it is the most suitable step before either direct *NO* release or further photoisomerization to MSI species and eventual *NO* liberation. In our experimental studies, however, we did not detect the intermediate state signatures, but we clearly observe that we always deal with a secondary photochemistry.

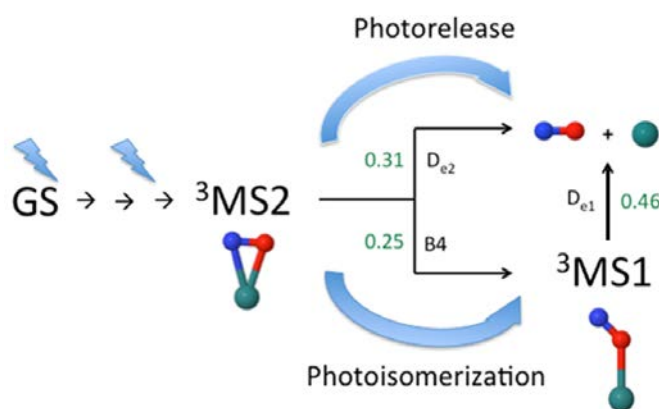


FIGURE 4.18: Energetic data (eV) of the photorelease (De1 and De2) of nitric oxide and photoisomerization (B4) of nitrosyl ligand proposed in work [92].

Based on the obtained experimental results and recent DFT calculations we can draw the following conclusions:

- The steady state UV-visible spectra with a large volume of the sample, flow cell and circulation system after a short light exposure shows the loss of the primary solution concentration. However, the typical evolution usually observed with much smaller volume without flow cell is not evidenced, which shows a strong effect of the sample volume and flow cell on the experimental results. Logically, after much longer time of irradiation, a clear optical signature around 640 nm is observed in steady state spectra, which indicates the presence of final $Ru^{III} - MeCN$ photoproduct.
- The diffusion does not play any crucial role as seen from the UV-visible absorption spectra of the sample kept overnight. Once the *NO*[•] radical is liberated, the molecule is recombined with the closest solvent molecule (MeCN), as it is energetically favourable. The experimental confirmation of the recombination of the molecule with the solvent after the *NO* release was also obtained by X-Ray absorption measurements performed during this thesis and presented in Appendix F.

- When we use large volume of the sample, flow cell and circulation system in time-resolved experiments, we irradiate during the first scans mainly the fresh sample at every pump pulse. And yet, we clearly observe the secondary photochemistry in time-resolved UV-visible spectra which is in a good agreement with DFT calculations where two photons are necessary for the *NO* liberation.
- The observed kinetics of signal at 640 *nm* in time-resolved UV-visible spectra is very fast (several *ps*) but the nature of formed photoproduct is not explicit. On one hand, we expect to see the formation of *Ru^{III}* photoproduct associated with the rise of 640 *nm* signal, on the other hand, within the recent DFT calculations this optical signature might be also assigned to the formation of MSI species at a short time scales. Therefore, both interpretations are valid for time-resolved experimental results. In future, it could be interesting to perform this experiment at a longer time delays and verify the kinetics of the 640 *nm* signal.
- Another way to detect the formation of the MSI species is the IR time-resolved experiment, which was done within this project. Unfortunately, within the present experimental setup we did not observe any signal from MSI species, which can be explained by sensitivity of experiment or MSI low population, for example, if MSI species do form. In future, to distinguish between MSI species and the *Ru^{III}* photoproduct formation, it could be interesting to follow the IR signature of the *NO₂⁻* (appears after the *NO* release) by the time-resolved IR experiment. Such a setup together with the time-resolved UV-visible experiment at a longer time delays might give an answer about the nature of the photoproduct at a short time scale observed in present work.

CONCLUSIONS

This Ph. D. thesis was focused on the experimental study of two photoinduced processes observed in various $[ML_5NO]$ complexes, where $M = Fe, Ru, \dots$, $L = CN, Cl, \dots$: (i) photoisomerization, where the system goes from N-bound state ($M-NO$, stable GS state) to O-bound state ($M-ON$, metastable MSI state) and a second metastable state, ‘side-on’ MSII ($M <^N_O$) is observed during the inverse phototransformation, $MSI \rightarrow$ ‘side-on’ MSII \rightarrow GS; (ii) photoinduced release of NO^\bullet radical.

The photoisomerization is investigated in single crystals of $[Ru(py)_4Cl(NO)](PF_6)_2 \cdot 1/2H_2O$ compound by means of X-Ray diffraction, steady state visible and time-resolved UV-visible absorption spectroscopies. Remarkably, in $[Ru(py)_4Cl(NO)](PF_6)_2 \cdot 1/2H_2O$ single crystals, a predominant two-step process through long-lived MSII species during the $Ru-NO$ to $Ru-ON$ photoswitching is observed with visible absorption spectroscopy under blue CW irradiation. The low concentration of the transient species MSII species hinders the detection of any structural signature (population of transient species lower than a few %). However, pronounced structural signatures of ‘side-on’ MSII^{IR} are observed during the $Ru-ON$ back to $Ru-NO$ process under IR light.

The visible absorbance of the MSII^{IR} state (mixed of GS and MSII ‘side-on’ configuration) has been experimentally determined. Evolution of spectra during $Ru-NO$ to $Ru-ON$ and the reverse process as well as a simple kinetic model used to reproduce the experimental evolution of the OD spectra during the $Ru-NO$ to $Ru-ON$ photoswitching (under blue light irradiation) agrees that the optical signature associated with the transient MSII species depends on the direction of the photochemical reaction. The ‘side-on’ configuration of the intermediate MSII species cannot be unambiguously revealed during the photoswitching under blue light irradiation, thus further investigations using ultrashort laser pulses are employed to clarify that point.

In prototype SNP system the time-resolved studies showed fast relaxation (less than 1 ps) from excited GS to MSII without any other intermediate state involved, while in case of single crystals of $[Ru(py)_4Cl(NO)](PF_6)_2 \cdot 1/2H_2O$ compound time-resolved studies show much longer time delays needed to reach a ‘plateau’, of the order of 15 – 20 ps. The observed signal of ‘plateau’ is quite weak which might be explained by inefficiency of GS to MSII transition. Two time constants found from the fitting of experimental data indicate multi-step pathway, which probably involves intermediate triplet states typical for ruthenium systems. It could be assigned to either decay

of two transient states or relaxation of a transient state and vibrational cooling process, and the latter one we consider to be the most probable. Unfortunately, the low efficiency of the photoisomerization to the MSII state limits our access to MSII optical signature under the blue light irradiation, we observe only a weak signal of intermediate state during the time-resolved studies.

Another part of our studies was devoted to the understanding the role of water molecule of crystal in photoisomerization process by means of photocrystallography. First of all, we evidenced a significant difference in lattice parameters evolution in dehydrated sample comparing to the hydrated one under the IR irradiation. One of the lattice parameters unexpectedly decreased under the IR irradiation with water departure, while it normally grows, and another parameter showed a much higher change in its value. It was also found that the kinetics of the system strongly depends on the water presence in the crystal structure for the MSI back to GS photoreaction under the 1064 nm, while the kinetics for GS to MSI under the blue light does not change. Another surprising effect of water departure is the very fast transformation of one of the independent sites, which is located close to water molecule in the unit cell, to GS (MSII^{IR} formation was not observed) under the IR irradiation in dehydrated sample. The rehydration of the crystal seems to restore all the main features of hydrated sample during the photoisomerization, even though less pronounced, the kinetics of the system seems to slow down after the rehydration. Even if we irradiate the rehydrated sample longer time we do not succeed in observing the complete phototransformation of $GS \rightarrow MSI$.

Finally, the photoinduced NO^\bullet release in *trans* - (Cl, Cl)[Ru^{II}(FT)Cl₂(NO)]PF₆ system in acetonitrile solution was studied by the UV-visible and mid-IR absorption spectroscopies, both steady state and time-resolved. By observing the ultrafast dynamics of phototransformation we evidenced a secondary photochemistry necessary for NO^\bullet release as well as the formation of final photoproduct within a few ps ([Ru^{III} - MeCN] or MSI species). However, we were not able to observe experimentally the nature of this intermediate state, which might be related either to experimental limitations or to potentially very low population of this transient state.

Bibliography

- [1] P. Coppens, I. Novozhilova, and A. Kovalevsky. *Chem. Rev.*, **102**, 861, 2002.
- [2] U. Hauser, V. Oestreich, and H. D. Rohrweck. *Z. Phys.*, **A280**, 17, 1977.
- [3] U. Hauser, V. Oestreich, and H. D. Rohrweck. *Z. Phys.*, **A280**, 125, 1977.
- [4] U. Hauser, V. Oestreich, and H. D. Rohrweck. *Z. Phys.*, **A284**, 9, 1978.
- [5] H. Zöllner, T. Woike, W. Krasse, and S. Haussühl. *Z. Kristallogr.*, **188**, 139, 1989.
- [6] M. R. Pressprich, M.A. White, Y. Vekhter, and P. Coppens. *JACS*, **116**, 5233, 1994.
- [7] H. U. Güdel. *Chem. Phys. Lett.*, **175**, 262, 1990.
- [8] M. Rüdlinger, J. Schefer, G. Chevrier, N. Furer, H. U. Güdel, S. Haussühl, G. Heger, P. Schweiss, T. Vogt, T. Woike, and H. Zöllner. *Z. Phys. B Condens. Matter*, **83**, 125, 1991.
- [9] M. Rüdlinger, J. Schefer, T. Vogt, T. Woike, S. Haussühl, and H. Zöllner. *Physica (Utrecht)*, **180/181**, 293, 1992.
- [10] M. D. Carducci, M.R. Pressprich, and P. Coppens. *JACS*, **119**, 2669, 1997.
- [11] P. Coppens, D. V. Fomitchev, M. D. Carducci, and K. Culp. *Dalton Trans.*, **6**, 865, 1998.
- [12] T. Woike, W. Krasser, H. Zöllner, W. Kirchner, and S. Haussühl. *Z. Phys.*, **D25**, 351, 1993.
- [13] D. Schaniel and T. Woike. *PCCP*, **11**, 4391, 2009.
- [14] D. Schaniel, T. Woike, J. Schefer, and V. Petricek. *Phys. Rev. B.*, **71**, 174112, 2005.
- [15] D. Schaniel, B. Cormary, I. Malfant, L. Valade, T. Woike, B. Delley, K. W. Krämer, and H.U. Güdel. *PCCP*, **9**, 3717, 2007.
- [16] V. Rusanov, S. Stankov, and A. X. Trautwein. *Hyperfine Inter.*, **144/145**, 307, 2002.
- [17] D. Schaniel, J. Schefer, B. Delley, M. Imlau, and T. Woike. *Phys. Rev. B*, **66**, 085103, 2002.
- [18] B. Delley, J. Schefer, and T. Woike. *J. Chem. Phys.*, **107**, 10067, 1997.

- [19] J. G. Vos and M. T. Pryce. *Coord. Chem. Rev.*, **254**, 2519, 2010.
- [20] B. O'Regan and M. Grätzel. *Nature*, **353**, 737, 1991.
- [21] A. Hagfeldt and M. Grätzel. *Acc. Chem. Res.*, **33**, 269, 2000.
- [22] A. C. Merkle, A. B. McQuarters, and N. Lehnert. *Dalton Trans.*, **41**, 8047, 2012.
- [23] P. P. Lainé, S. Campagna, and F. Loiseau. *Coord. Chem. Rev.*, **252**, 2552, 2008.
- [24] N. L. Fry, M. J. Rose, D. L. Rogow, C. Nyitray, M. Kaur, and P. K. Mascharak. *Inorg. Chem.*, **49**, 1487, 2010.
- [25] R. Prakash, A. U. Czaja, F. W. Heinemann, and D. Sellmann. *J. Am. Chem. Soc.*, **127**, 13758, 2005.
- [26] E. Tfouni, M. Krieger, B. R. McGarvey, and D. W. Franco. *Coord. Chem. Rev.*, **236**, 57, 2003.
- [27] K. Ghosh, A. A. Eroy-Reveles, B. Avila, T. R. Holman, M. M. Olmstead, and P. K. Mascharak. *Inorg. Chem.*, **43**, 2988, 2004.
- [28] C. G. Hoffman-Luca, A. A. Eroy-Reveles, J. Alvarenga, and P. K. Mascharak. *Inorg. Chem.*, **48**, 9104, 2009.
- [29] A. A. Eroy-Reveles, Y. Leung, and P. K. Mascharak. *J. Am. Chem. Soc.*, **128**, 7166, 2006.
- [30] C. Mallins, S. Fanni, H. G. Glever, J. G. Vos, and B. D. MacCraith. *Anal. Commun.*, **36**, 3, 1999.
- [31] A. Lobnik, I. Oehme, I. Murkovic, and O. S. Wolfbeis. *Anal. Chim. Acta*, **367**, 159, 1998.
- [32] P.-T. Chou and Y. Chi. *Chem. Eur. J.*, **13**, 380, 2007.
- [33] H. Inomata, K. Goushi, T. Masuko, T. Konno, T. Imai, H. Sasabe, J. J. Brown, and C. Adachi. *Chem. Mater.*, **16**, 1285, 2004.
- [34] M. Imlau, S. Haussühl, T. Woike, R. Schieder, V. Angelov, R. A. Rupp, and K. Schwarz. *Appl. Phys. B*, **68**, 877, 1999.
- [35] P. Gütlich, Y. Garcia, and T. Woike. *Coord. Chem. Rev.*, **219-221**, 839, 2001.
- [36] A. Y. Kovalevsky, K. A. Bagley, and P. Coppens. *J. Am. Chem. Soc.*, **124**, 9241, 2002.
- [37] D. P. Butcher, A. A. Rachford, J. L. Petersen, and J. J. Rack. *Inorg. Chem.*, **45**, 9178, 2006.
- [38] V. Dieckmann, S. Eicke, J. J. Rack, TH. Woike, and M. Imlau. *Opt. Express*, **17**, 15052, 2009.
- [39] P. Günter and J.-P. Huignard. *Springer, Photorefractive Materials and Their Applications* 3, 2007.

-
- [40] J. M. Cole. *Z. Kristallogr.*, **223**, 259, 2008.
- [41] J. J. Rack. *Coord. Chem. Rev.*, **253**, 78, 2009.
- [42] V. Dieckmann, S. Eicke, K. Springfeld, and M. Imlau. *Materials*, **5**, 1155, 2012.
- [43] K. Springfeld, V. Dieckmann, and M. Imlau. *Photo. Res.*, **1**, 197, 2013.
- [44] A. Y. Kovalevsky, G. King, K. A. Bagley, and P. Coppens. *Chem. Eur. J.*, **11**, 7254, 2005.
- [45] I. V. Novozhilova, P. Coppens, J. Lee, G. B. Richter-Addo, and K. A. Bagley. *J. Am. Chem. Soc.*, **128**, 2093, 2006.
- [46] N. Casaretto, S. Pillet, E. E. Bendeif, D. Schaniel, A. K. E. Gallien, P. Klüfers, and T. Woike. *IUCR J.*, **2**, 35, 2015.
- [47] D. Schaniel, M. Nicoul, and T. Woike. *PCCP*, **12**, 9029, 2010.
- [48] D. Schaniel, M. Imlau, T. Weisemoeller, T. Woike, K. W. Krämer, and H.U. Güdel. *Adv. Mater.*, **19**, 723, 2007.
- [49] M. R. Warren, S. K. Brayshaw, A. L. Johnson, S. Schiffrers, P. R. Raithby, T. L. Easun, M. W. George, J. E. Warren, and S. J. Teat. *Angew. Chem.*, **121**, 5821, 2009.
- [50] M. R. Warren, T. L. Easun, S. K. Brayshaw, R. J. Deeth, M. W. George, A. L. Johnson, S. Schiffrers, S. J. Teat, A. J. Warren, J. E. Warren, C. C. Wilson, C. H. Woodall, and P. R. Raithby. *Chem. Eur. J.*, **20**, 5468, 2014.
- [51] E. Cullotta and Jr. D. E. Koshland. *Science*, **258**, 1862, 1992.
- [52] S. H. Snyder and D. S. Brecht. *Sci. Am.*, **266**, 68, 1992.
- [53] D. D. Rees, R. M. J. Palmer, and S. Moncada. *Proc. Natl. Acad. Sci. USA*, **86**, 3375, 1989.
- [54] L. J. Ignarro. *Hypertension*, **16**, 477, 1990.
- [55] A. Levina, A. Mitra, and P. A. Lay. *Metallomics*, **1**, 458, 2009.
- [56] B. S. Howerton. *Ph. D. Thesis*, Lexington, Kentucky, 2012.
- [57] M. J. Rose and P. K. Mascharak. *Coordination Chemistry Reviews*, **252**, 2093, 2008.
- [58] B. P. Sullivan and T. J. Meyer. *Inorg. Chem.*, **21**, 1037, 1982.
- [59] J. L. Burgaud, E. Ongini, and P. Del Soldato. *Ann. N. Y. Acad. Sci.*, **962**, 360, 2002.
- [60] S. L. H. Higgins and K. J. Brewer. *Angew. Chem. Int. Ed.*, **51**, 11420, 2012.
- [61] D. Torre, A. Pugliese, and F. Speranza. *Lancet Infect. Dis.*, **2**, 273, 2002.
- [62] B. Cormary, I. Malfant, M. Buron-Le Cointe, L. Toupet, B. Delley, D. Schaniel, N. Mockus, T. Woike, K. Fejfarova, V. Petricek, and M. Dusek. *Acta Cryst.*, **B.65**, 612, 2009.

- [63] B. Cormary, S. Ladeira, K. Jacob, P. G. Lacroix, T. Woike, D. Schaniel, and I. Malfant. *Inorg. Chem.*, **51**, 7492, 2012.
- [64] L. Khadeeva, W. Kaszub, M. Lorenc, I. Malfant, and M. Buron-Le Cointe. *Inorg. Chem.*, **55**, 4117, 2016.
- [65] S. S. Batsanov. *Inorganic Materials*, **37**, 871, 2001.
- [66] C. F. Macrae, P. R. Edgington, P. McCabe, E. Pidcock, G. P. Shields, R. Taylor, M. Towler, and J. van de Streek. *J. Appl. Cryst.*, **39**, 453, 2006.
- [67] A. Bondi. *J. of Phys. Chem.*, **68**, 441, 1964.
- [68] D. Schaniel, T. Woike, C. Boskovic, and H.U. Güdel. *Chem. Phys. Lett.*, **390**, 347, 2004.
- [69] J. Sanz Garcia, F. Alary, M. Boggio-Pasqua, I. Dixon, I. Malfant, and J.-L. Heully. *Inorg. Chem.*, **54**, 8310, 2015.
- [70] M. Cammarata, M. Levantino, M. Wulff, and A. Cupane. *J. of Mol. Biology*, **400**, 951, 2010.
- [71] J. Baskin and A. Zewail. *J. of Chem. Ed.*, **78**, 737, 2001.
- [72] Etienne-Jules Marey. *Nature*, **51**, 80, 1894.
- [73] L. Freitag and L. Gonzalez. *Inorg. Chem.*, **53**, 6415, 2014.
- [74] L. Salassa, C. Garino, G. Salassa, R. Gobetto, and C. Nervi. *JACS*, **130**, 9590, 2008.
- [75] W. Henry, C. G. Coates, C. Brady, K. L. Ronayne, P. Matousek, M. Towrie, S. W. Botchway, A. W. Parker, J. G. Vos, W. R. Browne, and J. J. McGarvey. *J. Phys. Chem. A*, **112**, 4537, 2008.
- [76] N. H. Damrauer, G. Cerullo, Alvin Yeh, T. R. Boussie, C. V. Shank, and J. K. McCusker. *Science*, **275**, 54, 1997.
- [77] N. L. Fry and P. K. Mascharak. *Acc. of Chem. Research*, **44**, 289, 2011.
- [78] A. K. Patra, M. J. Rose, K. A. Murphy, M. M. Olmstead, and P. K. Mascharak. *Inorg. Chem.*, **43**, 4487, 2004.
- [79] J. Akl, I. Sasaki, P. G. Lacroix, V. Hugues, P. Vicendo, M. Bocé, S. Mallet-Ladeira, M. Blanchard-Desce, and I. Malfant. *Photochem. Photobiol. Sci.*, **15**, 1484, 2016.
- [80] A. G. de Candia, J. P. Marcolongo, R. Etchenique, and L. D. Slep. *Inorg. Chem.*, **49**, 6925, 2010.
- [81] R. Galvao de Lima, M. Gama Sauaia, D. Bonavenhira, A. C. Tedesco, L. M. Bendhack, and R. Santana da Silva. *Inorg. Chim. Acta*, **359**, 2543, 2006.

-
- [82] J. Akl, I. Sasaki, P. G. Lacroix, I. Malfant, S. Mallet-Ladeira, P. Vicendo, N. Farfanc, and R. Santilland. *Dalton Trans.*, **43**, 12721, 2014.
- [83] I. J. Bigio and S. G. Bown. *Cancer Biol. Ther.*, **3**, 259, 2004.
- [84] D. E. J. G. Dolmans, D. F. Kumura, and R. K. Jain. *Nature Rev. Cancer*, **3**, 380, 2003.
- [85] K. Karidi, A. Garoufis, A. Tsipis, N. Hadjiliadis, H. den Dulkb, and J. Reedijk. *Dalton Trans.*, 1176, 2005.
- [86] V. Dieckmann, M. Imlau, D. H. Taffa, L. Walder, R. Lepski, D. Shaniel, and T. Woike. *Phys. Chem. Chem. Phys.*, **12**, 3283, 2010.
- [87] M. S. Lynch, M. Cheng, B. E. van Kuiken, and M. Khalil. *JACS*, **133**, 5255, 2011.
- [88] C. F. Works and P. C. Ford. *JACS*, **122**, 7592, 2000.
- [89] J. Bordini, D. L. Hughes, J. D. Da Motta Neto, and C. J. da Cunha. *Inorg. Chem.*, **41**, 5410, 2002.
- [90] C. F. Works, C. J. Jocher, G. D. Bart, X. Bu, and P. C. Ford. *Inorg. Chem.*, **41**, 3728, 2002.
- [91] Manual for Cary 5000. <https://www.agilent.com/en-us/products/uv-vis-uv-vis-nir/uv-vis-uv-vis-nir-systems/cary-5000-uv-vis-nir>. 2016.
- [92] J. Sanz Garcia, F. Alary, M. Boggio-Pasqua, I. Dixon, and J.-L. Heully. *J. Mol. Model.*, **22**, 284, 2016.
- [93] Xcalibur series Manual Version 1.4. Oxford Diffraction Limited, 2004.
- [94] A. Altomare, M.C. Burla, M. Camalli, G. Cascareno, C. Giacovazzo, A. Guagliardi, A. G. G. Moliterni, G. Polidori, and R. Spagna. *J. Appl. Cryst.*, **32**, 115, 1999.
- [95] G. M. Sheldrick. *Acta Cryst.*, **A64**, 112, 2008.
- [96] O. V. Dolomanov, L. J. Bourhis, R. J. Gildea, J. A. K. Howard, and H. Puschmann. *J. Appl. Cryst.*, **42**, 339, 2009.
- [97] Users manual for SR830. Stanford Research Systems, 2006.
- [98] W. Kaszub. *PhD Thesis*, Rennes-Poznań, 2012.
- [99] W. Kaszub, E. Collet, H. Cailleau, M. Servol, M-L. Boillot, A. Tissot, and M. Lorenc. *Acta Phys. Pol. A*, **121**, 324, 2012.
- [100] D. E. Spence, P. N. Kean, and W. Sibbett. *Optics Letters*, **16**, 42, 1991.
- [101] B. Hitz. *Optics Letters*, **15**, 3309, 2007.

- [102] U. Demirbas, M. Schmalz, B. Sumpf, G. Erbert, G. S. Petrich, L. A. Kolodziejski, J. Fujimoto, F. X. Kärtner, and A. Leitenstorfer. *Proc. SPIE, Laser Sources and Applications*, **8433**, 84330D, 2012.
- [103] Users manual for Mira. Coherent Inc., 2005.
- [104] Users manual for Legend Elite II. Coherent Inc., 2010.
- [105] Performance Specifications for TOPAS-C. Light Conversion Ltd., 2016.
- [106] M. Lorenc, Ch. Balde, W. Kaszub, A. Tissot, N. Moisan, M. Servol, M. Buron, H. Cailleau, P. Chasle, P. Czarnecki, M. L. Boillot, and E. Collet. *Phys. Rev.*, **B 85**, 054302, 2012.
- [107] M. R. R. Vaziri. *Opt. Commun.*, **357**, 200, 2015.
- [108] Self phase modulation. <https://en.wikipedia.org>.
- [109] ESRF X-Ray Edge Energies, ID11. <http://www.esrf.eu>.
- [110] J. K. Kowalska, F. A. Lima, C. J. Pollock, J. A. Rees, and S. DeBeer. *Isr. J. Chem.*, **56**, 803, 2016.
- [111] Yves Joly and FDMNES User's Guide. Institut Neel, CNRS, 2014.
- [112] O. Bunau and Y. Joly. *J. Phys. : Condens. Matter*, **21**, 345501, 2009.
- [113] S. A. Guda, A. A. Guda, M. A. Soldatov, K. A. Lomachenko, A. L. Bugaev, C. Lamberti, W. Gawelda, C. Bressler, G. Smolentsev, A. V. Soldatov, and Y. Joly. *J. Chem. Theory Comput.*, **11**, 4512, 2015.

APPENDIX A: X-Ray diffraction studies

Single crystals of $[Ru(py)_4Cl(NO)](PF_6)_2 \cdot 1/2H_2O$ were grown by team of Isabelle Malfant in Laboratoire de Chimie de Coordination (LCC-UPR8241), Toulouse. Data was collected on the four-circle Oxford Diffraction Xcalibur 3 diffractometer (Mo K_α radiation) with a two-dimensional sapphire 3 CCD detector, on samples with typical sizes around $300 \times 200 \times 100 \mu m^3$. The single crystals were mounted in an Oxford Cryosystems nitrogen-flow cryostat (CryoJet 700) allowing a precise control of temperature at low values.

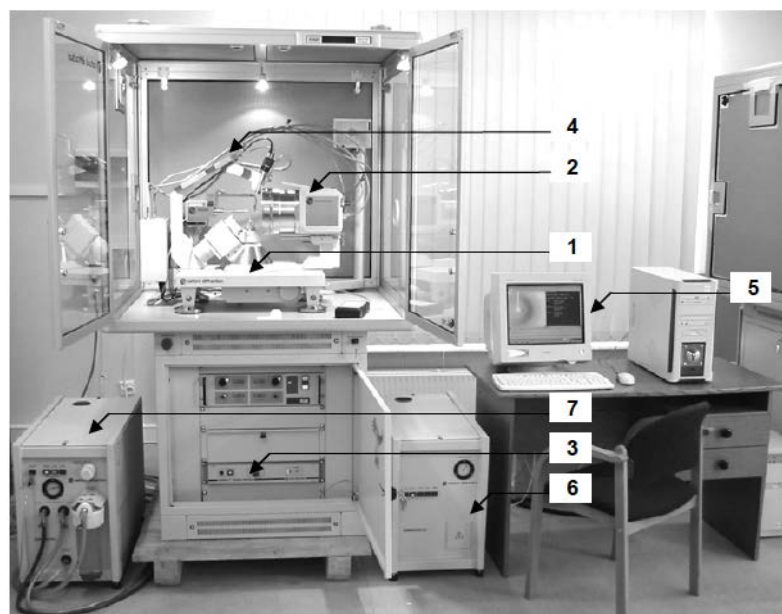


FIGURE A-1: Components of Xcalibur system (taken from [93]).

As presented in Figure A-1 the Xcalibur system consist of:

1. A kappa geometry, 4-circle diffractometer
2. A CCD are detector
3. An instrument cabinet with electronics rack
4. A stand for optional equipment

5. System software
6. A water chiller for the CCD detector
7. A water chiller for X-ray tube and X-ray generator

As shown in Figures A-2 the diffractometer consists of:

1. X-ray tube
2. 3-axis Kappa goniometer (ω , κ , and ϕ axis) for sample orientation and a detector arm (θ axis)
3. X-ray Shutter
4. Collimator
5. Beamstop
6. Beryllium Window

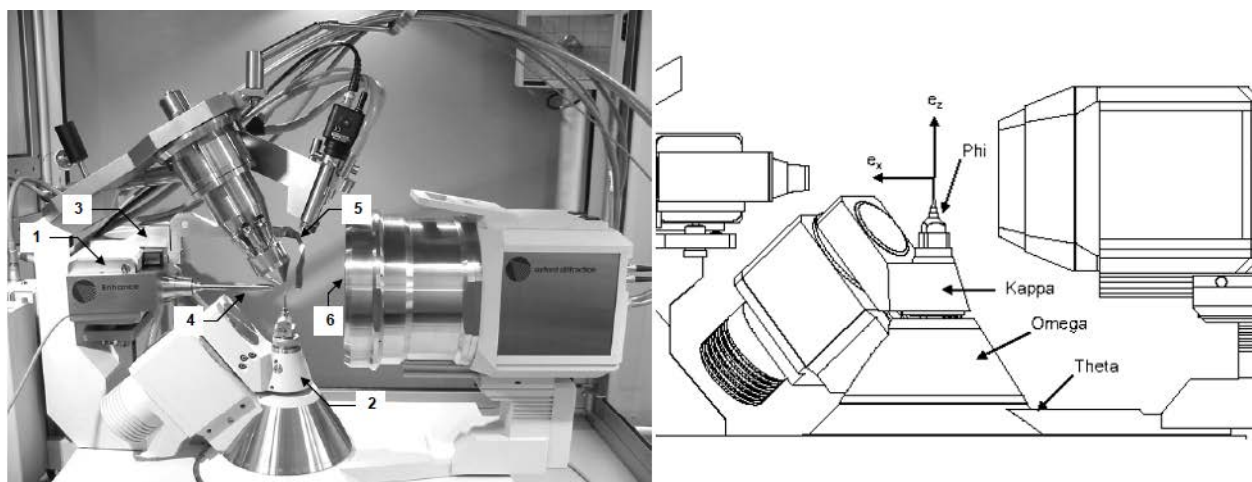


FIGURE A-2: View of the diffractometer (taken from [93]).

The X-rays are generated by a tube, which is mounted on the goniometer and powered by a high-voltage X-ray generator. The X-ray optics consist of a high speed shutter located next to the tube shield, a monochromator for selecting a specific bandwidth from tube spector and a collimator for limiting beam divergence [93].

The unit cell parameters and intensities of Bragg reflections were obtained with CrysAlis software (CrysAlis RED, Oxford Diffraction Ltd, Version 1.171.32.5 (2007)). In order to reduce a possible depopulation of metastable states by X-Ray irradiation [6], the exposure time was reduced. All unit cell parameter values are collected under light irradiation and each point corresponds to a time-average value of ten minutes. Data were collected with the resolution up to $\theta/\lambda \simeq 0.75 \text{ \AA}^{-1}$. The structures were solved with SIR-97 [94] and refined with SHELXL [95].

APPENDIX B: Experimental details of X-Ray data collections presented in Chapter 1

Data was collected on the four-circle Oxford Diffraction Xcalibur 3 diffractometer (Mo K_α radiation) with a two-dimensional sapphire 3 CCD detector, on samples with typical sizes around $300 \times 200 \times 100 \mu\text{m}^3$. The single crystals were mounted in an Oxford Cryosystems nitrogen-flow cryostat (CryoJet 700) allowing a precise control of temperature. All data was treated with CrysAlis software (CrysAlis RED, Oxford Diffraction Ltd, Version 1.171.38.41), the structures were previously solved with SIR97 [94] in WinGX environment and then refined with SHELXL97 [95] via OLEX2 GUI [96]. All non-hydrogen atoms were refined anisotropically, while all hydrogen atoms were constrained by geometry.

GS state of $[Ru(py)_4Cl(NO)](PF_6)_2 \cdot 1/2H_2O$ single crystal at 100 K

<i>Identification code</i>	runocl-hyd-GS-100K
<i>Empirical formula</i>	$C_{20} H_{21} Cl F_{12} N_5 O_{1.50} P_2 Ru$
<i>Formula weight</i>	781.88
<i>Temperature</i>	100.15 K
<i>Wavelength</i>	0.71069 Å
<i>Crystal system</i>	Monoclinic
<i>Space group</i>	P 1 2 ₁ /c 1
<i>Unit cell dimensions</i>	$a = 15.7277(8)$ Å $\alpha = 90^\circ$ $b = 13.4551(7)$ Å $\beta = 92.429(4)^\circ$ $c = 26.7672(13)$ Å $\gamma = 90^\circ$
<i>Volume</i>	5659.3(5) Å ³
<i>Z</i>	8
<i>Density (calculated)</i>	1.835 Mg/m ³
<i>Absorption coefficient</i>	0.869 mm ⁻¹
<i>F(000)</i>	3096
<i>Crystal size</i>	0.25 × 0.2 × 0.06 mm ³
<i>θ range for data collection</i>	3.073°–27.000°
<i>Index ranges</i>	–20 ≤ h ≤ 19, –17 ≤ k ≤ 15, –17 ≤ l ≤ 34
<i>Reflections collected</i>	26908
<i>Independent reflections</i>	12339, [$R_{int} = 0.0796$]
<i>Completeness to $\theta = 25.240^\circ$</i>	99.8%
<i>Absorption correction</i>	Semi-empirical from equivalents
<i>Max. and min. transmission</i>	1.00000, 0.97686
<i>Refinement method</i>	Full-matrix least-squares on F^2
<i>Data/restraints/parameters</i>	12339/78/828
<i>Goodness of fit on F^2</i>	0.956
<i>Final R indices [$I > 2\sigma(I)$]</i>	$R1 = 0.0529$, $wR2 = 0.0685$
<i>R indices (all data)</i>	$R1 = 0.1059$, $wR2 = 0.0862$
<i>Extinction coefficient</i>	n/a
$\Delta\rho_{max}$, $\Delta\rho_{min}$	0.673 eÅ ⁻³ , –0.698 eÅ ⁻³

TABLE B-1: Experimental details on crystal data and structure refinement for GS state of $[Ru(py)_4Cl(NO)](PF_6)_2 \cdot 1/2H_2O$ single crystal at 100 K.

MSII/GS mixed state of $[Ru(py)_4Cl(NO)](PF_6)_2 \cdot 1/2H_2O$ single crystal at 100 K

<i>Identification code</i>	runocl-hyd-MSII-GS-100K
<i>Empirical formula</i>	<i>C</i> 20 <i>H</i> 21 <i>Cl</i> <i>F</i> 12 <i>N</i> 5 <i>O</i> 1.50 <i>P</i> 2 <i>Ru</i>
<i>Formula weight</i>	781.88
<i>Temperature</i>	100 K
<i>Wavelength</i>	0.71069 Å
<i>Crystal system</i>	Monoclinic
<i>Space group</i>	P 1 2 ₁ /c 1
<i>Unit cell dimensions</i>	a = 15.7462(2) Å $\alpha = 90^\circ$ b = 13.4453(2) Å $\beta = 92.1921(17)^\circ$ c = 26.8024(6) Å $\gamma = 90^\circ$
<i>Volume</i>	5670.25(18) Å ³
<i>Z</i>	8
<i>Density (calculated)</i>	1.832 Mg/m ³
<i>Absorption coefficient</i>	0.867 mm ⁻¹
<i>F(000)</i>	3096
<i>Crystal size</i>	0.46 × 0.3 × 0.12 mm ³
<i>θ range for data collection</i>	2.952°–26.998°
<i>Index ranges</i>	−13 ≤ <i>h</i> ≤ 20, −13 ≤ <i>k</i> ≤ 17, −33 ≤ <i>l</i> ≤ 34
<i>Reflections collected</i>	84655
<i>Independent reflections</i>	12371, [<i>R</i> _{int} = 0.0635]
<i>Completeness to θ = 25.240°</i>	99.9%
<i>Absorption correction</i>	Semi-empirical from equivalents
<i>Max. and min. transmission</i>	1.00000, 0.98420
<i>Refinement method</i>	Full-matrix least-squares on <i>F</i> ²
<i>Data/restraints/parameters</i>	12371/38/866
<i>Goodness of fit on <i>F</i>²</i>	1.017
<i>Final <i>R</i> indices [<i>I</i> > 2σ(<i>I</i>)]</i>	<i>R</i> 1 = 0.0352, <i>wR</i> 2 = 0.0684
<i><i>R</i> indices (all data)</i>	<i>R</i> 1 = 0.0521, <i>wR</i> 2 = 0.0739
<i>Extinction coefficient</i>	n/a
<i>Δρ_{max}, Δρ_{min}</i>	0.849 eÅ ⁻³ , −0.491 eÅ ⁻³

TABLE B-2: Experimental details on crystal data and structure refinement for MSII/GS mixed state of $[Ru(py)_4Cl(NO)](PF_6)_2 \cdot 1/2H_2O$ single crystal at 100 K.

MSI state of $[Ru(py)_4Cl(NO)](PF_6)_2 \cdot 1/2H_2O$ single crystal at 8 K

<i>Identification code</i>	runocl-hyd-MSI-8K
<i>Empirical formula</i>	$C_{20} H_{21} Cl F_{12} N_5 O_{1.50} P_2 Ru$
<i>Formula weight</i>	781.88
<i>Temperature</i>	8 K
<i>Wavelength</i>	0.71069 Å
<i>Crystal system</i>	Monoclinic
<i>Space group</i>	P 1 2 ₁ /c 1
<i>Unit cell dimensions</i>	$a = 15.6738(2)$ Å $\alpha = 90^\circ$ $b = 13.3899(2)$ Å $\beta = 92.7474(13)^\circ$ $c = 26.7423(4)$ Å $\gamma = 90^\circ$
<i>Volume</i>	5605.94(14) Å ³
<i>Z</i>	8
<i>Density (calculated)</i>	1.853 Mg/m ³
<i>Absorption coefficient</i>	0.877 mm ⁻¹
<i>F(000)</i>	3096
<i>Crystal size</i>	0.44 × 0.21 × 0.11 mm ³
<i>θ range for data collection</i>	2.992°–26.999°
<i>Index ranges</i>	−20 ≤ h ≤ 19, −16 ≤ k ≤ 17, −34 ≤ l ≤ 33
<i>Reflections collected</i>	51692
<i>Independent reflections</i>	12217, [R _{int} = 0.0347]
<i>Completeness to θ = 25.240°</i>	99.8%
<i>Absorption correction</i>	Semi-empirical from equivalents
<i>Max. and min. transmission</i>	1.00000, 0.93990
<i>Refinement method</i>	Full-matrix least-squares on F ²
<i>Data/restraints/parameters</i>	12217/24/828
<i>Goodness of fit on F²</i>	1.021
<i>Final R indices [I > 2σ(I)]</i>	R1 = 0.0265, wR2 = 0.0584
<i>R indices (all data)</i>	R1 = 0.0335, wR2 = 0.0616
<i>Extinction coefficient</i>	n/a
<i>Δρ_{max}, Δρ_{min}</i>	0.886 eÅ ⁻³ , −0.889 eÅ ⁻³

TABLE B-3: Experimental details on crystal data and structure refinement for MSI state of $[Ru(py)_4Cl(NO)](PF_6)_2 \cdot 1/2H_2O$ single crystal at 8 K.

**MSII/MSI mixed state of $[Ru(py)_4Cl(NO)](PF_6)_2 \cdot 1/2H_2O$ single crystal at 8 K
(first data collection)**

<i>Identification code</i>	runocl-hyd-MSII-MSI-8K-1
<i>Empirical formula</i>	<i>C</i> 20 <i>H</i> 21 <i>Cl</i> <i>F</i> 12 <i>N</i> 5 <i>O</i> 1.50 <i>P</i> 2 <i>Ru</i>
<i>Formula weight</i>	781.88
<i>Temperature</i>	8 K
<i>Wavelength</i>	0.71069 Å
<i>Crystal system</i>	Monoclinic
<i>Space group</i>	P 1 2 ₁ /c 1
<i>Unit cell dimensions</i>	a = 15.6498(2) Å $\alpha = 90^\circ$ b = 13.4329(2) Å $\beta = 92.1845(15)^\circ$ c = 26.7836(5) Å $\gamma = 90^\circ$
<i>Volume</i>	5626.40(16) Å ³
<i>Z</i>	8
<i>Density (calculated)</i>	1.846 Mg/m ³
<i>Absorption coefficient</i>	0.874 mm ⁻¹
<i>F(000)</i>	3096
<i>Crystal size</i>	0.44 × 0.21 × 0.11 mm ³
<i>θ range for data collection</i>	2.997°–27.000°
<i>Index ranges</i>	−19 ≤ <i>h</i> ≤ 19, −16 ≤ <i>k</i> ≤ 17, −34 ≤ <i>l</i> ≤ 33
<i>Reflections collected</i>	51604
<i>Independent reflections</i>	12262, [<i>R</i> _{int} = 0.0468]
<i>Completeness to $\theta = 25.240^\circ$</i>	99.8%
<i>Absorption correction</i>	Semi-empirical from equivalents
<i>Max. and min. transmission</i>	1.00000, 0.94376
<i>Refinement method</i>	Full-matrix least-squares on <i>F</i> ²
<i>Data/restraints/parameters</i>	12262/90/854
<i>Goodness of fit on <i>F</i>²</i>	1.029
<i>Final <i>R</i> indices [<i>I</i> > 2σ(<i>I</i>)]</i>	<i>R</i> 1 = 0.0368, <i>wR</i> 2 = 0.0816
<i><i>R</i> indices (all data)</i>	<i>R</i> 1 = 0.0454, <i>wR</i> 2 = 0.0870
<i>Extinction coefficient</i>	n/a
<i>Δρ_{max}, Δρ_{min}</i>	2.274 eÅ ⁻³ , −1.287 eÅ ⁻³

TABLE B-4: Experimental details on crystal data and structure refinement for MSII/MSI mixed state of $[Ru(py)_4Cl(NO)](PF_6)_2 \cdot 1/2H_2O$ single crystal at 8 K (first data collection).

MSII/MSI and MSII/GS mixed states of $[Ru(py)_4Cl(NO)](PF_6)_2 \cdot 1/2H_2O$ single crystal at 8 K (second data collection)

<i>Identification code</i>	runocl-hyd-MSIIMSI-MSIIGS-8K-2
<i>Empirical formula</i>	$C_{20} H_{21} Cl F_{12} N_5 O_{1.50} P_2 Ru$
<i>Formula weight</i>	781.88
<i>Temperature</i>	8 K
<i>Wavelength</i>	0.71069 Å
<i>Crystal system</i>	Monoclinic
<i>Space group</i>	P 1 2 ₁ /c 1
<i>Unit cell dimensions</i>	$a = 15.65792(18) \text{ \AA} \quad \alpha = 90^\circ$ $b = 13.43400(18) \text{ \AA} \quad \beta = 92.1158(11)^\circ$ $c = 26.8100(4) \text{ \AA} \quad \gamma = 90^\circ$
<i>Volume</i>	5635.59(13) Å ³
<i>Z</i>	8
<i>Density (calculated)</i>	1.843 Mg/m ³
<i>Absorption coefficient</i>	0.872 mm ⁻¹
<i>F(000)</i>	3096
<i>Crystal size</i>	0.44 × 0.21 × 0.11 mm ³
<i>θ range for data collection</i>	2.996°–27.000°
<i>Index ranges</i>	−20 ≤ h ≤ 19, −16 ≤ k ≤ 17, −34 ≤ l ≤ 34
<i>Reflections collected</i>	51985
<i>Independent reflections</i>	12283, [<i>R</i> _{int} = 0.0371]
<i>Completeness to θ = 25.240°</i>	99.8%
<i>Absorption correction</i>	Semi-empirical from equivalents
<i>Max. and min. transmission</i>	1.00000, 0.95540
<i>Refinement method</i>	Full-matrix least-squares on <i>F</i> ²
<i>Data/restraints/parameters</i>	12283/54/965
<i>Goodness of fit on <i>F</i>²</i>	1.029
<i>Final <i>R</i> indices [<i>I</i> > 2σ(<i>I</i>)]</i>	<i>R</i> 1 = 0.0324, <i>wR</i> 2 = 0.0701
<i><i>R</i> indices (all data)</i>	<i>R</i> 1 = 0.0400, <i>wR</i> 2 = 0.0743
<i>Extinction coefficient</i>	n/a
<i>Δρ_{max}, Δρ_{min}</i>	1.567 eÅ ⁻³ , −0.920 eÅ ⁻³

TABLE B-5: Experimental details on crystal data and structure refinement for MSII/MSI and MSII/GS mixed states of $[Ru(py)_4Cl(NO)](PF_6)_2 \cdot 1/2H_2O$ single crystal at 8 K (second data collection).

APPENDIX C: Experimental details of X-Ray data collections in dehydration studies presented in Chapter 2

Data was collected on the four-circle Oxford Diffraction Xcalibur 3 diffractometer (Mo K_{α} radiation) with a two-dimensional sapphire 3 CCD detector, on samples with typical sizes around $300 \times 200 \times 100 \mu\text{m}^3$. The single crystals were mounted in an Oxford Cryosystems nitrogen-flow cryostat (CryoJet 700) allowing a precise control of temperature. All the data was treated with CrysAlis software (CrysAlis RED, Oxford Diffraction Ltd, Version 1.171.38.41), the structures were previously solved with SIR97 [94] in WinGX environment and then refined with SHELXL97 [95] via OLEX2 GUI [96].

Dehydrated $[Ru(py)_4Cl(NO)](PF_6)_2 \cdot 1/2H_2O$ single crystal: GS state at 100 K

<i>Identification code</i>	runocl-dehyd-GS-100K
<i>Empirical formula</i>	$C_{20} H_{20} Cl F_{12} N_5 O P_2 Ru$
<i>Formula weight</i>	772.87
<i>Temperature</i>	100.15 K
<i>Wavelength</i>	0.71073 Å
<i>Crystal system</i>	Monoclinic
<i>Space group</i>	P 1 2 ₁ /c 1
<i>Unit cell dimensions</i>	$a = 15.6486(3)$ Å $\alpha = 90^\circ$ $b = 13.4525(2)$ Å $\beta = 92.265(2)^\circ$ $c = 26.8254(5)$ Å $\gamma = 90^\circ$
<i>Volume</i>	5642.68(17) Å ³
<i>Z</i>	8
<i>Density (calculated)</i>	1.820 Mg/m ³
<i>Absorption coefficient</i>	0.869 mm ⁻¹
<i>F(000)</i>	3056
<i>Crystal size</i>	0.256 × 0.198 × 0.09 mm ³
<i>θ range for data collection</i>	3.014°–27.000°
<i>Index ranges</i>	–19 ≤ h ≤ 19, –17 ≤ k ≤ 17, –34 ≤ l ≤ 33
<i>Reflections collected</i>	28830
<i>Independent reflections</i>	12298, [$R_{int} = 0.0580$]
<i>Completeness to $\theta = 25.242^\circ$</i>	99.8%
<i>Absorption correction</i>	Analytical
<i>Max. and min. transmission</i>	0.937, 0.867
<i>Refinement method</i>	Full-matrix least-squares on F^2
<i>Data/restraints/parameters</i>	12298/6/767
<i>Goodness of fit on F^2</i>	1.003
<i>Final R indices [$I > 2\sigma(I)$]</i>	$R1 = 0.0449$, $wR2 = 0.0689$
<i>R indices (all data)</i>	$R1 = 0.0785$, $wR2 = 0.0798$
<i>Extinction coefficient</i>	n/a
$\Delta\rho_{max}$, $\Delta\rho_{min}$	0.723 eÅ ⁻³ , –0.607 eÅ ⁻³

TABLE C-1: Experimental details on crystal data and structure refinement for GS state of dehydrated $[Ru(py)_4Cl(NO)](PF_6)_2 \cdot 1/2H_2O$ single crystal at 100 K.

Rehydrated $[Ru(py)_4Cl(NO)](PF_6)_2 \cdot 1/2H_2O$ single crystal: GS state at 100 K

<i>Identification code</i>	runocl-rehyd-GS-100K
<i>Empirical formula</i>	$C_{20} H_{21} Cl F_{12} N_5 O_{1.50} P_2 Ru$
<i>Formula weight</i>	781.88
<i>Temperature</i>	100.15 K
<i>Wavelength</i>	0.71073 Å
<i>Crystal system</i>	Monoclinic
<i>Space group</i>	P 1 2 ₁ /c 1
<i>Unit cell dimensions</i>	$a = 15.7473(3)$ Å $\alpha = 90^\circ$ $b = 13.4389(2)$ Å $\beta = 92.4287(16)^\circ$ $c = 26.8141(5)$ Å $\gamma = 90^\circ$
<i>Volume</i>	5669.48(17) Å ³
<i>Z</i>	8
<i>Density (calculated)</i>	1.832 Mg/m ³
<i>Absorption coefficient</i>	0.867 mm ⁻¹
<i>F(000)</i>	3096
<i>Crystal size</i>	0.28 × 0.232 × 0.09 mm ³
<i>θ range for data collection</i>	3.000°–27.000°
<i>Index ranges</i>	−20 ≤ h ≤ 19, −17 ≤ k ≤ 17, −34 ≤ l ≤ 33
<i>Reflections collected</i>	28934
<i>Independent reflections</i>	12355, [R _{int} = 0.0579]
<i>Completeness to θ = 25.242°</i>	99.8%
<i>Absorption correction</i>	Analytical
<i>Max. and min. transmission</i>	0.955, 0.876
<i>Refinement method</i>	Full-matrix least-squares on F ²
<i>Data/restraints/parameters</i>	12355/107/872
<i>Goodness of fit on F²</i>	0.994
<i>Final R indices [I > 2σ(I)]</i>	R1 = 0.0430, wR2 = 0.0565
<i>R indices (all data)</i>	R1 = 0.0780, wR2 = 0.0657
<i>Extinction coefficient</i>	n/a
<i>Δρ_{max}, Δρ_{min}</i>	0.461 eÅ ⁻³ , −0.586 eÅ ⁻³

TABLE C-2: Experimental details on crystal data and structure refinement for GS state of rehydrated $[Ru(py)_4Cl(NO)](PF_6)_2 \cdot 1/2H_2O$ single crystal at 100 K.

Dehydrated $[Ru(py)_4Cl(NO)](PF_6)_2 \cdot 1/2H_2O$ single crystal: MSI state at 100 K

<i>Identification code</i>	runocl-dehyd-MSI-100K
<i>Empirical formula</i>	$C_{20} H_{20} Cl F_{12} N_5 O P_2 Ru$
<i>Formula weight</i>	772.87
<i>Temperature</i>	100.15 K
<i>Wavelength</i>	0.71073 Å
<i>Crystal system</i>	Monoclinic
<i>Space group</i>	P 1 2 ₁ /c 1
<i>Unit cell dimensions</i>	$a = 15.6690(3)$ Å $\alpha = 90^\circ$ $b = 13.4439(2)$ Å $\beta = 92.292(2)^\circ$ $c = 26.8473(5)$ Å $\gamma = 90^\circ$
<i>Volume</i>	5650.93(17) Å ³
<i>Z</i>	8
<i>Density (calculated)</i>	1.817 Mg/m ³
<i>Absorption coefficient</i>	0.868 mm ⁻¹
<i>F(000)</i>	3056
<i>Crystal size</i>	0.256 × 0.198 × 0.09 mm ³
<i>θ range for data collection</i>	3.011°–27.000°
<i>Index ranges</i>	–20 ≤ h ≤ 19, –17 ≤ k ≤ 17, –34 ≤ l ≤ 33
<i>Reflections collected</i>	28787
<i>Independent reflections</i>	12307, [$R_{int} = 0.0586$]
<i>Completeness to $\theta = 25.242^\circ$</i>	99.8%
<i>Absorption correction</i>	Analytical
<i>Max. and min. transmission</i>	0.937, 0.867
<i>Refinement method</i>	Full-matrix least-squares on F^2
<i>Data/restraints/parameters</i>	12307/0/767
<i>Goodness of fit on F^2</i>	0.988
<i>Final R indices [$I > 2\sigma(I)$]</i>	$R1 = 0.0441$, $wR2 = 0.0655$
<i>R indices (all data)</i>	$R1 = 0.0786$, $wR2 = 0.0762$
<i>Extinction coefficient</i>	n/a
$\Delta\rho_{max}$, $\Delta\rho_{min}$	0.537 eÅ ⁻³ , –0.600 eÅ ⁻³

TABLE C-3: Experimental details on crystal data and structure refinement for MSI state of dehydrated $[Ru(py)_4Cl(NO)](PF_6)_2 \cdot 1/2H_2O$ single crystal at 100 K.

Rehydrated $[Ru(py)_4Cl(NO)](PF_6)_2 \cdot 1/2H_2O$ single crystal: MSI state at 100 K

<i>Identification code</i>	runocl-rehyd-MSI-100K
<i>Empirical formula</i>	$C_{20} H_{21} Cl F_{12} N_5 O_{1.50} P_2 Ru$
<i>Formula weight</i>	781.88
<i>Temperature</i>	100.15 K
<i>Wavelength</i>	0.71073 Å
<i>Crystal system</i>	Monoclinic
<i>Space group</i>	P 1 2 ₁ /c 1
<i>Unit cell dimensions</i>	$a = 15.7696(3)$ Å $\alpha = 90^\circ$ $b = 13.4309(2)$ Å $\beta = 92.5143(16)^\circ$ $c = 26.8230(5)$ Å $\gamma = 90^\circ$
<i>Volume</i>	5675.60(17) Å ³
<i>Z</i>	8
<i>Density (calculated)</i>	1.830 Mg/m ³
<i>Absorption coefficient</i>	0.866 mm ⁻¹
<i>F(000)</i>	3096
<i>Crystal size</i>	0.28 × 0.232 × 0.09 mm ³
<i>θ range for data collection</i>	2.998°–27.000°
<i>Index ranges</i>	−20 ≤ h ≤ 19, −17 ≤ k ≤ 17, −34 ≤ l ≤ 33
<i>Reflections collected</i>	28962
<i>Independent reflections</i>	12373, [R _{int} = 0.0621]
<i>Completeness to θ = 25.242°</i>	99.8%
<i>Absorption correction</i>	Analytical
<i>Max. and min. transmission</i>	0.955, 0.876
<i>Refinement method</i>	Full-matrix least-squares on F ²
<i>Data/restraints/parameters</i>	12373/93/866
<i>Goodness of fit on F²</i>	0.999
<i>Final R indices [I > 2σ(I)]</i>	R1 = 0.0467, wR2 = 0.0623
<i>R indices (all data)</i>	R1 = 0.0818, wR2 = 0.0724
<i>Extinction coefficient</i>	n/a
<i>Δρ_{max}, Δρ_{min}</i>	0.589 eÅ ⁻³ , −1.300 eÅ ⁻³

TABLE C-4: Experimental details on crystal data and structure refinement for MSI state of rehydrated $[Ru(py)_4Cl(NO)](PF_6)_2 \cdot 1/2H_2O$ single crystal at 100 K.

**Dehydrated $[Ru(py)_4Cl(NO)](PF_6)_2 \cdot 1/2H_2O$ single crystal:
MSII/GS mixed state at 100 K**

<i>Identification code</i>	runocl-dehyd-MSII-GS-100K
<i>Empirical formula</i>	$C_{20} H_{20} Cl F_{12} N_5 O_2 Ru$
<i>Formula weight</i>	772.87
<i>Temperature</i>	100.15 K
<i>Wavelength</i>	0.71073 Å
<i>Crystal system</i>	Monoclinic
<i>Space group</i>	P 1 2 ₁ /c 1
<i>Unit cell dimensions</i>	$a = 15.6730(3) \text{ \AA}$ $\alpha = 90^\circ$ $b = 13.4364(2) \text{ \AA}$ $\beta = 92.019(2)^\circ$ $c = 26.8823(6) \text{ \AA}$ $\gamma = 90^\circ$
<i>Volume</i>	5657.59(19) Å ³
<i>Z</i>	8
<i>Density (calculated)</i>	1.815 Mg/m ³
<i>Absorption coefficient</i>	0.867 mm ⁻¹
<i>F(000)</i>	3056
<i>Crystal size</i>	0.256 × 0.198 × 0.09 mm ³
<i>θ range for data collection</i>	3.011°–27.000°
<i>Index ranges</i>	−20 ≤ h ≤ 19, −17 ≤ k ≤ 17, −34 ≤ l ≤ 33
<i>Reflections collected</i>	28920
<i>Independent reflections</i>	12333, [R _{int} = 0.0620]
<i>Completeness to θ = 25.242°</i>	99.8%
<i>Absorption correction</i>	Analytical
<i>Max. and min. transmission</i>	0.937, 0.867
<i>Refinement method</i>	Full-matrix least-squares on F ²
<i>Data/restraints/parameters</i>	12333/45/822
<i>Goodness of fit on F²</i>	1.006
<i>Final R indices [I > 2σ(I)]</i>	R1 = 0.0484, wR2 = 0.0770
<i>R indices (all data)</i>	R1 = 0.0854, wR2 = 0.0895
<i>Extinction coefficient</i>	n/a
<i>Δρ_{max}, Δρ_{min}</i>	1.317 eÅ ⁻³ , −0.809 eÅ ⁻³

TABLE C-5: Experimental details on crystal data and structure refinement for MSII/GS mixed state of dehydrated $[Ru(py)_4Cl(NO)](PF_6)_2 \cdot 1/2H_2O$ single crystal at 100 K.

**Dehydrated $[Ru(py)_4Cl(NO)](PF_6)_2 \cdot 1/2H_2O$ single crystal:
evolution of MSII/GS mixed state at 100 K (data collection 1/6)**

<i>Identification code</i>	runocl-dehyd-MSII-GS-100K-1
<i>Empirical formula</i>	<i>C</i> 20 <i>H</i> 20 <i>Cl</i> <i>F</i> 12 <i>N</i> 5 <i>O</i> <i>P</i> 2 <i>Ru</i>
<i>Formula weight</i>	772.87
<i>Temperature</i>	100.15 K
<i>Wavelength</i>	0.71073 Å
<i>Crystal system</i>	Monoclinic
<i>Space group</i>	P 1 2 ₁ /c 1
<i>Unit cell dimensions</i>	a = 15.6650(3) Å $\alpha = 90^\circ$ b = 13.4340(3) Å $\beta = 92.009(2)^\circ$ c = 26.9024(6) Å $\gamma = 90^\circ$
<i>Volume</i>	5658.0(2) Å ³
<i>Z</i>	8
<i>Density (calculated)</i>	1.815 Mg/m ³
<i>Absorption coefficient</i>	0.867 mm ⁻¹
<i>F(000)</i>	3056
<i>Crystal size</i>	0.256 × 0.198 × 0.09 mm ³
<i>θ range for data collection</i>	3.012°–27.000°
<i>Index ranges</i>	−20 ≤ <i>h</i> ≤ 19, −17 ≤ <i>k</i> ≤ 17, −34 ≤ <i>l</i> ≤ 33
<i>Reflections collected</i>	28848
<i>Independent reflections</i>	12335, [<i>R</i> _{int} = 0.0646]
<i>Completeness to θ = 25.242°</i>	99.8%
<i>Absorption correction</i>	Analytical
<i>Max. and min. transmission</i>	0.942, 0.877
<i>Refinement method</i>	Full-matrix least-squares on <i>F</i> ²
<i>Data/restraints/parameters</i>	12335/88/801
<i>Goodness of fit on <i>F</i>²</i>	1.005
<i>Final <i>R</i> indices [<i>I</i> > 2σ(<i>I</i>)]</i>	<i>R</i> 1 = 0.0478, <i>wR</i> 2 = 0.0720
<i><i>R</i> indices (all data)</i>	<i>R</i> 1 = 0.0856, <i>wR</i> 2 = 0.0847
<i>Extinction coefficient</i>	n/a
<i>Δρ_{max}, Δρ_{min}</i>	1.098 eÅ ⁻³ , −0.767 eÅ ⁻³

TABLE C-6: Experimental details on crystal data and structure refinement for MSII/GS mixed state evolution of dehydrated $[Ru(py)_4Cl(NO)](PF_6)_2 \cdot 1/2H_2O$ single crystal at 100 K (data collection №1 out of total 6).

**Dehydrated $[Ru(py)_4Cl(NO)](PF_6)_2 \cdot 1/2H_2O$ single crystal:
evolution of MSII/GS mixed state at 100 K (data collection 2/6)**

<i>Identification code</i>	runocl-dehyd-MSII-GS-100K-2
<i>Empirical formula</i>	$C_{20} H_{20} Cl F_{12} N_5 O P_2 Ru$
<i>Formula weight</i>	772.87
<i>Temperature</i>	100.15 K
<i>Wavelength</i>	0.71073 Å
<i>Crystal system</i>	Monoclinic
<i>Space group</i>	P 1 2 ₁ /c 1
<i>Unit cell dimensions</i>	$a = 15.6654(3)$ Å $\alpha = 90^\circ$ $b = 13.4337(2)$ Å $\beta = 91.987(2)^\circ$ $c = 26.9119(5)$ Å $\gamma = 90^\circ$
<i>Volume</i>	5660.05(17) Å ³
<i>Z</i>	8
<i>Density (calculated)</i>	1.814 Mg/m ³
<i>Absorption coefficient</i>	0.866 mm ⁻¹
<i>F(000)</i>	3056
<i>Crystal size</i>	0.274 × 0.204 × 0.092 mm ³
<i>θ range for data collection</i>	3.012°–27.000°
<i>Index ranges</i>	−20 ≤ h ≤ 19, −17 ≤ k ≤ 17, −34 ≤ l ≤ 33
<i>Reflections collected</i>	28906
<i>Independent reflections</i>	12340, [R _{int} = 0.0602]
<i>Completeness to θ = 25.242°</i>	99.8%
<i>Absorption correction</i>	Analytical
<i>Max. and min. transmission</i>	0.941, 0.868
<i>Refinement method</i>	Full-matrix least-squares on F ²
<i>Data/restraints/parameters</i>	12340/68/813
<i>Goodness of fit on F²</i>	1.012
<i>Final R indices [I > 2σ(I)]</i>	R1 = 0.0471, wR2 = 0.0711
<i>R indices (all data)</i>	R1 = 0.0844, wR2 = 0.0832
<i>Extinction coefficient</i>	n/a
<i>Δρ_{max}, Δρ_{min}</i>	0.828 eÅ ⁻³ , −0.813 eÅ ⁻³

TABLE C-7: Experimental details on crystal data and structure refinement for MSII/GS mixed state evolution of dehydrated $[Ru(py)_4Cl(NO)](PF_6)_2 \cdot 1/2H_2O$ single crystal at 100 K (data collection №2 out of total 6).

**Dehydrated $[Ru(py)_4Cl(NO)](PF_6)_2 \cdot 1/2H_2O$ single crystal:
evolution of MSII/GS mixed state at 100 K (data collection 3/6)**

<i>Identification code</i>	runocl-dehyd-MSII-GS-100K-3
<i>Empirical formula</i>	$C_{20} H_{20} Cl F_{12} N_5 O P_2 Ru$
<i>Formula weight</i>	772.87
<i>Temperature</i>	100.15 K
<i>Wavelength</i>	0.71073 Å
<i>Crystal system</i>	Monoclinic
<i>Space group</i>	P 1 2 ₁ /c 1
<i>Unit cell dimensions</i>	$a = 15.6635(3) \text{ \AA}$ $\alpha = 90^\circ$ $b = 13.4341(2) \text{ \AA}$ $\beta = 92.0001(18)^\circ$ $c = 26.9085(6) \text{ \AA}$ $\gamma = 90^\circ$
<i>Volume</i>	5658.73(19) Å ³
<i>Z</i>	8
<i>Density (calculated)</i>	1.814 Mg/m ³
<i>Absorption coefficient</i>	0.866 mm ⁻¹
<i>F(000)</i>	3056
<i>Crystal size</i>	0.274 × 0.204 × 0.092 mm ³
<i>θ range for data collection</i>	3.012°–27.000°
<i>Index ranges</i>	−20 ≤ h ≤ 19, −17 ≤ k ≤ 17, −34 ≤ l ≤ 33
<i>Reflections collected</i>	28895
<i>Independent reflections</i>	12335, [R _{int} = 0.0611]
<i>Completeness to θ = 25.242°</i>	99.8%
<i>Absorption correction</i>	Analytical
<i>Max. and min. transmission</i>	0.941, 0.868
<i>Refinement method</i>	Full-matrix least-squares on F ²
<i>Data/restraints/parameters</i>	12335/29/813
<i>Goodness of fit on F²</i>	1.010
<i>Final R indices [I > 2σ(I)]</i>	R1 = 0.0462, wR2 = 0.0669
<i>R indices (all data)</i>	R1 = 0.0849, wR2 = 0.0787
<i>Extinction coefficient</i>	n/a
<i>Δρ_{max}, Δρ_{min}</i>	0.779 eÅ ⁻³ , −0.695 eÅ ⁻³

TABLE C-8: Experimental details on crystal data and structure refinement for MSII/GS mixed state evolution of dehydrated $[Ru(py)_4Cl(NO)](PF_6)_2 \cdot 1/2H_2O$ single crystal at 100 K (data collection №3 out of total 6).

**Dehydrated $[Ru(py)_4Cl(NO)](PF_6)_2 \cdot 1/2H_2O$ single crystal:
evolution of MSII/GS mixed state at 100 K (data collection 4/6)**

<i>Identification code</i>	runocl-dehyd-MSII-GS-100K-4
<i>Empirical formula</i>	$C_{20} H_{20} Cl F_{12} N_5 O P_2 Ru$
<i>Formula weight</i>	772.87
<i>Temperature</i>	100.15 K
<i>Wavelength</i>	0.71073 Å
<i>Crystal system</i>	Monoclinic
<i>Space group</i>	P 1 2 ₁ /c 1
<i>Unit cell dimensions</i>	$a = 15.6636(3) \text{ \AA}$ $\alpha = 90^\circ$ $b = 13.4351(2) \text{ \AA}$ $\beta = 92.0110(18)^\circ$ $c = 26.9047(5) \text{ \AA}$ $\gamma = 90^\circ$
<i>Volume</i>	5658.40(18) Å ³
<i>Z</i>	8
<i>Density (calculated)</i>	1.814 Mg/m ³
<i>Absorption coefficient</i>	0.867 mm ⁻¹
<i>F(000)</i>	3056
<i>Crystal size</i>	0.274 × 0.204 × 0.092 mm ³
<i>θ range for data collection</i>	3.012°–27.000°
<i>Index ranges</i>	−20 ≤ h ≤ 19, −17 ≤ k ≤ 17, −34 ≤ l ≤ 33
<i>Reflections collected</i>	28868
<i>Independent reflections</i>	12335, [R _{int} = 0.0603]
<i>Completeness to θ = 25.242°</i>	99.8%
<i>Absorption correction</i>	Analytical
<i>Max. and min. transmission</i>	0.941, 0.868
<i>Refinement method</i>	Full-matrix least-squares on F ²
<i>Data/restraints/parameters</i>	12335/35/822
<i>Goodness of fit on F²</i>	0.998
<i>Final R indices [I > 2σ(I)]</i>	R1 = 0.0462, wR2 = 0.0699
<i>R indices (all data)</i>	R1 = 0.0834, wR2 = 0.0818
<i>Extinction coefficient</i>	n/a
<i>Δρ_{max}, Δρ_{min}</i>	0.697 eÅ ⁻³ , −0.585 eÅ ⁻³

TABLE C-9: Experimental details on crystal data and structure refinement for MSII/GS mixed state evolution of dehydrated $[Ru(py)_4Cl(NO)](PF_6)_2 \cdot 1/2H_2O$ single crystal at 100 K (data collection №4 out of total 6).

**Dehydrated $[Ru(py)_4Cl(NO)](PF_6)_2 \cdot 1/2H_2O$ single crystal:
evolution of MSII/GS mixed state at 100 K (data collection 5/6)**

<i>Identification code</i>	runocl-dehyd-MSII-GS-100K-5
<i>Empirical formula</i>	$C_{20} H_{20} Cl F_{12} N_5 O P_2 Ru$
<i>Formula weight</i>	772.87
<i>Temperature</i>	100.15 K
<i>Wavelength</i>	0.71073 Å
<i>Crystal system</i>	Monoclinic
<i>Space group</i>	P 1 2 ₁ /c 1
<i>Unit cell dimensions</i>	$a = 15.6633(3) \text{ \AA}$ $\alpha = 90^\circ$ $b = 13.4370(2) \text{ \AA}$ $\beta = 92.052(2)^\circ$ $c = 26.8972(5) \text{ \AA}$ $\gamma = 90^\circ$
<i>Volume</i>	5657.36(17) Å ³
<i>Z</i>	8
<i>Density (calculated)</i>	1.815 Mg/m ³
<i>Absorption coefficient</i>	0.867 mm ⁻¹
<i>F(000)</i>	3056
<i>Crystal size</i>	0.274 × 0.204 × 0.092 mm ³
<i>θ range for data collection</i>	3.012°–27.000°
<i>Index ranges</i>	−20 ≤ h ≤ 19, −17 ≤ k ≤ 17, −34 ≤ l ≤ 33
<i>Reflections collected</i>	28893
<i>Independent reflections</i>	12332, [R _{int} = 0.0610]
<i>Completeness to θ = 25.242°</i>	99.8%
<i>Absorption correction</i>	Analytical
<i>Max. and min. transmission</i>	0.941, 0.868
<i>Refinement method</i>	Full-matrix least-squares on F ²
<i>Data/restraints/parameters</i>	12332/60/810
<i>Goodness of fit on F²</i>	1.003
<i>Final R indices [I > 2σ(I)]</i>	R1 = 0.0469, wR2 = 0.0736
<i>R indices (all data)</i>	R1 = 0.0836, wR2 = 0.0858
<i>Extinction coefficient</i>	n/a
<i>Δρ_{max}, Δρ_{min}</i>	0.656 eÅ ⁻³ , −0.704 eÅ ⁻³

TABLE C-10: Experimental details on crystal data and structure refinement for MSII/GS mixed state evolution of dehydrated $[Ru(py)_4Cl(NO)](PF_6)_2 \cdot 1/2H_2O$ single crystal at 100 K (data collection №5 out of total 6).

**Dehydrated $[Ru(py)_4Cl(NO)](PF_6)_2 \cdot 1/2H_2O$ single crystal:
evolution of MSII/GS mixed state at 100 K (data collection 6/6)**

<i>Identification code</i>	runocl-dehyd-MSII-GS-100K-6
<i>Empirical formula</i>	$C_{20} H_{20} Cl F_{12} N_5 O P_2 Ru$
<i>Formula weight</i>	772.87
<i>Temperature</i>	100.15 K
<i>Wavelength</i>	0.71073 Å
<i>Crystal system</i>	Monoclinic
<i>Space group</i>	P 1 2 ₁ /c 1
<i>Unit cell dimensions</i>	$a = 15.6624(3)$ Å $\alpha = 90^\circ$ $b = 13.4396(3)$ Å $\beta = 92.0882(19)^\circ$ $c = 26.8831(6)$ Å $\gamma = 90^\circ$
<i>Volume</i>	5655.1(2) Å ³
<i>Z</i>	8
<i>Density (calculated)</i>	1.816 Mg/m ³
<i>Absorption coefficient</i>	0.867 mm ⁻¹
<i>F(000)</i>	3056
<i>Crystal size</i>	0.274 × 0.204 × 0.092 mm ³
<i>θ range for data collection</i>	3.012°–27.000°
<i>Index ranges</i>	$-20 \leq h \leq 19$, $-17 \leq k \leq 17$, $-34 \leq l \leq 33$
<i>Reflections collected</i>	28840
<i>Independent reflections</i>	12327, [$R_{int} = 0.0611$]
<i>Completeness to $\theta = 25.242^\circ$</i>	99.8%
<i>Absorption correction</i>	Analytical
<i>Max. and min. transmission</i>	0.941, 0.868
<i>Refinement method</i>	Full-matrix least-squares on F^2
<i>Data/restraints/parameters</i>	12327/57/822
<i>Goodness of fit on F^2</i>	1.001
<i>Final R indices [$I > 2\sigma(I)$]</i>	$R1 = 0.0462$, $wR2 = 0.0669$
<i>R indices (all data)</i>	$R1 = 0.0834$, $wR2 = 0.0782$
<i>Extinction coefficient</i>	n/a
$\Delta\rho_{max}$, $\Delta\rho_{min}$	0.804 eÅ ⁻³ , -0.576 eÅ ⁻³

TABLE C-11: Experimental details on crystal data and structure refinement for MSII/GS mixed state evolution of dehydrated $[Ru(py)_4Cl(NO)](PF_6)_2 \cdot 1/2H_2O$ single crystal at 100 K (data collection №6 out of total 6).

**Rehydrated $[Ru(py)_4Cl(NO)](PF_6)_2 \cdot 1/2H_2O$ single crystal:
evolution of MSII/GS mixed state at 100 K (data collection 1/6)**

<i>Identification code</i>	runocl-rehyd-MSII-GS-100K-1
<i>Empirical formula</i>	<i>C</i> 20 <i>H</i> 21 <i>Cl</i> <i>F</i> 12 <i>N</i> 5 <i>O</i> 1.50 <i>P</i> 2 <i>Ru</i>
<i>Formula weight</i>	781.88
<i>Temperature</i>	100.15 K
<i>Wavelength</i>	0.71073 Å
<i>Crystal system</i>	Monoclinic
<i>Space group</i>	P 1 2 ₁ /c 1
<i>Unit cell dimensions</i>	a = 15.7721(3) Å $\alpha = 90^\circ$ b = 13.4506(2) Å $\beta = 92.0993(17)^\circ$ c = 26.8351(5) Å $\gamma = 90^\circ$
<i>Volume</i>	5689.08(18) Å ³
<i>Z</i>	8
<i>Density (calculated)</i>	1.826 Mg/m ³
<i>Absorption coefficient</i>	0.864 mm ⁻¹
<i>F(000)</i>	3096
<i>Crystal size</i>	0.28 × 0.232 × 0.09 mm ³
<i>θ range for data collection</i>	2.996°–27.000°
<i>Index ranges</i>	−20 ≤ <i>h</i> ≤ 19, −17 ≤ <i>k</i> ≤ 17, −34 ≤ <i>l</i> ≤ 33
<i>Reflections collected</i>	29027
<i>Independent reflections</i>	12409, [<i>R</i> _{int} = 0.0606]
<i>Completeness to θ = 25.242°</i>	99.8%
<i>Absorption correction</i>	Analytical
<i>Max. and min. transmission</i>	0.955, 0.876
<i>Refinement method</i>	Full-matrix least-squares on <i>F</i> ²
<i>Data/restraints/parameters</i>	12409/232/922
<i>Goodness of fit on <i>F</i>²</i>	1.007
<i>Final <i>R</i> indices [<i>I</i> > 2σ(<i>I</i>)]</i>	<i>R</i> 1 = 0.0462, <i>wR</i> 2 = 0.0607
<i><i>R</i> indices (all data)</i>	<i>R</i> 1 = 0.0840, <i>wR</i> 2 = 0.0710
<i>Extinction coefficient</i>	n/a
<i>Δρ_{max}, Δρ_{min}</i>	0.628 eÅ ⁻³ , −0.545 eÅ ⁻³

TABLE C-12: Experimental details on crystal data and structure refinement for MSII/GS mixed state evolution of rehydrated $[Ru(py)_4Cl(NO)](PF_6)_2 \cdot 1/2H_2O$ single crystal at 100 K (data collection №1 out of total 6).

**Rehydrated $[Ru(py)_4Cl(NO)](PF_6)_2 \cdot 1/2H_2O$ single crystal:
evolution of MSII/GS mixed state at 100 K (data collection 2/6)**

<i>Identification code</i>	runocl-rehyd-MSII-GS-100K-2
<i>Empirical formula</i>	$C_{20} H_{21} Cl F_{12} N_5 O_{1.50} P_2 Ru$
<i>Formula weight</i>	781.88
<i>Temperature</i>	100.15 K
<i>Wavelength</i>	0.71073 Å
<i>Crystal system</i>	Monoclinic
<i>Space group</i>	P 1 2 ₁ /c 1
<i>Unit cell dimensions</i>	$a = 15.7684(3)$ Å $\alpha = 90^\circ$ $b = 13.4474(2)$ Å $\beta = 92.1407(16)^\circ$ $c = 26.8326(5)$ Å $\gamma = 90^\circ$
<i>Volume</i>	5685.73(17) Å ³
<i>Z</i>	8
<i>Density (calculated)</i>	1.827 Mg/m ³
<i>Absorption coefficient</i>	0.865 mm ⁻¹
<i>F(000)</i>	3096
<i>Crystal size</i>	0.28 × 0.232 × 0.09 mm ³
<i>θ range for data collection</i>	2.997°–27.000°
<i>Index ranges</i>	−20 ≤ h ≤ 19, −17 ≤ k ≤ 17, −34 ≤ l ≤ 33
<i>Reflections collected</i>	28994
<i>Independent reflections</i>	12396, [$R_{int} = 0.0612$]
<i>Completeness to θ = 25.242°</i>	99.8%
<i>Absorption correction</i>	Analytical
<i>Max. and min. transmission</i>	0.955, 0.876
<i>Refinement method</i>	Full-matrix least-squares on F^2
<i>Data/restraints/parameters</i>	12396/223/922
<i>Goodness of fit on F^2</i>	1.010
<i>Final R indices [$I > 2\sigma(I)$]</i>	$R1 = 0.0461$, $wR2 = 0.0556$
<i>R indices (all data)</i>	$R1 = 0.0831$, $wR2 = 0.0652$
<i>Extinction coefficient</i>	n/a
$\Delta\rho_{max}$, $\Delta\rho_{min}$	0.689 eÅ ⁻³ , −0.533 eÅ ⁻³

TABLE C-13: Experimental details on crystal data and structure refinement for MSII/GS mixed state evolution of rehydrated $[Ru(py)_4Cl(NO)](PF_6)_2 \cdot 1/2H_2O$ single crystal at 100 K (data collection №2 out of total 6).

**Rehydrated $[Ru(py)_4Cl(NO)](PF_6)_2 \cdot 1/2H_2O$ single crystal:
evolution of MSII/GS mixed state at 100 K (data collection 3/6)**

<i>Identification code</i>	runocl-rehyd-MSII-GS-100K-3
<i>Empirical formula</i>	$C_{20} H_{21} Cl F_{12} N_5 O_{1.50} P_2 Ru$
<i>Formula weight</i>	781.88
<i>Temperature</i>	100.15 K
<i>Wavelength</i>	0.71073 Å
<i>Crystal system</i>	Monoclinic
<i>Space group</i>	P 1 2 ₁ /c 1
<i>Unit cell dimensions</i>	$a = 15.7660(3) \text{ \AA}$ $\alpha = 90^\circ$ $b = 13.4458(2) \text{ \AA}$ $\beta = 92.1884(17)^\circ$ $c = 26.8323(5) \text{ \AA}$ $\gamma = 90^\circ$
<i>Volume</i>	5683.92(17) Å ³
<i>Z</i>	8
<i>Density (calculated)</i>	1.827 Mg/m ³
<i>Absorption coefficient</i>	0.865 mm ⁻¹
<i>F(000)</i>	3096
<i>Crystal size</i>	0.28 × 0.232 × 0.09 mm ³
<i>θ range for data collection</i>	2.997°–27.000°
<i>Index ranges</i>	−20 ≤ h ≤ 19, −17 ≤ k ≤ 17, −34 ≤ l ≤ 33
<i>Reflections collected</i>	29016
<i>Independent reflections</i>	12389, [R _{int} = 0.0614]
<i>Completeness to θ = 25.242°</i>	99.8%
<i>Absorption correction</i>	Analytical
<i>Max. and min. transmission</i>	0.955, 0.876
<i>Refinement method</i>	Full-matrix least-squares on F ²
<i>Data/restraints/parameters</i>	12389/171/922
<i>Goodness of fit on F²</i>	1.000
<i>Final R indices [I > 2σ(I)]</i>	R1 = 0.0455, wR2 = 0.0628
<i>R indices (all data)</i>	R1 = 0.0826, wR2 = 0.0734
<i>Extinction coefficient</i>	n/a
<i>Δρ_{max}, Δρ_{min}</i>	0.572 eÅ ⁻³ , −0.576 eÅ ⁻³

TABLE C-14: Experimental details on crystal data and structure refinement for MSII/GS mixed state evolution of rehydrated $[Ru(py)_4Cl(NO)](PF_6)_2 \cdot 1/2H_2O$ single crystal at 100 K (data collection №3 out of total 6).

**Rehydrated $[Ru(py)_4Cl(NO)](PF_6)_2 \cdot 1/2H_2O$ single crystal:
evolution of MSII/GS mixed state at 100 K (data collection 4/6)**

<i>Identification code</i>	runocl-rehyd-MSII-GS-100K-4
<i>Empirical formula</i>	$C_{20} H_{21} Cl F_{12} N_5 O_{1.50} P_2 Ru$
<i>Formula weight</i>	781.88
<i>Temperature</i>	100.15 K
<i>Wavelength</i>	0.71073 Å
<i>Crystal system</i>	Monoclinic
<i>Space group</i>	P 1 2 ₁ /c 1
<i>Unit cell dimensions</i>	$a = 15.7629(3)$ Å $\alpha = 90^\circ$ $b = 13.4434(2)$ Å $\beta = 92.2343(16)^\circ$ $c = 26.8317(5)$ Å $\gamma = 90^\circ$
<i>Volume</i>	5681.50(17) Å ³
<i>Z</i>	8
<i>Density (calculated)</i>	1.828 Mg/m ³
<i>Absorption coefficient</i>	0.865 mm ⁻¹
<i>F(000)</i>	3096
<i>Crystal size</i>	0.28 × 0.232 × 0.09 mm ³
<i>θ range for data collection</i>	2.998°–27.000°
<i>Index ranges</i>	−20 ≤ h ≤ 19, −17 ≤ k ≤ 17, −34 ≤ l ≤ 33
<i>Reflections collected</i>	28998
<i>Independent reflections</i>	12381, [R _{int} = 0.0604]
<i>Completeness to θ = 25.242°</i>	99.8%
<i>Absorption correction</i>	Analytical
<i>Max. and min. transmission</i>	0.955, 0.876
<i>Refinement method</i>	Full-matrix least-squares on F ²
<i>Data/restraints/parameters</i>	12381/169/922
<i>Goodness of fit on F²</i>	1.002
<i>Final R indices [I > 2σ(I)]</i>	R1 = 0.0457, wR2 = 0.0567
<i>R indices (all data)</i>	R1 = 0.0816, wR2 = 0.0656
<i>Extinction coefficient</i>	n/a
<i>Δρ_{max}, Δρ_{min}</i>	0.548 eÅ ⁻³ , −0.537 eÅ ⁻³

TABLE C-15: Experimental details on crystal data and structure refinement for MSII/GS mixed state evolution of rehydrated $[Ru(py)_4Cl(NO)](PF_6)_2 \cdot 1/2H_2O$ single crystal at 100 K (data collection №4 out of total 6).

**Rehydrated $[Ru(py)_4Cl(NO)](PF_6)_2 \cdot 1/2H_2O$ single crystal:
evolution of MSII/GS mixed state at 100 K (data collection 5/6)**

<i>Identification code</i>	runocl-rehyd-MSII-GS-100K-5
<i>Empirical formula</i>	$C_{20} H_{21} Cl F_{12} N_5 O_{1.50} P_2 Ru$
<i>Formula weight</i>	781.88
<i>Temperature</i>	100.15 K
<i>Wavelength</i>	0.71073 Å
<i>Crystal system</i>	Monoclinic
<i>Space group</i>	P 1 2 ₁ /c 1
<i>Unit cell dimensions</i>	$a = 15.7602(3) \text{ \AA}$ $\alpha = 90^\circ$ $b = 13.4417(2) \text{ \AA}$ $\beta = 92.2521(16)^\circ$ $c = 26.8296(5) \text{ \AA}$ $\gamma = 90^\circ$
<i>Volume</i>	5679.30(17) Å ³
<i>Z</i>	8
<i>Density (calculated)</i>	1.829 Mg/m ³
<i>Absorption coefficient</i>	0.866 mm ⁻¹
<i>F(000)</i>	3096
<i>Crystal size</i>	0.28 × 0.232 × 0.09 mm ³
<i>θ range for data collection</i>	2.998°–27.000°
<i>Index ranges</i>	−20 ≤ h ≤ 19, −17 ≤ k ≤ 17, −34 ≤ l ≤ 33
<i>Reflections collected</i>	28969
<i>Independent reflections</i>	12379, [R _{int} = 0.0603]
<i>Completeness to θ = 25.242°</i>	99.8%
<i>Absorption correction</i>	Analytical
<i>Max. and min. transmission</i>	0.955, 0.876
<i>Refinement method</i>	Full-matrix least-squares on F ²
<i>Data/restraints/parameters</i>	12379/249/922
<i>Goodness of fit on F²</i>	0.999
<i>Final R indices [I > 2σ(I)]</i>	R1 = 0.0456, wR2 = 0.0648
<i>R indices (all data)</i>	R1 = 0.0817, wR2 = 0.0754
<i>Extinction coefficient</i>	n/a
<i>Δρ_{max}, Δρ_{min}</i>	0.558 eÅ ⁻³ , −0.570 eÅ ⁻³

TABLE C-16: Experimental details on crystal data and structure refinement for MSII/GS mixed state evolution of rehydrated $[Ru(py)_4Cl(NO)](PF_6)_2 \cdot 1/2H_2O$ single crystal at 100 K (data collection №5 out of total 6).

**Rehydrated $[Ru(py)_4Cl(NO)](PF_6)_2 \cdot 1/2H_2O$ single crystal:
evolution of MSII/GS mixed state at 100 K (data collection 6/6)**

<i>Identification code</i>	runocl-rehyd-MSII-GS-100K-6
<i>Empirical formula</i>	$C_{20} H_{21} Cl F_{12} N_5 O_{1.50} P_2 Ru$
<i>Formula weight</i>	781.88
<i>Temperature</i>	100.15 K
<i>Wavelength</i>	0.71073 Å
<i>Crystal system</i>	Monoclinic
<i>Space group</i>	P 1 2 ₁ /c 1
<i>Unit cell dimensions</i>	$a = 15.7596(3)$ Å $\alpha = 90^\circ$ $b = 13.4411(2)$ Å $\beta = 92.2886(17)^\circ$ $c = 26.8322(5)$ Å $\gamma = 90^\circ$
<i>Volume</i>	5679.21(18) Å ³
<i>Z</i>	8
<i>Density (calculated)</i>	1.829 Mg/m ³
<i>Absorption coefficient</i>	0.866 mm ⁻¹
<i>F(000)</i>	3096
<i>Crystal size</i>	0.28 × 0.232 × 0.09 mm ³
<i>θ range for data collection</i>	2.998°–26.998°
<i>Index ranges</i>	−20 ≤ h ≤ 19, −17 ≤ k ≤ 17, −34 ≤ l ≤ 33
<i>Reflections collected</i>	28973
<i>Independent reflections</i>	12376, [$R_{int} = 0.0606$]
<i>Completeness to $\theta = 25.242^\circ$</i>	99.8%
<i>Absorption correction</i>	Analytical
<i>Max. and min. transmission</i>	0.955, 0.876
<i>Refinement method</i>	Full-matrix least-squares on F^2
<i>Data/restraints/parameters</i>	12376/255/922
<i>Goodness of fit on F^2</i>	1.010
<i>Final R indices [$I > 2\sigma(I)$]</i>	$R1 = 0.0452$, $wR2 = 0.0559$
<i>R indices (all data)</i>	$R1 = 0.0818$, $wR2 = 0.0657$
<i>Extinction coefficient</i>	n/a
$\Delta\rho_{max}$, $\Delta\rho_{min}$	0.575 eÅ ⁻³ , −0.573 eÅ ⁻³

TABLE C-17: Experimental details on crystal data and structure refinement for MSII/GS mixed state evolution of rehydrated $[Ru(py)_4Cl(NO)](PF_6)_2 \cdot 1/2H_2O$ single crystal at 100 K (data collection №6 out of total 6).

**Rehydrated $[Ru(py)_4Cl(NO)](PF_6)_2 \cdot 1/2H_2O$ single crystal:
MSII/GS mixed state at 100 K**

<i>Identification code</i>	runocl-rehyd-MSII-GS-100K
<i>Empirical formula</i>	$C_{20} H_{21} Cl F_{12} N_5 O_{1.50} P_2 Ru$
<i>Formula weight</i>	781.88
<i>Temperature</i>	100.15 K
<i>Wavelength</i>	0.71073 Å
<i>Crystal system</i>	Monoclinic
<i>Space group</i>	P 1 2 ₁ /c 1
<i>Unit cell dimensions</i>	$a = 15.7673(3)$ Å $\alpha = 90^\circ$ $b = 13.4415(2)$ Å $\beta = 92.3099(16)^\circ$ $c = 26.8186(5)$ Å $\gamma = 90^\circ$
<i>Volume</i>	5679.23(17) Å ³
<i>Z</i>	8
<i>Density (calculated)</i>	1.829 Mg/m ³
<i>Absorption coefficient</i>	0.866 mm ⁻¹
<i>F(000)</i>	3096
<i>Crystal size</i>	0.28 × 0.232 × 0.09 mm ³
<i>θ range for data collection</i>	2.997°–26.999°
<i>Index ranges</i>	−20 ≤ h ≤ 19, −17 ≤ k ≤ 17, −34 ≤ l ≤ 33
<i>Reflections collected</i>	29012
<i>Independent reflections</i>	12381, [$R_{int} = 0.0606$]
<i>Completeness to $\theta = 25.242^\circ$</i>	99.8%
<i>Absorption correction</i>	Analytical
<i>Max. and min. transmission</i>	0.955, 0.876
<i>Refinement method</i>	Full-matrix least-squares on F^2
<i>Data/restraints/parameters</i>	12381/260/922
<i>Goodness of fit on F^2</i>	1.011
<i>Final R indices [$I > 2\sigma(I)$]</i>	$R1 = 0.0459$, $wR2 = 0.0555$
<i>R indices (all data)</i>	$R1 = 0.0832$, $wR2 = 0.0654$
<i>Extinction coefficient</i>	n/a
$\Delta\rho_{max}$, $\Delta\rho_{min}$	0.680 eÅ ⁻³ , −0.565 eÅ ⁻³

TABLE C-18: Experimental details on crystal data and structure refinement for MSII/GS mixed state of rehydrated $[Ru(py)_4Cl(NO)](PF_6)_2 \cdot 1/2H_2O$ single crystal at 100 K.

APPENDIX D: Selected bond lengths
and angles in dehydrated and
rehydrated crystals during the
photo-isomerization

	Dehydrated GS		Dehydrated MSI		Dehydrated MSII	MSII Dat col 1	MSII Dat col 2	MSII Dat col 3	MSII Dat col 4	MSII Dat col 5	MSII Dat col 6
R1-factor	4.49%	R1-factor	4.41%	R1-factor	4.84%	4.78%	4.71%	4.62%	4.62%	4.69%	4.62%
GS	100%	MSI	100%	GS	65.7%	56.3%	50.8%	50.6%	54.1%	60.5%	68.8%
				MSII	34.3%	43.7%	49.2%	49.4%	45.9%	39.5%	31.2%
				N10 [†] - O10 [†]	1.074(5)	1.081(9)	1.088(9)	1.104(14)	1.102(15)	1.095(9)	1.099(9)
				Ru2 - N10 [†]	1.992(8)	1.977(13)	1.975(11)	1.964(11)	1.976(13)	1.977(15)	1.973(17)
				Ru2 - O10 [†]	2.129(11)	2.147(10)	2.149(10)	2.159(9)	2.148(10)	2.174(12)	2.155(13)
				N10 [†] -Ru2-O10 [†]	29.97(19)	30.0(3)	30.2(3)	30.6(4)	30.6(4)	30.1(3)	30.5(3)
				Cl2-Ru2-N10 [†]	158.4(3)	159.1(2)	158.7(2)	158.4(3)	158.3(3)	158.4(3)	157.9(3)
				Cl2-Ru2-O10 [†]	171.3(3)	170.6(2)	170.7(2)	170.7(2)	170.6(2)	171.0(3)	171.1(3)
Ru2 - N10	1.755(3)	Ru2 - O10	1.866(3)	Ru2 - N10	1.792(6)	1.758(8)	1.750(7)	1.752(7)	1.750(7)	1.757(9)	1.751(5)
N10 - O10	1.143(4)	O10 - N10	1.142(3)	N10 - O10	1.130(7)	1.143(8)	1.140(10)	1.144(8)	1.137(8)	1.138(8)	1.142(4)
Ru2-N10-O10	172.9(3)	Ru2-O10-N10	171.2(2)	Ru2-N10-O10	171.2(7)	170.6(10)	167.4(12)	169.5(10)	169.6(11)	170.0(9)	171.6(7)
Ru2 - N6	2.121(3)	Ru2 - N6	2.105(3)	Ru2 - N6	2.119(3)	2.110(3)	2.117(3)	2.118(3)	2.121(3)	2.115(3)	2.120(3)
Ru2 - N7	2.111(3)	Ru2 - N7	2.101(3)	Ru2 - N7	2.105(3)	2.113(3)	2.107(3)	2.112(3)	2.108(3)	2.112(3)	2.110(3)
Ru2 - N8	2.102(3)	Ru2 - N8	2.095(3)	Ru2 - N8	2.098(3)	2.098(3)	2.099(3)	2.096(3)	2.097(3)	2.101(3)	2.097(3)
Ru2 - N9	2.105(3)	Ru2 - N9	2.096(3)	Ru2 - N9	2.109(3)	2.110(3)	2.111(3)	2.114(3)	2.114(3)	2.110(3)	2.105(3)
Cl2-Ru2-N10	174.93(10)			Cl2-Ru2-N10	175.4(2)	175.4(4)	174.3(4)	175.1(4)	174.7(4)	175.1(3)	175.4(2)
		Cl2-Ru2-O10	175.28(8)								
Ru2-Cl2	2.3196(9)	Ru2-Cl2	2.2832(9)	Ru2-Cl2	2.2965(10)	2.3013(10)	2.3040(10)	2.3047(10)	2.3075(10)	2.3096(10)	2.3098(10)
Ru1 - N5	1.755(3)	Ru1 - O5	1.864(3)	Ru1 - N5	1.761(4)	1.757(4)	1.758(4)	1.756(3)	1.754(3)	1.756(3)	1.755(3)
N5 - O5	1.146(4)	O5 - N5	1.147(4)	N5 - O5	1.122(4)	1.132(4)	1.132(4)	1.137(4)	1.146(4)	1.146(4)	1.144(4)
Ru1-N5-O5	179.1(3)	Ru1-O5-N5	178.7(3)	Ru1-N5-O5	178.9(4)	178.6(4)	178.9(3)	178.9(3)	179.0(3)	178.4(3)	179.0(3)
Ru1 - N1	2.101(3)	Ru1 - N1	2.098(3)	Ru1 - N1	2.098(3)	2.105(3)	2.103(3)	2.100(3)	2.108(3)	2.099(3)	2.097(3)
Ru1 - N2	2.103(3)	Ru1 - N2	2.104(3)	Ru1 - N2	2.109(3)	2.103(3)	2.106(3)	2.100(3)	2.102(3)	2.106(3)	2.107(3)
Ru1 - N3	2.099(3)	Ru1 - N3	2.098(3)	Ru1 - N3	2.107(3)	2.0982(19)	2.105(3)	2.105(3)	2.102(3)	2.0959(19)	2.105(3)
Ru1 - N4	2.115(3)	Ru1 - N4	2.106(3)	Ru1 - N4	2.108(3)	2.112(3)	2.114(3)	2.118(3)	2.122(3)	2.110(3)	2.117(3)
Cl1-Ru1-N5	179.01(10)			Cl1-Ru1-N5	179.01(12)	179.12(12)	178.99(11)	179.04(11)	178.98(11)	179.03(11)	178.94(11)
		Cl1-Ru1-O5	179.26(8)								
Ru1-Cl1	2.3161(10)	Ru1-Cl1	2.2807(9)	Ru1-Cl1	2.3147(11)	2.3176(11)	2.3185(10)	2.3167(10)	2.3164(10)	2.3166(10)	2.3172(10)
Goof	1.003	Goof	0.988	Goof	1.006	1.005	1.012	1.01	0.998	1.003	1.001
Max peak	0.7	Max peak	0.5	Max peak	1.3	1.1	0.8	0.8	0.7	0.7	0.8
a, Å	15.6486(3)	a, Å	15.6690(3)	a, Å	15.6730(3)	15.6650(3)	15.6654(3)	15.6635(3)	15.6636(3)	15.6633(3)	15.6624(3)
b, Å	13.4525(2)	b, Å	13.4439(2)	b, Å	13.4364(2)	13.4340(3)	13.4337(2)	13.4341(2)	13.4351(2)	13.4370(2)	13.4396(3)
c, Å	26.8254(5)	c, Å	26.8473(5)	c, Å	26.8823(6)	26.9024(6)	26.9119(5)	26.9085(6)	26.9047(5)	26.8972(5)	26.8831(6)
β, (°)	92.265(2)	β, (°)	92.292(2)	β, (°)	92.019(2)	92.009(2)	91.987(2)	92.0001(18)	92.0110(18)	92.052(2)	92.0882(19)
v, Å ³	5642.68(17)	v, Å ³	5650.93(17)	v, Å ³	5657.59(19)	5658.0(2)	5660.05(17)	5658.73(19)	5658.40(18)	5657.36(17)	5655.1(2)

FIGURE D-1: Dehydrated system: selected bond distances (Å) and angles (°) in GS and MSI from SHELXL refinement. †Solid-state DFT calculations are performed on hydrated system only [62].

	Rehydrated GS		Rehydrated MSI		MSII Dat col 1	MSII Dat col 2	MSII Dat col 3	MSII Dat col 4	MSII Dat col 5	MSII Dat col 6	Rehydrated MSII
R1-factor	4.30%	R1-factor	4.67%	R1-factor	4.61%	4.59%	4.55%	4.57%	4.56%	4.52%	4.59%
GS	100%	MSI	100%	GS	50.1%	58.4%	63.7%	67.8%	72.4%	75.8%	79.6%
				MSII	49.9%	41.6%	36.3%	32.2%	27.6%	24.2%	20.4%
				N10' - O10'	1.039(8)	1.059(9)	1.071(9)	1.081(9)	1.083(10)	1.07(3)	1.079(10)
				Ru2 - N10'	1.985(10)	1.978(12)	1.993(8)	1.985(5)	1.985(9)	1.989(9)	1.986(10)
				Ru2 - O10'	2.133(10)	2.151(11)	2.139(11)	2.166(11)	2.149(16)	2.159(16)	2.154(9)
				N10'-Ru2-O10'	28.9(2)	29.3(3)	29.8(3)	29.8(3)	30.0(3)	29.5(8)	29.9(3)
				Cl2-Ru2-N10'	159.4(2)	159.4(2)	158.7(3)	159.0(3)	158.4(3)	158.4(6)	158.7(4)
				Cl2-Ru2-O10'	171.07(19)	170.6(2)	170.9(3)	170.7(3)	171.0(3)	171.4(5)	170.8(4)
Ru2 - N10	1.757(3)	Ru2 - O10	1.838(2)	Ru2 - N10	1.751(4)	1.751(4)	1.750(6)	1.749(4)	1.754(7)	1.747(5)	1.768(5)
N10 - O10	1.141(3)	O10 - N10	1.141(3)	N10 - O10	1.128(5)	1.115(6)	1.128(7)	1.132(4)	1.127(8)	1.142(6)	1.132(5)
Ru2-N10-O10	172.5(3)	Ru2-O10-N10	172.3(2)	Ru2-N10-O10	163.4(10)	166.9(9)	170.0(7)	170.6(6)	171.2(6)	171.3(6)	172.3(5)
Ru2 - N6	2.115(3)	Ru2 - N6	2.106(3)	Ru2 - N6	2.120(3)	2.121(3)	2.116(3)	2.112(3)	2.121(3)	2.118(3)	2.112(3)
Ru2 - N7	2.106(3)	Ru2 - N7	2.102(3)	Ru2 - N7	2.110(3)	2.110(3)	2.108(3)	2.114(3)	2.107(3)	2.111(3)	2.103(3)
Ru2 - N8	2.101(3)	Ru2 - N8	2.097(3)	Ru2 - N8	2.103(3)	2.098(3)	2.103(3)	2.101(3)	2.096(3)	2.099(3)	2.095(3)
Ru2 - N9	2.101(3)	Ru2 - N9	2.098(3)	Ru2 - N9	2.109(3)	2.103(3)	2.106(3)	2.109(3)	2.108(3)	2.106(3)	2.105(3)
Cl2-Ru2-N10	175.63(9)			Cl2-Ru2-N10	172.8(4)	174.8(3)	175.1(3)	175.6(2)	175.5(2)	175.5(2)	175.46(17)
		Cl2-Ru2-O10	175.44(8)								
Ru2 - Cl2	2.3211(9)	Ru2 - Cl2	2.2966(10)	Ru2 - Cl2	2.3048(10)	2.3091(10)	2.3113(10)	2.3125(9)	2.3135(10)	2.3147(9)	2.3077(10)
GS	100%	MSI	100%	GS	59.9%	67.6%	74.4%	79.6%	83.9%	86.9%	81.1%
				MSII	40.1%	32.4%	25.6%	20.4%	16.1%	13.1%	18.9%
				O5' - N5'	1.093(5)	1.11(3)	1.096(10)	1.093(10)	1.092(10)	1.089(10)	1.086(10)
				Ru1 - N5'	1.944(11)	1.968(16)	1.967(15)	1.979(19)	1.96(2)	1.974(10)	1.94(2)
				Ru1 - O5'	2.164(14)	2.16(2)	2.15(2)	2.148(10)	2.11(4)	2.145(10)	2.139(10)
				N5'-Ru1-O5'	30.3(2)	30.8(9)	30.5(4)	30.4(3)	30.8(6)	30.3(3)	30.4(3)
				Cl1-Ru1-N5'	158.0(3)	157.5(6)	157.6(4)	156.9(6)	157.2(6)	157.1(7)	158.6(5)
				Cl1-Ru1-O5'	170.9(3)	171.2(6)	171.5(4)	172.1(6)	171.6(7)	171.6(7)	170.8(5)
Ru1 - N5	1.759(3)	Ru1 - O5	1.846(3)	Ru1 - N5	1.753(9)	1.761(9)	1.745(7)	1.758(6)	1.753(7)	1.753(5)	1.769(3)
N5 - O5	1.144(3)	O5 - N5	1.140(4)	N5 - O5	1.144(8)	1.135(9)	1.152(9)	1.144(6)	1.143(8)	1.150(5)	1.149(4)
Ru1-N5-O5	178.6(3)	Ru1-O5-N5	178.1(3)	Ru1-N5-O5	179.0(10)	179.8(15)	178.2(8)	179.3(7)	177.9(7)	177.9(4)	177.9(5)
Ru1 - N1	2.106(3)	Ru1 - N1	2.099(3)	Ru1 - N1	2.104(3)	2.107(3)	2.103(3)	2.107(3)	2.106(3)	2.104(3)	2.103(3)
Ru1 - N2	2.105(3)	Ru1 - N2	2.094(3)	Ru1 - N2	2.103(3)	2.096(3)	2.101(3)	2.099(3)	2.100(3)	2.099(3)	2.096(3)
Ru1 - N3	2.097(3)	Ru1 - N3	2.086(3)	Ru1 - N3	2.104(3)	2.096(3)	2.102(3)	2.101(3)	2.100(3)	2.097(3)	2.095(3)
Ru1 - N4	2.117(3)	Ru1 - N4	2.112(3)	Ru1 - N4	2.112(3)	2.115(3)	2.111(3)	2.117(3)	2.116(3)	2.117(3)	2.112(3)
Cl1-Ru1-N5	178.84(9)			Cl1-Ru1-N5	178.2(3)	178.4(5)	178.6(2)	178.7(2)	179.0(3)	179.17(18)	178.7(2)
		Cl1-Ru1-O5	178.90(8)								
Ru1 - Cl1	2.3194(9)	Ru1 - Cl1	2.2941(10)	Ru1 - Cl1	2.3077(10)	2.3101(10)	2.3129(10)	2.3134(10)	2.3139(10)	2.3158(10)	2.3094(10)
Goof	0.994	Goof	0.999	Goof	1.006	1.01	1	1.002	0.999	1.01	1.011
Max peak	0.5	Max peak	0.6	Max peak	0.6	0.7	0.6	0.6	0.6	0.6	0.7
a, Å	15.7473(3)	a, Å	15.7696(3)	a, Å	15.7721(3)	15.7684(3)	15.7660(3)	15.7629(3)	15.7602(3)	15.7596(3)	15.7673(3)
b, Å	13.4389(2)	b, Å	13.4309(2)	b, Å	13.4506(2)	13.4474(2)	13.4458(2)	13.4434(2)	13.4417(2)	13.4411(2)	13.4415(2)
c, Å	26.8141(5)	c, Å	26.8230(5)	c, Å	26.8351(5)	26.8326(5)	26.8323(5)	26.8317(5)	26.8296(5)	26.8322(5)	26.8186(5)
β, (°)	92.4287(16)	β, (°)	92.5143(16)	β, (°)	92.0993(17)	92.1407(16)	92.1884(17)	92.2343(16)	92.2521(16)	92.2886(17)	92.3099(16)
v, Å³	5669.48(17)	v, Å³	5675.60(17)	v, Å³	5689.08(18)	5685.73(17)	5683.92(17)	5681.50(17)	5679.30(17)	5679.21(18)	5679.23(17)

FIGURE D-2: Rehydrated system: selected bond distances (Å) and angles (°) in GS and MSI from SHELXL refinement. ‡Solid-state DFT calculations are performed on hydrated system only [62].

APPENDIX E: Experimental details of absorption spectroscopy

Steady state visible absorption spectroscopy

Dedicated wavelength was chosen by monochromator (Digikröm CM110) equipped with the slit 0.6 mm , seeded by the halogen lamp (Spectral Products, model: ASBN-W150), see Figure E-1. Probe light was mechanically chopped down to 500 Hz and focused on the sample by home-made objective with spot size of the image of the halogen lamp filament around $150 \times 300\ \mu\text{m}^2$, while the typical size of the investigated crystal was $450 \times 500\ \mu\text{m}^2$. Spectral changes of transmitted light were detected by photodiode (Thorlabs DET10, DET36) and correlated with the reference signal recorded by second photodiode (reference, Thorlabs DET10, DET36) measuring copied by the beam splitter signal before sample, Figure E-1. Signals from photodiodes were transferred to computer via two lock-in amplifiers synchronized with the chopper (Thorlabs), the signal was recorded with accuracy $\text{noise}/\text{signal} \sim 10^{-5}$, the lock-in amplifier, model SR 830 [97], was triggered at frequency of 500 Hz (see section on **Lock-in detection system** in this Appendix for more details). Single measurement was controlled by LabView software correlating signals from detection system with monochromator setup and recording one spectrum in one file. The measurements were done at room temperature and at low temperatures, 100 K , 140 K , 180 K , where crystals were cooled down by CryoJet system from Oxford Cryogenics (CryoJet 700). To study the photo-induced phenomena the crystals were irradiated with diode lasers (473 nm , 532 nm , 782 nm , and 1064 nm). Precise determination of the laser powers was done using a combination of laser beam profiler (Spiricon SP620U) and pyroelectric measurements (Melles Griot Broadband power meter 13PEM001). The FWHM width of the gaussian laser profile was measured and the power delivered per cm^2 was deduced after taking into account the 0.76 factor between the power delivered within this FWHM width and the total power considering the whole gaussian beam.

Time-resolved pump-probe experiments

The most common time-resolved experiment is a pump-probe technique with two ultrashort pulses, where the first one is sent to trigger the sample while the second one detects its response. The broadband detection with monochromatic pump and white light probe [98, 99] was employed for the measurements on $[Ru(py)_4Cl(NO)](PF_6)_2 \cdot 1/2H_2O$ single crystals.

Generation of ultrashort laser pulses

Femtosecond pulses generation in the free space is entirely based on the Ti:Sapphire technology. Such pulses as short as 45 *fs* were first generated with Ti:Sapphire laser in 1991 [100]. Since then this laser system is largely used in ultrafast technologies though there is an on-going search for less expensive alternatives [101, 102]. To generate ultrashort laser pulses we use the laser setup shown Figure E-3. It consists of femtosecond oscillator Mira, regenerative amplifier Legend Elite II, and Optical Parametric Amplifiers (OPA) TOPAS. The pulses are generated by the femtosecond oscillator Mira seed (Coherent Inc.) in a Ti:Sapphire crystal pumped by the CW laser Verdi (Coherent Inc.) (Figure E-3). This crystal composed of Sapphire (Al_2O_3) doped with Titanium ions exhibits a broad emission spectrum which is necessary for generation of ultrashort pulses. The principle is then to give a common phase to the modes of the spectrum. In such mode-locked regime the interference of the components gives birth to an ultrashort pulse. The mode-locked spectrum with 40 *nm* FWHM centered around 800 *nm* is then seeded by Mira laser pulses of 76 *MHz* repetition rate, $P = 720$ *mW* and pulse duration of 35 *fs* [103].

As a next step the laser pulses are sent on regenerative amplifier, Legend Elite II, where the signal is stretched, amplified and compressed back to avoid the damage of laser components. Legend Elite II delivers ultrashort laser pulses with power up to 3.5 *W* [104] (see Figure E-3). Chirped-pulses are split then into two beams: the pump pulse is sent to OPA (Light Conversion, TOPAS-C [105]) from which it is possible to obtain any wavelength of the beam, between near-IR up to UV light due to the nonlinear crystals used in the OPA. The schematic view of OPA principle is presented in Figure E-2: the incident beam from Legend (800 *nm*) is split in three beams, one of them is sent to Ti:Sapphire crystal to generate white light and two others are used as a seed on BBO crystals to produce and amplify new frequencies. By mixing obtained new frequencies (signal, idler and fundamental beams) the necessary wavelength can be generated on the exit from the OPA.

The probe beam is either sent to the OPA to choose a certain wavelength in case of monochromatic probe or beam of $\lambda = 800$ *nm* coming from regenerative amplifier is kept in order to generate the white light probe afterwards. Pump and probe beams are sent then to the experimental setup presented in Figure E-7. The optical delay line (Newport IMS linear stage), which moves during the experiment, is used for the pump beam to choose time delays, while probe beam stays constant in time. Such optical delay stage allows us observation of the signal from the sample at a different time delays, for example the step of 0.15 *mm* on delay stage corresponds

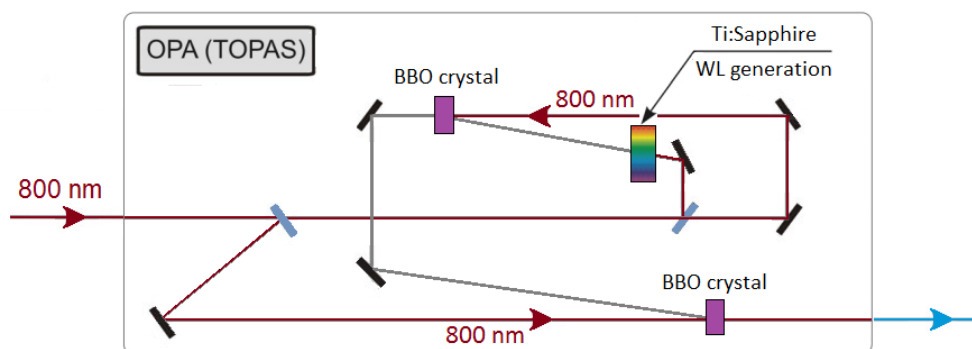


FIGURE E-2: Scheme of the signals in lock-in amplifier technique. Green curves correspond to experiment (reference and signal are frequency-locked), blue ones - to lock-in references oscillating 90° apart to eliminate the phase dependency.

to 1 *ps* of time delay between the pump and probe in experimental data. To adjust the power of the pump and probe we employed neutral filters, to avoid the unwanted background and reduce the noise we used pass filters.

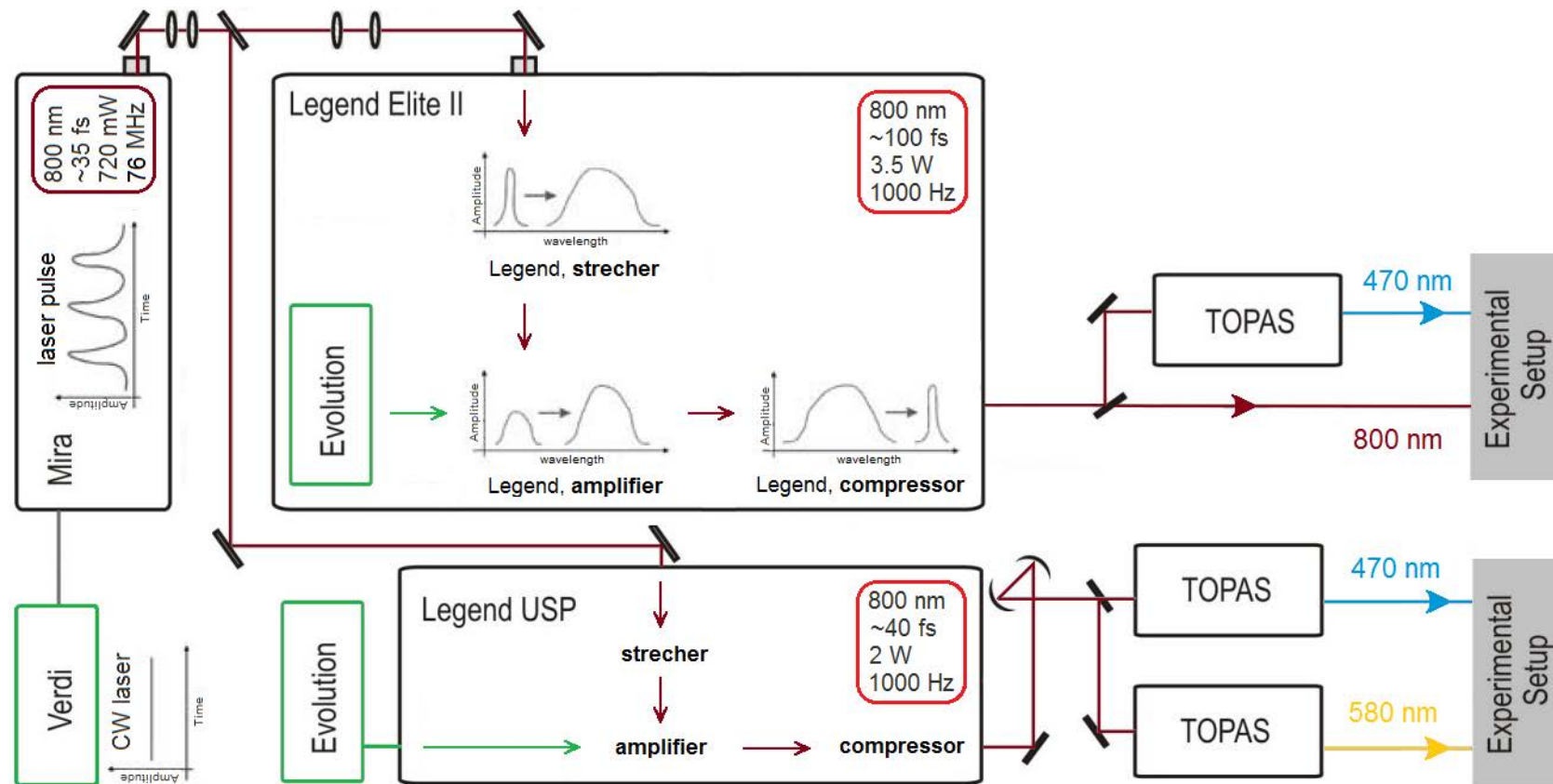


FIGURE E-3: The general scheme of laser source used in experiments (adapted from [98]). Legend Elite II is used to generate the pump and probe for the white light experiment while the Legend USP was employed for the single wavelength pump-probe experiments.

Monochromatic pump-probe experiment

Experimental setup. In this experimental setup femtosecond pulses were delivered from Mira and amplified by Legend USP at 1 kHz . The wavelengths for pump and probe were tuned in OPA systems and then pump was chopped to 500 Hz . The probe beam was split into signal and reference, signal was sent on channel A and reference on Channel B of the lock-in detection system. The difference $A - B$ was then registered during the scan which allowed to collect data with high sensitivity.

The pump-probe experimental setup with two monochromatic wavelengths is presented in Figure E-4 [98, 106]. Pump with a chosen wavelength of 470 nm was chopped to 500 Hz frequency (the chopper was synchronized with the laser) and delayed to the probe signal by optical delay line. Pump and probe beams were focused on the sample by two lenses, focal length of 200 mm for probe and 250 mm for pump, with a small angle of 12° between the two beams. The typical size of the sample was around $200 \times 150 \mu m^2$ and the probe spot was around $80 \times 80 \mu m^2$. The differential optical density, ΔOD , (with $A - B$ lock-in mode) then was measured on ruthenium nitrosyl system during the phototransformation. The probe beam (several wavelengths were tried: 530 nm , 580 nm and 750 nm) was split into signal (canal A on the Lock-In) and reference (canal B), which corresponds to the transmission of the GS. The photodiode from ThorLabs, InGas or Si-silica depending on the probe wavelength, were used feeding the photocurrent directly to the lock-in amplifier (SR 830, Stanford Research Systems [97]), the main principles of which are described below.

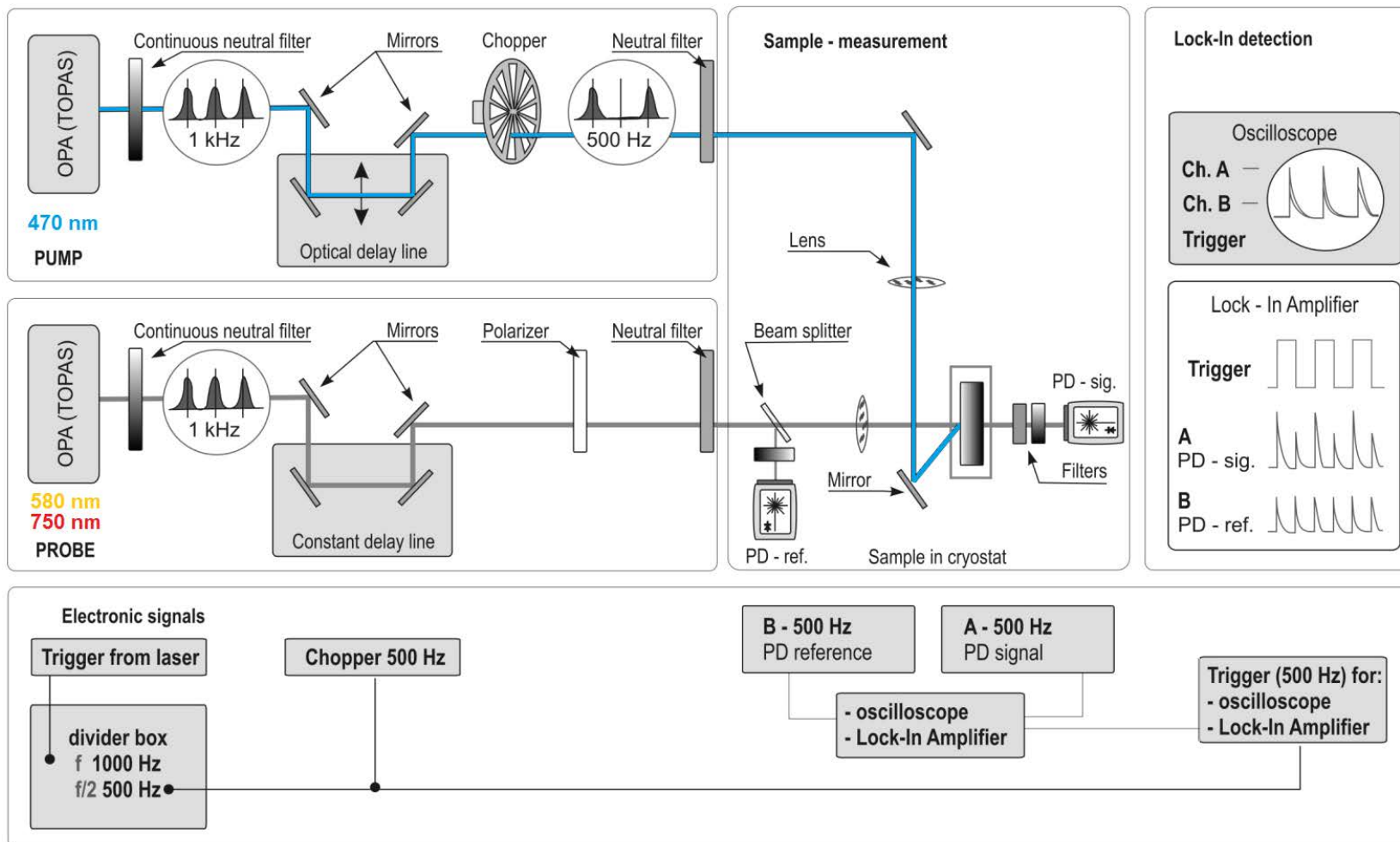


FIGURE E-4: The pump-probe experimental setup with two monochromatic beams [98]. The pump beam from OPA was sent to the optical delay line and then chopped mechanically. The probe beam was sent to the constant delay line with fixed delay time, after which it was split into reference and signal beams. Before hitting the crystal pump and probe beams were focused on its surface.

Lock-in detection system. Lock-in amplifier is a phase-sensitive detection (PSD) system which registers only signals whose frequencies and phases are very close to the lock-in reference frequency and phase. It is used to amplify and measure a very small signals, down to few nanovolts. Lock-in amplifier can detect the signal at a certain frequency with a bandwidth as narrow as 0.01 Hz , which brings down *noise/signal* ratio and is crucial when measuring weak changes on top of a strong signal.

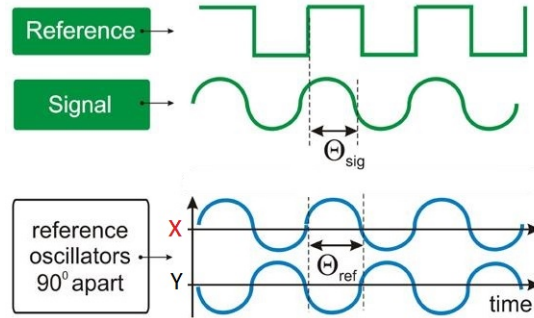


FIGURE E-5: Scheme of the signals in lock-in amplifier technique. Green curves correspond to experiment (reference and signal are frequency-locked), blue ones - to lock-in references oscillating 90° apart to eliminate the phase dependency.

The SR 830 generates lock-in reference (sine wave), amplifies the signal and then multiplies it by the lock-in reference. To eliminate the phase dependency two PSDs are combined, first one works with a same phase as signal measuring X component and second one amplifies the signal with the reference oscillator shifted by 90° , thus providing Y component of a signal as shown in Figure E-5. Eventually, the phase independent signal amplitude can be measured as $R = (X^2 + Y^2)$ (for more explanations check manual [97]).

Time-resolved white light experiment

Experimental setup. For this experiment both beams were slowed down from 1000 Hz to 500 Hz frequency by a mechanical chopper due to the $\sim 1.3 \text{ ms}$ readout rate of CCD camera, which represents together with spectrometer the detection system in our experiment (see details below). Then the pump, 470 nm from OPA, was delayed on the optical delay line and slowed down once more by another chopper to 250 Hz to be able to collect spectra with and without pump on the sample (see Figure E-7).

Meanwhile the probe, 800 nm directly from Legend Elite II, was sent on the sapphire crystal which generates white light supercontinuum due to a self-phase modulation (SPM), a nonlinear optical effect in this material. Due to the optical Kerr effect [107], the ultrashort light pulse can lead to a varying refractive index in the medium. For example, if for an ultrashort pulse with a Gaussian shape the intensity at time t is given by $I(t)$ [108]:

$$I(t) = I_0 \exp\left(-\frac{t^2}{\tau^2}\right)$$

where I_0 is the peak intensity, and τ is half the pulse duration, then the pulse travelling in a medium induces a variation of refractive index:

$$n(I) = n_0 + n_2 \cdot I$$

where n_0 is the linear refractive index, and n_2 is the second-order nonlinear refractive index of the medium. While the pulse is propagating through the material, it produces a time-dependent refractive index:

$$\frac{dn(I)}{dt} = n_2 \frac{dI}{dt} = n_2 \cdot I_0 \cdot \frac{-2t}{\tau^2} \cdot \exp\left(\frac{-t^2}{\tau^2}\right).$$

As a result, this time dependence of refractive index leads to a phase shift in the pulse and, therefore, to a change of the frequency spectrum of propagating light pulse (see Figure E-6), where the change to lower frequencies is observed in the front of the pulse, while the back is shifted to higher frequencies.

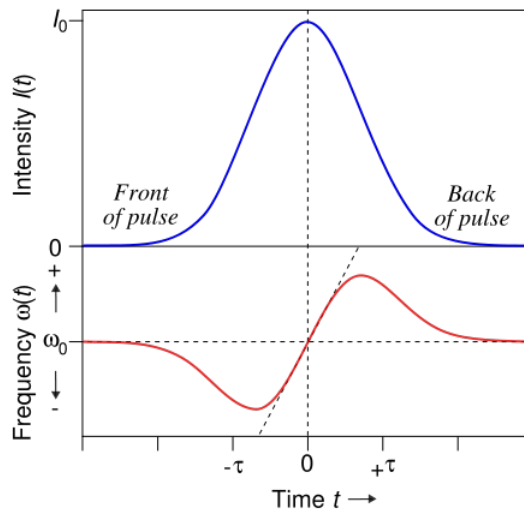


FIGURE E-6: A travelling pulse through a nonlinear medium (blue curve) experiences a frequency shift (red curve) due to self-phase modulation (SPM) [108].

The generated white light was split then into signal and reference to overcome the instability of white light in the measurements. Finally, the pump and probe were overlaid on the crystal surface in space and time (see Figure E-7). During the measurements the light from the signal and reference are transferred by two optical fibers to spectrometer first to be dispersed with the gratings and further to CCD chip, which is cooled to -75°C in order to decrease the thermal background [98].

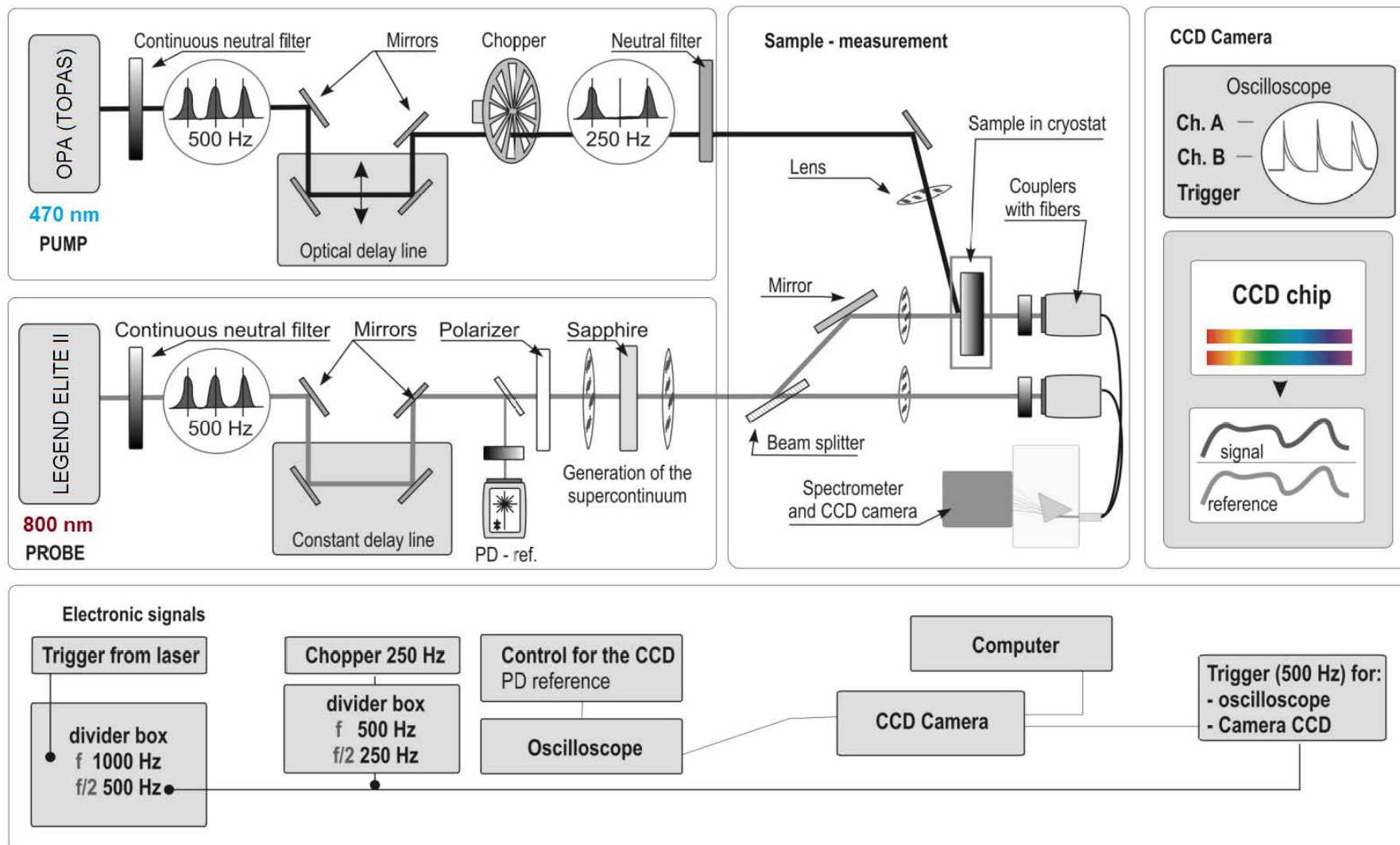


FIGURE E-7: Pump-probe experimental setup with monochromatic pump and polychromatic probe (adapted from [98]). The pump beam from OPA was sent to the optical delay line and then chopped mechanically. The probe beam was sent to the constant delay line with fixed delay time, after which it was split into reference and signal beams. Before hitting the crystal pump and probe beams were focused on its surface.

CCD camera detection system. As it was mentioned above in white light experiment the detection system consists of a spectrometer (Acton Research Corp., SPECTRAPro 2500i) and a CCD camera (Princeton Instruments, PIXIS 100). The CCD camera is synchronized with the probe and pump: pump is sent at frequency of 250 Hz , while the probe is sent at 500 Hz rate, and as a result, we collect half of total spectra with and half without pump on the sample. In Figure E-8 we see the cycle of measurements with a pump and the consequent cycle without the pump [98]. For the measurements with pump, for example, the CCD chip consists of dark zone (3, 4) and the zone of exposure (1, 2). The zone of exposure is divided as well into two parts: first one registers the reference spectra and second one is for the signal spectra. Once the signal and reference are obtained on the chip the spectra is recorded in the register area and the a dark buffer is used for the following exposure without pump. Typically, 20000 spectra were collected with the WinSPEC.

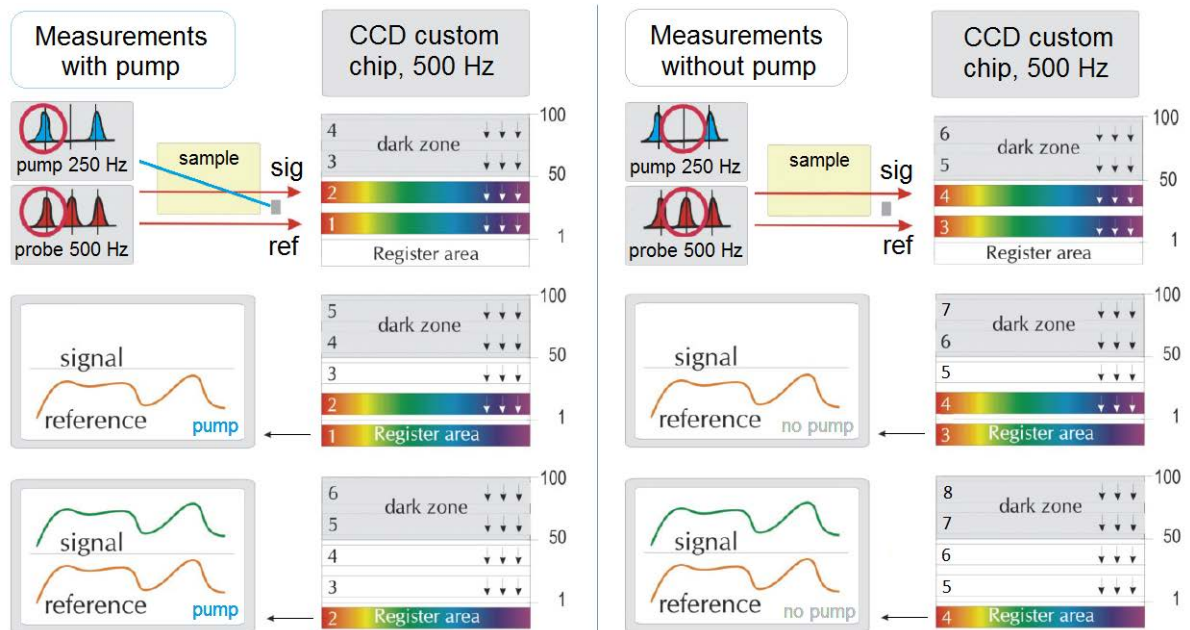
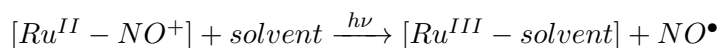


FIGURE E-8: Scheme of CCD camera readout. Two cycles of full data collection are presented: the cycle on the left corresponds to the data collection with pump, on the right - without pump (adapted from [98]).

APPENDIX F: X-Ray absorption spectroscopy studies

According to the review of ruthenium *NO* donors by Michael Rose and Pradip Mascharak [57] the photoinduced *NO* release is followed by the formation of *Ru(III) – solvent* photoproduct and could be schematized as follows:



Two issues can be addressed to be confirmed experimentally in this schematic representation of photochemical reaction: (i) the change of the oxidation state of *Ru* center from *Ru^{II}* to *Ru^{III}* and (ii) the recombination of molecule with solvent after the *NO* departure. One of the possibility to access the local geometry around the absorbing atom and the oxidation state of the metallic center of the studied complex is the X-Ray absorption spectroscopy (XAS).

X-Ray absorption spectroscopy

XAS is a technique for measuring the absorption coefficient of an element, $\mu(E)$, as a function of incident photon energy, E . Coefficient $\mu(E)$ gives the probability that X-Rays are absorbed according to the Beer's law:

$$I = I_0 e^{-\mu x},$$

where I_0 is the X-Ray incident intensity, x is the sample thickness, and I is the X-Ray transmitted intensity. Above a given threshold energy of incident X-Ray, core-level electrons can be promoted to empty bound states or completely ionised to the continuum of unbound states. Depending on the origin of the excited electron: (*1s*), (*2s, 2p*), (*3s, 3p, 3d*), the XAS spectra is referred to as *K – edge*, *L – edge*, *M – edge*, respectively (see Figure F-1 (a)). XAS is an element-specific technique, for example, the *Ru K – edge* occurs at approximately 22117 eV, while the *Rh K – edge* is at 23220 eV [109], therefore with this technique we can target the specific atom we are interested in. There are generally two main regions of XAS spectrum: X-Ray absorption

near edge structure (XANES), or edge region, and extended X-Ray absorption fine structure region (EXAFS) (Figure F-1 (b)) [110].

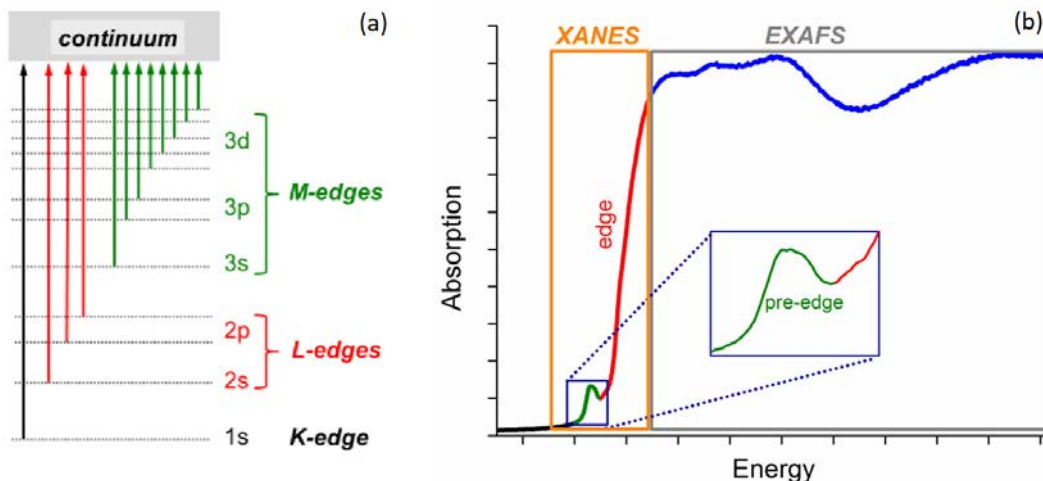


FIGURE F-1: (a) Absorption transitions resulting from the excitation of a core electron. (b) X-Ray absorption spectrum (XAS), X-Ray absorption near edge structure (XANES) and extended X-Ray absorption fine structure (EXAFS) regions. The XANES region includes the characteristic pre-edge and edge features (adapted from [110]).

As shown in Figure F-1 (b) the XANES region has a sharp absorption edge, presented in red (when the incident X-Ray energy reaches the ionisation energy of a core electron) and a weak pre-edge feature at lower energies, shown in green (observed when core electrons undergo bound-state transitions). Above the edge energy, the interaction of the propagating photoelectron wave with nearby atoms creates oscillations in the region called EXAFS (blue curve in Figure F-1 (b)). As a general rule, the energy shift in the absorption edge in XANES region can be related to the oxidation state of the absorbing atom. XANES also gives information about the symmetry and coordination number of the system, while EXAFS provides more quantitative geometric information on distances and types of neighbouring atoms.

FDMNES software

The FDMNES program (Finite Difference Method Near Edge Spectroscopy) is designed to simulate X-Ray spectroscopies, such as XANES, obtained with the synchrotron radiation, and to compare it to experimental one [111, 112, 113]. The code uses two techniques of fully relativistic monoelectronic calculations (DFT-LSDA): the first one is based on the Finite Difference Method (FDM) to solve the Schrödinger equation (the shape of the potential is free and the muffin-tin approximation is avoided) and the second one uses the Green formalism (multiple scattering) on a muffin-tin potential, which might be less precise but it is faster.

Results and discussion

In 2014 we ran XAS experiment on the SAMBA beamline (Spectroscopy Applied to Material Based on Absorption), SOLEIL synchrotron, Saint Aubin in collaboration with Emiliano Fonda and Marco Cammarata. The *Ru K – edge* (~ 22117 eV) XAS experiment was performed in the acetonitrile solution of *trans*-isomer of $[Ru^{II}(FT)Cl_2(NO)]PF_6$ to verify the change in the oxidation state of *Ru* atom, which is expected to undergo $Ru^{II} \rightarrow Ru^{III}$ shift during the *NO* photorelease, as well as to study the local geometry around the absorbing *Ru* atom. The obtained experimental curves are shown in Figure F-2. The XAS spectra was taken before (orange curve, yellow color of the sample) and after few minutes of sample irradiation with CW laser of 405 nm (green curve), which triggers the *NO* release process. The stationary UV-visible spectra were also measured before and after irradiation on one hand to verify the complete *NO* photorelease and compare results with those published in work [82] (see Figure F-3), and on the other hand to calculate the concentrations of studied solutions. As one can see, the UV-visible spectra are similar to those reported in the work [82].

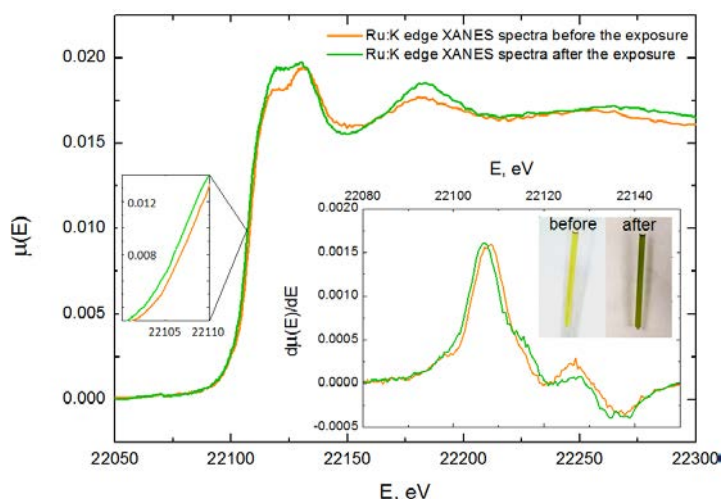


FIGURE F-2: XAS spectra of *trans* – $(Cl, Cl)[Ru^{II}(FT)Cl_2(NO)]PF_6$ in acetonitrile solution before (orange) and after few minutes of irradiation with CW light of 405 nm (green), when the *NO* release is complete. Inset: $d\mu/dE$

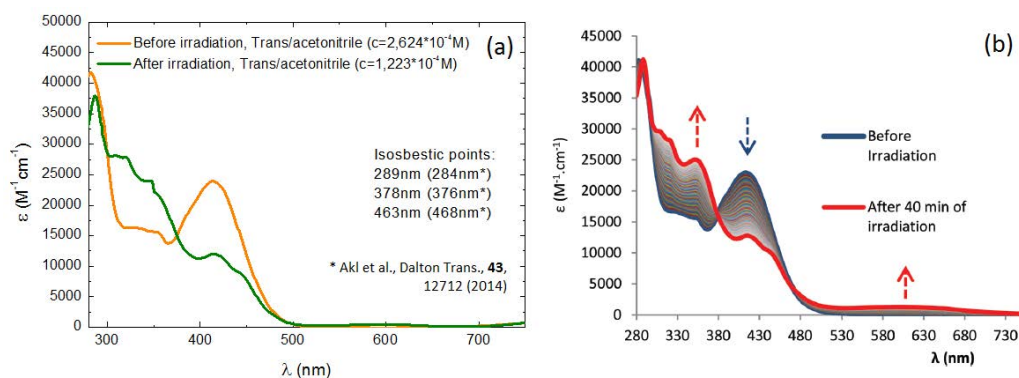


FIGURE F-3: UV-visible steady state spectra of (a) *trans* – $(Cl, Cl)[Ru^{II}(FT)Cl_2(NO)]PF_6$ in acetonitrile solution before (orange) and after few minutes of irradiation with CW light of 405 nm (green), when the *NO* release is complete. (b) The steady state UV-visible spectra from work [82] is given for comparison.

The experimental XANES results show the shift of the absorption threshold to a lower value (see zoom in Figure F-2). This is a clear evidence of the change in the oxidation state of the absorbing *Ru* atom after the *NO* release process. However, these curves do not give information on the exact values of the *Ru* oxidation state. It is interesting to at least find out if the oxidation state of *Ru* atom is increasing or decreasing after the photoreaction. To understand the change of the oxidation state as well to confirm the local geometry around the *Ru* atom after the *NO* liberation ab-initio calculations through the FDMNES package were performed [112, 113]. The simulation of the *Ru* absorbing atom with its closest neighbors was done in the configurations shown in Figure F-4 and the calculated spectra are presented in Figure F-5 in comparison with the experimental data. The main question to answer apart from the *Ru* oxidation state is if, after the *NO* departure, the rest of the molecule is directly recombined with the solvent or not. To test this we performed our simulation of the case of molecule after *NO* departure and the case of the molecule recombined with the solvent.

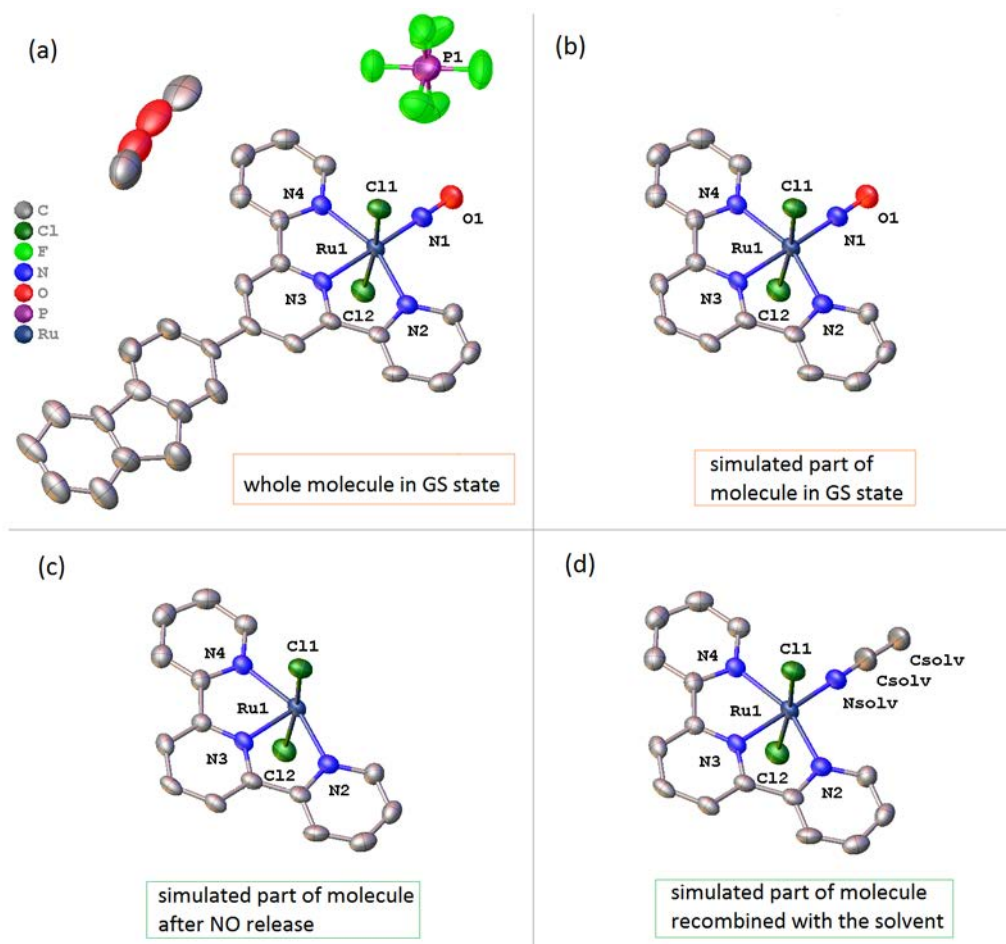


FIGURE F-4: (a) The structure of the *trans* – $(Cl, Cl)[Ru^{II}(FT)Cl_2(NO)]PF_6$ compound derived from the X-Ray diffraction measurements by group of I. Malfant [82]. The model of molecule used in our simulations (b) in GS state, (c) after the *NO* departure and (d) recombined with solvent (acetonitrile). In our simulations we took into the consideration the nearest neighbours of absorbing *Ru* atom, that is why in our model only part of the initial structure is presented.

The final curves obtained by FDMNES simulations are presented in Figure F-5 together with the experimental data. For convenience the calculated spectra are presented in a different scale. The

calculated XANES spectra in GS state is very similar to the experimental one, if we compare red and orange curves. As for the calculated spectra after the *NO* departure, we can see that a simple elimination of *NO* radical from the molecule (grey curve) does not reproduce well the experimental XANES spectra after *NO* release (green curve), nevertheless, the calculated spectra (blue curve) based on the model with molecule recombined with solvent (see Figure F-4 (d)) seem to fit better the experimental spectra (green curve). Therefore, based on FDMNES simulations, we experimentally confirmed that after the *NO* release the rest of the molecule is recombined with the solvent as proposed in the review [57]. Unfortunately, the shift of the absorption threshold is less evident in our simulations in both cases. The oxidation state determination, however, is more challenging for this compound and cannot be obtained within current experimental setup.

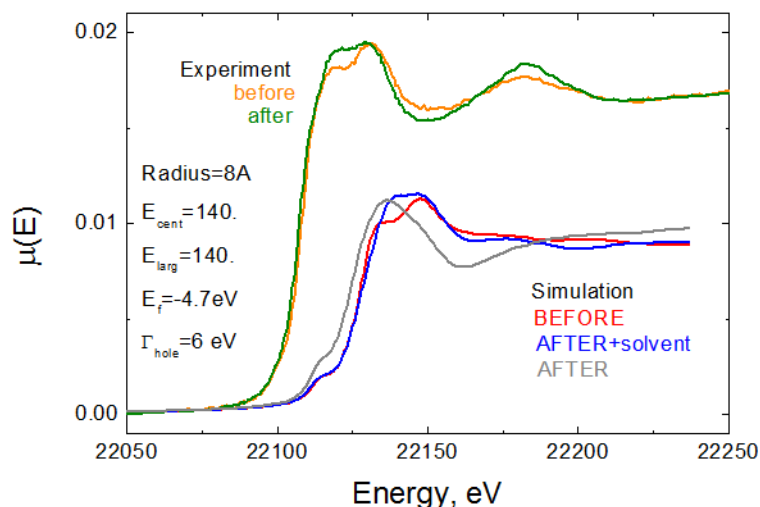


FIGURE F-5: XANES simulation by means of FDMNES software [112, 113]. The orange and green curves correspond to the experimental data before and after the irradiation with CW laser, 405 nm and complete *NO* photorelease, respectively. The red curve is the result of simulation of the XANES spectra of the molecule before the irradiation, the grey curve represents the simulation of the molecule after the *NO* departure (see Figure F-4 (c)) and the blue curve corresponds to the recombined molecule with the solvent (see Figure F-4 (d)).

Publications, Conferences

PUBLICATION

Liya Khadeeva, Wawrzyniec Kaszub, Maciej Lorenc, Isabelle Malfant, Marylise Buron-Le Cointe, "Two-step photon absorption driving the chemical reaction in the model ruthenium nitrosyl system $[Ru(py)_4Cl(NO)](PF_6)_2 \cdot 1/2H_2O$ ", *Inorg. Chem.*, **55**, 4117-4123 (2016).

CONFERENCES

1. "Structural and Dynamical Aspects of Oriented DNA Fibers", Liya Khadeeva, Jessica Valle Orero, William Trewby, Jean-Luc Garden, Andrew Wildes, Mark Johnson, Michel Peyrard International School and Symposium on Molecular Materials (ISSMM2013), November 4 - 8, 2013, Tokyo Institute of Technology, O-Okayama Campus, Tokyo, Japan.
2. "Towards two photon chemistry in a model of ruthenium nitrosyl compound", Liya Khadeeva, Marylise Buron-Le Cointe, Loïc Toupet, Wawrzyniec Kaszub, Maciej Lorenc, Marina Servol, Marco Cammarata, Joëlle Akl, Isabelle Malfant, Gordon Research Conference, Conductivity and Magnetism in Molecular Materials, August 3-8, 2014, Bates College, Lewiston, ME, USA.
3. "Two-step photon absorption in ruthenium nitrosyl system", Liya Khadeeva, Marylise Buron-Le Cointe, Loïc Toupet, Wawrzyniec Kaszub, Maciej Lorenc, Marina Servol, Marco Cammarata, Joëlle Akl, Isabelle Malfant, GdR MCM-2 : Magnétisme et Commutation Moléculaires, December 10-12, 2014, Dourdan, France.
4. "Two-step photon absorption during the photo-isomerization in a model of ruthenium nitrosyl compound", Liya Khadeeva, Marylise Buron-Le Cointe, Wawrzyniec Kaszub, Maciej Lorenc, Isabelle Malfant, 21st International Symposium on the Photochemistry and Photophysics of Coordination Compounds, July 5-9, 2015, Krakow, Poland.
5. "Photo-isomerization in a model of ruthenium nitrosyl compound: two-step photon absorption process", Liya Khadeeva, Marylise Buron-Le Cointe, Wawrzyniec Kaszub, Maciej Lorenc, Isabelle Malfant, Multiscale phenomena in molecular matter, July 6-10, 2015, Institute of Nuclear Physics PAN, Krakow, Poland.
6. "Photo-induced chemical transformation : the case of ruthenium nitrosyl compound", Liya Khadeeva, Marylise Buron-Le Cointe, Wawrzyniec Kaszub, Maciej Lorenc, Isabelle Malfant,

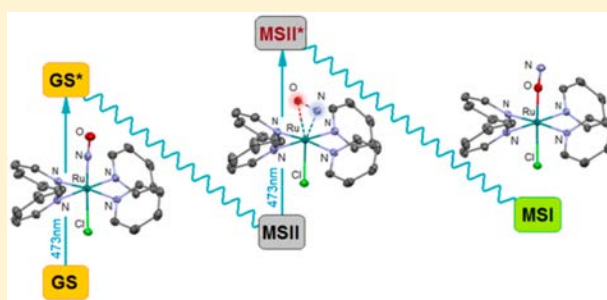
6ème Journée Recherche “Chimie, Biologie, Mathématiques et Physique : la recherche fondamentale au service du Médicament et de la Santé”, January 20, 2016, University of Rennes 1, Rennes, France.

7. “Photo-isomerization and photo-induced NO release in ruthenium nitrosyl compounds”, Liya Khadeeva, Elzbieta Trzop, Jacek Kubicki, Wawrzyniec Kaszub, Maciej Lorenc, Isabelle Malfant, Marylise Buron-Le Cointe, Gordon Research Seminar and Conference, Conductivity and Magnetism in Molecular Materials, August 13-19, 2016, Mount Holyoke College, South Hadley, MA, USA.

Two-Step Photon Absorption Driving the Chemical Reaction in the Model Ruthenium Nitrosyl System $[\text{Ru}(\text{py})_4\text{Cl}(\text{NO})](\text{PF}_6)_2 \cdot 1/2\text{H}_2\text{O}$ Liya Khadeeva,[†] Wawrzyniec Kaszub,^{†,§} Maciej Lorenc,[†] Isabelle Malfant,^{*,‡} and Marylise Buron-Le Cointe^{*,†}[†]Institut de Physique de Rennes, UMR URI-CNRS 6251, Université Rennes 1, avenue du général Leclerc, Rennes 35042 Cedex, France[‡]Laboratoire de Chimie de Coordination, CNRS UPR 8241, 205 route de Narbonne, Toulouse 31077 Cedex, France

Supporting Information

ABSTRACT: Various systems containing the $[\text{ML}_5\text{NO}]$ molecule, where $\text{M} = \text{Fe}, \text{Ru}, \dots$ and $\text{L} = \text{F}, \text{Cl}, \dots$, exhibit switching under continuous light (CW) irradiation between the ground-state nitrosyl (GS), isonitrosyl (MSI), and side-on (MSII) configurations. The metastable populations, however, are often limited to a few percent. The $[\text{Ru}(\text{py})_4\text{Cl}(\text{NO})](\text{PF}_6)_2 \cdot 1/2\text{H}_2\text{O}$ system is thus a remarkable model compound as the GS to MSI transformation is nearly complete in a single crystal. A predominant two-step photon absorption process during GS to MSI switching under blue light is revealed by visible absorption spectroscopy, although a low concentration of the transient species hinders the determination of this process by the structural signature. During the depopulation of MSI, both two-step and direct processes are evidenced under red CW irradiation. Different intermediate visible spectra revealing transient species during GS to MSI and the reverse photochemical processes are discussed in relation to MSII properties.



INTRODUCTION

After the discovery of the first long-lived photoinduced metastable state, MSI, at low temperature in sodium nitroprusside dihydrate compound (so-called SNP) in the 1970s,¹ a second long-lived metastable state, MSII, was evidenced 12 years later.^{2–4} Their identification as linkage isomers occurred in the 1990s owing to accurate diffraction studies:^{5,6} in MSI, the NO ligand is rotated by 180° to an O-bound configuration (isonitrosyl, M–ON), while the MSII state adopts a side-on configuration of the NO ligand. These conclusions were supported by calculations based on density functional theory.⁷ Similar photoisomerization between nitrosyl (GS), isonitrosyl (MSI), and side-on (MSII) configurations has been observed under continuous light (CW) irradiation in a number of similar systems containing the $[\text{ML}_5\text{NO}]$ molecule,^{8–11} where $\text{M} = \text{Fe}, \text{Ru}, \dots$ and $\text{L} = \text{F}, \text{Cl}, \text{Br}, \text{CN}, \dots$, however mainly with a low population of metastable species (MSI is often lower than 20%, and the population is less still for MSII, in SNP; however, MSI is up to 50%,⁹ and therefore, it is the prototype compound for most experimental investigations^{1–17}). In SNP, the photo-switching leads to a drastic change of the refractive index, allowing information to be written and erased with light in a broad spectral range.^{12,13} Furthermore, the excitation within the range of 350–580 nm leads to the MSI state, either directly or through the MSII state.¹⁴ Both channels are equally probable under the blue light, while only the MSII channel prevails with green laser irradiation. Recently, time-resolved absorption and

infrared (IR) spectroscopy^{15,16} on SNP gave access to the ultrafast dynamics of the GS to MSII transformation by pumping at 500 nm: the NO ligand rotates by about 90° within 300 fs, and the vibrational relaxation to the MSII minimum occurs within a few picoseconds. Applications in holographic recording media have now been reported.¹⁷

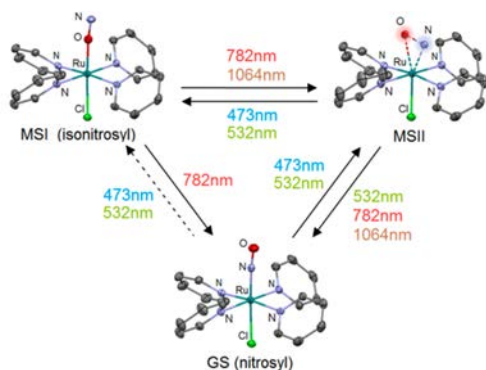
Quite recently, nearly complete conversion to the MSI state was reported in single crystals of $[\text{Ru}(\text{py})_4\text{Cl}(\text{NO})](\text{PF}_6)_2 \cdot 1/2\text{H}_2\text{O}$, which made this compound a model system for the M–NO to M–ON photoisomerization.¹⁸ Previous studies on powder samples of this system showed that (i) excitation leading to MSI species is possible in the range of 460–530 nm and (ii) MSI is subsequently transferred to MSII during the photoswitching to GS under IR light irradiation (920–1100 nm).¹⁹

Here we report the photoswitching dynamics driven by different wavelengths (Scheme 1) on a single crystal of $[\text{Ru}(\text{py})_4\text{Cl}(\text{NO})](\text{PF}_6)_2 \cdot 1/2\text{H}_2\text{O}$ by means of X-ray diffraction and absorption spectroscopy in the visible range. Time evolutions of Bragg peak intensities and lattice parameters, as well as of visible OD spectra under different light irradiation conditions, are presented. The critical role of an intermediate (referred to hereafter as the MSII state) in a two-step light-driven process of M–NO to M–ON transformation is

Received: November 6, 2015

Published: April 7, 2016

Scheme 1. Probed Wavelengths for the Photoswitching between the GS, MSI, and MSII States^a



^aSee refs 18 and 19. Here the MSII state view is the side-on configuration of the $[\text{Ru}(\text{py})_4\text{Cl}(\text{NO})](\text{PF}_6)_2 \cdot 1/2\text{H}_2\text{O}$ single crystal at low temperatures.

evidenced in the blue spectral range of irradiation. This spectacular finding might be related to the unprecedented efficiency (close to 1) of the photoisomerization in this model compound and is discussed in relation with previous results obtained on the prototype SNP compound.

RESULTS AND DISCUSSION

The Ru–NO to Ru–ON photoswitching and the reverse process were followed through the evolution of the optical density (OD) (color changing from orange to green¹⁸) and through the change of structural signatures, such as unit-cell parameters and Bragg peak intensities. At 100 K and 473 nm X-ray diffraction shows a saturation of the signal after around 2 h of laser exposure at around $280 \text{ mW}/\text{cm}^2$, i.e., around $2000 \text{ J}\cdot\text{cm}^{-2}$.

Unit-Cell Parameters as a Tool To Probe Linkage Isomers. The Ru–NO to Ru–ON photoisomerization and the reverse process were first probed at the atomic scale. The complete or quasi-complete population of the MSI species under blue light irradiation has been determined with structural data refinement²⁰ of X-ray diffraction measurements: there is no clear difference between a model with total conversion (100% MSI) and a mixed GS–MSI model refining the MSI conversion rate. The latter shows a mixing of 93(2)% MSI and 7(2)% GS states, but average atomic positions and thermal parameters obtained from the two models are identical within error bars.²⁰ In other words, the GS to MSI photochemical reaction is either complete or quasi-complete since the presence of a few percent of GS species cannot be excluded.

Following the evolution of lattice parameters under the blue light irradiation, the structural changes between GS and MSI show the highest change on evolution of the a crystallographic axis ($\Delta a = +0.032(2) \text{ \AA}$, Figures 1 and S1). They are greater than those measured in the SNP compound,⁵ most likely due to the higher photoconversion rates in $[\text{Ru}(\text{py})_4\text{Cl}(\text{NO})](\text{PF}_6)_2 \cdot 1/2\text{H}_2\text{O}$. Observed structural evolution during the Ru–NO to Ru–ON photoswitching at 473 nm is continuous; i.e., it does not show any signature of an intermediate state.

As known from the literature,^{5,6} the structural signature of the MSII state was obtained under IR irradiation of MSI. The long lifetime of the MSII species allows specific structural signatures on both unit-cell parameters and Bragg peak intensities to be recorded, and the side-on configuration of

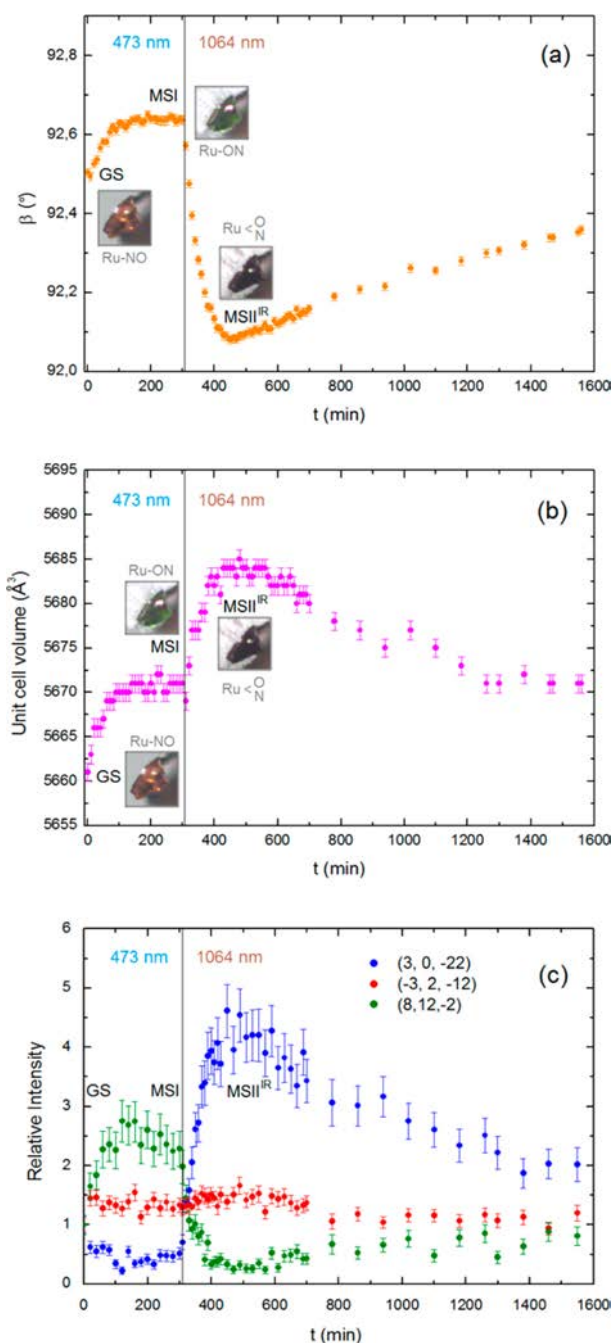


Figure 1. Time evolution of the (a) β angle (deg), (b) unit-cell volume, and (c) Bragg peak intensities when first irradiated at 473 nm, around $280 \text{ mW}/\text{cm}^2$, and second at 1064 nm, around $130 \text{ mW}/\text{cm}^2$, at 100 K.

MSII species is seen through additional electronic densities on both sides of Ru–N–O.^{18,21} The population of the MSII species (a few tens of percent) is highest when the monoclinic unit-cell volume is maximum and the β angle is minimum during the MSI to GS transition²¹ (Figure 1). The evolution of unit-cell parameters thus offers a precise way to follow the MSI to GS photochemical reaction under IR light. At 100 K, the maximum MSII population is observed after 120 min of irradiation with a fluence of about $130 \text{ mW}/\text{cm}^2$, i.e., $Q \approx 900 \text{ J}\cdot\text{cm}^{-2}$. Concomitantly with those structural changes, the

sample turns deep black. As the pure MSII state cannot be reached, this mixed GS–MSII state is hereafter labeled as the MSII^{IR} state. The evolution of lattice parameters during Ru–ON to Ru–NO photoswitching (Figures 1 and S1) differs from that during the Ru–NO to Ru–ON phototransformation under the blue light. Moreover, the intensity evolution of some Bragg peaks (Figure 1c) also shows significant dissimilarities between blue and IR light excitation, implying that the average atomic positions in the crystal evolve differently during these two photoprocesses. Very different molecular geometries between GS, MSI, and MSII can explain the important structural rearrangements (lattice and Bragg peak intensities) resolved during the solid-state photochemical reactions.^{18,21}

Following a few tens of minutes of relative stability of the MSII^{IR} state (Figure 1), a slow evolution toward the GS state is observed. Nonetheless, at 100 K the GS state is not reached even after 15 h of CW irradiation, which might be caused either by a very slow thermal relaxation or by a low population (a few percent) of the MSI state, as seen in the SNP compound.⁷ Nevertheless, the complete transformation back to GS under IR irradiation is possible at higher temperatures and is shown at 140 K in Figure S2. The stronger structural signatures at 100 K compared to 140 K (higher unit-cell volume and β angle changes; see Figures 1 and S2) imply that the lifetime and population of the MSII species grow with a decrease of temperature. The pronounced temperature dependence of the reaction kinetics during IR irradiation demonstrates that thermal decay of the MSII population drives the relaxation back to GS just as previously shown in the prototype SNP compound. The total conversion of the metastable MSI species back to the GS state occurs rapidly by heating the sample above 260 K. Moreover, the single crystal preserves its switching yield after several cycles contrary to a powder sample.¹⁹

Evidence of a Two-Step Photon Absorption Driving the Ru–NO to Ru–ON Switching. The significant color change observed on $[\text{Ru}(\text{py})_4\text{Cl}(\text{NO})](\text{PF}_6)_2 \cdot 1/2\text{H}_2\text{O}$ single crystals during the photochemical reaction has been quantitatively followed by visible (vis) absorption spectroscopy.²²

Figure 2a shows the time evolution of the optical density (OD) under blue light at different times of irradiation at 100 K. A stable OD spectrum is obtained after less than 2 h of irradiation (total exposure Q around $8000 \text{ J}\cdot\text{cm}^{-2}$), and for spectral discrimination of any intermediates hereafter, we consider that 100% MSI population is reached after such prolonged irradiation with a blue laser. OD evolution in time (Figure 2a) cannot be explained by a sum of only two contributions, i.e., GS and MSI: the lack of an isobestic point during spectral evolution unambiguously indicates the existence of intermediate state(s). The possibility of MSII being an intermediate state can be tested at 180 K, when MSII species relax too quickly to transfer enough population to MSI with CW¹⁹ (Figure 2b). The difference from the case of 100 K is significant: in spite of a small evolution on the red side of the OD, the quasi-complete MSI state cannot be reached. At 180 K, the saturation of the signal is observed after 30 min, and all spectra can be interpreted as a weighted contribution of GS and MSI, with the MSI population not exceeding 10%. Therefore, a two-step photon absorption process through MSII has to be considered as the most likely pathway for the Ru–NO to Ru–ON photoswitching in the model of the $[\text{Ru}(\text{py})_4\text{Cl}(\text{NO})](\text{PF}_6)_2 \cdot 1/2\text{H}_2\text{O}$ system (Scheme 2).

Such predominant two-step photon absorption in the blue spectral range differs from that observed on SNP, where both

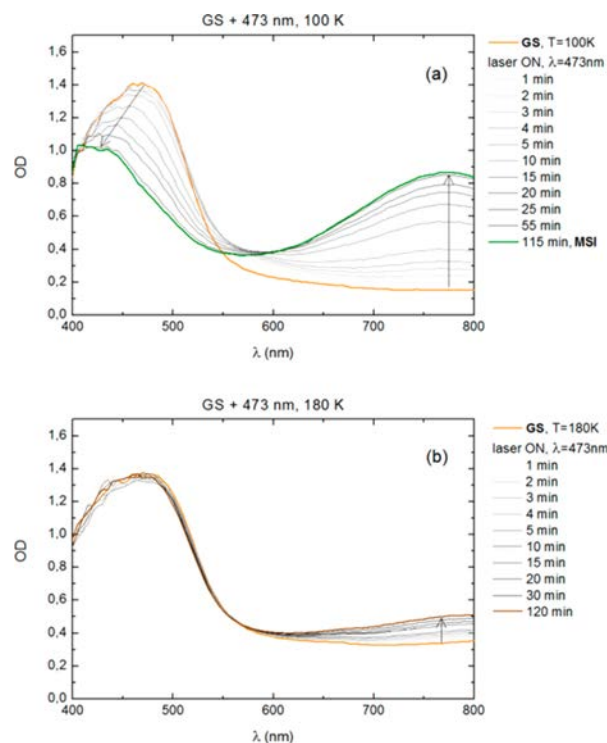
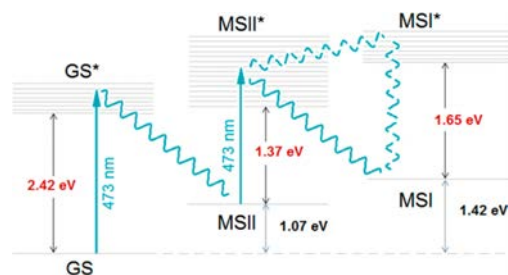


Figure 2. Ru–NO to Ru–ON photoswitching probed by the time evolution of the OD of one $[\text{Ru}(\text{py})_4\text{Cl}(\text{NO})](\text{PF}_6)_2 \cdot 1/2\text{H}_2\text{O}$ single crystal at 473 nm, around $1100 \text{ mW}/\text{cm}^2$, and (a) at 100 K and (b) at 180 K.

Scheme 2. Relative Positions of the MSI and MSII States of the $[\text{Ru}(\text{py})_4\text{Cl}(\text{NO})]^{2+}$ Complex and Their Excited States and the Excited Level of the GS State^a



^aVertical arrows represent irradiation of 473 nm with a two-step photon absorption process through the MSII state. The red numbers stand for the calculated values of energy,¹⁹ while the black ones stand for the measured values.¹⁹ Dashed wavy lines express a possible complex pathway between the MSII* and MSI* excited states²⁴ which cannot be probed by continuous light irradiation.

direct and two-step channels are equally involved.¹⁴ Such a two-step photon absorption process was previously observed on other ruthenium nitrosyl compounds such as $[\text{Ru}(\text{NH}_3)_5\text{NO}]\text{Cl}_3 \cdot \text{H}_2\text{O}$;²³ however, it is associated with a quasi-complete GS to MSI photochemical efficiency (only 11% in $[\text{Ru}(\text{NH}_3)_5\text{NO}]\text{Cl}_3 \cdot \text{H}_2\text{O}$). In the prototype SNP, a two-step process is favored by shifting the wavelength to the green; however, its efficiency is low (only a few percent).¹⁴ For the $[\text{Ru}(\text{py})_4\text{Cl}(\text{NO})](\text{PF}_6)_2 \cdot 1/2\text{H}_2\text{O}$ system, the change of wavelength to green, 532 nm, strongly affects the photochemical reaction too, and at 100 K the MSI population reaches 10% at most (Figure

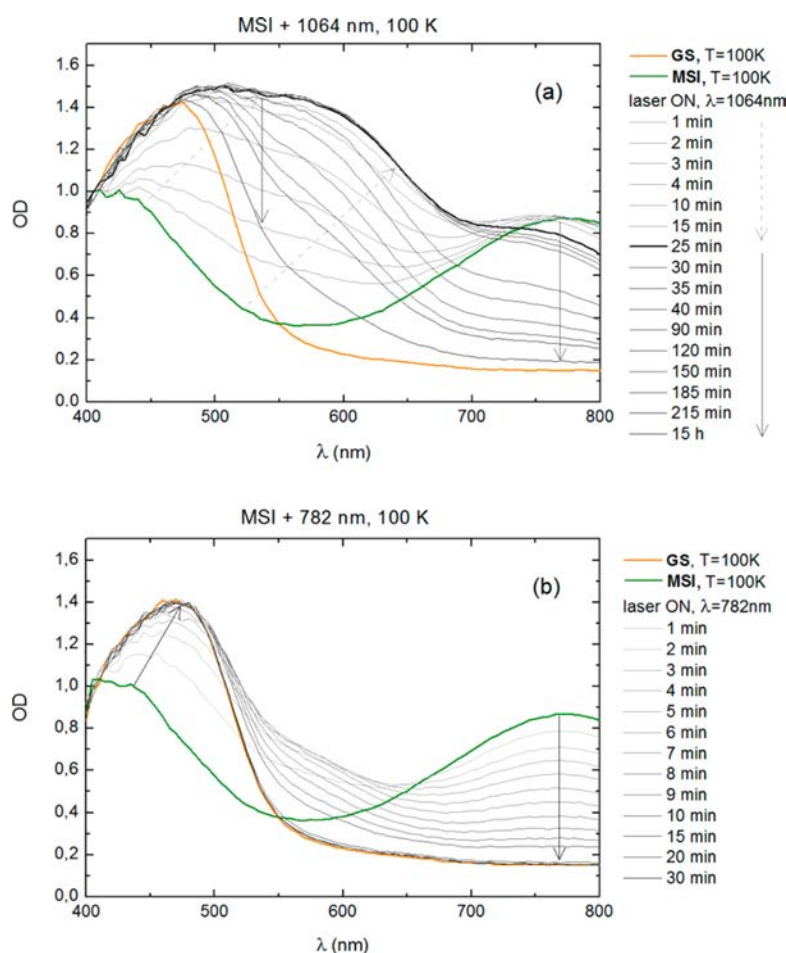


Figure 3. Ru–ON to Ru–NO photoswitching probed by the time evolution of the OD of one $[\text{Ru}(\text{py})_4\text{Cl}(\text{NO})](\text{PF}_6)_2 \cdot \frac{1}{2}\text{H}_2\text{O}$ single crystal at 100 K and (a) 1064 nm, around $600 \text{ mW}/\text{cm}^2$, and (b) 782 nm, around $180 \text{ mW}/\text{cm}^2$.

S3). We rationalize this irradiation wavelength dependency in the following paragraphs. Under 532 nm, the low transformation rate results in the absence of lattice parameter evolution during the X-ray diffraction experiment. The higher sensitivity of the optical measurements²² is better suited to follow a low percentage of metastable species.

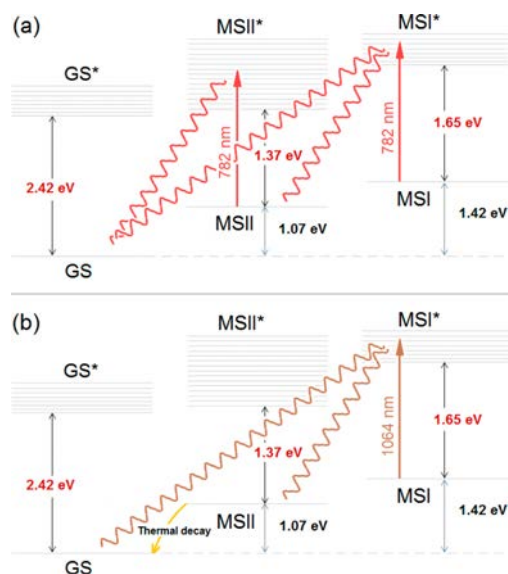
Ru–ON to Ru–NO Reverse Photoswitching Probed by Visible Spectroscopy. The reverse photochemical process, i.e., the Ru–ON to Ru–NO photoswitching under the red and IR light irradiation has been followed with visible spectroscopy. One can see that IR light (1064 nm) causes the blackening of the crystal¹⁸ as illustrated by the increase of the OD within the whole visible range. We obtained a high population of MSII species, referred to MSII^{IR} in X-ray studies, after around 25 min of irradiation at about $600 \text{ mW}/\text{cm}^2$, i.e., $Q \approx 900 \text{ J}\cdot\text{cm}^{-2}$ (Figure 3a). Opposite the Ru–NO to Ru–ON photoswitching, which predominantly proceeds through two-step photon absorption, the reverse process under IR irradiation proceeds through thermal decay of the MSII species, which substantially slows the kinetics of photochemical reaction with a temperature decrease.

As well as in the prototype SNP compound,¹⁴ the irradiation of the MSI state of the $[\text{Ru}(\text{py})_4\text{Cl}(\text{NO})](\text{PF}_6)_2 \cdot \frac{1}{2}\text{H}_2\text{O}$ complex at 100 K with red light, 782 nm, leads to the complete and quite fast relaxation back to the GS state (Figure 3b). The missing isosbestic point in the time evolution at 100 K, its

observation at 180 K (Figure S4a) and the relaxation back to the GS state from the MSII^{IR} state at 100 K under red light (Figure S4b) support the idea of an intermediate MSII state. Unlike the Ru–NO to Ru–ON photoswitching with the blue light, at 180 K (see and compare Figure 2b and Figure S4a), the complete transformation to GS with the red irradiation suggests that both the two-step process through MSII and direct de-excitation to GS coexist. Indeed, we cannot distinguish between these two channels with measurements under CW irradiation. Scheme 3 summarizes the various possibilities for the Ru–ON to Ru–NO photoswitching. Two main differences between red and IR light irradiations can be underlined. Under the red light irradiation, a very efficient back-switching occurs either through a direct de-excitation or through a two-step process via the MSII and MSII* species. Under IR irradiation, the process is dominated by the thermal decay of the MSII species not absorbing IR light. Absorption of IR light by the MSI species suggests that the energy difference between the MSI and MSII* species, 1.65 eV,¹⁹ is significantly overestimated.

OD Spectra and Properties of MSII. The major result of our work is the experimental evidence of a two-step photon absorption process during the Ru–NO to Ru–ON photoswitching under blue light irradiation through the absence of an isosbestic point on the time evolution of the OD spectra (Figure 2 a). This result is supported by new DFT calculations.²⁴ Irradiation with IR light is a unique way to

Scheme 3. Relative Positions of the MSI and MSII States of the $[\text{Ru}(\text{py})_4\text{Cl}(\text{NO})]^{2+}$ Complex and Their Excited States and the Excited Level of the GS State^a



^aAll energy values were taken from ref 19. Vertical arrows represent irradiation of (a) 782 nm and (b) 1064 nm. The darker red numbers stand for the calculated values, while the black ones stand for the measured values.

observe both clear optical and structural signatures (Figures 1 and 3a) thanks to the nonabsorption of IR light by the MSII species (Scheme 3). The MSII state (side-on configuration) is clearly the transient state observed during the Ru–ON to Ru–NO switching under IR light.

The OD spectrum of the MSII^{IR} state (Figure 3a) corroborates the idea of the MSII species (side-on configuration) as a possible intermediate during the two-step process from Ru–NO to Ru–ON: the black color evidence on absorption in the visible range, though it does not explain the difference between the results at 100 K upon irradiation with the blue, 473 nm, and green, 532 nm, light (see and compare Figure 2a and Figure S3). To understand this, we studied the effect of these two wavelengths on MSII^{IR} (black color) (see Figure S5). With the blue light the crystal returns to the MSI state, while the green light irradiation brings the system to the mixed GS–MSI state with a population of the MSI species not higher than 10%. Therefore, the predominant relaxation of the excited MSII species (MSII*) back to the GS state instead of the MSI state under the green light irradiation is responsible for the obtained differences (see and compare Schemes 2 and S1). The very high efficiency of the photoprocess in the blue spectral range means that the relaxation between MSII* and GS is negligible (therefore not represented in Scheme 2).

Two-step photon absorption is observed here both for the complete Ru–NO to Ru–ON switching under blue light and for the reverse process under red light irradiation. The continuous light allows only species with a long lifetime to be probed, i.e., GS, MSI, and MSII (see Schemes 2 and 3), and not the corresponding excited states, labeled GS*, MSI*, and MSII*. All intermediate spectra in Figures 2a and 3b result from a combination of GS, MSI, and MSII. However, it seems that the MSII species reveal different spectra for the Ru–NO to Ru–ON switching and for the reverse process (compare

Figures 2a and 3b). On one hand, under 782 nm (Figure 3b), the quite high OD in the interval 550–650 nm is consistent with the MSII OD signature observed under IR light (Figure 3a). On the other hand, the intermediate OD in the interval 550–650 nm observed during the Ru–NO to Ru–ON process under 473 nm irradiation (Figure 2a) does not exhibit similar high values.

Under continuous light irradiation, the unique possibility to obtain an absorption spectrum of the intermediate is to retrieve it with a kinetic model.²⁵ The simplest one considers three states (GS, MSI, and MSII) and two kinetic constants ($K_{\text{GS} \rightarrow \text{MSII}}$, $K_{\text{MSII} \rightarrow \text{MSI}}$); i.e., it neglects the direct transformation from GS to MSI because of the predominant two-step photon absorption (see the experimental section provided in the Supporting Information). The model optimizes the contribution of the residual spectrum to reproduce the time evolution of OD spectra during the photoconversion (Figure 2a) with OD spectra of GS and MSI unambiguously determined. Thus, the OD spectrum of the intermediate MSII state is obtained, and it is shown in Figure 4. It reveals a maximum of absorption in the

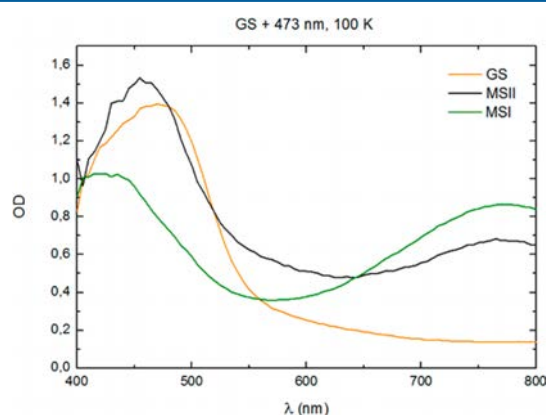


Figure 4. OD spectra of the GS and MSI states (experimental data) and OD spectra of the intermediate MSII state deduced from the kinetic model reproducing the OD evolution under 473 nm.

blue region. The use of the obtained OD signature of the long-lived transient MSII state to reproduce the experimental spectrum of MSII^{IR} turns out to be impossible because of the broad maximum of the OD spectrum in the green-yellow region (Figure 3a).

As the molecular geometry can strongly influence the optical properties (see Figures 1 and 2), we suggest that the geometry of the transient MSII species under blue light excitation differs from the 90° side-on configuration.^{18,21} However, the optical signature of the pure transient MSII species and/or structural signature of the transient species during the Ru–NO to Ru–ON process will be necessary for clear-cut evidence. Ultrashort laser pump and time-resolved experiments hold the promise of providing such evidence.

CONCLUSION

The Ru–NO to Ru–ON phototransformation and the reverse process have been studied in detail on single crystals of $[\text{Ru}(\text{py})_4\text{Cl}(\text{NO})](\text{PF}_6)_2 \cdot 1/2\text{H}_2\text{O}$, the model system for the M–NO/M–ON photoisomerization. Arguably, a precise knowledge about this process could help to understand the NO release process, as MSI and MSII species are suggested to be intermediate states upon this irreversible bond breaking.²⁶

Remarkably, in $[\text{Ru}(\text{py})_4\text{Cl}(\text{NO})](\text{PF}_6)_2 \cdot 1/2\text{H}_2\text{O}$ single crystals, a predominant two-step process through long-lived MSII species during the Ru–NO to Ru–ON photoswitching is observed with visible absorption spectroscopy under blue CW irradiation. The low concentration of the transient MSII species hinders the detection of any structural signature (population of transient species lower than a few percent). However, pronounced structural signatures (in particular on the monoclinic angle β) are evidenced during the Ru–ON back to Ru–NO process under IR light.

The visible absorbance of the MSII^{IR} state (mixture of GS and the MSII side-on configuration) has been experimentally determined. Evolution of the spectra during Ru–NO to Ru–ON and the reverse process as well as a simple kinetic model used to reproduce the experimental evolution of the OD spectra during the Ru–NO to Ru–ON photoswitching (under blue light irradiation) show that the optical signature associated with the transient MSII species depends on the direction of the photochemical reaction. The side-on configuration of the intermediate MSII species cannot be unambiguously revealed during the photoswitching under blue light irradiation; thus, further investigations using ultrashort laser pulses are necessary to clarify that point.

■ ASSOCIATED CONTENT

Supporting Information

The Supporting Information is available free of charge on the ACS Publications website at DOI: [10.1021/acs.inorgchem.5b02572](https://doi.org/10.1021/acs.inorgchem.5b02572).

Experimental Section, evolution of unit-cell parameters during Ru–NO to Ru–ON photoswitching and the reverse process at 100 K (Figure S1) and 140 K (Figure S2), Ru–NO to Ru–ON photoswitching probed using green light irradiation, 532 nm (Figure S3), effect of red light irradiation, 782 nm, at 180 K and effect of red light irradiation of the MSII^{IR} state at 100 K probed by visible absorption spectroscopy (Figure S4), effect of blue, 473 nm, and green, 532 nm, light irradiation on the MSII^{IR} state at 100 K probed by visible absorption spectroscopy (Figure S5), time evolution of the OD spectra under blue light irradiation reproducing the experimental data with a three-state (GS, MSI, and MSII) kinetic model (Figure S6), and relative positions of GS, MSI and MSII energy levels with possible photoswitching pathways under green light irradiation (Scheme 1) (PDF)

GS state, 100 K (CIF)

Mixed GS–MSI state, 100 K (CIF)

MSI state, 100 K (CIF)

■ AUTHOR INFORMATION

Corresponding Authors

*E-mail: marylise.buron@univ-rennes1.fr.

*E-mail: isabelle.malfant@lcc-toulouse.fr.

Present Address

[§]W.K.: Institute of Electronic Materials Technology, 133 Wolczynska Street, 01-919 Warszawa, Poland.

Funding

This work was financially supported by the French Ministry of Research (Ph.D. grant to L.K.), the Centre National de la Recherche Scientifique (CNRS), Région Bretagne, the Agence Nationale de la Recherche (ANR) (Grant 13-BS04-0002), and the European Regional Development Fund (FEDER).

Notes

The authors declare no competing financial interest.

■ ACKNOWLEDGMENTS

We thank Marco Cammarata for fruitful discussions, in particular concerning the kinetic model, and Loïc Toupet for technical assistance during the X-ray diffraction experiments.

■ REFERENCES

- (1) (a) Hauser, U.; Oestreich, V.; Rohrweck, H. D. *Z. Phys. A: At. Nucl.* **1977**, *A280*, 17–25. (b) Hauser, U.; Oestreich, V.; Rohrweck, H. D. *Z. Phys. A: At. Nucl.* **1977**, *A280*, 125–130. (c) Hauser, U.; Oestreich, V.; Rohrweck, H. D. *Z. Phys. A: At. Nucl.* **1978**, *A284*, 9–19.
- (2) Zöllner, H.; Woike, T.; Krasser, W.; Haussühl, S. *Z. Kristallogr.* **1989**, *188*, 139–153.
- (3) Pressprich, M. R.; White, M. A.; Vekhter, Y.; Coppens, P. *J. Am. Chem. Soc.* **1994**, *116*, 5233–5238.
- (4) Güdel, H. U. *Chem. Phys. Lett.* **1990**, *175*, 262–266.
- (5) Carducci, M. D.; Pressprich, M. R.; Coppens, P. *J. Am. Chem. Soc.* **1997**, *119*, 2669.
- (6) Schaniel, D.; Woike, T.; Schefer, J.; Petricek, V. *Phys. Rev. B: Condens. Matter Mater. Phys.* **2005**, *71*, 174112.
- (7) Delley, B.; Schefer, J.; Woike, T. *J. Chem. Phys.* **1997**, *107*, 10067.
- (8) Zöllner, H.; Krasser, W.; Woike, T.; Haussühl, S. *Chem. Phys. Lett.* **1989**, *161*, 497–501.
- (9) Coppens, P.; Novozhilova, I.; Kovalevsky, A. *Chem. Rev.* **2002**, *102*, 861–883.
- (10) Schaniel, D.; Woike, T. *Phys. Chem. Chem. Phys.* **2009**, *11*, 4391–4395.
- (11) *NOx Related Chemistry*; van Eldik, R., Olabe, J. A., Eds.; Advances in Inorganic Chemistry, Vol. 67; Academic Press: New York, 2015.
- (12) Woike, T.; Krasser, W.; Bechthold, P. S.; Haussühl, S. *Phys. Rev. Lett.* **1984**, *53*, 1767–1770.
- (13) Gütlich, P.; Garcia, Y.; Woike, T. *Coord. Chem. Rev.* **2001**, *219–221*, 839–879.
- (14) Woike, T.; Krasser, W.; Zöllner, H.; Kirchner, W.; Haussühl, S. *Z. Phys. D: At. Mol. Clusters* **1993**, *D25*, 351–356.
- (15) Schaniel, D.; Nicoul, M.; Woike, T. *Phys. Chem. Chem. Phys.* **2010**, *12*, 9029–9033.
- (16) Gallé, G.; Nicoul, M.; Woike, T.; Schaniel, D.; Freysz, E. *Chem. Phys. Lett.* **2012**, *552*, 64–68.
- (17) Dieckmann, V.; Eicke, S.; Springfeld, K.; Imlau, M. *Materials* **2012**, *5*, 1155–1175.
- (18) Cormary, B.; Malfant, I.; Buron-Le Cointe, M.; Toupet, L.; Delley, B.; Schaniel, D.; Mockus, N.; Woike, T.; Fejfarova, K.; Petricek, V.; Dusek, M. *Acta Crystallogr., Sect. B: Struct. Sci.* **2009**, *B65*, 612–623.
- (19) Schaniel, D.; Cormary, B.; Malfant, I.; Valade, L.; Woike, T.; Delley, B.; Krämer, K. W.; Güdel, H. U. *Phys. Chem. Chem. Phys.* **2007**, *9*, 3717–3724.
- (20) CCDC-1040140 (GS), CCDC-1040141 (mixed GS–MSI), and CCDC-1040190 (MSI) contain the supplementary crystallographic data for this paper. The mixed GS–MSI model refines the MSI conversion rate under restricted position constraints (same positions and thermal parameters for N and O). These data can be obtained free of charge via www.ccdc.cam.ac.uk/conts/retrieving.html (or from the Cambridge Crystallographic Data Centre, 12 Union Rd., Cambridge CB21EZ, U.K.; fax (+44) 1223-336033; e-mail deposit@ccdc.cam.ac.uk).
- (21) A detailed structural analysis will be published separately.
- (22) Whether X-ray diffraction can capture transient species depends essentially on the concentration of those species and their structure factors (atomic constitution). Visible absorption spectroscopy can be more sensitive in capturing transients, in that a low concentration of species can be compensated by their significant extinction coefficients. Electronic transition moments may be very different despite identical atomic constitutions of the molecules under consideration.
- (23) Schaniel, D.; Woike, T.; Boskovic, C.; Güdel, H. U. *Chem. Phys. Lett.* **2004**, *390*, 347–351.

(24) Sanz Garcia, J.; Alary, F.; Boggio-Pasqua, M.; Dixon, I.; Malfant, I.; Heully, J.-L. *Inorg. Chem.* **2015**, *54*, 8310–8318.

(25) Cammarata, M.; Levantino, M.; Wulff, M.; Cupane, A. *J. Mol. Biol.* **2010**, *400*, 951–962.

(26) Karidi, K.; Garoufis, A.; Tsepis, A.; Hadjiliadis, N.; den Dulk, H.; Reedijk, J. *Dalton Trans.* **2005**, 1176–1187.

Two-Step Photon Absorption Driving the Chemical Reaction in the Model Ruthenium Nitrosyl System $[\text{Ru}(\text{py})_4\text{Cl}(\text{NO})](\text{PF}_6)_2 \cdot 1/2 \text{H}_2\text{O}$.

Liya Khadeeva #, Wawrzyniec Kaszub #†, Maciej Lorenc #, Isabelle Malfant §*, and Marylise Buron-Le Cointe #*.

Institut de Physique de Rennes, UMR UR1-CNRS 6251, Université Rennes 1, avenue du général Leclerc, 35042 Rennes, Cedex, FRANCE.

§ Laboratoire de Chimie de Coordination, CNRS UPR 8241, 205 route de Narbonne, 31077 Toulouse Cedex, FRANCE.

Supporting Information:

Contents:

Experimental section.

Figure S1. Evolution of the lattice parameters a, b and c during the light irradiation of the $[\text{Ru}(\text{py})_4\text{Cl}(\text{NO})](\text{PF}_6)_2 \cdot 1/2\text{H}_2\text{O}$ single crystal at 100 K with 473 nm, around $280 \text{ mW} \cdot \text{cm}^{-2}$ and then 1064 nm, around $130 \text{ mW} \cdot \text{cm}^{-2}$.

Figure S2. Time evolution of (a) the β angle (degree) and (b) unit cell volume when first using 473 nm, ($280 \text{ mW} \cdot \text{cm}^{-2}$) (Ru-NO to Ru-ON photo-switching) and second using 1064 nm, $130 \text{ mW} \cdot \text{cm}^{-2}$ (Ru-ON to Ru-NO photoswitching through MSII state) at 140 K.

Figure S3. Evolution of the OD during the light irradiation of the $[\text{Ru}(\text{py})_4\text{Cl}(\text{NO})](\text{PF}_6)_2 \cdot 1/2\text{H}_2\text{O}$ single crystal at 100 K with 532 nm, around $1500 \text{ mW} \cdot \text{cm}^{-2}$.

Figure S4. (a) Evolution of the OD during the light irradiation of the $[\text{Ru}(\text{py})_4\text{Cl}(\text{NO})](\text{PF}_6)_2 \cdot 1/2\text{H}_2\text{O}$ single crystal with 782 nm, $180 \text{ mW} \cdot \text{cm}^{-2}$ at 180 K. (b) Evolution of the OD during the light irradiation of the $[\text{Ru}(\text{py})_4\text{Cl}(\text{NO})](\text{PF}_6)_2 \cdot 1/2\text{H}_2\text{O}$ single crystal with 1064 nm, $600 \text{ mW} \cdot \text{cm}^{-2}$ up to MSII^{IR} (black thick line) and then with 782 nm, $180 \text{ mW} \cdot \text{cm}^{-2}$ at 100 K. MSII^{IR} indicates the highest population of MSII species reached during the experiment.

Figure S5. Evolution of the OD during the light irradiation of the $[\text{Ru}(\text{py})_4\text{Cl}(\text{NO})](\text{PF}_6)_2 \cdot 1/2\text{H}_2\text{O}$ single crystal at 100 K with 1064 nm, 600 $\text{mW}\cdot\text{cm}^{-2}$ up to MSII^{IR} (black thick line) and then (a) with 473 nm, around 1100 $\text{mW}\cdot\text{cm}^{-2}$, (b) with 532 nm, around 1500 $\text{mW}\cdot\text{cm}^{-2}$. MSII^{IR} indicates the highest population of MSII species reached during the experiment.

Figure S6. Agreement between the experimental data (points) and the three state (GS, MSI and MSII) kinetic model for reproducing the experimental intermediate OD spectra during the GS to MSI photo-transformation. View in 3D.

Scheme S1. Relative positions of the MSI and MSII states of $[\text{Ru}(\text{py})_4\text{Cl}(\text{NO})]^{2+}$ complex, their excited states and excited level of the GS state. (From Ref [19]). Arrows represent green, 532 nm, irradiation. The red numbers stand for the calculated values, while the black ones for the measured values.

Experimental section:

Visible absorption spectroscopy. Absorption spectra of single crystals were collected by home-made spectrograph able to cover visible range with accuracy down to $d\lambda = 5\text{nm}$. Dedicated wavelength was chosen by monochromator (Digikröm CM110) equipped with the slit 0,6 mm, seeded by the halogen lamp (Spectral Products, model: ASBN-W150). Higher orders of the diffraction grating are rejected. Probe light was mechanically chopped down to 500 Hz and focused on the sample by home-made objective with spot size of the image of the halogen lamp filament around $150 \times 300 \mu\text{m}^2$, while the typical size of the investigated crystal was $450 \times 500 \mu\text{m}^2$ for a thickness of about 100 μm . Spectral changes of transmitted light were detected by photodiode (Thorlabs DET10, DET36) and correlated with the reference signal recorded by second photodiode (reference, Thorlabs DET10, DET36) measuring copied by the beam splitter signal before sample. Signals from photodiodes were transferred to computer via two Lock-In Amplifiers synchronized with the chopper (Thorlabs). Single measurement was controlled by LabView software correlating signals from detection system with monochromator setup and recording one spectrum in one file. The measurements were done at room temperature and at low temperatures, 100 K, 140 K, 180 K, where crystals were cooled down by CryoJet system from Oxford Cryogenics (CryoJet 700). To study the photo-induced phenomena the crystals were irradiated with diode lasers (473 nm, 532 nm, 782 nm, and 1064 nm). Precise determination of the laser powers was done using a combination of laser beam profiler (Spiricon SP620U) and pyroelectric measurements (Melles Griot Broadband power meter 13PEM001). The FWHM width of the gaussian laser profile was measured and the power delivered per cm^2 was deduced after taking into account the 0.76 factor between the power delivered within this FWHM width and the total power considering the whole gaussian beam.

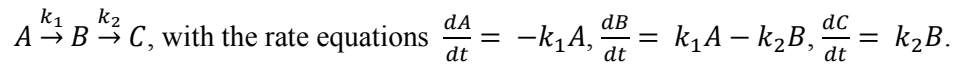
X-Ray diffraction. Structural investigations under continuous light irradiation were performed by X-ray diffraction on single crystals (473 nm, $280 \text{mW}\cdot\text{cm}^{-2}$; 1064 nm, $130 \text{mW}\cdot\text{cm}^{-2}$). Data were collected on a four-circle Oxford Diffraction Xcalibur 3 diffractometer (MoK_α radiation) with a 2D Sapphire 3 CCD detector, on samples with typical sizes around $300 \times 200 \times 100 \mu\text{m}^3$. The single crystals were mounted in an Oxford Cryosystems nitrogen-flow cryostat allowing a precise control of temperature at 100 and 140 K. The unit cell parameters and the data reduction were obtained with CrysAlis software from Oxford Diffractionⁱ. All unit-cell parameter values are collected under light irradiation and each point corresponds to a time-average value of ten minutes. The structures were solved with SIR-97ⁱⁱ and refined with SHELXLⁱⁱⁱ. Structure refinement of the GS state and MSI one (or mixed GS-MSI) gives a final R1 factor equal to 0.0387 and 0.0384 respectively^{iv}.

Polarization effect. The study of the light polarization effect was carried out in ruthenium nitrosyl complex to see if there is a strong influence on the MSI population as in prototype SNP compound.

The visible absorption spectroscopy was performed with the use of the Berek Polarization Compensator on (ab) platelets. It was found that the polarization of the laser light, either parallel to **a** or parallel to **b** crystallographic axis does not play any significant role in the Ru-NO to Ru-ON photoswitching of the ruthenium nitrosyl system (identical final OD spectra in both cases).

For the X-Ray studies polarization of the laser beam is not important as the crystal is rotated along different axes during the data collection. Evolution of unit-cell parameters are collected with light on.

Kinetic model: For Ru-NO to Ru-ON photoswitching process, the following kinetic model with one intermediate state and exponential growth and decay was probed:



The model takes into account the two-step process with the following kinetic constants: $k_1 = K_{GS \rightarrow MSII}$, $k_2 = K_{MSII \rightarrow MSI}$. The kinetic constants are free parameters which are found in the data fitting.

For the analysis we consider that the experimental data can be presented as follows:

$$D(\lambda, \tau) = P(\tau) \cdot B(\lambda),$$

where $D(\lambda, \tau)$ is a matrix of spectral data points at a certain wavelength λ and time τ , $B(\lambda)$ is a matrix containing the basic spectra and $P(\tau)$ shows the populations in each basic spectra. The basic spectra consist of three components: two known spectra of GS and MSI taken from the measurements, and the spectrum of MSII state deduced from the OD evolution. Following the assumption above we can present the basis and the expected data as below:

$$B = (P_M^T \cdot P_M)^{-1} \cdot P_M^T \cdot D$$

$$D_M = P_M \cdot B$$

where subscript M stands for the model used. During the fitting procedure we verify the goodness of fit of the experimental data to the expected one by chi-squared tests, $\chi^2 = \sum_{\lambda, \tau} \left(\frac{D - D_M}{\sigma} \right)^2$.

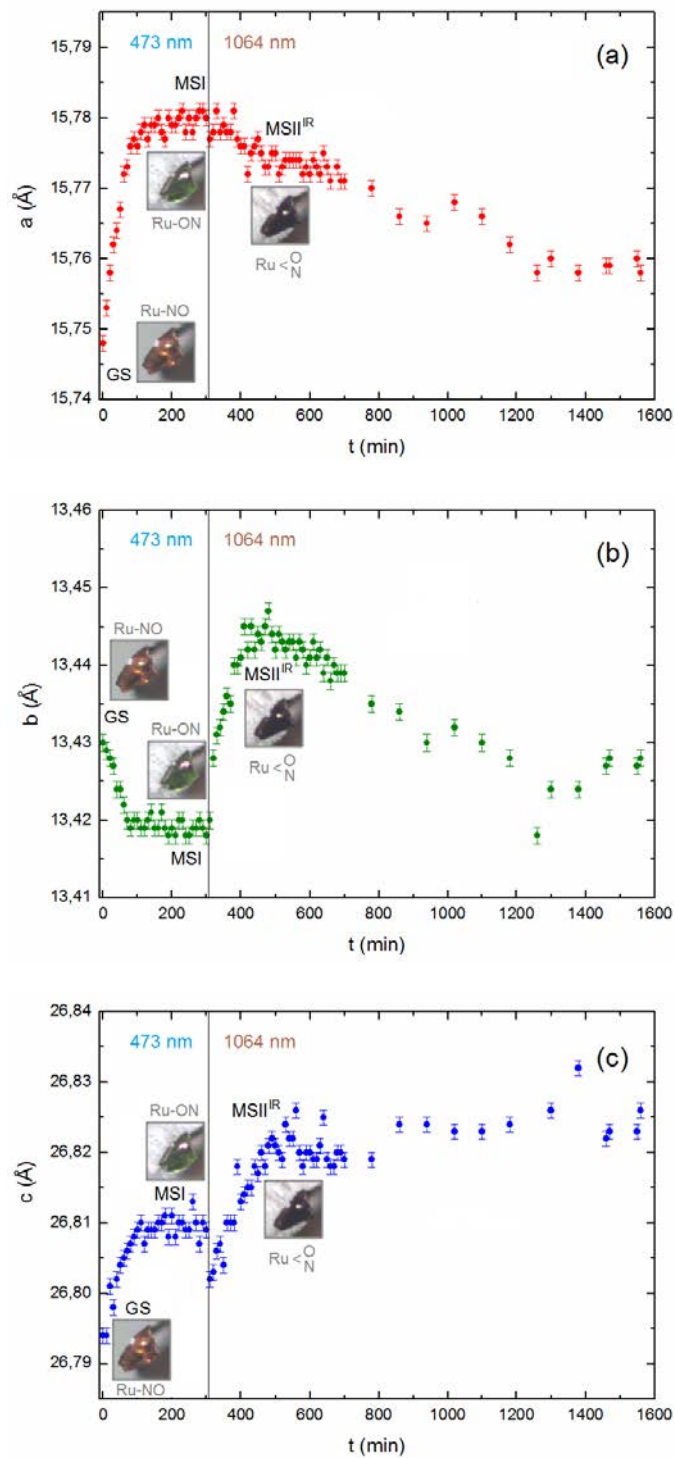


Figure S1. Evolution of the lattice parameters *a*, *b* and *c* during the light irradiation of the $[\text{Ru}(\text{py})_4\text{Cl}(\text{NO})](\text{PF}_6)_2 \cdot 1/2\text{H}_2\text{O}$ single crystal at 100 K with 473 nm, around $280 \text{ mW} \cdot \text{cm}^{-2}$ and then 1064 nm, around $130 \text{ mW} \cdot \text{cm}^{-2}$.

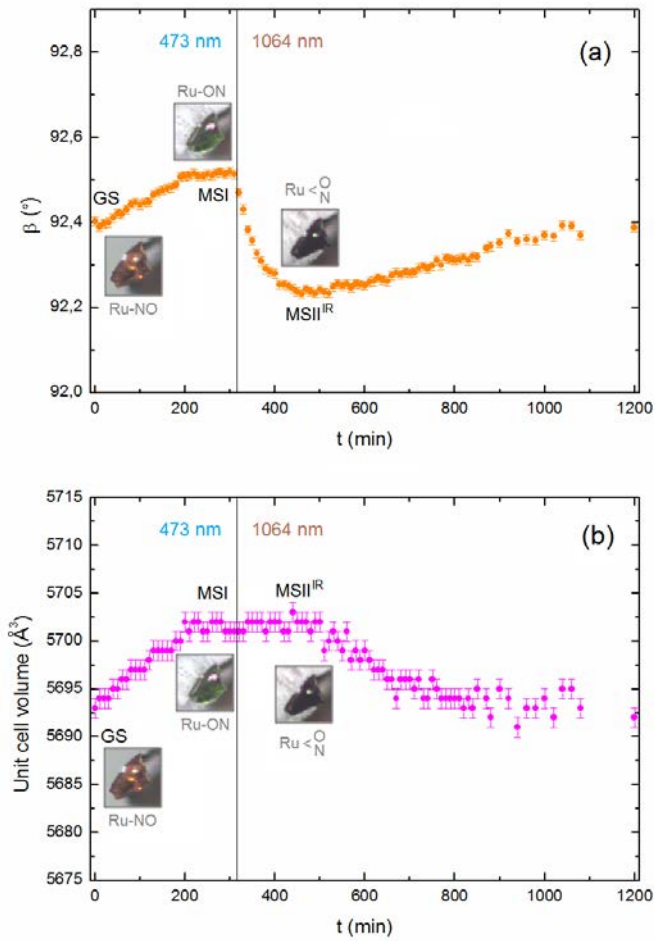


Figure S2. Time evolution of (a) the β angle (degree) and (b) unit cell volume when first using 473 nm, (280 mW.cm^{-2}) (Ru-NO to Ru-ON photo-switching) and second using 1064 nm, (130 mW.cm^{-2}) (Ru-ON to Ru-NO photoswitching through MSII state) at 140 K.

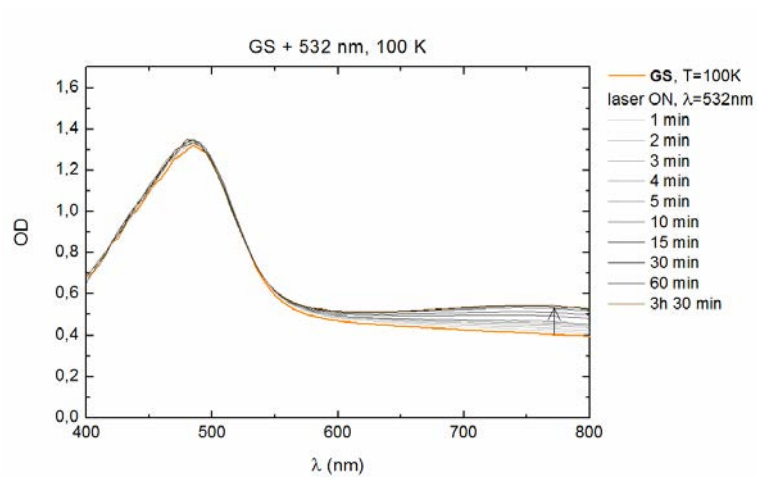


Figure S3. Evolution of the OD during the light irradiation of the $[\text{Ru}(\text{py})_4\text{Cl}(\text{NO})](\text{PF}_6)_2 \cdot 1/2\text{H}_2\text{O}$ single crystal at 100 K with 532 nm, around $1500 \text{ mW} \cdot \text{cm}^{-2}$.

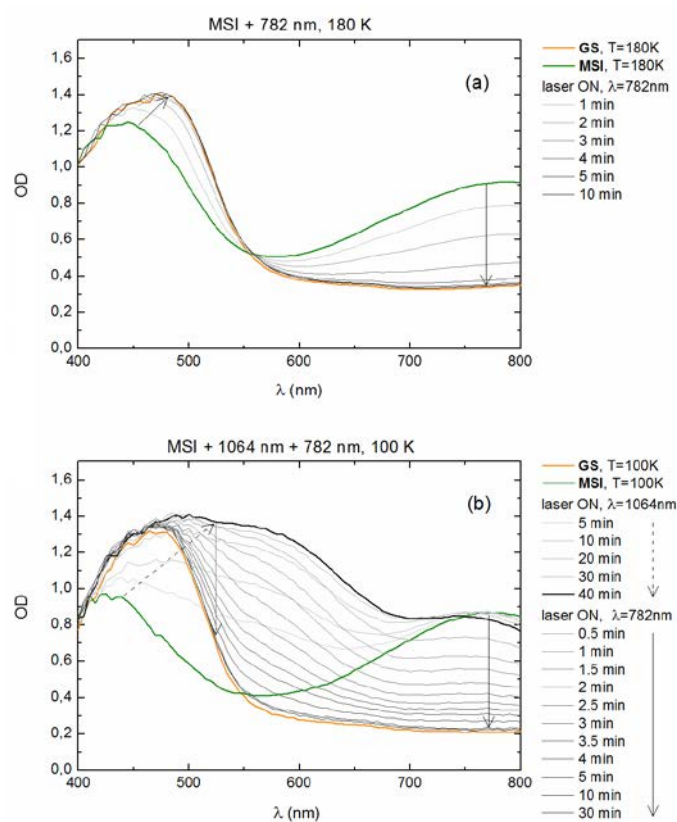


Figure S4. (a) Evolution of the OD during the light irradiation of the [Ru(py)₄Cl(NO)](PF₆)₂·1/2H₂O single crystal with 782 nm, 180 mW·cm⁻² at 180 K. (b) Evolution of the OD during the light irradiation of the [Ru(py)₄Cl(NO)](PF₆)₂·1/2H₂O single crystal with 1064 nm, 600 mW·cm⁻² up to MSII^{IR} (black thick line) and then with 782 nm, 180 mW·cm⁻² at 100 K. MSII^{IR} indicates the highest population of MSII species reached during the experiment.

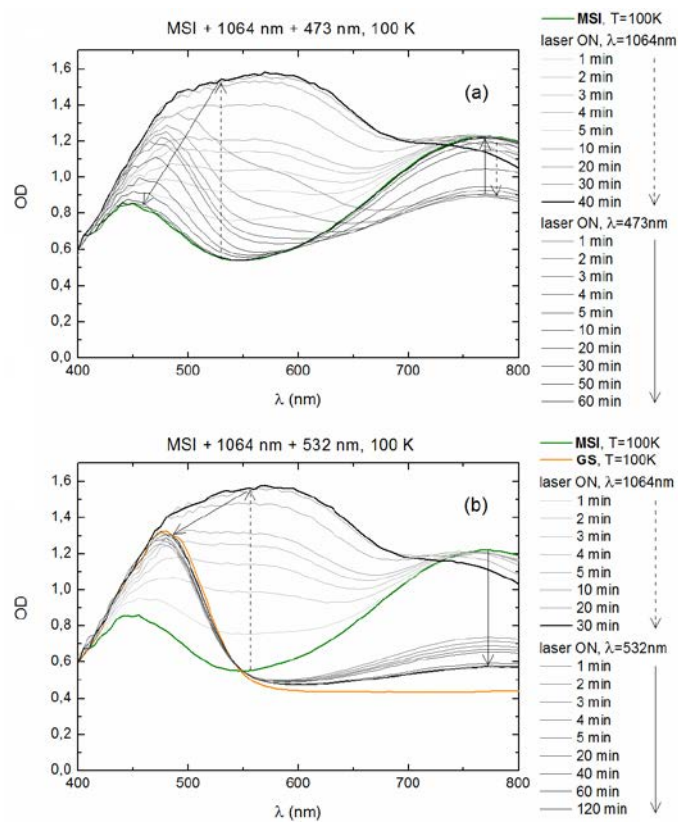


Figure S5. Evolution of the OD during the light irradiation of the $[\text{Ru}(\text{py})_4\text{Cl}(\text{NO})](\text{PF}_6)_2 \cdot 1/2\text{H}_2\text{O}$ single crystal at 100 K with 1064 nm, $600 \text{ mW}\cdot\text{cm}^{-2}$ up to MSII^{IR} (black thick line) and then (a) with 473 nm, around $1100 \text{ mW}\cdot\text{cm}^{-2}$, (b) with 532 nm, around $1500 \text{ mW}\cdot\text{cm}^{-2}$. MSII^{IR} indicates the highest population of MSII species reached during the experiment.

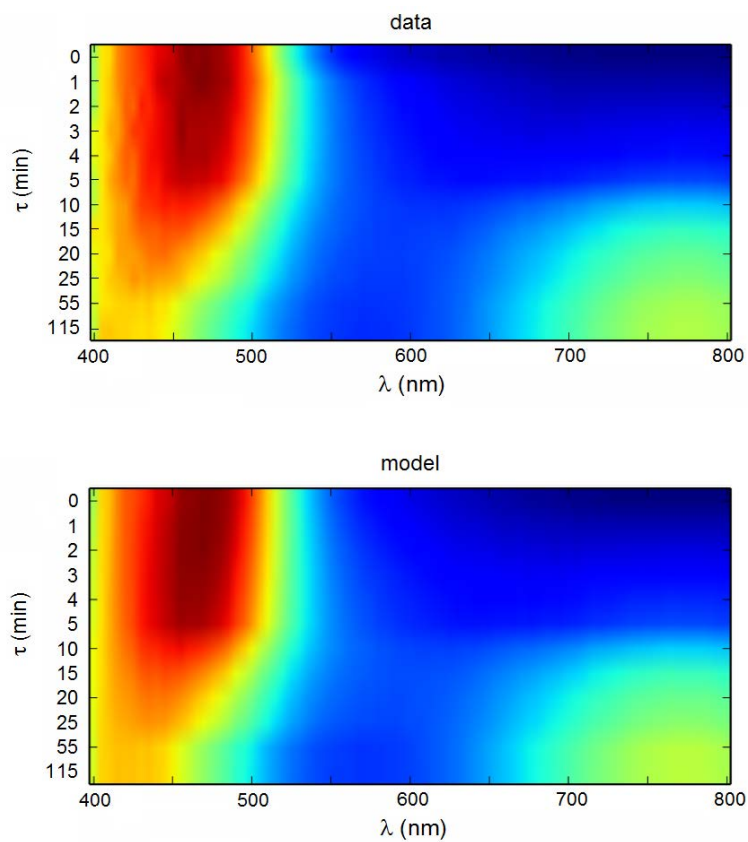
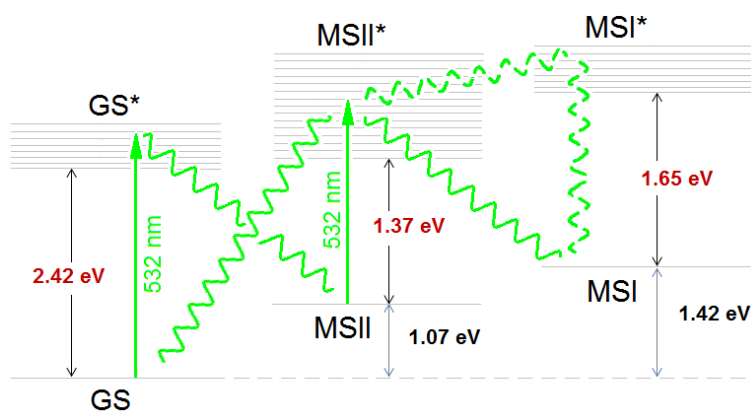


Figure S6. Agreement between the experimental data (points) and the three state (GS, MSI and MSII) kinetic model for reproducing the experimental intermediate OD spectra during the GS to MSI photo-transformation. View in 3D.



Scheme S1. Relative positions of the MSI and MSII states of $[\text{Ru}(\text{py})_4\text{Cl}(\text{NO})]^{2+}$ complex, their excited states and excited level of the GS state. (From Ref [19]). Arrows represent green, 532 nm, irradiation. The red numbers stand for the calculated values, while the black ones stand for the measured values.

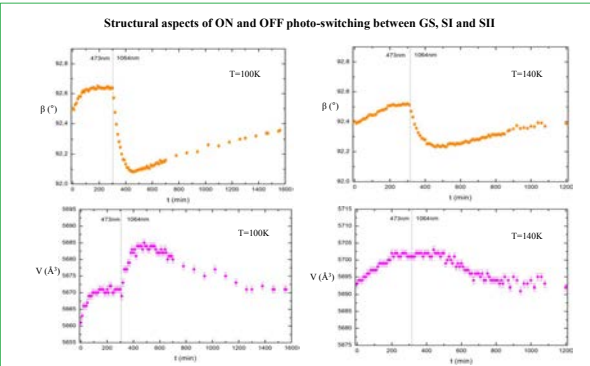
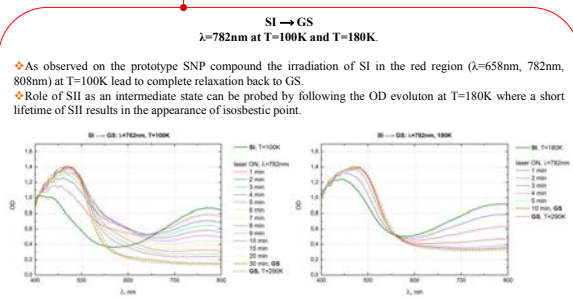
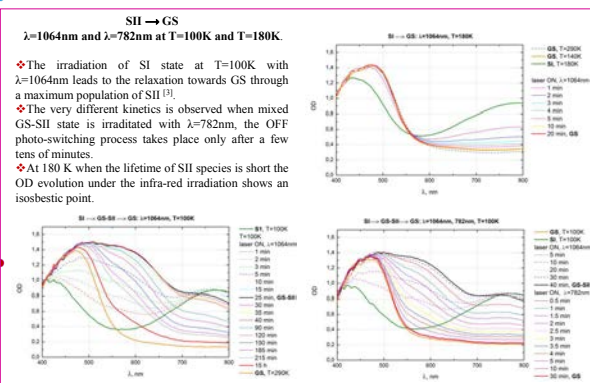
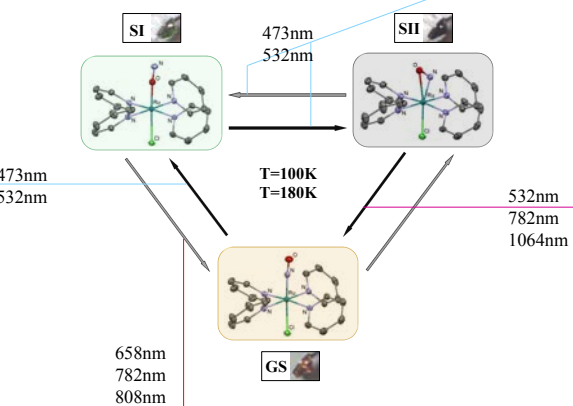
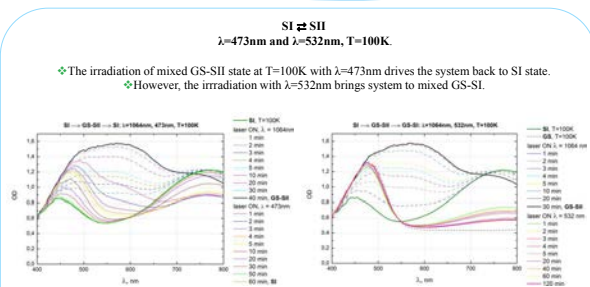
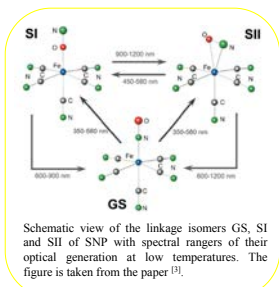
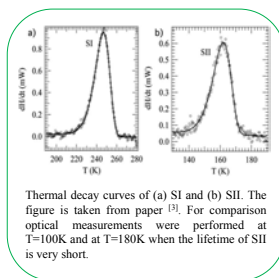
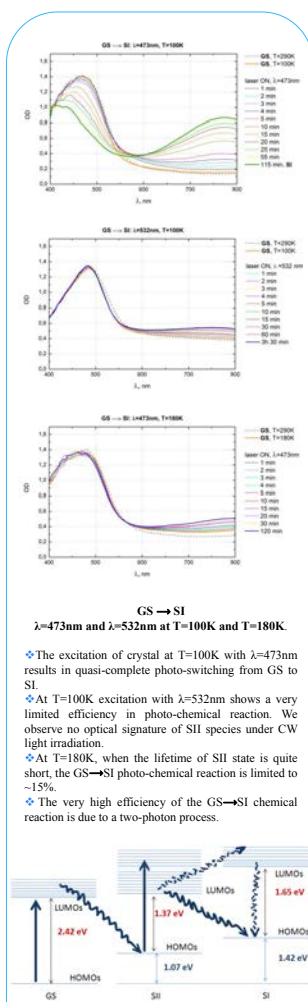
ⁱ CrysAlis RED, Oxford Diffraction Ltd, Version 1.171.32.5 (2007).

ⁱⁱ A. Altomare, M.C. Burla, M. Camalli, G. Cascareno, C. Giacovazzo, A. Guagliardi, A. G. G. Moliterni, G. Polidori, and R. Spagna *J. Appl. Cryst.* **32**, 115 (1999).

ⁱⁱⁱ G. M. Sheldrick, *Acta Cryst. A* **64**, 112 (2008).

^{iv} CCDC-1040140 (GS), CCDC-1040141 (mixed GS-MSI) and CCDC-1040190 (MSI) contain the supplementary crystallographic data for this paper. These data can be obtained free of charge via www.ccdc.cam.ac.uk/conts/retrieving.html (or from the Cambridge Crystallographic Data Centre, 12 Union Road, Cambridge CB21EZ, UK; fax: (+44) 1223-336033; or deposit@ccdc.cam.ac.uk).

Since the discovery of long-lived photo-induced metastable states at low temperature in sodium nitroprusside dihydrate compound (so-called SNP)^[1], the photo-switching between nitrosyl (GS), isonitrosyl (SI) and side-on (SII) configurations has been observed in many analogous systems containing the [ML₅NO] molecule, where M = Fe, Ru, etc. and L = F, Cl, Br, CN, etc. The obtained population rates can vary from one compound to another and reasons for such differences remain unclear. We present here the experimental investigations by absorption spectroscopy and X-Ray diffraction on single crystals of [Ru(py)₄Cl(NO)](PF₆)₂·1/2H₂O, which presents a GS to SI transformation rate close to 100%^[2].

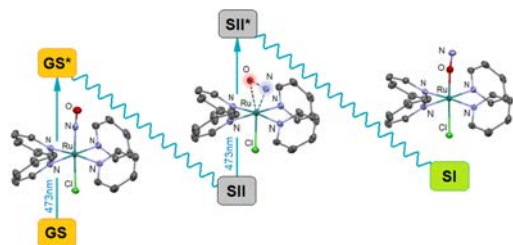


References
 [1] a) U. Hauser, V. Oestreich, H.D. Rohrweck, *Z. Phys.* 1977, A280, 17-25; b) U. Hauser, V. Oestreich, H.D. Rohrweck, *Z. Phys.* 1977, A280, 125-130; c) U. Hauser, V. Oestreich, H.D. Rohrweck, *Z. Phys.* 1978, A284, 9-19.
 [2] B. Cormary, I. Malfant, L. Valade, M. Buron-Le Cointe, L. Toupet, B. Delley, D. Schaniel, N. Mockus, T. Woike, K. Fejfarova, V. Petricek, M. Dusek, *Acta Cryst.* 2009 B65 612-623.
 [3] D. Schaniel, B. Cormary, I. Malfant, L. Valade, T. Woike, B. Delley, K. W. Krämer, H.U. Güdel, *PCCP* 2007 9 3717-3724.

Acknowledgment. We thank Fabienne Alary for fruitful discussion.

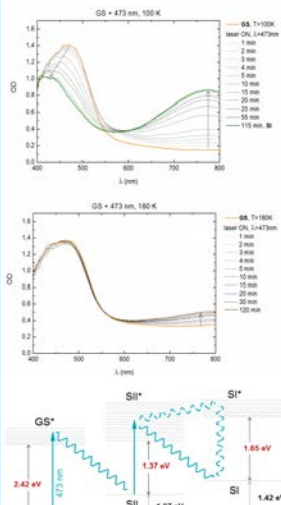
Conclusions

- ✦ A two photon process is found to play the predominant role in ON and OFF photo-switching processes in blue and red spectral ranges.
- ✦ A different pathway and kinetics are observed when IR irradiation is used: the highest SII population is then reached before the thermal relaxation back to GS.
- ✦ Clear structural changes follow the formation of SII species.

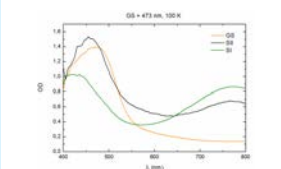


GS → SI under blue light irradiation

- ❖ The excitation of crystal at T=100K with $\lambda=473\text{nm}$ results in quasi-complete photo-switching from GS to SI (almost complete transformation).
- ❖ At T=180K, when the lifetime of SII state is quite short, the GS→SI photo-chemical reaction is limited to ~10%.

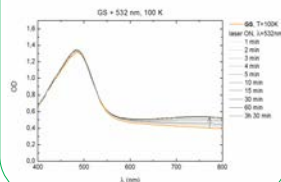


- ❖ The very high efficiency of the GS→SI chemical reaction is due to a two-step photon absorption process^[4].
- ❖ The simple kinetic model was used to deduce the optical signature of intermediate SII state.



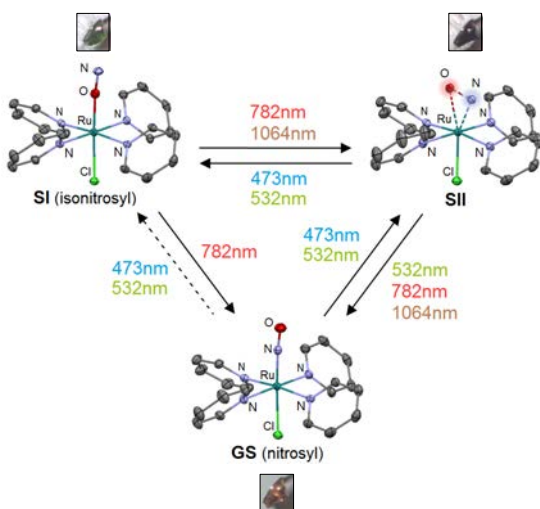
GS → SI under green light irradiation

- ❖ At T=100K excitation with $\lambda=532\text{nm}$ shows a very limited efficiency in photo-chemical reaction. We observe no optical signature of SII species under CW light irradiation.

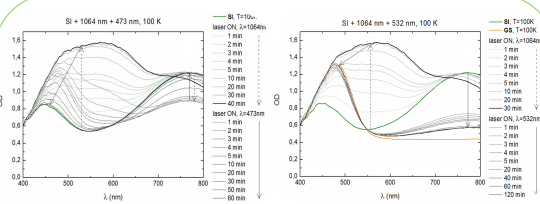


Since the discovery of long-lived photo-induced metastable states at low temperature in sodium nitroprusside dihydrate compound (so-called SNP)^[1], the photo-switching between nitrosyl (GS), isonitrosyl (SI) and side-on (SII) configurations has been observed in many analogous systems containing the $[\text{ML}_5\text{NO}]$ molecule, where M = Fe, Ru, etc. and L = F, Cl, Br, CN, etc.

The obtained population rates can vary from one compound to another and reasons for such differences remain unclear. We present here the experimental investigations by visible absorption spectroscopy and X-Ray diffraction on single crystals of $[\text{Ru}(\text{py})_4\text{Cl}(\text{NO})](\text{PF}_6)_2 \cdot 1/2\text{H}_2\text{O}$, which presents a GS to SI transformation rate close to 100%^[2].



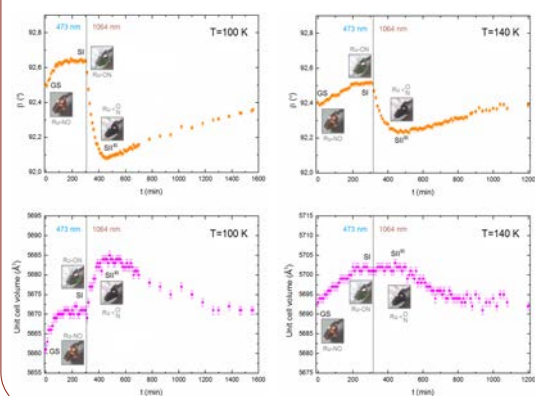
Thermal decay curves of (a) SI and (b) SII. The figure is taken from paper^[3]. For comparison optical measurements were performed at T=100K and at T=180K when the lifetime of SII is very short. This allows to probe the role of SII as an intermediate one.



Starting from SII^{IR} (mixed GS-SII state^[3]) at 100K

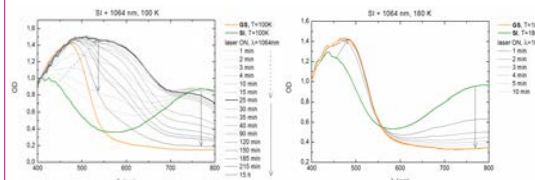
- ❖ The irradiation with $\lambda=473\text{nm}$ drives the system back to SI state.
- ❖ And the irradiation with $\lambda=532\text{nm}$ brings system to mixed GS-SI.

Clear structural signatures on lattice parameters during the photo-switching between GS, SI and SII



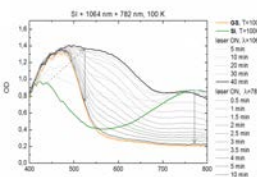
SI → SII → GS under IR light irradiation

- ❖ The irradiation of SI state at T=100K with $\lambda=1064\text{nm}$ leads to the relaxation towards GS through a high population of SII^[3].
- ❖ At 180K when the lifetime of SII species is short the OD evolution under the infra-red irradiation shows an isosbestic point.



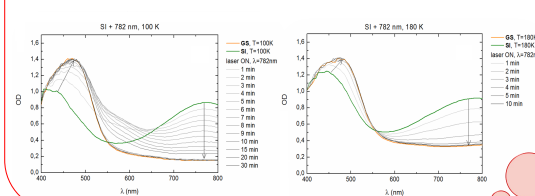
SI → SII under IR light irradiation and SII → GS under red light irradiation

- ❖ The very different kinetics is observed when mixed GS-SII state is irradiated with $\lambda=782\text{nm}$, the back photo-switching process takes place only after a few tens of minutes.



SI → GS under red light irradiation

- ❖ As observed on the prototype SNP compound the irradiation of SI in the red region $\lambda=782\text{nm}$ at T=100K leads to complete transformation back to GS.
- ❖ The role of SII as an intermediate state can be probed by following the OD evolution at T=180K, where a short lifetime of SII results in the appearance of isosbestic point.



References

- [1] a) U. Hauser, V. Oestreich, H.D. Rohrweck, *Z. Phys.* **1977**, A280, 17-25; b) U. Hauser, V. Oestreich, H.D. Rohrweck, *Z. Phys.* **1977**, A280, 125-130; c) U. Hauser, V. Oestreich, H.D. Rohrweck, *Z. Phys.* **1978**, A284, 9-19.
- [2] B. Cormary, I. Malfant, L. Valade, M. Buron-Le Cointe, L. Toupet, B. Delley, D. Schaniel, N. Mockus, T. Woike, K. Fejfarova, V. Petricek, M. Dusek, *Acta Cryst.* **2009** B.65 612-623.
- [3] D. Schaniel, B. Cormary, I. Malfant, L. Valade, T. Woike, B. Delley, K. W. Krämer, H.U. Güdel, *PCCP* **2007** 9 3717-3724.
- [4] L. Khadeeva et al., submitted

Acknowledgement. We thank Fabienne Alary, Loic Toupet and Marco Cammarata for fruitful discussion.

Conclusions

- ❖ A two-step photon absorption is found to play the predominant role in Ru-NO to Ru-ON photo-switching process in blue spectral range.
- ❖ A different pathway and kinetics are observed when IR irradiation is used.
- ❖ The optical signature of SII during Ru-NO/Ru-ON transition is extracted from a simple kinetic model and is different from that experimentally observed during photo-switching back to Ru-NO, SII^{IR}. The geometry of the transient SII species is suggested to be different under the blue and IR irradiations.
- ❖ Future time-resolved experiments will allow to characterize both long-lived SII state(s) and the transient short-lived SI* and SII* species.

Nitric oxide (NO) is recognized to be involved in a wide variety of physiological processes, including blood pressure control, neurotransmission, cell death and inhibition of tumor growth^[1].

1992 NO was named «Molecule of the year», the active development of NO donors has began
1998 Nobel prize in Physiology and Medicine for the discovery of NO signaling role in cardiovascular and nervous systems was awarded to L. Ignarro, R. Furchtgott, F. Murad

At present a lot of efforts are directed towards the synthesis of new NO donor molecules able to deliver NO on specific targets. Ruthenium nitrosyl compounds are of particular interest because of their inherent stability in aqueous media in comparison with most of alternative metallic complexes (Fe, Mn, Cr). Indeed they release NO only when exposed to light, which makes them perfect candidates for the photodynamic therapy (PDT).

Photo-induced chemical transformation: the case of ruthenium nitrosyl compound

Liya Khadeeva,^a Marylise Buron-Le Cointe,^a
Wawrzyniec Kaszub,^a Maciej Lorenc,^a
Isabelle Malfant^b

^a Institut de Physique de Rennes, Université de Rennes 1,
CNRS, 263 av. G. Leclerc, 35042 Rennes, France
^b Laboratoire de Chimie de Coordination,
205 route de Narbonne, F-32077 Toulouse, France

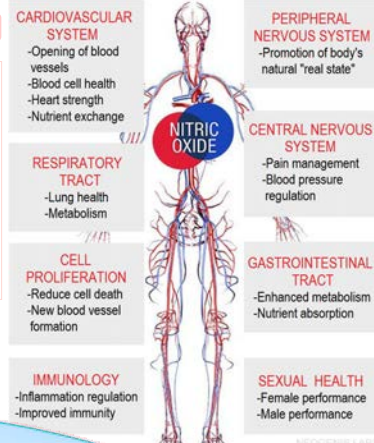
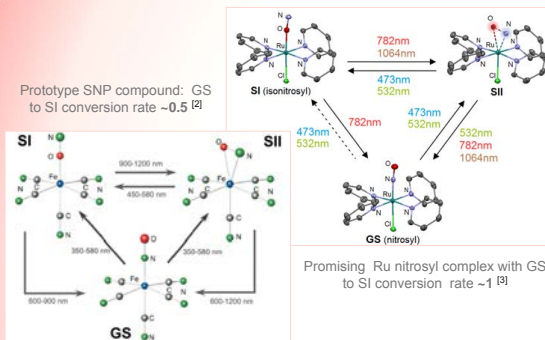
E-mail: liya.khadeeva@univ-rennes1.fr

Journée Recherche 2016
January, Rennes,
FRANCE

Photo-isomerization

NO molecule

NO donors and their linkage isomers



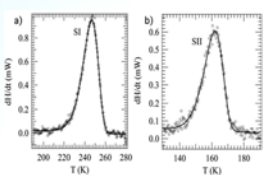
Since the discovery of long-lived photo-induced metastable states at low temperature in sodium nitroprusside dihydrate compound (so-called SNP)^[4],

the photo-switching between nitrosyl (GS), isonitrosyl (SI) and side-on (SII) configurations has been observed in many analogous systems containing the [ML₅NO] molecule, where M = Fe, Ru, etc. and L = F, Cl, Br, CN, etc.

The obtained population rates can vary from one compound to another and reasons for such differences remain unclear.

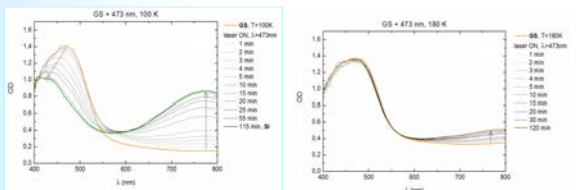
We present here the experimental investigations by visible absorption spectroscopy and X-Ray diffraction on single crystals of [Ru(py)₄Cl(NO)](PF₆)₂·1/2H₂O, which presents a GS to SI transformation rate close to 100%^[3].

Thermal decay curves of (a) SI and (b) SII. The figure is taken from paper^[2]. For comparison optical measurements were performed at 100K and at 180K when the lifetime of SII is very short. This allows to probe the role of SII as an intermediate.



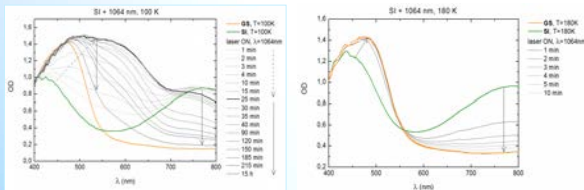
Single crystal: optical signatures during the photo-switching between GS, SI and SII

- GS → SII → SI under blue light irradiation
- The excitation of crystal at T=100K with λ=473nm results in quasi-complete photo-switching from GS to SI (almost complete transformation).
- At T=180K, when the lifetime of SII state is quite short, the GS→SI photo-chemical reaction is limited to ~10%.



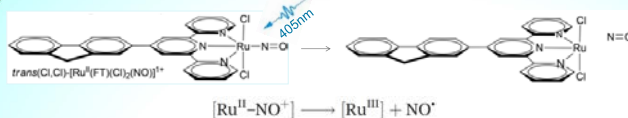
SI → SII → GS under IR light irradiation

- The irradiation of SI state at T=100K with λ=1064nm leads to the relaxation towards GS through a high population of SII^[2].
- At 180 K when the lifetime of SII species is short the OD evolution under the infra-red irradiation shows an isosbestic point.



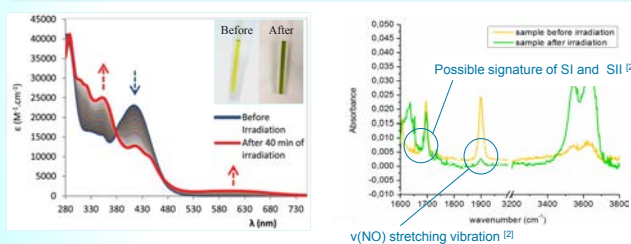
NO release

Ruthenium nitrosyl complexes are promising candidates in PDT, which allows the drug delivery to occur specifically in targeted cells on which the light irradiation can be focused. We study a different system in here as it shows fair quantum yield.

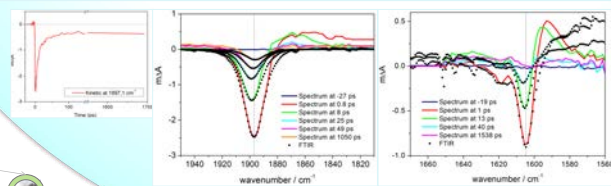


Trans(Cl,Cl)-[Ru^{II}(FT)Cl₂(NO)]PF₆ isomer solution in acetonitrile, which shows under continuous light irradiation (405 nm) the complete NO photo-release after around 40 minutes^[5]. It can be detected by significant changes in the absorption spectra in the UV-visible region.

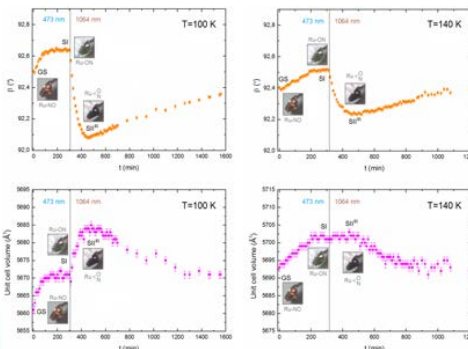
Solution: changes in the UV-visible and IR absorption spectra under 405nm irradiation



Solution: time-resolved IR absorption spectra probing ν(NO) stretching vibration and possible photo-isomerization before the NO release.



Single crystal: structural signatures during the photo-switching between GS, SI and SII



Conclusions

- Single crystal: a two-step photon absorption is found to play the predominant role in Ru-NO to Ru-ON photo-switching process in blue spectral range.
- Single crystal: a different pathway and kinetics are observed when IR irradiation is used.
- Solution: the formation of photo-product under the 405nm irradiation was shown, however the photo-isomerization process before the NO release was not observed in studied compound.

References

- [1] NOx Related. Chemistry, 2015, Vol.67, Academic Press, Ed. R. v. Eldik, J.A. Olabe.
- [2] D. Schaniel, et al., PCCP 2007, 9, 3717-3724.
- [3] B. Cormary, et al., Acta Cryst. 2009, B.65, 612.
- [4] a) U. Hauser, V. Oestreich, H.D. Rohrweck, Z. Phys. 1977, A280, 17-25; b) U. Hauser, V. Oestreich, H.D. Rohrweck, Z. Phys. 1977, A280, 125-130; c) U. Hauser, V. Oestreich, H.D. Rohrweck, Z. Phys. 1978, A284, 9-19.
- [5] J.Akl, et al., Dalton Trans, 2014, 43, 12721.

